



HAL
open science

Multiscale modeling of the radiation-induced segregation in Ni-based and Fe-based dilute alloys

Liangzhao Huang

► **To cite this version:**

Liangzhao Huang. Multiscale modeling of the radiation-induced segregation in Ni-based and Fe-based dilute alloys. Materials Science [cond-mat.mtrl-sci]. Université Paris-Saclay, 2020. English. NNT : 2020UPASP048 . tel-03551870

HAL Id: tel-03551870

<https://theses.hal.science/tel-03551870>

Submitted on 2 Feb 2022

HAL is a multi-disciplinary open access archive for the deposit and dissemination of scientific research documents, whether they are published or not. The documents may come from teaching and research institutions in France or abroad, or from public or private research centers.

L'archive ouverte pluridisciplinaire **HAL**, est destinée au dépôt et à la diffusion de documents scientifiques de niveau recherche, publiés ou non, émanant des établissements d'enseignement et de recherche français ou étrangers, des laboratoires publics ou privés.

Multiscale modeling of the radiation-induced segregation in Ni-based and Fe-based dilute alloys

Thèse de doctorat de l'université Paris-Saclay

École doctorale n° 564, Physique en Île-de-France (PIF)
Spécialité de doctorat : Physique
Unité de recherche : Université Paris-Saclay, CEA, Service de Recherches de
Métallurgie Physique, 91191, Gif-sur-Yvette, France
Référent : Faculté des sciences d'Orsay

**Thèse présentée et soutenue en visioconférence totale,
le 10 novembre 2020, par**

Liangzhao Huang

Composition du jury :

Frederico Garrido Professeur, Université Paris-Saclay, CNRS/IN2P3	Président
Frédéric Christien Professeur, École des Mines de Saint-Étienne	Rapporteur & Examineur
Pascal Bellon Professeur, University of Illinois at Urbana-Champaign	Rapporteur & Examineur
Gilles Adjanor Ingénieur de recherche, EDF	Examineur
Maylise Nastar Directrice de recherche, CEA Saclay	Directrice de thèse

Acknowledgements

Ce travail de thèse a été réalisé au sein du Service de Recherche de Métallurgie Physique (SRMP) du CEA de Saclay. C'est une belle aventure qui a duré 1126 jours. Je tiens donc d'abord à remercier le guide de cette aventure, Maylise Nastar, pour ta curiosité sans limite et ton expertise qui m'ont beaucoup aidé à apprécier les vues. Je te remercie également pour ton enthousiasme immense et ton optimisme sans faille lorsque je me suis senti perdu pendant le voyage. Étant ton premier doctorant qui n'avait pas fait de stage avec toi, je te remercie du fond du cur de m'avoir fait confiance et, surtout, de m'avoir donné le temps de réfléchir et de découvrir la beauté des équations. De plus, merci de m'avoir montré et convaincu que les problèmes complexes et difficiles peuvent aussi être "marrants" et "intéressants", ce qui m'a donné le courage de franchir toutes les barrières dans le domaine de la science et de la vie. Je m'estime extrêmement chanceux d'avoir été dirigé par toi.

Je tiens à remercier Frédéric Christien et Pascal Bellon pour avoir accepté d'être rapporteurs de cette thèse. Leurs remarques et commentaires m'ont permis de mieux apprécier certaines possibilités et limites de mon travail de thèse. Je remercie également le président Frederico Garrido et l'examinateur Gilles Adjanor d'avoir fait partie du jury de la soutenance. Grâce à vous, la soutenance a été un véritable moment de plaisir avec des discussions intéressantes.

Cette aventure n'aurait pas été la même si elle n'avait pas été menée au SRMP. Je tiens à remercier toutes les personnes du laboratoire qui ont contribué à maintenir une atmosphère de recherche très dynamique et motivante. J'avoue que les présentations (devant tous les spécialistes de la métallurgie qui connaissent toujours bien le sujet) pendant les journées annuelles étaient toujours très stressantes, mais les discussions qui suivent étaient souvent très inspirantes. J'adresse des remerciements particuliers à Jean-Luc Bechade pour m'avoir bien aidé à m'intégrer dans le SRMP ; Patricia Matysiak et Rosabelle Berger qui résolvent très efficacement tous nos problèmes administratifs ; mon co-bureau Thomas Schuler pour son immense aide sur le code KineCluE (très puissant !), et pour toutes les discussions éclairantes couvrant presque tous les sujets de ma thèse ; Kan Ma, Marie Loyer-Prost, Lisa Belkacemi-Rebrab et Estelle Meslin, qui m'ont beaucoup aidé à découvrir le charme unique des approches expérimentales ; Frédéric Soisson pour des discussions fructueuses sur le fameux effet balistique sur la diffusion et la ségrégation (et pour tes efforts pour chercher des livres pour moi de temps en temps) ; Thomas Jourdan pour des échanges intéressantes sur le calcul de la force de puits ; Emmanuel Clouet pour des discussions rigoureuses sur le calcul de la force motrice de la diffusion ; Jean-Paul Crocombette sur ses remarques très pertinentes concernant la modélisation du cascade de déplacement ; Thomas Soyez, avec qui on s'est plaint de tout (la vie quotidienne, la politique en Chine ou en France, et surtout les "agréables" procédures administratives qu'on a

eu pendent nos thèses). Un grand merci également aux camarades des premiers jours, Marie, Ivan, Anton, Anne-Hélène, Camille, Emile, Elric, Denise, Adrien, Pierre, Aurélien, qui avaient l'air chaleureux à mon arrivée et m'ont beaucoup encouragé à m'intégrer au SRMP. Bien entendu, je n'oublie pas les camarades qui sont toujours à leurs propres aventures au laboratoire : Kangming, Yimi, Océane, Clovis, Pamela, Orane, Xixi, Yunho. Je remercie encore une fois l'ensemble des non-permanents et des permanents du SRMP. Je garde un excellent souvenir de vous tous et j'espère que nous aurons des occasions de nous retrouver après 2020 qui a été une année difficile.

Je n'oublie évidemment pas à remercier Luca Messina, pour le partage de ses données de la simulation DFT, notre nombreuse discussion et notre étroite collaboration.

Merci également à mes chers amis : Kan, Ziling, Zijie, Zijun, Guodong, Yanshu, Nan, avec qui nous avons passé six ans ensemble à l'IFCEN et décidé de venir découvrir la France en même temps.

Je remercie infiniment mes parents, ma soeur et mon beau-frère, qui m'ont beaucoup soutenu durant ces trois années, malgré la distance de 10 000 kilomètres qui nous sépare : *My heartfelt thanks to my family for your unconditional love and understanding when I was a long way from home!* Finalement, un grand merci à une personne infiniment importante, Lu, qui est toujours là pour moi, comme le soleil de mes jours et l'astre de mes nuits.

Contents

Nomenclature	2
Introduction	5
1 Bibliographical research	7
1.1 Equilibrium properties of lattice defects	8
1.2 Radiation damage and microstructure	13
1.3 Phenomenology of diffusion under irradiation	26
1.4 Atomic-scale modeling of diffusion under irradiation	40
1.5 Summary	46
2 Calculation of phenomenological transport coefficients	49
2.1 Introduction of diffusion in non-equilibrium system	50
2.2 Modeling of diffusion mechanisms under irradiation	51
2.3 Diffusion theory of systems under forced atomic relocations	54
2.4 Diffusion in far-from-equilibrium systems: beyond the linear response theory . .	64
2.5 Diffusion properties in model alloys	69
2.6 Sensitivity study with respect to the model and alloy parameters	73
2.7 Summary and concluding remarks	78
3 Analytical modeling of RIS: application to Ni- and Fe-based alloys	81

3.1	Introduction	82
3.2	Modeling of RIS	84
3.3	DFT energy database of Ni- and Fe-based alloys	93
3.4	Diffusion properties in Ni- and Fe-based alloys	98
3.5	RIS in Ni- and Fe-based alloys	103
3.6	Comparison between experimental measurement and analytical results	121
3.7	Summary and concluding remarks	126
4	Effect of strains on the point-defect concentration and solute RIS in pure Fe and Fe-based alloys	129
4.1	Introduction	130
4.2	Diffusion and elasticity	130
4.3	Elastodiffusion in Fe	135
4.4	Elastodiffusion in Fe-based alloys	141
4.5	Sink strength and bias factors of an edge-dislocation	145
4.6	Radiation-induced segregation at an edge dislocation in Fe-based alloys	155
4.7	Summary	160
	Conclusions and prospects	163
	A Elastic dipole tensors of solute-point defect pairs	167
	B Résumé substantiel	177

Nomenclature

AKMC Atomic kinetic Monte Carlo

bcc Body-centered cubic

CPG Chemical potential gradient

DFT Density functional theory

dpa Displacement per atom

DTE Displacement threshold energy

EBR Experimental breeder reactor

FAR Forced atomic relocation

fcc Face-centered cubic

FP Frenkel pair

I Interstitial

MD Molecular dynamics

NESS Non-equilibrium steady state

NN Nearest neighbour

NRT NorgettRobinsonTorrens

PD Point defect / point-defect

PKA Primary knock-on atom

PPM Path probability method

RCS Replacement collision sequence

RIP Radiation-induced precipitation

RIS Radiation-induced segregation

SCMF Self-consistent mean-field

SI Spherical inclusion
SIA Self-interstitial atom
SRO Short-range order
TIP Thermodynamics of irreversible processes
V Vacancy

Introduction

Excess point defects (PDs) are massively generated in materials under irradiation [1–3] or during severe plastic deformation such as shearing [4, 5], torsion [6, 7] and ball milling [8–10]. Irradiation produces Frenkel pairs of vacancy and self-interstitial. They diffuse, and they interact between them, or with atoms, as well as with the microstructure of the material [11]. They are absorbed by structural lattice defects (e.g., grain boundaries, dislocation lines) acting as PD sinks. The elimination of PDs at structural defects induces sustained fluxes of PDs from the bulk area towards sinks. By exchanging with nearest neighbour atoms, PDs produce net fluxes of atoms: this is the so-called flux coupling phenomenon. Unlike PDs, sustained flux of solute atoms may go in both directions, towards or away from the PD sinks, depending on the sign of the solute-vacancy kinetic correlations. Flux coupling is the main kinetic process controlling the redistribution of solute atoms in alloys driven by an excess of PDs [12–20].

In materials under irradiation, the non-equilibrium solute redistribution in the vicinity of PD sinks is called Radiation-Induced Segregation (RIS). Not only chemical species but also PDs form a concentration profile at sinks. We choose to call it RIS of PDs. The latter is systematically negative, with a concentration profile dropping to thermal equilibrium concentration at sinks. Solute RIS results from the PD RIS. It occurs at every PD sink even at very small radiation dose [21]. Therefore, RIS is often a precursor for heterogeneous precipitation of secondary phases at PDs sinks [19]. RIS may lead to strong modifications of the mechanical, corrosion and dimensional properties of materials [11].

There are experimental studies investigating the dependence of RIS on the microstructure of the irradiated sample and the irradiation conditions, including the nature of the irradiation particles [22, 23], the radiation dose and dose rate [24, 25], and temperature [16, 26]. However, it is still very difficult to obtain an accurate estimation of the RIS amount of PDs and solute atoms at different conditions. This should be complemented with theoretical studies. Up to now, there is no modeling method of RIS accounting for the full set of reactions between PDs, solute atoms, and structural defects.

As long as RIS is not coupled to a precipitation phenomenon, RIS profiles can be obtained by solving the PD and solute diffusion equations near PD sinks. Main input parameters of the diffusion equations are the phenomenological Onsager transport coefficients of the systems. These coefficient resulting from the atomic transport are affected by irradiation and stress. Irradiation introduces new atomic transport mechanisms—the forced atomic relocations (FARs), which involve the collective motion of atoms within irradiation displacement cascades. Unlike the thermally activated mechanisms leading the system toward equilibrium, these diffusion

mechanisms are mostly athermal. They do not obey the microscopic detailed balance. They compete with thermal diffusion mechanisms by promoting disordered atomic configurations [27]. The microstructure of an irradiated material results from the interplay between thermal and athermal PD reactions and jumps. Athermal microscopic events prevent the use of standard methods of statistical thermodynamics and kinetics. The stress-strain field generated by structural defects modifies the PD and solute diffusion properties [28]. A heterogeneous stress-strain field also modifies the diffusion driving forces, i.e., the gradients of chemical potentials [29].

The purposes of the present work are to (i) extend the self-consistent mean-field (SCMF) theory to athermal diffusion mechanisms to calculate the transport coefficients from an *ab initio* PD jump frequency database; (ii) develop a RIS model accounting for the full set of PD reactions and solute-PD interactions in dilute alloys; (iii) investigate the effects of elasticity on diffusion and RIS properties of PDs and solute atoms.

In Chapter 1, we review a few experimental and theoretical studies dedicated to the equilibrium segregation properties of structural lattice defects, the modeling of primary radiation damage, and the characterization and calculation of diffusion properties of materials under irradiation. Equilibrium and RIS are atomic scale phenomena depending on atomic scale PD reactions, an averaged sink strength of the microstructure, and macroscopic diffusion coefficients. Therefore, RIS is by essence a multi-scale phenomenon, that requires simulation techniques from atomic to macroscopic scales, and phenomenological analytical modeling from mesoscopic to macroscopic scales.

In Chapter 2, we present the modeling of athermal mechanisms specific to a displacement cascade. Then, we explain our theoretical developments of the SCMF theory, to extend its application to the athermal diffusion mechanisms. We apply our theoretic development to the calculation of the phenomenological transport coefficients in model binary alloys.

In Chapter 3, we derive an analytical RIS model based on the one developed by Martínez et al. [30] for a kinetic regime dominated by the PD annihilation reactions at sinks. In the present model, we include the FAR diffusion mechanism and the recombination reactions between vacancy and self-interstitial, and we account for the variation of both driving forces and Onsager transport coefficients with local concentration. Relying on our model, we systematically investigate the effect of the sink strength, the radiation flux, or the temperature on the RIS properties of a few Ni- and Fe-based alloys.

Finally, in Chapter 4, we solve the PD and solute diffusion equations near an edge-dislocation using the finite-difference method. The elastodiffusion effects are incorporated and a particular emphasis is placed on the effects of the matrix elastic anisotropy, the PD anisotropy and PD-solute interactions on the diffusion properties, the sink strength, the sink bias, and the steady-state distribution of PDs and solute atoms in Fe-based alloys.

Chapter 1

Bibliographical research

Contents

1.1	Equilibrium properties of lattice defects	8
1.1.1	Formation enthalpy of a solute atom in the dilute limit	8
1.1.2	Formation enthalpy of a point defect	10
1.1.2.1	Pure metal	10
1.1.2.2	Dilute binary alloy	11
1.1.3	Equilibrium segregation at extended lattice defects	12
1.1.3.1	Experimental observations	12
1.1.3.2	Modeling approaches	13
1.2	Radiation damage and microstructure	13
1.2.1	Primary damage	14
1.2.1.1	Modeling of a displacement cascade	14
1.2.1.2	Experimental characterization of the primary damage	14
1.2.1.3	PD production models and dpa concept	15
1.2.1.4	Numerical simulation of displacement cascades	15
1.2.1.5	Effects of solute atoms on defect production	17
1.2.1.6	Forced atomic relocation in displacement cascades	18
1.2.2	Point defect concentration and sink strength	20
1.2.2.1	Elastic bias and mean-field rate theory	20
1.2.2.2	Analytical calculation of the sink strength	22
1.2.2.3	Numerical calculation of the sink strength	25
1.3	Phenomenology of diffusion under irradiation	26
1.3.1	Diffusion within the Thermodynamics of Irreversible Processes	26
1.3.1.1	Atomic fluxes in terms of chemical potential gradients	27
1.3.1.2	Atomic fluxes in terms of concentration gradients	28

1.3.2	Measurement of tracer diffusion coefficients under irradiation	29
1.3.2.1	Tracer diffusion experiment	29
1.3.2.2	Calculation of the phenomenological coefficients	31
1.3.3	Radiation-induced segregation	33
1.3.3.1	Pioneering work and first observations of RIS	33
1.3.3.2	Effect of temperature	35
1.3.3.3	Effect of dose, dose rate and radiation particles	36
1.3.3.4	Emulation of neutron irradiation with respect to RIS	36
1.3.3.5	Evaluation of flux couplings	38
1.3.3.6	Analytical solutions of radiation-induced segregation in steady state	39
1.4	Atomic-scale modeling of diffusion under irradiation	40
1.4.1	Point defect diffusion models	40
1.4.2	Effect of elastic interactions on point defect diffusion	42
1.4.3	On-lattice modeling of FAR effect on the long-term radiation damage evolution	45
1.5	Summary	46

This chapter aims at presenting a few previous studies dedicated to the equilibrium and radiation-induced segregation at structural defects. The production of point defects under irradiation, their diffusion, their coupling with atomic diffusion, have a strong impact on solute segregation. In Section 1.1, we briefly introduce the methods of calculation of the equilibrium point defect concentration, and the thermodynamic driving forces of solute segregation. In Section 1.2, we focus on the primary damage that is created under irradiation. We give a brief presentation of the methods used to simulate the radiation primary damage including displacement cascades. In Section 1.3, we introduce the phenomenological description of diffusion under irradiation. In Section 1.4, we present atomic-scale methods that are developed for the modeling of complex diffusion phenomena such as flux coupling induced by irradiation.

1.1 Equilibrium properties of lattice defects

In this section, we present the equilibrium properties of solute atoms, point defects (PDs), and their interactions with extended lattice defects.

1.1.1 Formation enthalpy of a solute atom in the dilute limit

We consider a dilute substitutional solution of B atoms in a matrix of A atoms at fixed temperature, T , and pressure, p_{ext} . We compute the formation enthalpy, $H_{\text{f,B}}$, of B in the A matrix. As illustrated in Fig. 1.1, $H_{\text{f,B}}$ corresponds to the difference of enthalpies between a

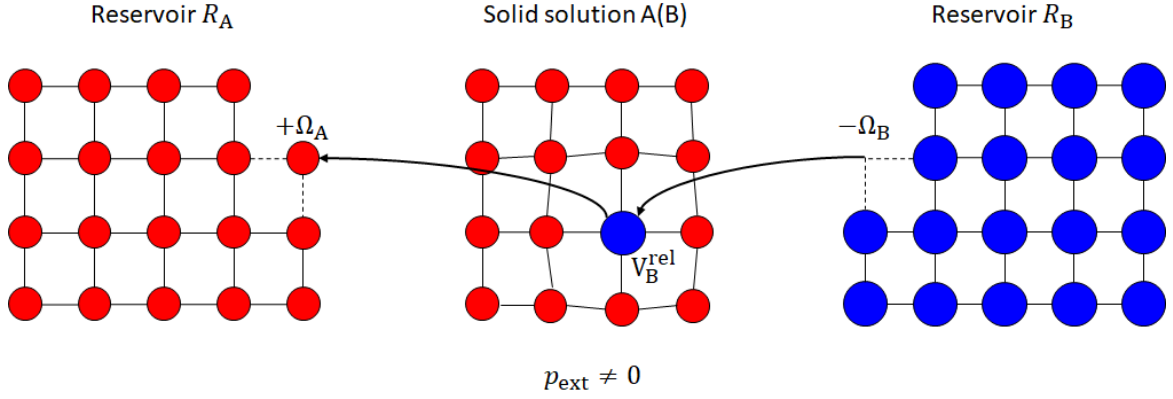


Figure 1.1: The process required in the definition of the formation enthalpy of solute atoms in a solid solute A(B): an A atom is removed from the solid solution, and placed at a site on the surface of a reservoir (R_A) of A atoms; and a B atom is removed from a reservoir (R_B) of B atoms, and placed at in the site previously occupied by the removed A atom. The process is at fixed temperature T and pressure p_{ext} .

system composed of a solid solution of N A atoms, a reservoir (R_B) of N_R B atoms, and a reservoir (R_A) of N_R A atoms; and a system composed of a solid solution containing 1 B atom and $(N - 1)$ A atoms, the reservoir R_B with a B atom less, and the reservoir R_A with an extra A atom:

$$H_{f,B} = E_{f,B}^0 - p_{\text{ext}} V_B^{\text{rel}} - p_{\text{ext}} \Omega_A + p_{\text{ext}} \Omega_B, \quad (1.1)$$

where $E_{f,B}^0$ is the solute formation energy, V_B^{rel} is the relaxation volume of solute atom B, and Ω_α is the atomic volume of atom $\alpha \equiv \text{A, B}$. The term $-p_{\text{ext}} V_B^{\text{rel}}$ corresponds to the work done during the relaxation of the solid solution when an A atom is replaced by a B atom. $-p_{\text{ext}} \Omega_A$ is the work done to place an A atom in the reservoir R_A , and $+p_{\text{ext}} \Omega_B$ is the one to remove a B atom from the reservoir R_B . For $\Omega_A \simeq \Omega_B$, the formation enthalpy of solute atoms writes

$$H_{f,B} = E_{f,B}^0 - p_{\text{ext}} V_B^{\text{rel}}. \quad (1.2)$$

Note that $H_{f,B}$ is the so-called the ordering (or mixing) enthalpy of the solid solution A(B). If negative, the system has an ordering tendency: there is no possible equilibrium between the solid solution A(B) and the reservoir of atoms B. If the ordering enthalpy is positive, the system has a clustering tendency and we may study the two-phase equilibrium, the dilute A-rich solid solution A(B) in equilibrium with the B-rich solid solution B(A). In the dilute limit, the equilibrium concentration (or solubility limit) of solute B in matrix A, in equilibrium with a Reservoir of atoms B, is given by [31]:

$$C_B^{\text{eq}} = \exp\left(-\frac{H_{f,B}}{k_B T}\right), \quad (1.3)$$

where $H_{f,B}$ is the formation enthalpy of B in matrix A.

1.1.2 Formation enthalpy of a point defect

We are now interested in the equilibrium concentration of PD (d with $d \equiv V$ for vacancies and I for self-interstitial atoms (SIAs)), C_d^{eq} , in alloys. As for the solubility limit solute B in a metal A in equilibrium with a B-rich solid solution, the equilibrium PD concentration in a metal A in equilibrium with its vapor, is an exponential of the formation enthalpy [31–33]

$$C_d^{\text{eq}} = \exp\left(-\frac{H_{f,d}}{k_B T}\right), \quad (1.4)$$

where the formation enthalpy $H_{f,d}$ depends on the applied pressure. Note that here, the reservoir of vacancy is the vapor phase.

1.1.2.1 Pure metal

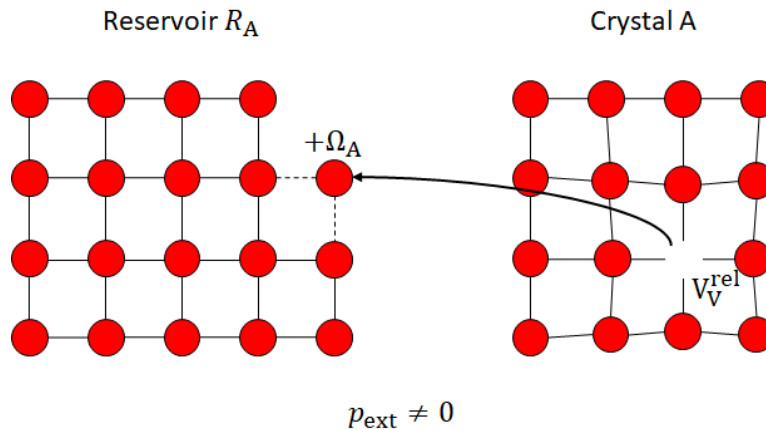


Figure 1.2: The process required in the definition of the formation enthalpy of vacancies in crystal A: removal of an atom from crystal A, and its placement at a site on the surface of reservoir R_A . The process is at fixed temperature T and pressure p_{ext} .

As for the solute B in metal A, we compute the PD formation enthalpy as a difference of enthalpy. As illustrated in Fig. 1.2, a vacancy is formed by removing an atom of crystal A, and placing such atom on the surface of reservoir R_A . During this process, the variation of the volume of crystal A corresponds to the relaxation volume of the vacancy (V_V^{rel}). The volume of the reservoir R_A is increased by one atomic volume of atom A, Ω_A .

Regarding SIAs, their formation is an inverse process of the vacancy one. As shown in Fig. 1.3, a SIA is formed by removing an atom from the surface of reservoir R_A , and placing such atom close to an occupied site of crystal A. The variation of the volume of crystal A corresponds to the relaxation volume of the SIA (V_I^{rel}), and the volume of the reservoir R_A is decreased by Ω_A .

We express the formation enthalpy of PD ($d \equiv V, I$) as the total change of the Gibbs free energy (free enthalpy) during the formation process:

$$H_{f,d} = E_{f,d}^0 - p_{\text{ext}} V_d^{\text{rel}} - s_d p_{\text{ext}} \Omega_A, \quad (1.5)$$

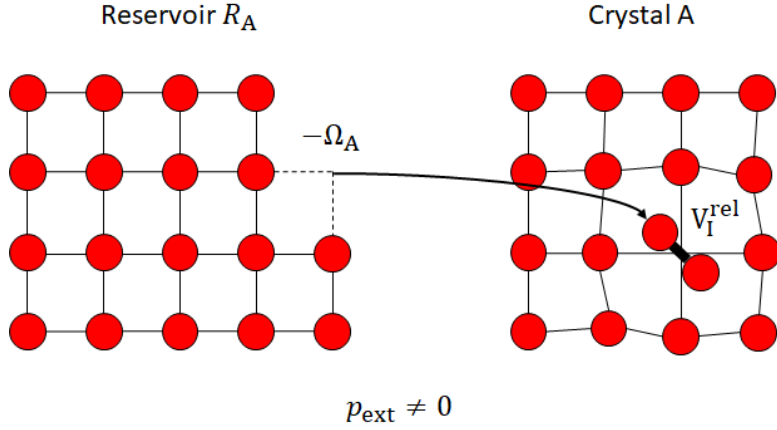


Figure 1.3: The process required in the definition of the formation enthalpy of dumbbell-SIAs in a crystal A: removal of an atom from the surface of reservoir R_A , and its placement at an unoccupied site of crystal A. The process is at fixed temperature T and pressure p_{ext} .

where $E_{f,d}^0$ is the vacancy formation energy and s_d is the number of created lattice site during the process, i.e., $s_d = +1$ for vacancies and -1 for SIAs.

1.1.2.2 Dilute binary alloy

In alloys, the equilibrium PD concentration depends on the solute concentration due to the presence of solute-PD interactions. In the dilute limit, where interactions between solute atoms are ignored, Lomer has introduced a formulation of the alloying effect on the equilibrium PD concentration [34–36]:

$$C_V^{\text{eq}} = C_V^{\text{eq},0} \left\{ 1 + z C_B \left[\exp \left(-\frac{E_b^{1\text{NN}}}{k_B T} \right) - 1 \right] \right\}, \quad (1.6)$$

where $C_V^{\text{eq},0}$ is the vacancy equilibrium concentration in the pure metal, z is the coordination number, and $E_b^{1\text{NN}}$ is the solute-vacancy binding energy at the 1-st nearest neighbour (1-NN) distance. A more general expression of the equilibrium PD concentration in dilute alloys can be derived from the low-temperature expansion (LTE) formalism [37–41]. In a very dilute binary alloy, we consider five clusters only: monomer vacancies, monomer SIAs, monomer solute atoms, the solute-vacancy pair, and the solute-SIA pair. All pair configurations within the defined kinetic radius r_k are accounted for. The equilibrium PD concentration includes the concentrations of all corresponding monomers and pairs:

$$C_d^{\text{eq}} = C_d^{\text{mono}} + C_d^{\text{pair}} - C^{\text{corr}}. \quad (1.7)$$

By definition, the total mono-PD concentration $C_d^{\text{mono}} = C_d^{\text{eq},0}$. Besides, it is given by $C_d^{\text{mono}} = C_d^0 Z_d$, where C_d^0 is the concentration of each component of monomer d , and Z_d is the partition function of the monomer d (e.g., $Z_V = 1$ for vacancies, and $Z_I = 6$ for $\langle 110 \rangle$ -dumbbells due to their six possible orientations in a cubic lattice). Over most cases, PD equilibrium concentrations are much smaller than the solute concentration, C_B , even within a dilute approach. In

this case, the pair concentration can be expressed as:

$$C_d^{\text{pair}} = C_d^0 C_B Z_{Bd}, \quad (1.8)$$

where Z_{Bd} is the partition function of the B- d pair. C^{corr} is a correction term accounting for the sites that monomers cannot occupy because they are occupied by pairs. This correction term equals to $C_d^{\text{eq},0} C_B Z_{Bd}^0$, where Z_{Bd}^0 is the number of all possible pair configuration within the kinetic radius, r_k . Therefore, Eq. (1.7) becomes

$$C_d^{\text{eq}} = C_d^{\text{eq},0} \left(1 + C_B \frac{Z_{Bd} - Z_{Bd}^0}{Z_d} \right). \quad (1.9)$$

In the case where the solute-vacancy interactions are restricted to 1-NN pair interactions, $Z_{BV} - Z_{BV}^0 = z \left[\exp\left(-\frac{E_b^{1NN}}{k_B T}\right) - 1 \right]$, we recover Lomer’s expression (Eq. (1.6)). As shown in Ref. [42], a LTE of the equilibrium PD concentration may include bigger cluster than pairs.

1.1.3 Equilibrium segregation at extended lattice defects

The equilibrium segregation refers to compositional changes near the extended structural defects of an alloy in thermodynamic equilibrium [43]. This segregation usually affects the composition of only a few atomic planes around the defect. The thermal segregation at dislocations and interfaces like surfaces and grain boundaries, is a common phenomenon in metallurgy and has been the subject of numerous experimental and theoretical studies. Note that structural extended defects such as grain boundaries and dislocations are not equilibrium defects. Under the hypothesis that these are static defects that do not evolve, there have been investigations of “the equilibrium segregation” at these defects.

1.1.3.1 Experimental observations

Many techniques are developed to investigate the interfacial segregation, at different scales according to their sensitivity to the interface—from the atomic scale to a upper scale over a few atomic planes. First, we present the most used techniques dedicated to the characterization of segregation at surfaces. The Auger electron spectroscopy (AES) [44,45] gives averaged information on a few atomic planes under the surface. The ion scattering spectroscopy (ISS) gives more information than AES, depending on the energy of the incident ions: low-energy ion scattering (LEIS) allows to determine the composition at the surface plane only [46]; whereas, Rutherford backscattering spectrometry (RBS) gives information deep below the surface [47,48]. Regarding grain boundaries (GBs), an additional difficulty occurs because they are located inside the materials. Since intergranular segregation often leads to the embrittlement of materials, it is, in general, possible to cleave the material along the plan of GB [45,49]. In this case, the techniques dedicated to free surfaces (e.g., AES in most cases) may also be used to investigate GBs. It is also possible to detect and quantify the composition on the atomic plans near the surface or GB by wavelength dispersive X-ray spectroscopy (WDS) [50–52]. This technique is almost insensitive to the surface contamination and oxidation. This is a significant advantage

with respect to AES because WDS makes it possible to quantify GB segregation on an *ex-situ* fractured specimen [51]. The transmission electron microscopy (TEM) [53] and the atom probe tomography (APT) [54–56] are more straightforward techniques of inter-granular segregation analysis because one does not need to cleave the material along the GB. Both techniques achieve atomic-scale resolution, and provide a fine description of segregation at defects other than GBs, as for instance dislocation lines [57, 58].

1.1.3.2 Modeling approaches

Most of the theoretical work is dedicated to the investigation of interfacial segregation, based on energetic models [59–64]. From these studies, it is possible to draw the three main thermodynamic driving forces of the interfacial segregation phenomenon in a stable solid solute A(B):

- The first one involves the difference of interface enthalpies of pure metals A and B (corresponding to the surface tension multiplied by the surface area per atom): the species with the lowest surface enthalpy tends to segregate.
- The second one results from the elastic strain due to the difference in size of the solute and solvent atoms: the species with the biggest size tends to segregate.
- The third one is related to the ordering (or mixing enthalpy) of the alloy: in an alloy with a clustering tendency, the minority species tends to segregate, whereas in an alloy with an ordering tendency, it is the opposite.

Note that the third driving force is identified to mainly control the segregation profile. At temperatures where the solid solution is less stable than a two-phase equilibrium, or an ordered phase, the interface may trigger the bulk ordering [65] and disordering [66], the phase separation [67], and the formation of specific 23 ordered structures [68].

There are structural defects such as dislocations, that produce a long range elastic field. The size effect contribution to the equilibrium segregation then results from the elastic interactions between the structural defect and the various atomic species. We will show in Section 4.6, how these elastic interactions produce a change of the solute concentration in the vicinity of an edge dislocation.

1.2 Radiation damage and microstructure

Irradiation first leads to primary damage where atoms are relocated, and excess PDs are created. In this section, we present models of primary radiation damage leading to the production of PDs (Section 1.2.1). Then, we present the standard mean-field reaction-diffusion model of the PD population under irradiation (Section 1.2.2).

1.2.1 Primary damage

Primary damage resulting from an ion or neutron irradiation is generally modeled as a cascade of atomic displacements. PD production and forced relocation of atoms are by-products of the displacement cascade. Here, we present models and experimental characterization techniques of the primary radiation damage.

1.2.1.1 Modeling of a displacement cascade

During irradiation, atoms are regularly hit by incident particles. At the time of the collision, the incident particle transfers kinetic energy to the primary knock-on atom (PKA). If this energy is below the displacement threshold energy (DTE), the PKA will only vibrate around its position unless a PD is located nearby, in which case the atom may exchange its position with the PD [27, 69]. For a recoil energy well above DTE (e.g., typically 1 keV in metals), the PKA will move away from its original site, thereby creating Frenkel pairs (FPs) and transferring kinetic energy to neighbouring atoms. Then, the latter will move away from their positions, so on so forth, resulting in recoil atomic collision processes and locally intense material heating. Many experimental studies and numerical simulations [70–72] have shown that the recoil collision time scale is of the order of 0.1 to 1 picoseconds. The following process is a quench-like event where the locally heating area rapidly cools down at a time scale of 1 to 10 picoseconds. The above stage is commonly considered to be athermal in the sense that the thermally-activated processes are not significant because the time scale is too short. This athermal event is conceptually referred to as an atomic displacement cascade, which is first proposed by Brinkman [73, 74]. However, there are some shreds of evidence showing that the displacement cascade is, in fact, affected by thermodynamics [75]. This process is the so-called primary damage of an irradiation.

1.2.1.2 Experimental characterization of the primary damage

Direct observation of the atomic displacement cascade is difficult due to their short time scale and small size scale [72]. However, some of the characteristics of the displacement cascades can be deduced from the examination of the fine microstructural features formed after irradiation at low doses. The experimental investigations yielding the best estimation of PD production consists of measuring a characteristic parameter such as the electrical resistivity after cryogenic irradiation and subsequent annealing [76, 77]. There are less direct experimental measurements, such as X-ray scattering [78], positron annihilation spectroscopy [79], and small-angle neutron scattering [80]. Transmission electron microscopy is broadly used to characterize the defects formed at the end of the cascades, including the dislocation loops [81, 82], and stacking fault tetrahedra [83].

1.2.1.3 PD production models and dpa concept

Given the difficulty to directly observe displacement cascades by experimental techniques, a few models are proposed to estimate the number of displacements. The latter is referred to as the number of FPs produced by a cascade. Norgett, Robinson, and Torrens (NRT) propose a model to predict the total number of created FPs (N_d) in function of the total deposited energy (T_d) in the cascade [84], which is given by

$$N_d(T_d) = \begin{cases} 0, & T_d < E_d, \\ 1, & E_d < T_d < \frac{2E_d}{0.8}, \\ \frac{0.8T_d}{2E_d}, & T_d > \frac{2E_d}{0.8}, \end{cases} \quad (1.10)$$

where E_d is the DTE ranging from 20 to 100 eV for different materials [85]. Note that T_d equals to the total incident particle energy minus the energy lost in electronic stopping power. The NRT model gives a good estimation of the number of FPs created upon the recoil collision stage [86]. However, it overestimates the number of remaining FPs at the end of the cascade because it ignores the in-cascade recombination. In order to account for the athermal recombination, Nordlund et al. [87] introduce an efficiency factor ξ_{arc} into the NRT model:

$$N_d(T_d) = \begin{cases} 0, & T_d < E_d, \\ 1, & E_d < T_d < \frac{2E_d}{0.8}, \\ \xi_{arc} \frac{0.8T_d}{2E_d}, & T_d > \frac{2E_d}{0.8}, \end{cases} \quad (1.11)$$

where ξ_{arc} is referred to as the fraction of defects surviving from the in-cascade recombination. It is a function of the deposited energy in the cascade, T_d .

However, the NRT model is still widely used as a standard to compute atomic displacement rates because of its simplicity. The number of displacements in a given volume of material normalized by the number of atoms in the same volume, yields the displacements-per-atom (dpa) unitless quantity:

$$\text{dpa} = \frac{\text{Number of displacements in the volume}}{\text{Number of atoms in the volume}}. \quad (1.12)$$

The dpa unit is widely used to quantify primary radiation damage in materials. It corresponds to the fraction of displaced atoms per atom. A significant advantage of this dpa unit is that it provides a general basis for the comparison of data extracted from different irradiation sources [72].

1.2.1.4 Numerical simulation of displacement cascades

Besides the analytical NRT model, atomic-scale simulation methods provide a more detailed description of displacement cascade. The molecular dynamic (MD) method is an essential

tool for investigating the cascade behaviors. This method relies on an inter-atomic function describing the system energy and the forces applied on each atom as a function of the positions and chemical nature of the surrounding atoms [72, 86]. Even if the time and size scales of displacement cascades are small (typically a few nanometers and a few hundred picoseconds), MD simulation can be computationally demanding [72]. Below we present the main characteristics of a radiation cascade with a focus on the properties of PDs and atoms that will impact long-distance atomic diffusion. Extensive reviews on the cascade modeling can be found in Refs. [11, 72, 86].

The typical evolution of a displacement cascade simulated by a MD method is as follows. A highly energetic and disordered region is initially developed in the cascade during the stage of recoil collision. Locally, the displacement cascade process produces a large excess number of PDs, as well as atomic mixing, since most of the atoms are displaced [88]. The evolution of the created Frenkel pair numbers with time is shown in Fig. 1.4. The number of PDs sharply increases in the recoil collision stage, and reaches a peak value at around 0.1 to 1 picoseconds, depending on the deposited energy in the cascade. After this first stage, the cascade becomes a so-called heat spike, where the material is locally liquid-like, and the diffusion of atoms can be rapid in this region [89]. The excess energy eventually dissipates, leading to a quench-like process, where the crystalline structure is recovered. During this process, many vacancy-SIA pairs nearby recombine in the cascade [73, 90, 91]. Note that this in-cascade recombination regime is different from the long-range recombination reaction regime resulting from long-range diffusion of PDs. They are athermal recombination reactions, which do not depend on the diffusion properties of PDs. This leads to a reduction of the PD numbers down to a steady-state value at the end of the quench-like process (after about 2 to 10 picoseconds). In the final state of the cascade, the remaining PDs are well separated.

A few studies rationalize the final state of the cascade by introducing replacement collision sequences (RCSs) [92, 93]. The first atom (i.e., PKA) is pushed off its site; then, it dissipates energy by pushing a second atom, which in turn pushes a third atom, so on so forth. The last displaced atom is left on an interstitial site because it is not energetic enough to displace another atom. At the end, a chain of atoms are displaced by one atomic site. A vacancy and a SIA are formed respectively at the beginning and the end of this chain. Such a RCS mechanism is consistent with the observed properties of the final cascade state, in particular the vacancy-rich central region that is surrounded by a region rich in interstitial-type defects. Calder et al. [94] shows that RCSs occur particularly in low-energy cascades. However, they do not appear to be the dominant mechanism explaining the defect separation in higher energy cascades (above 1 keV in their studies). The cascade dynamics would result from a more collective motion of numerous atoms [72]. For instance, Nordlund et al. [95] have reported coherent displacement events involving multiple atoms. Besides, a recent work of Calder et al. [96] identified a shockwave-induced mechanism leading to the formation of SIA-cluster at the periphery of the cascade.

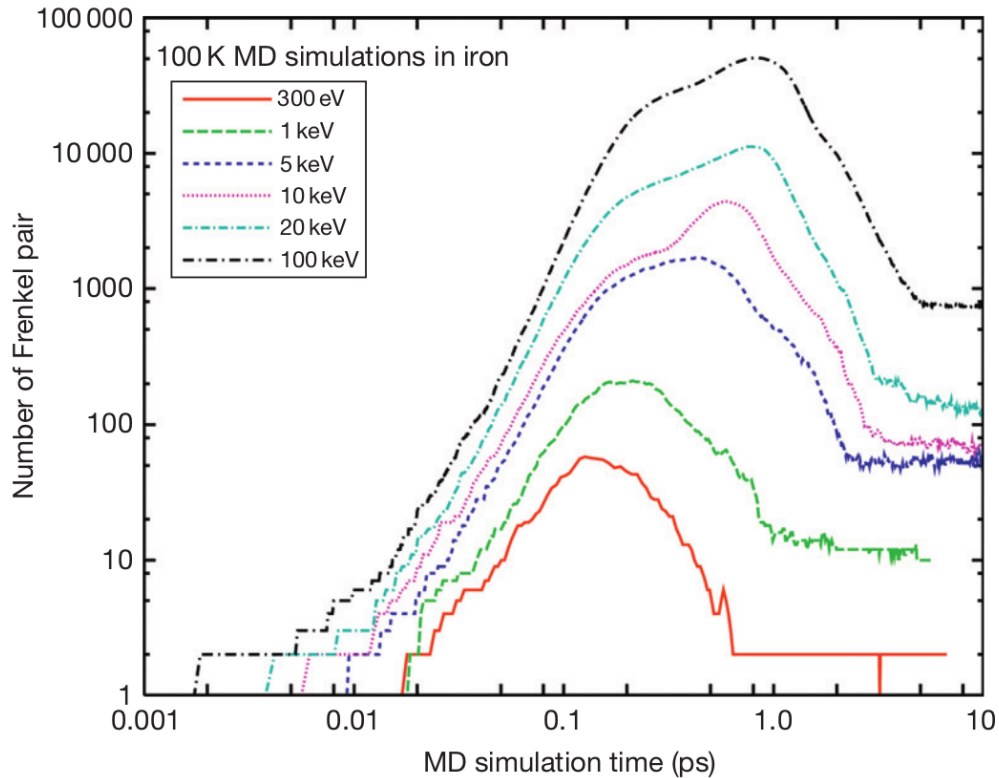


Figure 1.4: Time evolution of Frenkel pairs created during simulated displacement cascades in pure iron with different deposited energies in cascade. This figure is reproduced from Ref. [72]

1.2.1.5 Effects of solute atoms on defect production

Numerous MD studies are dedicated to the comparison of the displacement cascade behaviors between pure Fe and Fe-based alloys.

Malerba et al. [97] investigate the effect of Cr on displacement cascades. The MD simulations are carried out at 300 K for PKA energies from 0.5 to 15 keV. Compared to the primary damage in pure Fe, a slight increase of remaining defects is observed in Fe-10 at.%Cr. They claim that the presence of Cr does not affect the recoil collision phase because the mass of Cr is close to Fe, while it reduces the in-cascade recombination during the quench-like process. This finding appears to be related to the formation of a mixed Fe-Cr dumbbell that is highly stable at 300 K. They show that about 60% of the dumbbell interstitials contained a Cr atom, which is much higher than the nominal Cr concentration of 10%. However, a high mixed dumbbell fraction does not lead to a significant difference in the fraction of clustering PDs. Nevertheless, the stability and mobility of PD clusters containing solute atoms is different from the mono-chemical species clusters. Therefore, we expect the non-equilibrium distribution of dumbbells will have an impact on the damage accumulation. Such conclusions seem to be consistent with the experimental measurements [98]. Okada et al. [99] show that the addition of 0.1 at.% of Cr to ultra-pure Fe leads to more frequent formation of small SIA loops than ultra-pure Fe. Arakawa et al. [100] observe that interstitial loop mobility is significantly reduced, while its stability is much increased by the presence of Cr in α -Fe.

Becquart et al. [101] perform MD simulations of Fe(Cu) alloys, expecting an effect of vacancy clustering during the quench-like process on Cu precipitation. Simulations are performed at 600 K for PKA energies of 5, 10, and 20 keV, with Cu concentrations of 0, 0.2, and 2.0 at.%. They find that Cu has a great tendency to bind to mixed solute-defect clusters. This trend may have an influence on the long-term evolution of the microstructure, such as the formation of Cu clusters. However, no evidence for Cu clustering is observed during MD simulations.

Calder et al. [102] perform simulations of displacement cascades in Fe(C) alloys, with a carbon concentration between 0 and 1 at. % in order to analyze the effect of carbon on defect production. Simulations are carried out at 100 and 600 K for PKA energies of 5, 10, and 20 keV. In contrast to Fe(Cr), the presence of C does not show a significant effect on the volume fraction of the remaining PDs and the PD clustering. However, an important association of C atoms with vacancies and SIAs occurs. These mixed clusters are certainly due to the attractive binding energy between PDs and C. Similar to Fe(Cu), the primary damage is not affected by solute-PD binding even though this trapping may affect the long-term damage accumulation.

1.2.1.6 Forced atomic relocation in displacement cascades

After a quench-like process, many atoms of the displacement cascade are relocated from their original lattice sites. This forced atomic relocation (FAR) is broadly considered in the community of ion-beam mixing [86]. In pure materials, FAR has little effect on the microstructure because there is only one chemical species. However, most materials of interest are alloys of two and more components, and inevitably, include a few impurity elements. FAR has a great importance for understanding the dissolution of precipitates [103, 104] and the chemical disordering [105] in alloys. For instance, Siegel [106] investigate the effect of neutron irradiation on the order of Cu_3Au alloys at low temperatures. He estimated that, for each stable Frenkel pair created, many Cu and Au atoms exchange positions because of the massive changes in the electrical resistivity that occur after irradiation.

FAR occurs in the recoil collision stage as well as in the heat-spike stage. Various models are proposed to quantify the intensity of FAR in these two stages of displacement cascades. For instance, Sigmund et al. [107] attempt to calculate the magnitude of FAR in the recoil collision stage. They characterize the FAR intensity by an effective diffusion coefficient associated with FAR only. They conclude that this coefficient is proportional to the fluence Ψ (in ion/m²), and to the energy-deposition rate per ion F_D , which is referred to the deposited energy per depth and per ion going into collision:

$$Dt = \frac{\Psi F_D \gamma_{21} r^2}{3.648 N E_a}, \quad (1.13)$$

where t is the irradiation time, r is the mean range of the recoil distance of target atoms of average energy E_a , N is the atomic density in the matrix, and

$$\gamma_{21} = \sqrt{4(m_1 m_2) / (m_1 + m_2)^2}, \quad (1.14)$$

with m_1 and m_2 being the atomic masses of projectile and target, respectively.

There are also models accounting for FAR during the heat spike stage. For instance, in the model of Vineyard [89], FAR is assimilated to thermally-activated jumps in the region of

Table 1.1: Relocation efficiency in different materials.

	C	Al	Ti	Fe	Ni	Cu	Mo	Ru	Ag	Hf	Ta	W	Pt	Au
ξ [$\text{\AA}^5/\text{eV}$]	14	112	36	27	39	450	28	44	450	90	54	72	115	730

heat spike. Relying on a temperature model of the heat spike, one can obtain the total number of jumps

$$\eta = \frac{A_0 \lambda^2}{8\pi\kappa C Q^2}, \quad (1.15)$$

where λ is the energy per unit length along the ion trajectory, κ is the thermal conductivity of the matrix, C is the specific heat, and Q is the activation barrier of the jump. Many studies focused on the calculation of Q , which is suggested to be related to the cohesive energy of the target materials [108, 109].

Direct MD simulation is an efficient investigative tool of FAR without conceptually dividing the cascade into different stages. Norlund et al. [110] investigate FAR in many semiconductors and metals. They point out that in materials like Si, with low atomic mass and relatively high melting temperature, FAR mostly occurs in the recoil collision stage, while in most metals like Al, FAR mainly takes place in the heat-spike stage. Surprisingly, the relocation strength of Fe and Ni are close to the values predicted by analytical models in the recoil collision stage, indicating that the contribution of heat spike is low in these metals [86].

In order to compare the FAR intensities in different irradiated systems, Kim et al. [111] measure the tracer diffusion coefficients at a low temperature (6 K), so that the diffusion is mainly due to FAR. They define a normalized quantity

$$\xi = \frac{Dt}{\Psi F_D}, \quad (1.16)$$

which is nearly independent of the irradiation particle and dose. Note that the product ΨF_D is the deposited energy per unit volume. It can be calculated from a software like SRIM [112] and IRADINA [113, 114]. Besides, it can be related to dpa unit. According to the NRT model, the dpa and the product ΨF_D are related by the following equation

$$\text{dpa} = \frac{0.8\Omega}{2E_d} \Psi F_D, \quad (1.17)$$

where Ω is the atomic volume. In the same spirit, one can define the number of FAR per NRT-dpa as

$$\xi_{\text{NRT-dpa}} = \frac{Dt}{\text{dpa}} = \frac{2E_d}{0.8\Omega} \xi. \quad (1.18)$$

Note that ξ is often used to compare the relocation efficiencies deduced from different samples and irradiation energies [111]. Some of these results obtained from high energy ion irradiation are summarized in Tab. 1.1. In the same study, Kim et al. observe that the relocation

efficiency is dependent on the tracer element. Workman and coworkers [75] also evidence this thermodynamic effect on FAR.

1.2.2 Point defect concentration and sink strength

Main consequence of the primary radiation damage is the production of an excess of PDs [115, 116]. Then, PDs can be eliminated by mutual recombination, clustering, or annihilation on preexisting or radiation-induced defects in the microstructure, such as surfaces, grain boundaries, dislocations, or PD clusters. This non-equilibrium concentration of PDs directly affects diffusion under irradiation. We present here, the phenomenological models describing the evolution of the PD concentrations in irradiated systems.

1.2.2.1 Elastic bias and mean-field rate theory

The elimination rate of PDs at sinks depends on the nature of sink and PDs. Long-range elastic interaction between PDs and sinks mainly determine this elimination rate. For instance, dislocation have an absorption bias for SIA compared to vacancy. This preferential absorption of SIA, first proposed by Greenwood et al. [117], leads to an unbalanced elimination rate of SIA and vacancy, which may result in the precipitation of voids. This bias is due to the fact that the elastic interaction between the dislocations and SIAs is larger than the one between dislocations and vacancies due to the larger SIA relaxation volume. This elastic bias is introduced by Brailisford et al. in a mean-field model of PD kinetics (also called rate theory), in order to investigate the growth of PD clusters [118]. Within this model, rate equations are established for vacancies and SIAs by considering that the concentrations of sinks and PDs are homogeneous in space. The bulk concentrations of vacancies (C_V^b) and SIAs (C_I^b) are given by the following mean-field kinetic equations:

$$\begin{cases} \frac{dC_V^b}{dt} = \phi - K_R C_V^b C_I^b - \sum_s k_{s,V}^2 D_V (C_V^b - C_V^{\text{eq}}), \\ \frac{dC_I^b}{dt} = \phi - K_R C_V^b C_I^b - \sum_s k_{s,I}^2 D_I (C_I^b - C_I^{\text{eq}}). \end{cases} \quad (1.19)$$

In these equations, C_V^{eq} and C_I^{eq} are respectively the vacancy and SIA concentration at thermal equilibrium. D_I and D_V are respectively the SIA and vacancy diffusion coefficients. Note that, in general, the SIA diffuses much faster than the vacancies towards PD sinks (i.e. $D_I \gg D_V$) [11]. $K_R = (4\pi r_{\text{rec}}/\Omega)(D_I + D_V)$ stands for the SIA-V recombination rate. r_{rec} is the SIA-V recombination radius usually assumed to be of the same order of magnitude as the lattice parameter a_0 . Ω is the atomic volume. ϕ is the radiation dose rate i.e. the PD production rate in dpa/s. The index s designates the nature of sink, such as the dislocations and cavities. $\sum_s k_{s,V}^2 D_V$ and $\sum_s k_{s,I}^2 D_I$ correspond to the absorption rates of vacancies and SIAs, respectively. These rates depend on the nature, dimension and concentration of sinks [119]. $k_{s,V}^2$ and $k_{s,I}^2$ are the sink strength for respectively vacancies and SIAs. These parameters are directly related

to the mean free paths of migrating PDs in the lattice [119]. Heald et al. [120] quantified the absorption bias from the relative difference between the total sink strengths $k_V^2 = \sum_s k_{s,V}^2$ and $k_I^2 = \sum_s k_{s,I}^2$ by

$$B = \frac{k_I^2 - k_V^2}{k_I^2}. \quad (1.20)$$

By analogy, the bias of each sink writes

$$B_s = \frac{k_{s,V}^2 - k_{s,I}^2}{k_{s,I}^2}. \quad (1.21)$$

By construction, the bias value varies from 0 to 1 and $B_s = 0$ for a neutral sink (no bias).

In the stationary state, Eq. (1.19) gives the relationship between the bulk concentrations of vacancies (C_V^b) and SIAs (C_I^b)

$$\sum_s k_{s,V}^2 D_V (C_V^b - C_V^{\text{eq}}) = \sum_s k_{s,I}^2 D_I (C_I^b - C_I^{\text{eq}}), \quad (1.22)$$

where C_V^{eq} and C_I^{eq} are equilibrium concentrations of vacancies and SIAs at sinks, respectively.

Thereafter, we focus on the calculation of C_V^b , and use Eq. (1.22) to deduce C_I^b . Note that, in general, the SIA diffuses much faster than the vacancies towards PD sinks (i.e. $D_I \gg D_V$) [11]. Moreover, in metals, we may ignore the equilibrium concentration of SIA because, due to very large formation energies, its value is very small compared to C_I^b at any temperature and dose rate. Therefore, the stationary-state solution of system (1.19) for C_V^b is given by:

$$C_V^b = \frac{C_V^{\text{eq}}}{2} - \frac{k_V^2 \Omega}{8\pi r_{\text{rec}}(1-B)} + \sqrt{\left[\frac{C_V^{\text{eq}}}{2} + \frac{k_V^2 \Omega}{8\pi r_{\text{rec}}(1-B)} \right]^2 + \frac{\Omega}{4\pi r_{\text{rec}}(1-B)} \left(\frac{\phi}{D_V} \right)}. \quad (1.23)$$

At high temperature, C_V^b is close to C_V^{eq} . However, C_V^{eq} is negligible over most irradiation temperatures of interest [11]. Furthermore, in the case where the elimination of PD at PD sinks is dominant versus the SIA-V recombination i.e. $K_V \gg R$ with $K_V = k_V^2 D_V (C_V^b - C_V^{\text{eq}})$ and $R = K_R C_V^b C_I^b$, the vacancy concentration C_V^b is proportional to the ratio ϕ/D_V and given by:

$$C_V^b = \frac{1}{k_V^2} \left(\frac{\phi}{D_V} \right). \quad (1.24)$$

Furthermore, when $K_V \ll R$, the vacancy concentration is proportional to $\sqrt{\phi/D_V}$:

$$C_V^b = \sqrt{\frac{\Omega}{4\pi r_{\text{rec}}} \left(\frac{\phi}{D_V} \right)}. \quad (1.25)$$

One considers the effect of solute on the vacancy equilibrium concentration in dilute alloys by means of a low temperature expansion formalism [40, 121, 122]. Eventually, C_V^{eq} of a binary alloy is given by

$$C_V^{\text{eq}} = C_V^{\text{eq},0} \left[1 + \frac{(z - z_0) \bar{C}_B}{1 + (z - z_0) C_V^{\text{eq},0}} \right], \quad (1.26)$$

where \bar{C}_B is the nominal concentration of solute atoms B and $C_V^{\text{eq},0}$ is the equilibrium concentration in pure metal obtained from the vacancy formation enthalpy H_V^f and entropy S_V^f by:

$$C_V^{\text{eq},0} = \exp\left(-\frac{H_V^f - T S_V^f}{k_B T}\right). \quad (1.27)$$

z is the partition function associated with solute-vacancy pairs and z_0 is the one without any solute-vacancy interaction.

1.2.2.2 Analytical calculation of the sink strength

The mean-field rate model provides a way to predict the average PD concentrations in space. As shown by Eq. (1.24), in the sink-dominated regime, the concentration of PDs largely depends on the sink strength. We present below the analytical methods used to calculate the sink strength.

Close to the sink, we explicitly introduce the flux of PDs towards sink. Then, we solve the corresponding diffusion equation of PDs:

$$\begin{cases} \frac{\partial C_V}{\partial t} = \phi - K_R C_V C_I - \nabla \cdot \mathbf{J}_V, \\ \frac{\partial C_I}{\partial t} = \phi - K_R C_V C_I - \nabla \cdot \mathbf{J}_I, \end{cases} \quad (1.28)$$

where \mathbf{J}_V and \mathbf{J}_I are respectively the fluxes of vacancies and SIAs.

Nichols [119] proposes analytical solutions for various sink geometries, with different boundary conditions, at stationary state (i.e. $\partial C_V/\partial t = 0$, $\partial C_I/\partial t = 0$). Elastic interactions and the SIA-vacancy recombination are not considered (i.e. $B = 0$ and $K_R = 0$). In addition, the PD diffusion coefficients D_V and D_I are assumed to be homogeneous in space. Here, we present the general principles of this method. A sink is considered to be surrounded by a region free of sink, which has the same symmetry as the sink geometry. The volume of the surrounding region is directly related to the sink density ρ . In the approaches of Laplace and Poisson, boundary conditions are set at the outer surface of the region, δS_o , and at the surface of the sink, δS_i (Fig. 1.5). Boundary conditions are imposed on PD concentration or PD flux.

In the Laplace approach, PD production is neglected (i.e. $\phi = 0$). We obtain the vacancy concentration profile by solving the Laplace equation

$$\nabla \cdot \mathbf{J}_V = 0, \quad (1.29)$$

with the boundary conditions

$$\begin{cases} C_V(\delta S_i) = C_V^i, \\ C_V(\delta S_o) = C_V^o. \end{cases} \quad (1.30)$$

We deduce the vacancy flux, \mathbf{J}_V , as well as the current of vacancy I_V entering the sink across the surface δS_i :

$$I_V = \iint_{\delta S_i} \mathbf{J}_V \cdot \mathbf{n} \, dS, \quad (1.31)$$

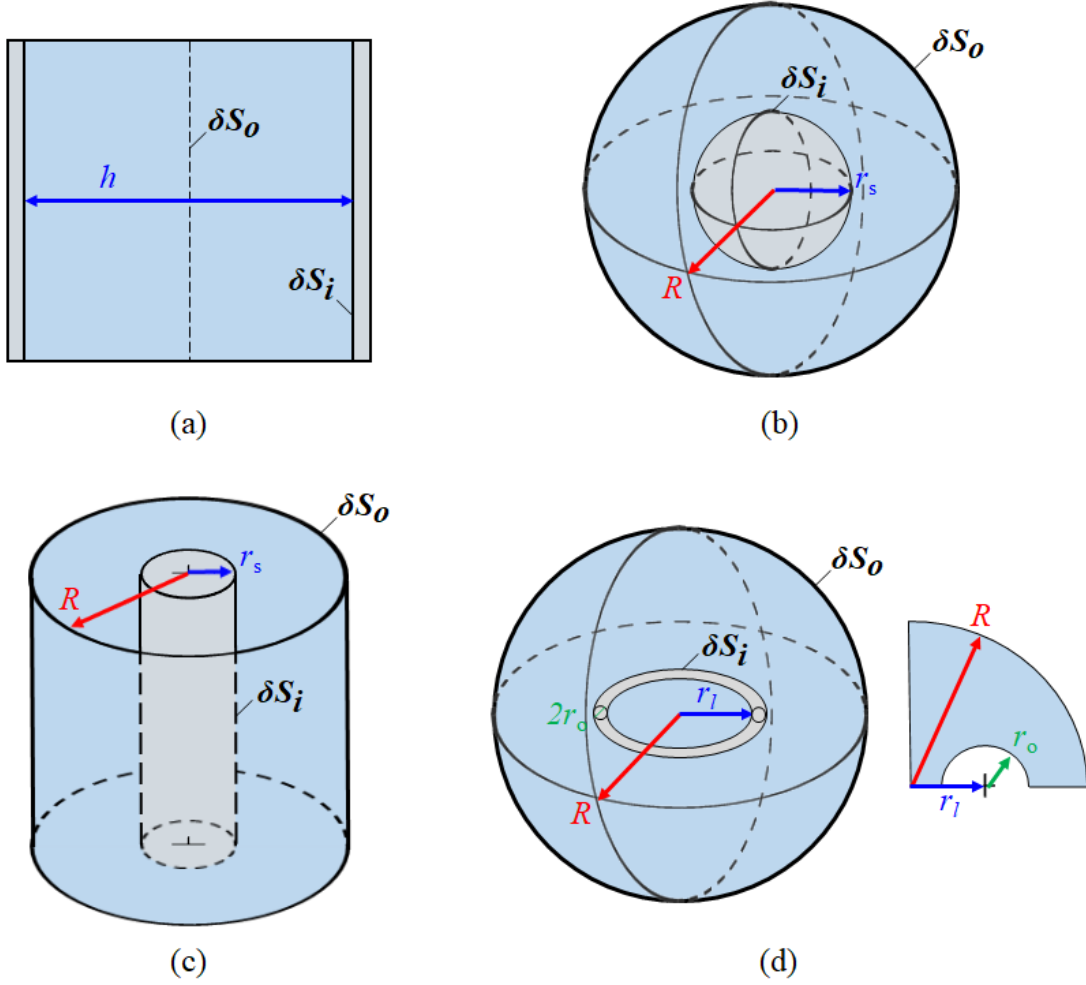


Figure 1.5: Sink geometries with (a) planar, (b) spherical, (c) cylindrical, and (d) toroidal symmetries.

with \mathbf{n} the normal vector of the surface δS_i . The total rate of vacancy loss at sinks is given by $k_V^2 D_V (C_V^o - C_V^i)$. The latter equals to total amount of vacancy entering those sinks per unit time, which is ρI_V . The sink strength k_V^2 is then deduced:

$$k_V^2 = \frac{\rho}{D_V (C_V^o - C_V^i)} I_V. \quad (1.32)$$

Note that the calculation of the SIA sink strength is similar. k_I^2 is deduced from Eq. (1.32) by replacing the index ‘V’ by ‘I’.

In the Poisson approach, we account for the radiation flux. In this case the vacancy concentration profile is obtained by solving the Poisson equation

$$\nabla \cdot \mathbf{J}_V = \phi, \quad (1.33)$$

where the concentration at the sink surface, δS_i , is fixed and the flux across the surface δS_o is set to 0:

$$\begin{cases} C_V(\delta S_i) = C_V^i, \\ \nabla C_V(\delta S_o) = 0. \end{cases} \quad (1.34)$$

Table 1.2: Analytical solution of sink strengths by various approaches, with different sink geometries.

Approach	Planar	Cylindrical	Spherical
Laplace	$\frac{4}{h^2}$	$\frac{2\pi\rho}{\ln\left(\frac{R}{r_s}\right)}$	$\frac{4\pi\rho r_s}{1 - \left(\frac{r_s}{R}\right)}$
Poisson	$\frac{8}{h^2}$	$\frac{2\pi\rho}{\ln\left(\frac{R}{r_s}\right) - \frac{1}{2} + \frac{1}{2}\left(\frac{r_s}{R}\right)^2}$	$\frac{4\pi\rho r_s \left(1 - \left(\frac{r_s}{R}\right)^3\right)}{1 - \frac{3}{2}\left(\frac{r_s}{R}\right) + \frac{1}{2}\left(\frac{r_s}{R}\right)^2}$
Wiedersich	$\frac{12}{h^2}$	$\frac{2\pi\rho \left(1 - \left(\frac{r_s}{R}\right)^2\right)}{\ln\left(\frac{R}{r_s}\right) - \frac{3}{4} + \left(\frac{r_s}{R}\right)^2 - \frac{1}{4}\left(\frac{r_s}{R}\right)^4}$	$\frac{4\pi\rho r_s \left(1 - \left(\frac{r_s}{R}\right)^3\right)}{1 - \frac{9}{5}\left(\frac{r_s}{R}\right) + \left(\frac{r_s}{R}\right)^3 + \frac{1}{5}\left(\frac{r_s}{R}\right)^6}$

In this table, for sinks with planar symmetric (e.g. interfaces), h is the spacing between two parallel sink surfaces. For sinks with cylindrical symmetric (e.g. dislocation lines), $\rho = (\pi R^2)^{-1}$ whereas, for sinks with spherical symmetric (e.g. cavities), $\rho = \left(\frac{4}{3}\pi R^3\right)^{-1}$

We obtain I_V by solving Eq. (1.34) and then, the sink strength k_V^2 is given from Eq. (1.32).

Wiedersich [123] has introduced a third method to determine the sink strength. He starts from Eq. (1.33), with the same boundary conditions. However, the total rate of vacancy loss in the region surrounding the sink is determined from the average concentration of vacancy \bar{C}_V in the region. The loss rate is then $k_V^2 D_V (\bar{C}_V - C_i)$. Thus, this approach requires a spatial integration of the vacancy concentration over the region between surfaces δS_o and δS_i . The sink strength k_V^2 is given by

$$k_V^2 = \frac{\rho}{D_V (\bar{C}_V - C_V^i)} I_V. \quad (1.35)$$

In Tab. 1.2, we provide the sink strength expressions of the most common sink geometries obtained by the Laplace, Poisson and Wiedersich approaches. Among these three approaches, the Wiedersich approach is considered to be the most realistic one [119, 124]. However, the Wiedersich as well as the Poisson approach does not provide a solution for toroidal symmetry such as dislocation loops (Fig. 1.5 (d)). For a loop of radius r_1 with a circular section of radius r_0 , surrounded by a spherical region of radius R , we obtain an analytical solution with the Laplace approach, by assuming that $R \gg r_1$. After Seeger and Gösele [125], the corresponding sink strength is given by

$$k_I^2 = k_V^2 = \frac{4\pi^2 \rho r_1}{\ln\left(\frac{8r_1}{r_0}\right)}. \quad (1.36)$$

It is worth noting that there exist analytical models of the sink strength, which account for the elastic interactions between PDs and the sink. Rauh and Simon [126] propose a solution for edge dislocations in an isotropic system by adding a drift term in the PD diffusion equations in order to account for the modification of the diffusion driving force due to the elastic interactions. Considering that the PD (d) is a spherical inclusion [127], i.e., the PD is perfectly spherical and isotropic, the elastic interaction energy is given by [128, 129]

$$E_d = p V_d^{\text{rel}}, \quad (1.37)$$

where V_d^{rel} is the relaxation volume of d , and p is the effective pressure acting on an unit volume which is given by:

$$p = -\frac{1}{3} \text{Tr}(\underline{\sigma}), \quad (1.38)$$

where $\underline{\sigma}$ is the tensor of the external stress applied to the system. For an isotropic material, Eq. (1.37) can be written as

$$E_d(r, \theta) = \pm k_B T L_d \frac{\sin(\theta)}{r}, \quad (1.39)$$

in polar coordinates (r, θ) . In this equation, L_d is a characteristic range of interaction between the dislocation and the PD (d):

$$L_d = \|\mathbf{b}\| \frac{\mu}{3\pi} \frac{1 + \nu}{1 - \nu} |V_d^{\text{rel}}|, \quad (1.40)$$

where μ is the shear modulus, ν is the Poisson's ratio, and \mathbf{b} is the Burgers vector. The sign \pm in Eq. (1.39) comes from the sign of the relaxation volume of PDs, which is positive for a SIA and negative for a vacancy. The analytical solution of Eq. (1.29) with the addition of the interaction energy (Eq. (1.39)) leads to the sink strength [126]:

$$k_d^2 = 2\pi\rho \sum_{n=0}^{\infty} (2 - \delta_{n,0}) (-1)^n \frac{I_n\left(\frac{L_d}{2r_s}\right) I_n\left(\frac{L_d}{2R}\right)}{I_n\left(\frac{L_d}{2r_s}\right) K_n\left(\frac{L_d}{2R}\right) - I_n\left(\frac{L_d}{2R}\right) K_n\left(\frac{L_d}{2r_s}\right)}, \quad (1.41)$$

where I_n and K_n are the modified Bessel functions of the first and second kinds, and δ is the Dirac function.

Dederichs and Schroeder [28], in addition to the elastic driving force, added the elasto-diffusion contribution resulting from the effect of the elastic interactions on the migration barriers. Based on this approach, Borodin et al. [130] propose an elastic model of the sink strength of a spherical cavity, though the elastic field generated by the cavity is assumed to be isotropic.

1.2.2.3 Numerical calculation of the sink strength

Compared to the analytical approaches, a numerical approach gives the possibility to consider non-isotropic elastic interactions and complex geometries of sinks. There are two categories of methods.

Continuous methods consist in solving the diffusion equation in order to obtain the PD concentration profiles and the total loss rate of PDs at sinks. Atomic-scale kinetic Monte Carlo methods solve the master equation by computing the jump probabilities of PDs, and applying a residential time algorithm.

First, we present the continuous methods used to solve the diffusion equation. They include finite difference methods [131,132], finite element methods [133–135], and more recently a phase-field method [136,137]. The studies relying on a finite difference or finite element method are in general, performed on a finite-size volume, including the sink. The boundary conditions applied to the PD concentration or flux are similar to the ones of Laplace or Poisson approaches. As for the numerical phase-field method, one may deal with complex PD sink microstructures by passing the problem into the reciprocal space. This method enables to consider the migration of PDs in a dislocation network that is close to realistic conditions. It naturally takes into account the long-range interactions between the sinks and the migrating PDs [136]. However, the interface between the sink and the solid is treated as a diffusing interface. This treatment can be inappropriate in case the sink strength is sensitive to the concentration and elastic strain close to the interface.

In kinetic Monte Carlo simulations [138–141], one generates PDs with a constant production rate (e.g., ϕ in the case of irradiation) in a simulation box containing the sink. Periodic boundary conditions are applied. The vacancy-SIA recombination is neglected. Therefore, at each Monte Carlo step, the possible events are the creation of a vacancy, the jump of a vacancy in the elastic field of the sink, and the elimination of a vacancy located within a given radius of the sink. The sink is assumed to be immobile, and its shape does not change. The sink strength is then deduced from the average PD concentration at the stationary state [139].

1.3 Phenomenology of diffusion under irradiation

In this section, we introduce the phenomenological diffusion phenomena in materials under irradiation. We present in Section 1.3.1 a macroscopic description of diffusion in the framework of the thermodynamics of irreversible process (TIP), where the definitions of phenomenological coefficients and diffusion coefficients are introduced. We describe in Section 1.3.2 some approaches to evaluate these kinetic coefficients. We then introduce in Section 1.3.3 an essential radiation-induced diffusion phenomenon, the so-called radiation-induced segregation (RIS).

1.3.1 Diffusion within the Thermodynamics of Irreversible Processes

Within the theoretical framework of the thermodynamics of irreversible processes, the fundamental driving force of diffusion is the chemical potential gradient (CPG) divided by temperature. However, it is difficult to measure the CPG in experiments. Since the chemical potential is related to the concentrations of species, atomic fluxes are often written in function of concentration gradients, which are easily accessible by experimental measurements. In this section, we present different formulations of the atomic fluxes, as well as the relationship

between them.

1.3.1.1 Atomic fluxes in terms of chemical potential gradients

According to TIP [19], the system is divided into cells, which are large enough to be in local equilibrium and small enough so that the compositions in a cell can be considered to be homogeneous. The transfer of the species α between two cells is described by a flux J_α . The evolution of PD concentration variation is obtained from Eq. (1.28), and the evolution of the local atomic concentration is derived from the continuity equation

$$\frac{\partial C_\alpha}{\partial t} = -\nabla \cdot \mathbf{J}_\alpha. \quad (1.42)$$

Within TIP, the flux of species α between neighbouring cells is assumed to be a linear combination of the thermodynamic driving forces (i.e. the chemical potential gradient). It is given by

$$\mathbf{J}_\alpha = -\sum_{\beta} L_{\alpha\beta} \frac{\nabla \mu_\beta}{k_B T}. \quad (1.43)$$

In this equation, k_B is the Boltzmann constant and T is the temperature. μ_β is the local chemical potential of species β in a cell. $\nabla \mu_\beta$ can be considered to be the difference of μ_β between neighbouring cells divided by the size of the cell. $L_{\alpha\beta}$ are the phenomenological L -coefficients of the Onsager matrix. By construction, the vacancy diffusion mechanism leads to the relation between fluxes of atoms and vacancies:

$$\mathbf{J}_V = -\sum_{\alpha} \mathbf{J}_\alpha^V. \quad (1.44)$$

From Eq. (1.43) and Eq. (1.44), we deduce an expression of the atomic flux \mathbf{J}_α^V as a linear combination of independent driving forces:

$$\mathbf{J}_\alpha^V = -\sum_{\beta} L_{\alpha\beta}^V \frac{\nabla \mu_\beta - \nabla \mu_V}{k_B T}. \quad (1.45)$$

As for the SIA-mediated transport, by construction of the diffusion mechanism, we have

$$\mathbf{J}_I = \sum_{\alpha} \mathbf{J}_\alpha^I, \quad (1.46)$$

In this case, from Eq. (1.43) and Eq. (1.46), \mathbf{J}_α^I is given by [19]

$$\mathbf{J}_\alpha^I = -\sum_{\beta \neq I} L_{\alpha\beta}^I \frac{\nabla \mu_\beta + \nabla \mu_I}{k_B T}. \quad (1.47)$$

Under irradiation, atomic diffusion is controlled by both vacancies and SIAs. By assuming these two contributions are additive, we obtain that

$$\mathbf{J}_\alpha = \mathbf{J}_\alpha^V + \mathbf{J}_\alpha^I. \quad (1.48)$$

1.3.1.2 Atomic fluxes in terms of concentration gradients

Here we present how we relate the concentration gradient to the thermodynamic driving forces in order to express the atomic fluxes in function of concentration gradients. The chemical potential of species α corresponds to the partial derivative of the Gibbs free energy G of the alloy, with respect to the number of atoms of species α , that is, N_α . The resulting chemical potential is a function of temperature and atomic fractions of the alloy components, $C_\alpha = N_\alpha/N$, with N being the total number of atoms. To obtain the relationship between the CPG and concentration gradient, we rely on the Gibbs-Duhem relationship [142]

$$\sum_{\alpha} C_{\alpha} \nabla \mu_{\alpha} = 0, \quad (1.49)$$

and the conservation law

$$\sum_{\alpha} C_{\alpha} = 1, \quad (1.50)$$

where the sum runs over the number of species including PDs, though in front of the interstitial concentration we need to add a minus sign. To deduce relationships between CPGs, we introduce either vacancies or SIAs into the alloy. Indeed, we ignore the interactions between them and assume their interactions with atomic species are additive. These interactions should be negligible because whenever vacancies and SIAs are close to each other, they annihilate through mutual recombination reaction. From Eq. (1.49) and Eq. (1.50), we deduce CPG of atomic species α in terms of the alloy and point defect driving forces

$$\nabla(\mu_{\alpha} - \mu_{\text{V}}) = - \sum_{k \neq \alpha} \frac{C_k}{1 - C_{\text{V}}} \nabla(\mu_k - \mu_{\alpha}) - \frac{1}{1 - C_{\text{V}}} \nabla \mu_{\text{V}}, \quad (1.51)$$

$$\nabla(\mu_{\alpha} + \mu_{\text{I}}) = - \sum_{k \neq \alpha} \frac{C_k}{1 + C_{\text{I}}} \nabla(\mu_k - \mu_{\alpha}) + \frac{1}{1 + C_{\text{I}}} \nabla \mu_{\text{I}}. \quad (1.52)$$

From the Gibbs free energy, we deduce the alloy and PD CPGs in function of concentration gradients. To compute the alloy CPG $\nabla(\mu_k - \mu_{\alpha})$ of species k relative to species α , we ignore the PD contributions. The latter is then equal to

$$\frac{\nabla(\mu_k - \mu_{\alpha})}{k_{\text{B}}T} = \frac{1}{k_{\text{B}}T} \sum_{j \neq \alpha} \left[\frac{\partial(\mu_k - \mu_{\alpha})}{\partial C_j} \right] \nabla C_j. \quad (1.53)$$

In a binary alloy A(B), there is a single alloy CPG $\nabla(\mu_{\text{B}} - \mu_{\text{A}})$. The CPG of a particle α is given by

$$\frac{\nabla \mu_{\text{B}}}{k_{\text{B}}T} = \Phi \frac{\nabla C_{\text{B}}}{C_{\text{B}}} \quad (1.54)$$

where Φ is the thermodynamic factor, which is equal to

$$\Phi = C_{\text{A}} C_{\text{B}} \frac{1}{k_{\text{B}}T} \frac{\partial(\mu_{\text{A}} - \mu_{\text{B}})}{\partial C_{\text{A}}}. \quad (1.55)$$

In systems under irradiation, the CPGs of vacancies and SIAs are non zero. Since vacancies and SIAs are dilute species, we can write the corresponding CPGs in function of their equilibrium concentrations C_V^{eq} and C_I^{eq} :

$$\mu_V = k_B T \ln \left(\frac{C_V}{C_V^{\text{eq}}} \right) \text{ and } \mu_I = k_B T \ln \left(\frac{C_I}{C_I^{\text{eq}}} \right). \quad (1.56)$$

Therefore, the CPG of vacancies is given by

$$\frac{\nabla \mu_V}{k_B T} = \frac{1}{C_V} \nabla C_V - \frac{\xi_{VB}}{C_B} \nabla C_B, \text{ with } \xi_{VB} = \frac{\partial \ln C_V^{\text{eq}}}{\partial \ln C_B}. \quad (1.57)$$

The expression of the CPG of SIA is the same except that letter ‘V’ is replaced by letter ‘I’.

CPGs and concentration gradients are related by Eq. (1.54) and Eq. (1.57). Hence, we can write the flux of species α in terms of concentration gradients:

$$\mathbf{J}_\alpha = - \sum_{\beta} D_{\alpha\beta} \nabla C_\beta, \quad (1.58)$$

where $D_{\alpha\beta}$ are the diffusion coefficients. They are functions of L -coefficients and partial derivatives of chemical potentials with respect to the atomic and point defect concentrations [19]. We can identify the analytical expressions of $D_{\alpha\beta}$ from Wolfer’s formulation (cf. Eq. (1.66) presented later in Section 1.3.3.6).

In the limit of dilute alloy, we have $C_B \ll C_A$ and $\Phi = 1$. In this case, the solute diffusion coefficient (D_B) and L_{BB} are directly related by

$$D_B = L_{BB}/C_B. \quad (1.59)$$

Moreover, since vacancy is very dilute even in a system under irradiation, the vacancy diffusion coefficient can be given by

$$D_V = D_{VV} = L_{VV}/C_V. \quad (1.60)$$

1.3.2 Measurement of tracer diffusion coefficients under irradiation

We review a few diffusion experiments to show how to measure diffusion coefficients in alloys submitted to irradiation. We also present the typical variation of diffusion coefficients with temperature at different damage rates in order to highlight the essential role of the PD sink strength. Given the difficulty of obtaining the full set L -coefficients from diffusion experiments, we introduce the numerical and analytical approaches that are developed to calculate these coefficients.

1.3.2.1 Tracer diffusion experiment

Irradiation produces freely-migrating PDs [11]. The increase of PD concentration accelerates the PD-mediated atomic diffusion under irradiation [11]. This phenomenon is the so-called

radiation-enhanced diffusion. Furthermore, atoms are also displaced through the FAR mechanism. The latter is dominant over radiation-enhanced diffusion at low temperatures. Atomic diffusion resulting from both migration mechanisms can be measured by following the movement of tracer atoms [143], which diffuse from the plane surface into the bulk of the material. The tracer diffusion coefficient is deduced from the resulting concentration profile of the tracer atoms, obtained by sectioning the materials into thin slices [143].

Müller et al. investigate self-diffusion in pure Ni irradiated by self-ions of 300 KeV [144]. Diffusion coefficients of the tracer ^{63}Ni are measured at different temperatures. The results are presented in Fig. 1.6. We observe an enhancement of tracer diffusion under irradiation. In addition, the self-diffusion coefficients deviate from the Arrhenius plot. At low temperatures, the diffusion coefficients are much higher than the thermal diffusion coefficients. Moreover, at a displacement rate of 1.2×10^{-2} dpa/s, we observe a temperature-independent diffusion coefficient below 600 K. We identify the latter as a diffusion regime dominated by FAR. The enhanced PD-mediated diffusion coefficient D_{acc} is written in terms of the PD diffusion coefficients D_V and D_I as [11]:

$$D_{\text{acc}} = f_V C_V D_V + f_I C_I D_I, \quad (1.61)$$

where C_V and C_I are respectively the concentrations of freely-migrating vacancies and self-interstitial atoms (SIAs). f_V and f_I are correlation factors accounting for the kinetic correlation during tracer diffusion [11]. D_{acc} is temperature-dependent. In most cases, the total diffusion coefficient D_{irr} is assumed to be the sum of the radiation-enhanced diffusion coefficient (D_{acc}) and the FAR contribution to diffusion (D_{FAR}):

$$D_{\text{irr}} = D_{\text{acc}} + D_{\text{FAR}}. \quad (1.62)$$

Between 600 and 900 K, the slope of D_{irr} differs from the slope of thermal diffusion. We observe that the slopes of D_{irr} vary with the displacement rate. It is suggested in Ref. [144] that this is due to the difference of microstructures resulting from different displacement rates. Indeed, as expected from a mean-field rate model (cf. Eq. (1.22)), concentrations of the excess freely-migrating PDs and their variation with temperature vary with the irradiation conditions and the sink microstructures. By assuming the recombination to be the dominant PD kinetic compared to the elimination at sinks, the PD concentration is independent of the sink microstructure. In this case, PD concentrations can be calculated relying on the rate theory model even though the sink information is missing. Therefore, D_{acc} can be deduced from Eq. (1.61). If the sink effect is dominant versus the recombination reaction, the analysis of the diffusion behaviors happens to be very difficult without any information on the sink microstructures.

Solute atom diffusion coefficients are measured in several systems under irradiation [145–149]. However, these data are not as complete as the self-diffusion data in Ni [144]. In most cases, only the temperature dependence is studied, whereas the effects of the displacement rate are not investigated. Also, information on the microstructure, in particular the PD sink density, is often missing. In this regard, we present below one of the full investigation of solute atom diffusion in Ref. [149]. Macht et al. measured the tracer diffusion coefficients of Ni in Cu under 300 KeV Cu^+ ions irradiation [149]. The FAR contribution, D_{FAR} , is measured to be $1.8 \times 10^{-20} \text{ m}^2\text{s}^{-1}$ from data obtained at temperature below 650 K. One obtains the enhanced diffusion coefficient after subtracting D_{FAR} , as shown in Fig. 1.7. We observe that the behavior of the tracer Ni diffusion coefficient in Cu with temperature is similar to the one

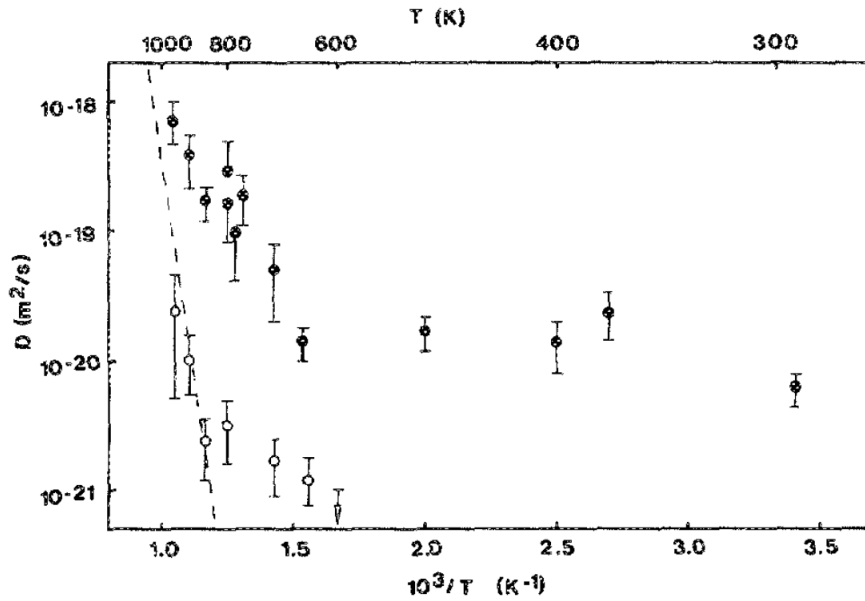


Figure 1.6: Self-diffusion coefficient in pure Ni under 300 KeV Ni⁺ irradiation with displacement rates estimated to be 1.2×10^{-2} dpa/s (●) and 1.2×10^{-4} dpa/s (○). The dashed line is the Arrhenius plot of the thermal self-diffusion in Ni. This figure is reproduced from Ref. [144].

of Ni self-diffusion plotted in Fig. 1.6. A deviation from the Arrhenius law is observed. Again, the concentration of PDs explains this deviation. By assuming the recombination to be the dominant PD kinetic compared to the elimination at sinks, one obtains D_{acc} from Eq. (1.61) and the results are plotted as dashed line in Fig. 1.7. The coherency with the measured coefficients is not satisfying, indicating that the sink effect cannot be neglected under such irradiation conditions. A more complete analysis of the diffusion behaviors is not possible due to the lack of information on the sink microstructures.

In the dilute binary alloy Ni(Cu), we deduce the L_{CuCu} coefficient from the Cu tracer diffusion coefficient by applying Eq. (1.59). Even if we know the self-diffusion coefficient of Ni, it is not enough to trace back the full L -coefficient matrix. We should rely on numerical simulation or analytical calculations to obtain the other L -coefficients.

1.3.2.2 Calculation of the phenomenological coefficients

Based on the atomic jump frequencies (presented later in Section 1.4.1), we can calculate the phenomenological L -coefficients by using different approaches.

The atomic kinetic Monte Carlo method is a powerful method to calculate these coefficients [150]. Relying on the Allnatt formulae [151, 152], we simulate and measure the equilibrium displacement fluctuations of the system and deduce from them the phenomenological L -coefficients. However, this method is limited to small domains of composition and temperature. Furthermore, it becomes unworkable when binding energies between PDs and neighboring atoms are high [153, 154]. In this case, the simulated trajectory can be trapped in low-energy

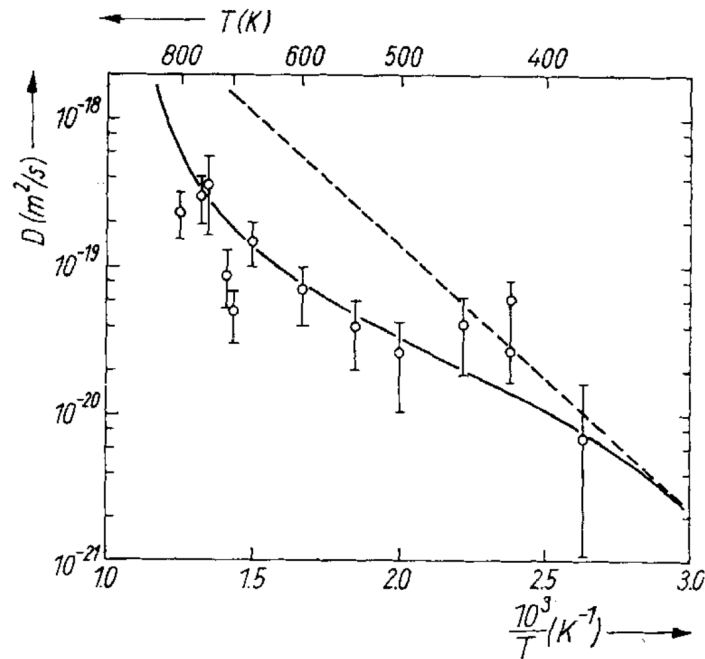


Figure 1.7: Ni tracer diffusion coefficient in Cu under 300 KeV Cu^+ irradiation with displacement rates estimated to be 2.0×10^{-2} dpa/s (\circ). The solid line is an eye-guide. The dashed line is obtained by assuming recombination to be the dominant PD kinetic. This figure is reproduced from Ref. [149]

PD-solute configurations, leading to correlation effects: after a jump, an atom has a high probability of exchanging again with the same PD and canceling its first jump. It is worth mentioning that in presence of an athermal diffusion mechanism, for instance the FAR mechanism in case of irradiation, the Allnatt formulae are not valid [40].

In concentrated alloys, approximate expressions can be deduced from mean-field diffusion models. The first diffusion model of concentrated alloys is proposed by Manning for the vacancy-mediated diffusion mechanism, by modeling the alloy as a random lattice gas model [155]. This model is then extended to the SIA-mediated diffusion mechanism [156]. However, the effect of short-range order (SRO) on the L -coefficients is not accounted for. Some attempts are made to include SRO effects using a Manning-type formulation, but such a formulation is not consistent with the thermodynamics [157, 158]. The current diffusion models, including SRO effects, are based on either the self-consistent mean-field theory (SCMF) [153, 159–162] or the path probability method (PPM) [163–165]. The PPM models of vacancy-mediated diffusion are proposed in ordered alloys [164] and body-centered solid solution [163, 165]. As for the approach based on the SCMF theory, models of vacancy diffusion in fcc alloys, including the solute drag phenomenon, and models of SIA in alloys are proposed [153, 154, 166].

In dilute alloys, it is possible to deduce exact analytical expression of the L -coefficients because the count of vacancy paths is relatively limited (cf. Refs [19] and [20] for reviews). We will present in Chapter 2 our method of calculation of the L -coefficients relying on the self-consistent mean-field theory [159, 160], and the KineCluE code [167].

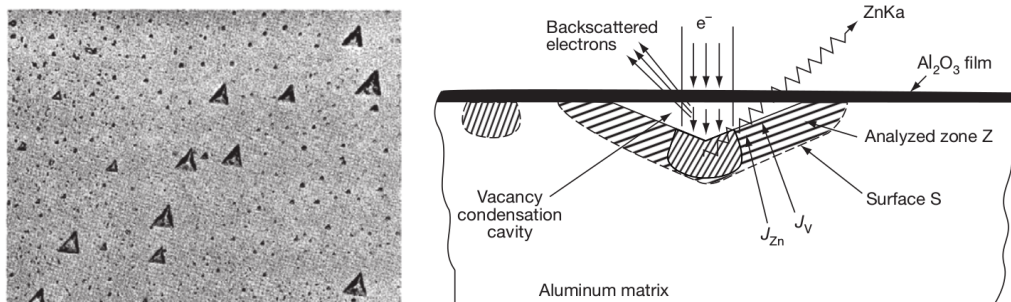


Figure 1.8: One of Anthony's experiments. After quenching of an AlZn alloy, vacancies condense in small pyramidal cavities (left). Electronic probe measurements reveal enrichment of Zn around the cavities. This figure is reproduced from Ref. [169]

1.3.3 Radiation-induced segregation

Permanent irradiation produces sustained fluxes of PDs towards PD sinks. Due to differences of diffusion coefficients between species and flux couplings, a preferential transport of one of the alloy components may occur. This leads to a local chemical redistribution in the vicinity of sinks. The latter phenomenon is the so-called radiation-induced segregation (RIS). RIS phenomena are very common in alloys under irradiation and have important technological implications. For instance, RIS may be strong enough to transform austenite grains into ferrite in stainless steel due to the segregation of Ni towards grain boundaries under neutron irradiation [168].

While an equilibrium segregation modifies the composition of the alloy on a few atomic planes, RIS generally extends over 5–20 nanometers. RIS is an out-of-equilibrium phenomenon mainly controlled by the kinetic properties of point defects, whereas equilibrium segregation results from the thermodynamic properties of the alloy. Though RIS is the result of both thermodynamics and flux couplings, RIS modeling studies usually ignore the thermodynamic segregation tendencies.

In order to better understand RIS, in this section, we present a few experimental observations. Then, we give a brief description of the RIS models.

1.3.3.1 Pioneering work and first observations of RIS

From systematic studies of non-equilibrium segregation in aluminum alloys resulting from the creation and elimination of quenched vacancies, Anthony predicts the RIS phenomenon [12, 13, 169]. He suggests that the segregation under irradiation should be much stronger than that in quenched alloys because the excess vacancy concentration and their flow towards sinks can be sustained for much longer time [12]. Anthony and coworkers observe non-equilibrium segregation of various solute atoms at pyramidal cavities resulting from the clustering of vacancies at the oxide metal interface. This segregation is explained by a coupling between the flux of vacancy into the cavities and the flux of solute atoms (e.g. Zn as shown in Fig. 1.8). Within the framework of the thermodynamics of irreversible processes, Anthony [12, 13, 169] also discussed

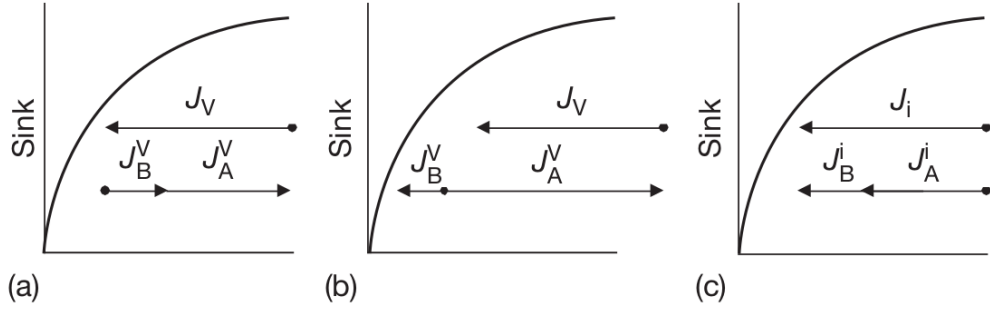


Figure 1.9: Segregation mechanisms with respect to the coupling between point defect and atom fluxes in a binary A(B) alloy. (a) An enrichment of B occurs if $J_B^V/C_B < J_A^V/C_A$, and a depletion if not. (b) An enrichment of B due to the vacancy drag. (c) An enrichment of B occurs if $J_B^I/C_B > J_A^I/C_A$ and a depletion if not.

the mechanisms of the non-equilibrium segregation based on previous results in Refs. [170, 171]. He analyzed the impact of flux coupling on solute segregation by distinguishing two separate flux coupling regimes. The total flux of atoms is equal to the vacancy flux, but they are in the opposite directions. If both the fluxes of A and B are in opposite direction to the vacancy flux (Fig. 1.9 (a)), one can expect an enrichment of B when the J_B^V/C_B is smaller than J_A^V/C_A , whereas in the opposite case, when $J_B^V/C_B > J_A^V/C_A$, a depletion of B is expected. If the fluxes of A and B are in opposite directions (Fig. 1.9 (b)), the vacancy drags the solute atom B by following circular jump sequences around B between two exchanges with B. In this case, the vacancy and solute fluxes are in the same direction moving towards sinks. In such a situation, an enrichment of B is expected.

Experimental evidences of RIS are obtained since the first observation in austenitic steels [14–16, 26, 172, 173]. The measurement of the concentration profiles by Auger spectroscopy reveals a systematic positive RIS of undersized solute atoms (e.g., Ni), which can be more easily found in interstitial sites, but a negative RIS of oversized solute atoms (e.g., Cr). Following these results, Okamoto and Wiedersich conclude that RIS in austenitic steels is controlled by the migration of solute-SIA complexes [14]. They introduce this new RIS mechanism (Fig. 1.9 (c)) in addition to the vacancy-controlled mechanisms. However, Marwick explains later the same experimental observations by introducing a modeling of the solute-vacancy flux coupling in concentrated alloys, as illustrated in Fig. 1.9 (a). This flux coupling is named as an inverse Kirkendall effect [173]. According to the thermal diffusion data, he states that Ni diffuses more slowly compared with Cr. To this day, we do not know the relative contribution of vacancies and SIAs to RIS in austenitic steels. This is because we lack information on the stability and mobility of PD clusters and the effect of local environment on these parameters.

In dilute alloys, the number of different solute-PD configurations is small. Thus, solute-PD binding energies are clearly defined and often play a key role in RIS. Hence, RIS in dilute alloys is commonly explained by the diffusion of solute-PD complexes.

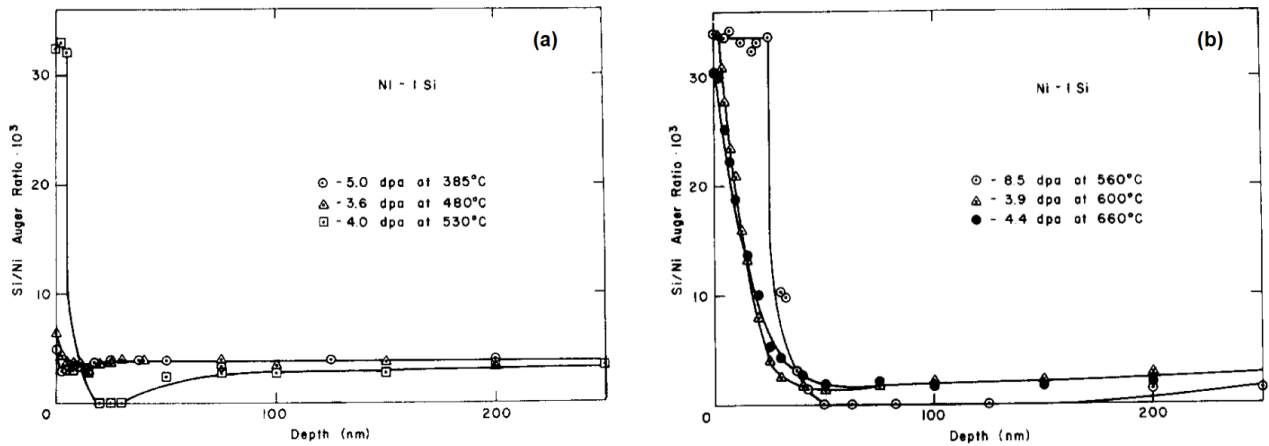


Figure 1.10: Si depth profiles measured by Auger spectroscopy at various temperatures for a Ni-1 at.% Si alloy. (a) The irradiation is up to 5.0 dpa at 385°C, 3.6 dpa at 480°C and 4.0 dpa at 530°C. (b) The irradiation is up to 8.5 dpa at 560°C, 3.9 dpa at 600°C and 4.4 dpa at 660°C. The Si/Ni Auger ratio corresponds to 25 at.% Si in the alloy. The figure is reproduced from Ref. [26].

1.3.3.2 Effect of temperature

RIS results from the sustained PD flux towards sinks, which typically happens at temperatures between 0.3 and 0.6 times of the melting temperature [11, 16]. Rehn et al. investigate the temperature dependence of solute Si segregation in a dilute binary Ni(Si) alloy under self-ion irradiation at a peak damage rate around 2.5×10^{-3} dpa/s [26]. Little segregation of Si occurs below 400°C and above 660°C. The depth profiles of Si concentration measured by Auger spectroscopy between 385°C and 660°C are shown in Fig. 1.10. The maximum segregation of Si occurs around 560°C, where a thin layer of the Ni_3Si γ' -phase is formed. The temperature dependence of solute segregation presented in Fig. 1.10 can be readily understood qualitatively. At low temperatures, vacancies are immobile, and PDs annihilate by mutual recombination. As a result, fluxes of the solute-PD complex towards sinks are reduced. At high temperatures, the thermal equilibrium concentration of vacancies is high: a back diffusion of solute atoms and a lower vacancy supersaturation completely suppress the segregation. Temperature can also modify the competition between vacancy and SIA mechanisms of RIS. This may lead to a change of sign of RIS. One expects an effect of temperature on this competition occurs in Fe-Cr alloy [174–176]: the SIA mechanism prevails at moderate temperatures, leading to a Cr enrichment, whereas the vacancy mechanism leads to a Cr depletion at high temperatures. Moreover, Marwick et al. show that Ti is enriched at the surface of Ni-Ti alloys. They explain the change of sign of Ti RIS by involving the migration of Ti-vacancy complexes at $T < 400^\circ\text{C}$, and an inverse Kirkendall effect at high temperatures [177]. A similar temperature dependence is observed in Ni-Si alloys [178] and a few model alloys [179]. This tendency is as well obtained from recent DFT-based flux coupling studies on a few fcc and bcc alloys [180, 181].

1.3.3.3 Effect of dose, dose rate and radiation particles

Rehn et al. observe an enrichment of Si in Ni-1 at.% Si at the surface at 525°C and 600°C after an irradiation dose of 0.05 dpa and 0.06 dpa, respectively [24]. Such doses are very small compared to those required for the effects of swelling [11] and ballistic disordering [27].

Allen et al. investigate the effect of dose rate on the segregation in 304L stainless steels irradiated in the EBR-II reactor at around 375°C [25]. They measured the Cr and Ni solute concentration profiles across voids for samples irradiated in different row positions in the core. The samples in different rows are irradiated to nearly the same dose (around 10 dpa) but with different dose rates. The experimental observations evidence a greater amount of Cr depletion and Ni enrichment occurs in samples irradiated at lower dose rate [25]. This trend is explained by Was [11] as follows: at a given temperature, a lower dose rate leads to a smaller production of PDs per unit time. Thus with fewer PDs produced in the material, the probability for a PD to find a sink versus to recombine with another PD is increased. Therefore, the contribution of PD elimination at sinks is more important at a lower dose rate.

It is worth mentioning that, when irradiation particles are light particles (electrons or light ions), the segregation amount of solute at a given dose is often greater than that resulting from neutron or heavy ion irradiation [11]. This is due to the differences in the primary damage produced by these particles. In the case of neutrons or heavy ion irradiation, PDs are created in very localized areas within a displacement cascade [86]. Therefore, most of the produced PDs recombine or form clusters rather than diffusing at long distance, and contributing to the solute redistribution at PD sinks. On the other hand, in the case of light particle irradiation, PDs are created more homogeneously within a displacement cascade; thus a larger fraction of them survive from the recombination and clustering reactions, and diffuse towards sinks [11].

1.3.3.4 Emulation of neutron irradiation with respect to RIS

RIS is dependent on both temperature and dose rate. Robrock et al. [16] investigate the temperature dependence of Ni₃Si coating resulting from Si RIS at the surface of Ni-6 at.% Si alloys irradiated by 3.5 MeV Ni⁺ at different dose rates. The characterization of the Ni₃Si coating is performed at a radiation dose of 3 dpa. For a dose rate of 4.5×10^{-4} dpa/s, at 420°C, precipitates of Ni₃Si are found on dislocation loops but not on the surface; at 530°C, a continuous film of Ni₃Si occurs on the surface; at 610°C only small Ni₃Si precipitates are found; and at 717°C, no Ni₃Si phase is found. According to the authors, this behavior indicates that the position of the peak of RIS is around 530°C, the temperature at which the precipitation of Ni₃Si is the most important. Similar behavior is found at 2×10^{-2} dpa/s, though the position of the RIS peak is shifted to 615°C. Moreover, previous results on Ni-1 at.% Si [26] and Ni-12.7 at.% Si [178] indicate that peak temperatures are about 530, 560 and 645°C at dose rates of 4.5×10^{-4} , 3×10^{-3} and 2×10^{-2} dpa/s, respectively [16]. In order to explain these observations, Okamoto et al. [16] apply John-Lam RIS model [182] to calculate the maximum segregation amount for different irradiation conditions. They conclude the discussion by providing a temperature-dose rate diagram (Fig. 1.11). This diagram shows the temperature range for which a significant Si segregation at surfaces is expected.

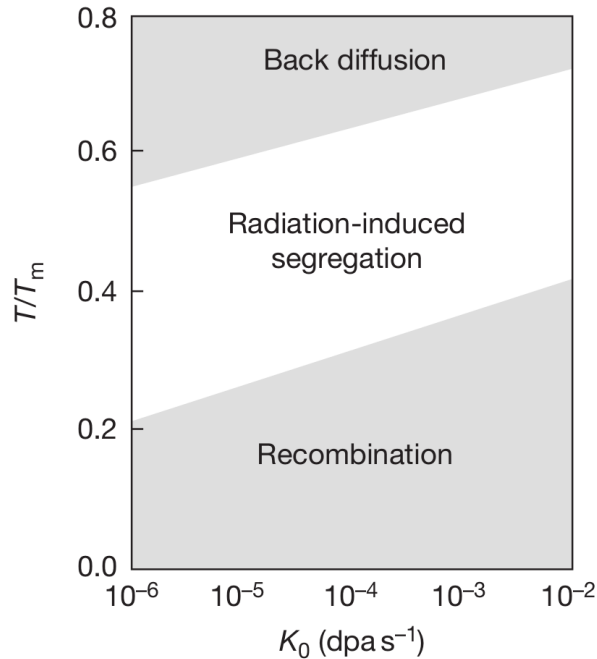


Figure 1.11: Temperature-dose rate diagram of radiation-induced segregation.

Investigating the effect of large neutron radiation dose (a few dpa or more) is difficult because it would require very long irradiation times (typically in years) [11]. For these reasons, one may simulate the neutron irradiation by heavy ion irradiation. The latter yields high damage rates compared to neutron irradiation. However, most of the phenomena occurring under irradiation are sensitive to the radiation flux. According to simple mean-field rate theories, the PD concentrations obtained at a low radiation flux and a given temperature are identical to the ones obtained at a higher flux provided the temperature is increased by a specific amount, which suggests that a difference in radiation flux can be compensated by a temperature shift [11, 22, 23, 183, 184]. This theory has been first applied to investigate the swelling phenomena, but it relies on the assumption that solute atoms do not interfere with the kinetics of PDs and the overall PD sink strength is fixed by the initial microstructure. According to this theory, there are three kinetic domains: (i) at low temperature and high radiation flux, the recombination domain in which the PD concentration is controlled by the PD recombination reaction, (ii) at intermediate temperature and low radiation flux, the sink domain in which the PD concentration is controlled by the elimination of PDs at sinks, and (iii) at high temperature and low radiation flux, the thermal domain in which the PD concentration are close to thermal equilibrium concentrations [183]. Estimations of the temperature shift required to compensate for a large radiation flux depend on the kinetic domain of the experiment and whether the system is at steady state or in a transient state. These temperature shifts require the definition of an invariant quantity, either the bulk concentration of PDs at steady state [11] or the amount of PDs absorbed by sinks [184]. Attempts have been made to apply Mansur's invariant PD-absorption relation to the study of solute RIS [11, 22, 23]. The estimation of the temperature shift was good enough to yield similar RIS profiles of Cr and Ni in 304L stainless steels, respectively irradiated with neutrons and self ions [23]. Nevertheless, in the same publication, the authors observe that the temperature shift predicted by Mansur's invariant relation is not accurate for alloys with a high dislocation density. Yet, a material with an ini-

tial high dislocation density seems to be more appropriate to test Mansur’s invariant relation, because the high PD sink strength of a microstructure full of dislocations is less sensitive to the radiation flux and dose, and can be considered to be fixed as assumed in Mansur’s theory. A recent analytical model of steady-state RIS in the sink domain precisely predicts that solute RIS does not depend on the radiation flux, whereas PD concentration does [30]. However, as explained by the authors, we should not ignore that an increase of the dislocation density may induce a transition from the recombination domain to the sink domain, hence, shift the system from a radiation-flux dependence to another. Therefore, there is a need for a PD-RIS model accounting for both the transitions between the various PDs kinetic domains, and the effect of the irradiation conditions and the microstructure on the RIS profile within each PDs kinetic domain.

1.3.3.5 Evaluation of flux couplings

RIS results from a flux coupling between PDs and solute atoms. The investigation of flux couplings is a primary step towards the modeling of RIS. From the Onsager formalism of the atomic fluxes (subsection 1.3.1.1), the ratio between PD flux (J_d for $d = V, I$) and solute flux (J_B) is given by

$$\frac{J_B}{J_d} = \frac{L_{BB}\nabla\mu_B + L_{BA}\nabla\mu_A + L_{Bd}\nabla\mu_d}{L_{dB}\nabla\mu_B + L_{dA}\nabla\mu_A + L_{dd}\nabla\mu_d}. \quad (1.63)$$

During irradiation, PD concentration is far from the equilibrium concentration. Therefore, $\nabla\mu_I$ and $\nabla\mu_V$ are essential driving force in irradiated alloys. In order to quantify flux couplings triggered by a PD CPG, we set every CPG to zero except $\nabla\mu_V$ or $\nabla\mu_I$ [40]. As a result, for solute-vacancy coupling, J_B/J_V is represented by the wind factor:

$$\delta_V = \frac{L_{BV}}{L_{VV}}. \quad (1.64)$$

and the solute-SIA coupling is given by

$$\delta_I = \frac{L_{BI}}{L_{II}}. \quad (1.65)$$

The wind factor, δ_d , informs on the average number of solute atoms following the vacancy or SIA. Note that L_{VV} , L_{II} and L_{BI} are systematically positive, while L_{BV} may be negative. The off-diagonal L -coefficient determines the sign of the flux coupling. If the wind factor δ_d is positive, the vacancy or SIA drags B. Relying on the wind factor, we can tell whether the diffusion of solute and PD as a complex contributes to the RIS.

Note that the wind factor depends on the concentration of solute atoms, even in the dilute limit, because, in opposite to L_{BV} , L_{VV} is not proportional to C_B . In cases we are only interested in the sign of the flux coupling, we introduce the ratio L_{BV}/L_{BB} [181, 185–187]. In this ratio, L_{BB} is always positive and can be considered as a normalization constant. In addition, this ratio is independent of the alloy compositions because, in dilute alloys, L_{BV} and L_{BB} are proportional to the concentrations of vacancies and solute atoms. Relying on the ratio L_{BV}/L_{BB} , Garnier et al. [185–187] investigate the strain effect on the flux coupling in dilute Ni(Si) alloy. Messina et al. [181] compute the ratio L_{BV}/L_{BB} in dilute body-centered cubic Fe-based alloys with PDs in order to predict the solute-drag tendency at various temperatures.

1.3.3.6 Analytical solutions of radiation-induced segregation in steady state

RIS results from the flux of PDs towards sinks and the atomic back diffusion away from sinks. Wiedersich et al. [188] establish a relationship between the concentration profiles of PD and solute atoms during the RIS in steady state. Extensive reviews regarding to this topic can be found in Refs. [11, 19, 20]: here we introduce the models that are directly related to our own studies of RIS.

A RIS model must reproduce the atomic diffusion enhancement resulting from an increase of PD concentration. If we ignore the thermodynamic and kinetic contributions of PD clusters, the L -coefficients vary linearly with PD concentrations. To highlight the role of PD concentration, one introduces normalized L -coefficients, the so-called partial diffusion coefficients, which are PD concentration free [173, 188, 189]. In the following, we rely on Wolfer's formulation [189] because the approximation made to calculate the partial diffusion coefficients and driving forces are clearly stated. The fluxes of atoms and PDs in a binary alloy A(B) are given by

$$\begin{aligned}
\mathbf{J}_A &= -(d_{AV}^c C_V + d_{AI}^c C_I) \Phi \nabla C_A + C_A (d_{AV} \nabla C_V - d_{AI} \nabla C_I), \\
\mathbf{J}_B &= -(d_{BV}^c C_V + d_{BI}^c C_I) \Phi \nabla C_B + C_B (d_{BV} \nabla C_V - d_{BI} \nabla C_I), \\
\mathbf{J}_V &= -(C_A d_{AV} + C_B d_{BV}) \nabla C_V + C_V \Phi (d_{AV}^c \nabla C_A + d_{BV}^c \nabla C_B), \\
\mathbf{J}_I &= -(C_A d_{AI} + C_B d_{BI}) \nabla C_I + C_I \Phi (d_{AI}^c \nabla C_A + d_{BI}^c \nabla C_B)
\end{aligned} \tag{1.66}$$

where the partial diffusion coefficients are given by

$$\begin{aligned}
d_{AV} &= -\frac{L_{AA}^V + L_{AB}^V}{C_A C_V}, \quad d_{BV} = \frac{L_{BB}^V + L_{BA}^V}{C_B C_V}, \quad d_{AI} = \frac{L_{AA}^I + L_{AB}^I}{C_A C_I}, \quad d_{BI} = \frac{L_{BB}^I + L_{BA}^I}{C_B C_I}, \\
d_{AV}^c &= \frac{L_{AA}^V}{C_A C_V} - \frac{L_{AB}^V}{C_B C_V} + d_{AV} \frac{1}{\Phi} \xi_{VA}, \quad d_{BV}^c = \frac{L_{BB}^V}{C_B C_V} - \frac{L_{BA}^V}{C_A C_V} + d_{BV} \frac{1}{\Phi} \xi_{VB}, \\
d_{AI}^c &= \frac{L_{AA}^I}{C_A C_I} - \frac{L_{AB}^I}{C_B C_I} + d_{AI} \frac{1}{\Phi} \xi_{IA}, \quad d_{BI}^c = \frac{L_{BB}^I}{C_B C_I} - \frac{L_{BA}^I}{C_A C_I} + d_{BI} \frac{1}{\Phi} \xi_{IB}.
\end{aligned} \tag{1.67}$$

In steady state, the time derivative of atomic and PD concentrations are zero. Therefore, the atomic flux controlling the atomic concentration (Eq. (1.42)) at the PD sink, is zero. Step by step from the sink surface plane, we demonstrate every flux of a given atomic species α is zero

$$\mathbf{J}_\alpha = 0. \tag{1.68}$$

In case of a single population of PD sinks, setting to zero the time-derivatives of PD concentrations in Eq. (1.28) leads to the relationship

$$\mathbf{J}_V = \mathbf{J}_I. \tag{1.69}$$

In a binary alloy, Eqs. (1.66), (1.68) and (1.69) yields the Wiedersich's relationship [188] between the concentration gradients of solute and vacancy near an ideal sink:

$$\nabla C_B = -\alpha \nabla C_V, \tag{1.70}$$

with the coupling factor

$$\alpha = \frac{d_{AI} d_{AV} C_A C_B}{d_{AI} D_B C_A + d_{BI} D_A C_B} \alpha_s, \tag{1.71}$$

where

$$\alpha_s = \frac{d_{BI}}{d_{AI}} - \frac{d_{BV}}{d_{AV}}. \quad (1.72)$$

Note that the intrinsic diffusion coefficients D_A and D_B of components A and B can be written in function of PD-related diffusion coefficients and PD concentrations:

$$D_\beta = d_{\beta V}^c C_V + d_{\beta I}^c C_I, \text{ with } \beta = \{A, B\}. \quad (1.73)$$

The sign of α is determined by the sign of α_s . The latter is related to the off-diagonal coefficients of the Onsager matrix. $\alpha > 0$ leads to an enrichment of B at sinks.

Relying on the SCMF theory, Messina et al. [181] have calculated the ratio d_{BV}/d_{AV} in dilute binary Fe-based alloys in order to predict the tendencies of RIS driven by a vacancy flux. They predict that solute RIS in Fe is mainly controlled by the drag of solute by vacancy except in Fe-Cr alloy. The vacancy inverse Kirkendall effect leads to Cr depletion at all temperatures. In contrast, the solute drag mechanism leads to sinks enriched in Cu, Mn, Ni, P, and Si at low temperatures. Let us mention that the FAR mechanism is not considered.

Relying on the Wiedersich RIS model (Eq. (1.70)), Martínez et al. [30] obtain the analytical expression of the RIS profile of solute atoms at planar sinks. The vacancy concentration profile is given by solving the Poisson equation (Eq. (1.33)) near interfaces with $C_V = C_V^{\text{eq}}$ at the interfaces and $\mathbf{J}_V = 0$ at the midpoint between two successive planar sinks. The analytical solute concentration profile is obtained by integrating Eq. (1.70) with a boundary condition on the mass conservation of solute atoms. The segregation amount of solute atoms, S_B , is directly related to the microstructure and given by

$$S_B = \alpha_0 h (\ln 2 - 1), \quad (1.74)$$

where h is the average spacing between successive planar sinks. In this approach, the recombination between vacancies and SIAs are not considered. In Section 3.2, we present a method to obtain analytical concentration profiles of PDs and solute atoms, which account for the competition between PD recombination reactions and PD elimination reactions at sinks.

1.4 Atomic-scale modeling of diffusion under irradiation

There are semi-analytical or numerical methods calculating the L -coefficients from an on-lattice modeling of PD jumps, including the effect of local solute concentration and strain. In this section, we present the jump frequency models, including the effect of elastic strain. We introduce as well an on-lattice modeling of FAR diffusion mechanisms occurring in a displacement cascade.

1.4.1 Point defect diffusion models

Vacancy and SIA are two intrinsic lattice PDs. Here we introduce the most frequent crystallographic structures of metallic alloys—face-centered cubic (fcc) and body-centered cubic

(bcc) lattice structures. A vacancy is an occupied lattice site of the crystal. There is a large variety of SIA configurations: the octahedral and tetragonal interstitial sites, the crowdion and the split-interstitial (also called dumbbell) configurations. The most stable SIA configuration in fcc and bcc alloys is commonly the dumbbell configuration with two atoms sharing the same lattice site [11]. In general, the most stable dumbbell direction in bcc structures is the $\langle 111 \rangle$ direction, while in fcc structure is the $\langle 100 \rangle$ direction in [190]. However, in bcc Fe-based alloys, the $\langle 110 \rangle$ -dumbbell is more stable than the $\langle 111 \rangle$ -dumbbell mainly due to the magnetic effects [191].

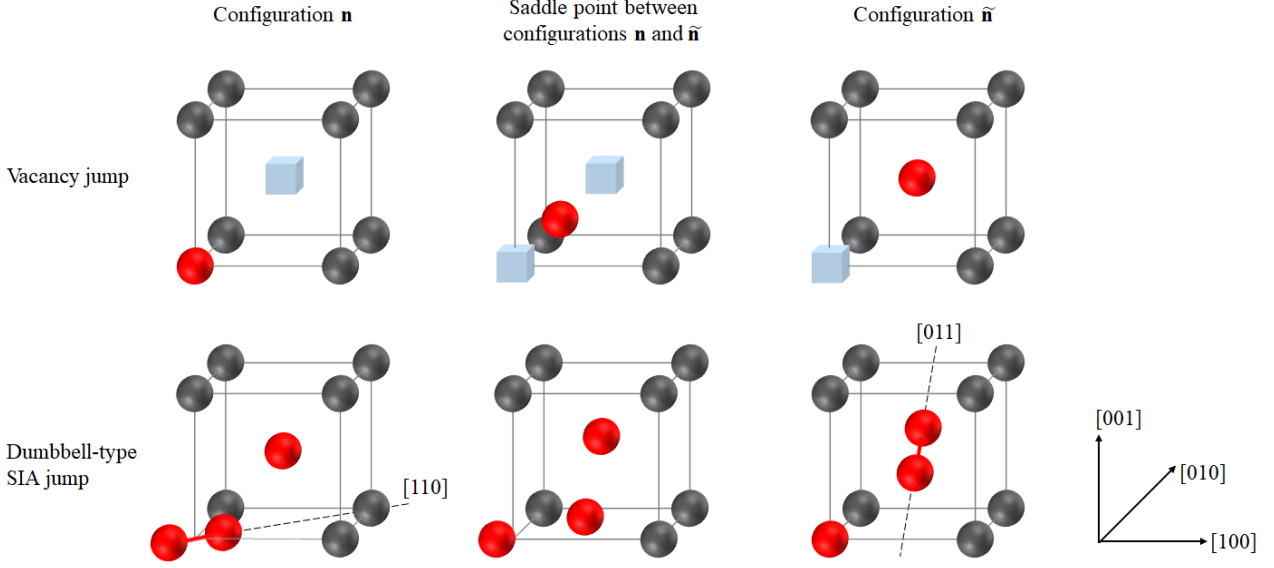


Figure 1.12: Possible point defect migration mechanisms in bcc metal Fe. Black and red spheres represent Fe atoms and the blue cubic represents the vacancy.

Thermally-activated diffusion is controlled by the jump of PDs. It proceeds by atom-PD exchanges between the first nearest neighbour (1-NN) lattice sites (Fig. 1.12 and Fig. 1.13). Therefore, for a given PD in bcc metals, there are 8 possible jumps of different directions, whereas, in fcc metals, there are 12 jumps.

The SIA jump is more complex than the one of vacancy. The dumbbell transition mechanisms include on-site rotation, translation, and translation-rotation. The latter is, in general, the most favorable mechanism: an atom at a dumbbell position translates to bind with another 1-NN atom and form a new dumbbell in a different $\langle 110 \rangle$ direction (cf. Fig. 1.12 and Fig. 1.13).

From the initial and final state of a PD jumps, PD goes through a saddle-point position where the energy of the system along the PD jump pathway reaches its maximum. The difference between this maximum and the energy of the initial configuration is the so-called migration energy. We use the transition state theory to model the thermally-activated frequency of a PD jump [192]. We define the thermal jump frequency $\omega_{\mathbf{n} \rightarrow \tilde{\mathbf{n}}}^{\alpha V}$ (resp. $\omega_{\mathbf{n} \rightarrow \tilde{\mathbf{n}}}^{\alpha I}$) mediated by the exchange of vacancy (resp. SIA) with an atom of species α from configuration \mathbf{n} to $\tilde{\mathbf{n}}$:

$$\omega_{\mathbf{n} \rightarrow \tilde{\mathbf{n}}}^{\alpha d} = \nu \exp \left(-\frac{E_{\mathbf{n} \rightarrow \tilde{\mathbf{n}}}^{\text{mig}}}{k_B T} \right), \quad (d = V, I), \quad (1.75)$$

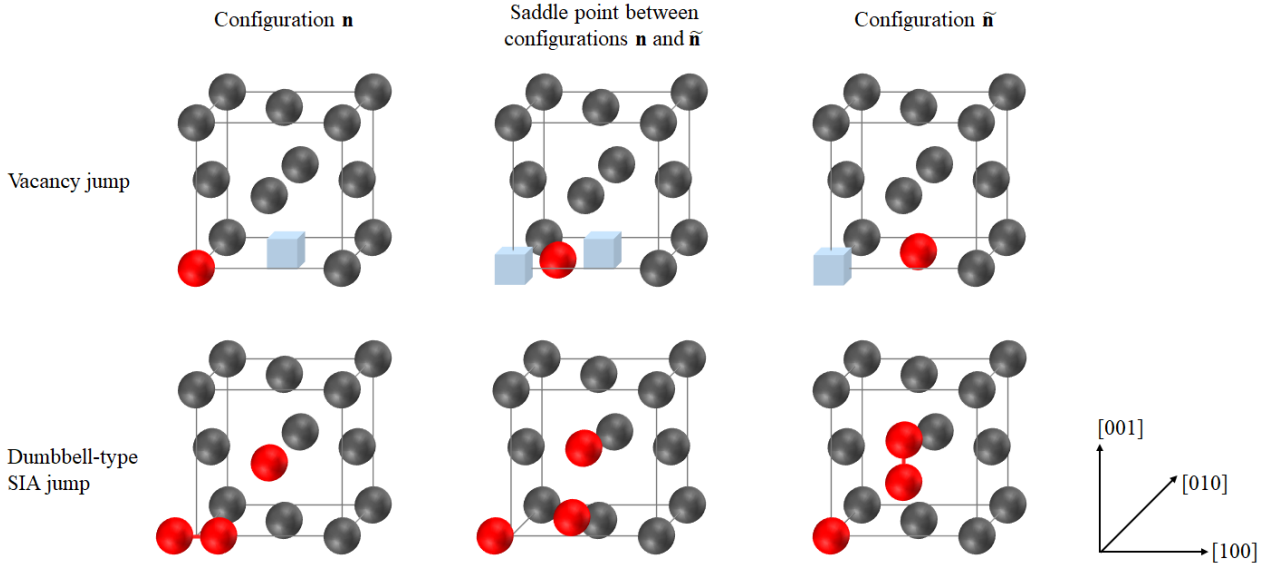


Figure 1.13: Possible point defect migration mechanisms in fcc metal. Black and red spheres represent Fe atoms and the blue cubic represents the vacancy.

where ν is the attempt frequency, k_B is the Boltzmann constant, T is the temperature and $E_{\mathbf{n} \rightarrow \tilde{\mathbf{n}}}^{\text{mig}}$ is the migration barrier from configuration \mathbf{n} to $\tilde{\mathbf{n}}$, which can be deduced from *ab initio* calculation database [181, 193].

It is noteworthy that the migration energy is dependent on the local alloy configuration. Hence the presence of solute atoms near the PD can modify the PD jump frequency. We use solute-PD interactions to model this effect. For instance, in dilute fcc alloys including a vacancy, with energy interactions limited to 1-NN pairwise interactions, five different jump frequencies are required to describe the vacancy migration in presence of a single solute atom [194] (see Fig. 1.14). Here, we designate these five frequencies as $\omega_{i=0,1,2,3,4}$ after the Lidiard's nomenclature [194]. The solute-vacancy exchange frequency is noted ω_2 . The vacancy jump conserving the 1-NN distance from the solute atoms is noted ω_1 . The jump dissociating the solute-vacancy pair is noted ω_3 , while the one associating the solute-vacancy pair is noted ω_4 . All the other vacancy jumps far from the solute atom are noted ω_0 . This 1-NN model is favorable for the analytical calculation of diffusion properties because the number of kinetic paths of PD is relatively limited. For instance, from this 1-NN frequency model and a first-shell approximation (kinetic interactions beyond 1-NN are neglected), Lidiard [194, 195] derived a five-frequency model to calculate the tracer atom diffusion coefficient. Using the same approximation, we will present later in Section 2.3 the derivation of the analytical expressions of the L -coefficients, including both PD jumps and FAR.

1.4.2 Effect of elastic interactions on point defect diffusion

Irradiation leads to the formation of PD clusters such as voids and dislocation loops acting as PD sinks. The latter generates a strain field which affects the energetic and jump frequencies

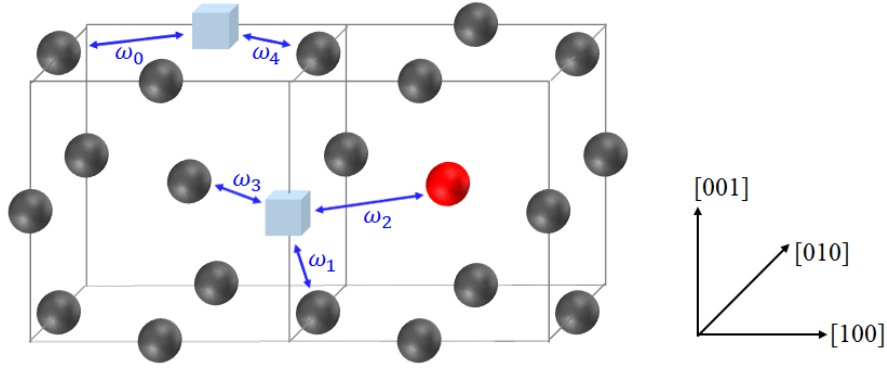


Figure 1.14: Network of the five vacancy jump frequencies with the presence of a solute atom. The cubic represents the vacancy. The black spheres stand for the bulk atoms, while the red one is for the solute atom.

of PDs. Therefore, this elastic strain field modifies CPGs and the L -coefficients. The variation of the L -coefficients with strain is the so-called elasto-diffusion.

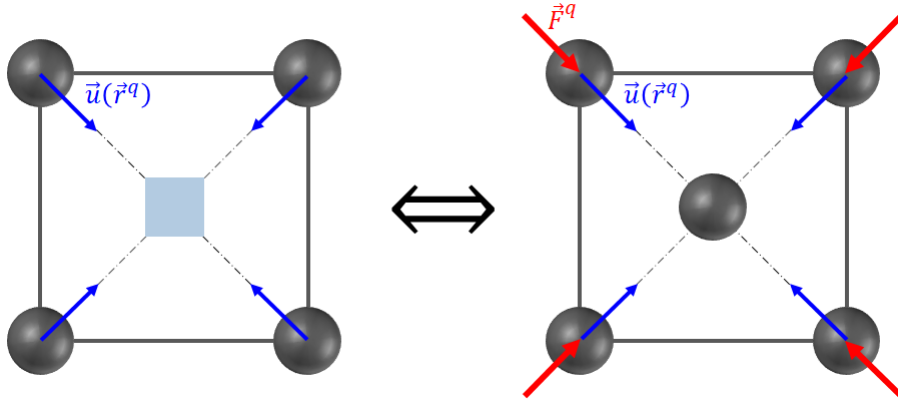


Figure 1.15: Representation of a vacancy by the Kanzaki forces. \mathbf{u} is the displacement field of atoms (black circle) induced by the vacancy (blue square), while \mathbf{F} is the field of Kanzaki forces applied to a perfect lattice in order to produce the same displacement field \mathbf{u} .

The elastic effects on PD jump frequencies are investigated within elasticity theory with different descriptions of a PD: elastic dipole, the infinitesimal Eshelby inclusion, and the analogy with an infinitesimal dislocation loop. These approaches are shown to be equivalent [141]. We rely on the elastic dipole formulation to describe the PD properties.

A PD is described as a distribution of equilibrated point-forces [196–199], the so-called Kanzaki forces [200–204]. The latter are defined as the forces \mathbf{F}^q to be applied to the neighbouring atoms q of the PD in order to produce the same displacement field (cf. Fig. 1.15). The PD produces an elastic displacement field $\mathbf{u}(\mathbf{r})$. The i -th component of $\mathbf{u}(\mathbf{r})$ is related to the force distribution \mathbf{F}^q by:

$$u_i(\mathbf{r}) = \sum_{q=1}^N G_{ij}(\mathbf{r} - \mathbf{r}^q) F_j^q, \quad (1.76)$$

where N is the number of neighbouring atoms at positions \mathbf{r}^q of the PD and G_{ij} is the elastic

Green's function. Far from the PD (i.e. $\|\mathbf{r}\| \gg \|\mathbf{r}^q\|$), Eq. (1.76) can be rewritten in the form of a Taylor series, with Einstein convention on the summation over repeated indices:

$$u_i(\mathbf{r}) = G_{ij}(\mathbf{r}) \sum_{q=1}^N F_j^q - G_{ij,k}(\mathbf{r}) \sum_{q=1}^N F_j^q r_k^q + o(\|\mathbf{r}^q\|), \quad (1.77)$$

where $G_{ij,k} = \partial G_{ij} / \partial r_k$. Note that $\sum_{q=1}^N F_j^q = 0$ because the forces are equilibrated. Therefore, by neglecting the term beyond the first order, Eq. (1.77) can be rewritten as:

$$u_i(\mathbf{r}) = -G_{ij,k}(\mathbf{r}) \underline{P}_{jk}, \quad (1.78)$$

where \underline{P}_{jk} is the elastic dipole, defined as:

$$\underline{P}_{jk} = \sum_{q=1}^N F_j^q r_k^q. \quad (1.79)$$

This dipole, \underline{P} , is a tensor of second rank. It is symmetric because the torque $\sum_q \mathbf{F}^q \times \mathbf{r}^q = 0$ due to the equilibrium properties of the force distribution [141].

We derive the elastic interaction energy E^{int} between a PD and an external displacement field \mathbf{u}^{ext} from the Kanzaki forces \mathbf{F}^q :

$$E^{\text{int}}(\mathbf{u}^{\text{ext}}) = - \sum_{q=1}^N \mathbf{F}^q \cdot \mathbf{u}^{\text{ext}}(\mathbf{r}^q). \quad (1.80)$$

By assuming that \mathbf{u}^{ext} varies little close to the PD, one can rewrite Eq. (1.80) by means of a series expansion as:

$$E^{\text{int}}(\mathbf{u}^{\text{ext}}) = -u_i^{\text{ext}}(\mathbf{0}) \sum_{q=1}^N F_i^q - u_{i,j}^{\text{ext}}(\mathbf{0}) \sum_{q=1}^N F_i^q r_j^q, \quad (1.81)$$

where $u_{i,j}^{\text{ext}} = \partial u_i^{\text{ext}} / \partial r_j$ and Einstein summation convention is implicit for indices i, j . The first term in the right-hand side is null because the forces are equilibrated and thus the interaction energy is a function of the elastic dipole:

$$E^{\text{int}}(\mathbf{u}^{\text{ext}}) = -\underline{P}_{ij} u_{i,j}^{\text{ext}}. \quad (1.82)$$

Since \underline{P} is a symmetric tensor, we express E^{int} as a function of the symmetric strain field tensor $\underline{\epsilon}^{\text{ext}}$:

$$E^{\text{int}}(\underline{\epsilon}^{\text{ext}}) = -\underline{P}_{ij} \epsilon_{ij}^{\text{ext}}, \quad (1.83)$$

where $\epsilon_{ij}^{\text{ext}} = (u_{i,j}^{\text{ext}} + u_{j,i}^{\text{ext}})/2$.

We have access to the PD properties from indirect experimental techniques, such as the measurement of the elastic constant [205], or the inelastic relaxation [206]. However, it is difficult to obtain all the components of the elastic dipole tensor \underline{P} . Therefore, of particular importance are numerical methods such as the *ab initio* calculations of the elastic constants and PD elastic dipoles [185, 186].

To conclude, the effect of the elastic interactions between PDs and the strain field is two-fold. First, this interaction modifies the energy of the system. This modification depends on the amplitude of the strain, which is in general non-homogeneous in space, thereby creating a gradient of the system energy. The latter changes the thermodynamic driving force (i.e., the CPG) of the PD diffusion. Second, the elastic interaction modifies the migration barriers of PD jumps. The latter is the energy difference between the saddle-point and the stable states. Between these two states, the elastic dipole properties of PD as well as the strain field can be different. Therefore, the interaction energies at these two states should also be different, leading to a variation of the migration barrier. In brief, we should consider the above two aspects in order to have a get a full picture of diffusion in a strain field.

1.4.3 On-lattice modeling of FAR effect on the long-term radiation damage evolution

In a displacement cascade, positions of numerous atoms are changed, and Frenkel pairs are created. Relying on the RCS model to describe the displacement cascade, Martin and Bellon [27] account for the contribution of FAR events to the atomic mobility. They introduce the FAR mechanisms as isotropic and non-thermally-activated jumps. The frequency of these athermal jumps is assumed to be proportional to the frequency of the events leading to FAR i.e., irradiation flux. Such jumps are treated as diffusion events, in addition to the thermally-activated jumps (presented in Section 1.4.1).

Averback et al. [3] estimate the length of a RCS by the average distance between the vacancy and the SIA of a Frenkel pair. This distance can be measured by a few experimental techniques such as the field ion microscopy methods. According to the histogram of RCS lengths measured in a few experiments, the distribution drops approximately exponentially with the distance. If we approximate forced relocation sequences of 1-NN jumps involving n atoms by a single atomic jump of n -NN distance, one expect the an exponential decrease of the FAR frequency with the FAR distance. Later, Enrique and Bellon [207] investigate the effects of both relocation frequency and relocation distance on the microstructure of irradiated materials. FAR is modeled as athermal exchanges of atomic positions. They introduce a characteristic distance of FAR. They use a Cahn-Hilliard-type approach to simulate the effect of FAR on the spinodal decomposition of a supersaturated solid solution. They report a patterning of the secondary phase with a wavelength of the concentration fluctuations equal to the FAR characteristic distance. Based on the same approach of the FAR mechanism, Roussel and Bellon [69] introduced the athermal atomic exchanges into the standard five-frequency model [194, 195], to calculate the solute diffusion coefficient in binary fcc model alloys. They point out that accurate calculation of the diffusion coefficient under irradiation requires to simultaneously consider the FAR events and thermally-activated atomic jumps. They show that the total diffusion coefficient resulting from these two mechanisms is not the simple addition of two separate diffusion coefficients due to the interplay between both atomic jump mechanisms.

It is worth noting that PDs are also relocated in displacement cascades. In the recoil collision stage of the displacement cascade, PDs are randomly produced in space because the process is so quick that the thermodynamic solute-PD interactions can be neglected. Then, the

produced PDs may “disappear” in the heat spike because the material is locally a liquid-like phase where there is no notion of PD. Later, they reappear somewhere in the cascade area, as if they had effectively jumped to another crystalline site during the cascade. However, as stated in subsection 1.2.1.5, the reappeared PDs after the heat spike tends to combine with solute atoms in the cascade if they have a thermodynamic attraction, even if they are far away from the solute atom before the heat spike. Although this PD relocation in the displacement cascade is scarcely investigated, it should affect the long-term evolution of the damage.

1.5 Summary

Under equilibrium conditions, changes of the alloy composition occur at structural defects due to the differences in interface energies and sizes of solute and solvent atoms, and to the mixing tendencies of the alloy.

The primary radiation damage is characterized by athermal relocations of atoms and PDs (FAR events) and the production of excess freely-migrating PDs. We review the latter phenomena in Section 1.2. It is difficult to experimentally characterize the primary damage because the duration of the corresponding displacement cascade process is very short (about 10 picoseconds). We commonly rely on theoretical models and numerical simulations to predict the behaviors of atoms and PDs resulting from displacement cascades. In addition to the thermally-activated diffusion, FAR may lead to long-range atomic diffusion. The calculation of the excess PD concentration in irradiated systems, usually relies on mean-field rate theories. In such approach, a precise estimation of the sink strength parameter is essential. There exist numerous analytical models to calculate this parameter for defect sinks with simple geometries. On the other hand, numerical approaches give the possibility to consider elastic interactions and complex sink geometries.

The long-term evolution of the radiation damage is controlled by diffusion processes. These include the radiation-induced diffusion and RIS. In Section 1.3, we present a review of the experimental characterization of tracer diffusion under irradiation. The tracer diffusion coefficient is commonly modelled as the addition of two separate coefficients: the radiation-enhanced diffusion and the FAR-mediated diffusion. However, its validity is questionable because one has shown an interplay between radiation-enhanced diffusion and FAR.

We give a review of the first experimental observations of RIS and the general trends of RIS with respect to the irradiation conditions. We introduce the phenomenological models of RIS, starting from a TIP formulation of the PD and atomic fluxes. We present in details the passage between a flux expression in terms of L -coefficients together with CPGs and a flux in functions of diffusion coefficients together with gradients of concentration. Whereas, up to now, the PD recombination reaction and the athermal FAR mechanism are not included in the RIS models, even in the most recent ones [30].

Given an atomic jump frequency model of a dilute alloy, it is possible to calculate the full Onsager matrix of the L -coefficients. We present in Section 1.4 the on-lattice models of PD jumps. A precise calculation of the L -coefficients of an irradiated system requires to account

for the effects of local solute concentration, a strain field, and the FAR events on the atomic jumps. FAR mechanisms and their effects are modeled as athermal atomic jumps leading to disordering of alloys. An atomic-scale diffusion model including FAR is achieved though a calculation method of the full Onsager transport matrix is still missing, and FAR of PDs are not considered. One formalizes the elastic effects on the PD migration barriers and the thermodynamic driving forces by means of the elastic dipoles associated with PDs and solute atoms.

Chapter 2

Calculation of phenomenological transport coefficients

Contents

2.1	Introduction of diffusion in non-equilibrium system	50
2.2	Modeling of diffusion mechanisms under irradiation	51
2.2.1	Thermally activated jump frequencies	51
2.2.2	Irradiation damage	51
2.2.3	Forced atomic relocation frequencies	53
2.2.4	Point defect concentration	54
2.3	Diffusion theory of systems under forced atomic relocations	54
2.3.1	Nomenclature and the Master Equation	54
2.3.2	Dynamical short range order	55
2.3.3	Transport coefficients	55
2.3.4	SCMF theory under first shell approximation	58
2.3.5	Extension of the KineCluE code	61
2.3.6	Comparison between KineCluE results and Monte Carlo simulations	61
2.4	Diffusion in far-from-equilibrium systems: beyond the linear response theory	64
2.4.1	Two-state uni-dimensional model of vacancy-mediated atomic jumps	64
2.4.2	Description of the dynamics using generating functions	66
2.4.3	Far-from-equilibrium kinetic properties of the two-state model	67
2.5	Diffusion properties in model alloys	69
2.5.1	Dynamical short range order	69
2.5.2	Tracer diffusion coefficient	70
2.5.3	Flux coupling	72
2.6	Sensitivity study with respect to the model and alloy parameters	73

2.6.1	Kinetic radius	73
2.6.2	Mean relocation range	74
2.6.3	Atomic mixing rate	75
2.6.4	FAR-d frequencies	76
2.6.5	Thermal jump frequencies	76
2.7	Summary and concluding remarks	78

2.1 Introduction of diffusion in non-equilibrium system

There exist microscopic models that effectively reproduce the atomic mixing by the irradiation [208,209]. Microscopic events of a displacement cascade are described in Section 1.2. They include (1) the creation of single PDs and PD clusters, (2) the shuffling of atomic positions. The latter process is often considered as a random displacement mechanism [210,211] but there are some evidences showing that it is in fact partially driven by thermodynamics [75]. Besides, recent investigations on concentrated alloys [98, 212, 213] and high entropy alloys [214] have shown that during the quenching stage, the spatial distribution of PDs relative to the solute atoms is partially related to the thermodynamic short range order (i.e. binding interaction).

The mixing of atomic positions in the displacement cascade was previously modeled as a FAR mechanism which consists in forced exchanges of positions between an atom and its nearest neighbour including atom and PD [104, 207, 208, 215]. However, spatial correlations between solute atoms and PDs due to the thermodynamic interactions were neglected. Moreover, the thermal mechanism and FAR were considered separately. For instance, the tracer diffusion coefficient of the solute atom was written as the sum of a thermal and a FAR diffusion coefficients [11]. The interplay between these two mechanisms was neglected. An improved version of the model was proposed in Ref. [69]. The five-frequency model [194, 195] of dilute face-centered cubic (fcc) alloys was generalized to account for both transport mechanisms at the atomic scale. The resulting solute diffusion coefficient includes a FAR-thermal coupling term that affects solute diffusion. The five-frequency model deals with short range thermodynamic and kinetic interactions between vacancy and solute. However, the characteristic distance of a FAR mechanism is related to the size of the displacement cascade [207, 216]. Therefore, only a diffusion model including long-range interactions can properly tackle FAR. Besides, a five-frequency model does not provide the full Onsager matrix.

Thermodynamic and kinetic properties such as flux coupling coefficients and tracer diffusion coefficients of an alloy are deduced from the Onsager matrix of the transport coefficients. Whenever the diffusion mechanism satisfies the microscopic detailed balance, Onsager has demonstrated that this matrix is symmetric [217, 218]. We may calculate it either from the equilibrium atomic displacement fluctuations using the Allnatt formulae [151, 152] or from the flow of matter resulting from an applied external force. However, in driven alloys, there are athermal mechanisms that do not satisfy the microscopic detailed balance. In these systems, we cannot compute the transport coefficients by means of a Monte Carlo numerical approach based on the Allnatt formulae. Yet, recent statistical theories have shown that it is possible to

derive an effective Onsager matrix from the fluctuation theorem [219, 220], though the resulting matrix is non symmetric. These theories go beyond the linear response theory. They provide a methodology for the investigation of far from equilibrium kinetics. Such an approach has been applied to the study of a molecular motor driven by forced chemical reactions [221, 222]. However, it is not directly applicable to properly model systems with FAR because there are no notions of alloying effects and kinetic correlations in this model. In the context of research on diffusion in alloys, one knows how to deal with the complexity of calculating a sequence of PD jumps when the frequency of each jump depends on the local environment of the defect as long as the diffusion mechanism satisfies the microscopic detailed balance [160, 181, 185, 186, 223–226].

Following the ideas of previous studies, we present in Section 2.2 the modeling of the athermal FAR mechanisms. Then, we show in Section 2.3, the theoretical development on the calculation of the transport coefficients using the generalized SCMF theory by taking into account the FAR mechanisms. An implementation of the extended SCMF theory into the KineCluE code yields automatic calculation of the transport coefficients. We present in Section 2.4 a preliminary generalization of molecular motor model in Ref. [221] to calculate the transport coefficients beyond the linear response approximation. Whereas, for now, our investigation is only limited to highly-simplified diffusion model. The application of the extended SCMF theory to model alloys is presented in Section 2.5. Finally, in Section 2.6, a systematic parametric study is performed to emphasize the effect of FAR distances and the solute-defect interaction on the diffusion properties. This study allows us to identify the conditions in which FAR significantly affects the material thermodynamic and kinetic properties.

2.2 Modeling of diffusion mechanisms under irradiation

2.2.1 Thermally activated jump frequencies

We use the transition state theory to model thermally activated diffusion [192]. The thermal jump frequency $\omega_{\mathbf{n} \rightarrow \tilde{\mathbf{n}}}^{\alpha V}$, associated with the thermally activated exchange of atom α and vacancy V which brings the system from configuration \mathbf{n} to $\tilde{\mathbf{n}}$, is given by Eq. (1.75). This mechanism is mediated by PDs and the jump rate depends on the temperature as well as the initial and saddle-point configurations. Note that it satisfies the principle of the microscopic detailed balance:

$$P_{\mathbf{n}} \omega_{\mathbf{n} \rightarrow \tilde{\mathbf{n}}}^{\alpha V} = P_{\tilde{\mathbf{n}}} \omega_{\tilde{\mathbf{n}} \rightarrow \mathbf{n}}^{\alpha V}, \quad (2.1)$$

where $P_{\mathbf{n}}$ is the probability of configuration \mathbf{n} .

2.2.2 Irradiation damage

We follow the ideas of previous studies to model the radiation damage by FAR. The latter includes two mechanisms: (1) FAR between two randomly chosen atoms (FAR-a) which consists in exchanging the positions of two atoms on lattice sites, and (2) FAR between a randomly chosen atom and a PD (FAR-d) which consists in exchanging the positions between an atom

and a vacancy (V) or a self-interstitial atom (SIA). We need to account for the removing and creation of PDs within a cascade. Here we consider that the PDs “disappear” during the heat spike, because the material is locally a liquid-like phase where there is no notion of PD. Later, during the process of quenching, only a small fraction of the PDs “reappears” somewhere in the cascade area, as if they had effectively jumped to another crystalline site during the cascade. The effective result of this process is modeled by FAR-d.

For recoil energy well above DTE producing displacement cascade, the overall effect of the mixing is modeled by FAR characterized by a relocation distance r . FAR occurs at a given frequency proportional to the radiation flux. First for FAR-a, we assume that the probability density function $p(r)$ of the relocation distance follows an exponential decay [207, 227, 228]:

$$p(r) = \frac{1}{r_m} \exp\left(-\frac{r}{r_m}\right), \quad (2.2)$$

where r_m is the mean relocation distance which is related to the size of the displacement cascade. Note that the latter depends on the material and the recoil energy of PKA. For example, the sizes of cascades generated in metals by fast neutrons or by heavy ions typically range between 10 and 100 Å [210, 229]. At the atomic scale, the relocation distance r is discrete and is equal to one of the i -th NN distances. We define the probability mass function $\mathcal{P}(i)$ so that the distribution $p(r)$ in the interval $[r_i, r_{i+1}]$ is averaged to the i -NN point:

$$\mathcal{P}(i) = \int_{r_i}^{r_{i+1}} p(r) dr, \quad (2.3)$$

where r_i corresponds to the i -NN distance. In practice, we consider only a finite set of nearest neighbours, meaning that there is a cut-off relocation distance L -NN beyond which the probability is set to 0. In this case, we define the normalized probability mass function $\mathcal{P}_L(i)$ as:

$$\mathcal{P}_L(i) = \frac{\mathcal{P}(i)}{\sum_{s=0}^L \mathcal{P}(s)}. \quad (2.4)$$

We introduce as well a simplified model associated with a single relocation distance r_m because it gives access to an analytical solution.

Here we ignore FAR-d of SIA and this assumption is justified in Section 2.2.3. Therefore, we consider only FAR-d of vacancy. We propose two categories of FAR-d models: either the same relocation model employed for FAR-a, or a model favoring the relocation sites close to the solute atoms in case of attractive binding energies between vacancy and solute atoms. The latter model makes sense because in the quench-like process at the end of the displacement cascade, the remaining PDs form preferentially where their formation energy is the lowest, that is in the vicinity of solute atoms.

In order to represent both categories of models, we introduce three models (listed in Tab. 2.1). Models 1 and 2 for the first category, and Model 3 for the second category including a thermodynamic effect on FAR-d. Model 1 includes a single relocation distance for both solute and vacancy, while Model 2 includes an exponential law for the relocation distance (Eq. (2.4)) for both species. Model 3 is similar to Model 2, the only difference is that when the relocated vacancy is located at a distance lower than a threshold value R_c from the solute atom

Table 2.1: Definition of relocation models for solute atoms and vacancies.

Models	Solute relocation	Vacancy relocation
1	A single relocation distance (<i>i</i> NN) for both solute and vacancy relocations	
2	An exponential law (Eq. (2.4)) for both solute and vacancy relocations	
3	Eq. (2.4)	<ul style="list-style-type: none"> • If $R_{\text{BV}} > R_c$¹: Eq. (2.4) • If $R_{\text{BV}} \leq R_c$¹: exchange of vacancies with a 1-NN atom of the solute

¹ R_{BV} is the solute-vacancy distance, and R_c is a threshold distance that we set.

B, the vacancy is systematically exchanged with an atom randomly chosen among the 1-NN atoms of B (chemically biased FAR-d).

For recoil energy below DTE, the effective result of the sub-threshold collision is modeled only by FAR-d. The model of FAR-d is the same in Model 1 while FAR-a is not performed. The relocation distance is set to 1-NN distance r_1 .

2.2.3 Forced atomic relocation frequencies

The FAR-d frequency is denoted Γ^{ad} , and the FAR-a frequency is denoted Γ^{aa} .

When the recoil energy is above DTE, the relocation frequency Γ^{aa} can be deduced from the radiation dose rate ϕ based on the ion-beam mixing framework [1, 209]. In our model, FAR-a reproduces the mixing of atoms in the displacement cascade, which is related to the number of PDs produced by the PKA. After the quenching phase, there is only a small fraction of surviving defects, which defines the unit of displacement per atom (dpa). Therefore, there is a factor n_{FAR} relating Γ^{aa} and the radiation dose rate in unit of dpa/s (see Eq. (2.5)).

$$\Gamma^{\text{aa}} = n_{\text{FAR}} \phi. \quad (2.5)$$

From the literature, we set $n_{\text{FAR}} = 100$ [144, 209, 230]. The latter number varies with the alloy thermodynamics due to the thermal effect on the atomic mixing rate in the cascade [75]. The frequencies of FAR-a and FAR-d depend on the number of cascades formed per unit of time as stated in Section 2.2.2. Therefore, Γ^{aa} and Γ^{ad} are both proportional to the dose rate. Hence, they are proportionally related by:

$$\Gamma^{\text{ad}} = \gamma \Gamma^{\text{aa}}, \quad (2.6)$$

with γ the proportionality constant. Note that γ is set to 1 if not specified, i.e. $\Gamma^{\text{ad}} = \Gamma^{\text{aa}} = \Gamma$. Sensitivity studies concerning the value of γ are shown in Section 2.6.4.

When the recoil energy is below DTE, the sub-threshold irradiation does not induce FAR-a because no displacement cascade is produced, thus $\Gamma^{\text{aa}} = 0$. In this case, the calculation of Γ^{ad} is not related to Γ^{aa} and is directly deduced from the recoil energy.

Note that the maximum dose rate under realistic irradiation condition is around 1 dpa/s [11], thereby leading to a relocation frequency of about 100 s^{-1} . The latter is still very small compared to the thermal jump frequency of SIA, even at low temperature. For instance, the SIA thermal jump frequency in pure nickel at 300 K is around 10^{10} s^{-1} according to the atomic diffusion data given in Ref. [193]. Therefore, we do not expect an important impact of FAR-d on the SIA-mediated diffusion properties. Therefore, we consider only FAR-d with vacancies, as stated in Section 2.2.3. Yet, we emphasize that the extension of our framework to account for FAR-d of SIAs is straightforward.

2.2.4 Point defect concentration

The global concentration of PD varies under irradiation, mainly due to the production of Frenkel pairs, the mutual recombination between SIA and V, the elimination of PD at PD sinks such as grain boundaries and dislocations. The vacancy concentration at NESS C_V^{ness} is estimated from a rate theory model [121, 231]—Eq. (1.23). In case we neglect the elastic bias, we have

$$C_V^{\text{ness}} = C_V^{\text{eq}} - \frac{k^2\Omega}{8\pi r_{\text{rec}}} + \sqrt{\left(\frac{k^2\Omega}{8\pi r_{\text{rec}}}\right)^2 + \frac{\phi\Omega}{4\pi r_{\text{rec}}D_V}}. \quad (2.7)$$

We may then replace the flux ϕ by its expression in terms of Γ from Eq. (2.5) into Eq. (2.7), leading to a direct relationship between the vacancy concentration at NESS and Γ .

2.3 Diffusion theory of systems under forced atomic relocations

2.3.1 Nomenclature and the Master Equation

For the total exchange frequencies, we use the notation:

$$W_{\mathbf{n}\rightarrow\tilde{\mathbf{n}}} = W_{\mathbf{n}\rightarrow\tilde{\mathbf{n}}}^{\text{AV}} + W_{\mathbf{n}\rightarrow\tilde{\mathbf{n}}}^{\text{BV}} + W_{\mathbf{n}\rightarrow\tilde{\mathbf{n}}}^{\text{AB}}, \quad (2.8)$$

where $W_{\mathbf{n}\rightarrow\tilde{\mathbf{n}}}^{\text{AV}} = \omega_{\mathbf{n}\rightarrow\tilde{\mathbf{n}}}^{\text{AV}} + \Gamma_{\mathbf{n}\rightarrow\tilde{\mathbf{n}}}^{\text{AV}}$, $W_{\mathbf{n}\rightarrow\tilde{\mathbf{n}}}^{\text{BV}} = \omega_{\mathbf{n}\rightarrow\tilde{\mathbf{n}}}^{\text{BV}} + \Gamma_{\mathbf{n}\rightarrow\tilde{\mathbf{n}}}^{\text{BV}}$ and $W_{\mathbf{n}\rightarrow\tilde{\mathbf{n}}}^{\text{AB}} = \Gamma_{\mathbf{n}\rightarrow\tilde{\mathbf{n}}}^{\text{AB}}$. Note that, although relocation frequencies do not depend on the configuration before and after the exchange, for the sake of clarity, we choose to follow the notation of the thermal jump frequencies.

We start from a Master Equation expressing the fact that the probability distribution of different configurations is controlled by the transition probabilities between two configurations:

$$\frac{d}{dt}\mathbf{P} = \mathbf{W}\mathbf{P}, \quad (2.9)$$

where \mathbf{W} is a matrix with components $W_{\mathbf{n}\tilde{\mathbf{n}}} = W_{\tilde{\mathbf{n}}\rightarrow\mathbf{n}}$ if $\mathbf{n} \neq \tilde{\mathbf{n}}$ and $W_{\mathbf{n}\mathbf{n}} = -\sum_{\tilde{\mathbf{n}}\neq\mathbf{n}} W_{\mathbf{n}\rightarrow\tilde{\mathbf{n}}}$. $\mathbf{P} = (P_{\mathbf{n}})$ is a linear vector of probabilities of configurations (\mathbf{n}).

For now, the recombination reactions between SIA and V are introduced at the upper scale, within the mean field rate theory model of the average PD concentrations (see Section 2.2.4). These athermal events are not treated on the same foot as FAR because SIA and V are considered to be well-separated at the end of the displacement cascade under dilute approximation [86]. In this case, the SIA-V recombination requires long-range diffusion, thereby it is not incorporated in the microscopic Master Equation.

Below, we explain the method we use to determine the dynamical short range order (SRO) parameters at NESS and the diffusion properties from the Master Equation.

2.3.2 Dynamical short range order

Starting from the thermal equilibrium state, the mix of thermal jumps and FAR leads to NESS. The latter state is characterized by dynamical SRO parameters which depend on FAR frequencies and thermal jump frequencies. We define them from the configurational probabilities, deduced from a stationary condition applied to the Master Equation (Eq. (2.9)), also called the global detailed balance condition:

$$\forall \mathbf{n}, \sum_{\tilde{\mathbf{n}}} W_{\tilde{\mathbf{n}} \rightarrow \mathbf{n}} P_{\tilde{\mathbf{n}}} - W_{\mathbf{n} \rightarrow \tilde{\mathbf{n}}} P_{\mathbf{n}} = 0. \quad (2.10)$$

The solution of Eq. (2.9) at NESS is noted $\mathbf{P}^{\text{ness}} = (P_{\mathbf{n}}^{\text{ness}})$. The SRO parameter for configuration \mathbf{n} is defined as the ratio between the configurational probability $P_{\mathbf{n}}^{\text{ness}}$ and the one of the a reference configuration denoted P_0^{ness} .

2.3.3 Transport coefficients

The phenomenological transport coefficients ($L_{\alpha\beta}$) of the Onsager matrix are fundamental parameters describing the diffusion properties of chemical species (α, β) at the macroscopic scale. Flux of chemical species (\mathbf{J}_{α}) is proportional to these coefficients:

$$\mathbf{J}_{\alpha} = - \sum_{\beta} L_{\alpha\beta} \frac{\nabla \mu_{\beta}}{k_{\text{B}} T}, \quad (2.11)$$

with $\nabla \mu_{\beta}/k_{\text{B}} T$ the established driving force imposing to the system a deviation from equilibrium. Starting from NESS, we apply a small gradient of chemical potential and compute the resulting fluxes of atoms and vacancy. Here we extend the SCMF theory to jump mechanisms not obeying the microscopic detailed balance. This theory was first proposed to study diffusion process with atomic jumps following the principle of microscopic detailed balance [160]. By following the nomenclature of Ref. [160], the configuration is defined by a vector \mathbf{n} . The latter consists in occupation numbers of all species on all sites i.e. $\{n_1^{\text{A}}, n_1^{\text{B}}, n_1^{\text{V}}; n_2^{\text{A}}, n_2^{\text{B}}, n_2^{\text{V}}; \dots\}$, with n_i^{α} equal to one if the site i is occupied by species α and zero if not. The transition from configuration \mathbf{n} to $\tilde{\mathbf{n}}$ is realized by thermally activated jumps or FAR, with a total frequency $W_{\mathbf{n} \rightarrow \tilde{\mathbf{n}}}$. Within the standard SCMF theory in Ref. [160], $P_{\mathbf{n}}(t)$, the non-equilibrium distribution

function of configuration \mathbf{n} , is expressed as the product of the equilibrium probability $P_{\mathbf{n}}^{\text{eq}}$ and a non-equilibrium contribution. Here we choose the reference state to be NESS, and replace $P_{\mathbf{n}}^{\text{eq}}$ by the probability distribution function $P_{\mathbf{n}}^{\text{ness}}$:

$$P_{\mathbf{n}}(t) = P_{\mathbf{n}}^{\text{ness}} \times \delta P_{\mathbf{n}}(t). \quad (2.12)$$

The Master Equation (see Eq. (2.9)) is written for a certain configuration \mathbf{n} as

$$\frac{dP_{\mathbf{n}}(t)}{dt} = \sum_{\tilde{\mathbf{n}}} [W_{\tilde{\mathbf{n}} \rightarrow \mathbf{n}} P_{\tilde{\mathbf{n}}}^{\text{ness}} \delta P_{\tilde{\mathbf{n}}}(t) - W_{\mathbf{n} \rightarrow \tilde{\mathbf{n}}} P_{\mathbf{n}}^{\text{ness}} \delta P_{\mathbf{n}}(t)]. \quad (2.13)$$

By applying the global detailed balance condition, i.e. Eq. (2.10), we obtain a reformulation of the Master Equation:

$$\frac{dP_{\mathbf{n}}(t)}{dt} = \sum_{\tilde{\mathbf{n}}} W_{\tilde{\mathbf{n}} \rightarrow \mathbf{n}} P_{\tilde{\mathbf{n}}}^{\text{ness}} [\delta P_{\tilde{\mathbf{n}}}(t) - \delta P_{\mathbf{n}}(t)]. \quad (2.14)$$

Note that the standard SCMF theory relies on the microscopic detailed balance ($W_{\tilde{\mathbf{n}} \rightarrow \mathbf{n}} P_{\tilde{\mathbf{n}}}^{\text{ness}} = W_{\mathbf{n} \rightarrow \tilde{\mathbf{n}}} P_{\mathbf{n}}^{\text{ness}}$). In that case, it is equivalent to consider the transition probabilities entering or exiting a given configuration. When the microscopic detailed balance is not satisfied the transition frequencies to be retained are the entering configurations. The derivation from the Master Equation (Eq. (2.14)) of the transport coefficients is similar to the standard SCMF theory in Ref. [160, 232].

Note that $\delta P_{\mathbf{n}}(t)$ in Eq. (2.14) is a corrective term representing the modification of the effective distribution function $P_{\mathbf{n}}^{\text{ness}}$ due to the presence of an applied driving force. It is written as

$$\delta P_{\mathbf{n}}(t) = \exp \left[\beta \left(\delta \Omega(t) + \sum_{\alpha, i} \delta \mu_i^\alpha(t) n_i^\alpha - h(t) \right) \right], \quad (2.15)$$

where $\beta = 1/k_B T$, $\delta \Omega$ is the normalization factor, $\delta \mu_i^\alpha$ is the deviation from the stationary-state chemical potential on site i of the chemical species α compared to the bulk atom, and h is the time-dependent effective Hamiltonian restricted to the pair interaction written as

$$h(t) = \frac{1}{2} \sum_{\alpha, \gamma, i \neq j} \nu_{ij}^{\alpha\gamma}(t) n_i^\alpha n_j^\gamma, \quad (2.16)$$

where $\nu_{ij}^{\alpha\beta}(t)$ is the time-dependent effective pair interactions. The latter can be determined by solving the kinetic equations deduced from the Master Equation. Here, Eq. (2.15) is linearized with respect to the terms $\beta \delta \mu_i^\alpha$ and βh because we are close to NESS:

$$\delta P_{\mathbf{n}}(t) = 1 + \beta \delta \Omega(t) + \beta \sum_{\alpha, i} \delta \mu_i^\alpha(t) n_i^\alpha - \frac{1}{2} \beta \sum_{\alpha, \gamma, i \neq j} \nu_{ij}^{\alpha\gamma}(t) n_i^\alpha n_j^\gamma.$$

Starting from the Master Equation Eq. (2.14), the time derivative of the ensemble average can be given by

$$\frac{d}{dt} \langle n_i^\alpha n_j^\beta \cdots \rangle = \beta \sum_{\mathbf{n}, \tilde{\mathbf{n}}} n_i^\alpha n_j^\beta \cdots P_{\tilde{\mathbf{n}}}^{\text{ness}} W_{\tilde{\mathbf{n}} \rightarrow \mathbf{n}} \left[\sum_{\alpha, i} \delta \mu_i^\alpha (\tilde{n}_i^\alpha - n_i^\alpha) - \frac{1}{2} \sum_{\alpha, \beta, i \neq j} \nu_{ij}^{\alpha\beta}(t) (\tilde{n}_i^\alpha \tilde{n}_j^\beta - n_i^\alpha n_j^\beta) \right], \quad (2.17)$$

where \tilde{n}_i^α is the occupation number of the configuration $\tilde{\mathbf{n}}$. By denoting $\langle \cdot \rangle$ the ensemble average over the distribution function at NESS (i.e. $P_{\mathbf{n}}^{\text{ness}}$), the derivative of the one-point average $\langle n_i^\alpha \rangle$ can be given by

$$\frac{d}{dt} \langle n_i^\alpha \rangle = \beta \sum_{s \neq i} \sum_{\gamma} \left\langle \tilde{n}_s^\alpha \tilde{n}_i^\gamma W_{si}^{\alpha\gamma} \left[(\delta\mu_s^{\alpha\gamma} - \delta\mu_i^{\alpha\gamma}) + 2\nu_{si}^{\alpha\gamma} + \frac{1}{2} \sum_{\delta, k \neq i \neq s} (\nu_{sk}^{\alpha\delta} - \nu_{ik}^{\alpha\delta} + \nu_{ik}^{\gamma\delta} - \nu_{sk}^{\gamma\delta}) \right] \right\rangle, \quad (2.18)$$

$$\begin{aligned} \frac{d}{dt} \langle n_i^\alpha n_j^\gamma \rangle &= \beta \sum_{s \neq i} \sum_{\delta} \left\langle \tilde{n}_s^\alpha \tilde{n}_j^\gamma \tilde{n}_i^\delta W_{si}^{\alpha\delta} \left[(\delta\mu_s^{\alpha\delta} - \delta\mu_i^{\alpha\delta}) + 2\nu_{si}^{\alpha\delta} + \frac{1}{2} \sum_{\epsilon, k \neq i \neq s} (\nu_{sk}^{\alpha\epsilon} - \nu_{ik}^{\alpha\epsilon} + \nu_{ik}^{\delta\epsilon} - \nu_{sk}^{\delta\epsilon}) \right] \right\rangle \\ &+ \beta \sum_{s \neq i} \sum_{\delta} \left\langle \tilde{n}_i^\alpha \tilde{n}_s^\gamma \tilde{n}_j^\delta W_{sj}^{\gamma\delta} \left[(\delta\mu_s^{\gamma\delta} - \delta\mu_j^{\gamma\delta}) + 2\nu_{sj}^{\gamma\delta} + \frac{1}{2} \sum_{\epsilon, k \neq j \neq s} (\nu_{sk}^{\gamma\epsilon} - \nu_{jk}^{\gamma\epsilon} + \nu_{jk}^{\delta\epsilon} - \nu_{sk}^{\delta\epsilon}) \right] \right\rangle \\ &+ \beta \left\langle \tilde{n}_j^\alpha \tilde{n}_i^\gamma W_{ji}^{\alpha\gamma} \left[(\delta\mu_j^{\alpha\gamma} - \delta\mu_i^{\alpha\gamma}) + 2\nu_{ji}^{\alpha\gamma} + \frac{1}{2} \sum_{\delta, k \neq i \neq j} (\nu_{jk}^{\alpha\delta} - \nu_{ik}^{\alpha\delta} + \nu_{ik}^{\gamma\delta} - \nu_{jk}^{\gamma\delta}) \right] \right\rangle, \end{aligned} \quad (2.19)$$

where $\delta\mu_i^{\alpha\gamma} = \delta\mu_i^\alpha - \delta\mu_i^\gamma$. By applying the continuity equation to the kinetic equation of the one-point average written as:

$$\frac{d}{dt} \langle n_i^\alpha \rangle = - \sum_{s \neq i} J_{i \rightarrow s}^\alpha, \quad (2.20)$$

we can deduce the expression of the flux of chemical species. The fluxes of solute atom and vacancy under first shell approximation are recognized to be:

$$J_{i \rightarrow s}^V = -\beta \left\langle \tilde{n}_s^V \tilde{n}_i^A W_{si}^{VA} \left[\vec{\nabla} \mu^{VA} \cdot \vec{i}_s + \frac{1}{2} \sum_{k \neq i \neq s} n_k^B (\hat{\nu}_{ks}^{BV} - \hat{\nu}_{ki}^{BV}) \right] + \tilde{n}_s^V \tilde{n}_i^B W_{si}^{VB} \left(\vec{\nabla} \mu^{VB} \cdot \vec{i}_s + 2\hat{\nu}_{is}^{BV} \right) \right\rangle, \quad (2.21)$$

$$J_{i \rightarrow s}^B = -\beta \left\langle \tilde{n}_s^B \tilde{n}_i^A W_{si}^{BA} \left[\vec{\nabla} \mu^{BA} \cdot \vec{i}_s + \frac{1}{2} \sum_{k \neq i \neq s} n_k^V (\hat{\nu}_{sk}^{BV} - \hat{\nu}_{ik}^{BV}) \right] + \tilde{n}_s^B \tilde{n}_i^V W_{si}^{BV} \left(\vec{\nabla} \mu^{BV} \cdot \vec{i}_s + 2\hat{\nu}_{si}^{BV} \right) \right\rangle, \quad (2.22)$$

where $\hat{\nu}_{ij}^{BV} = \nu_{ij}^{BV} - \nu_{ij}^{BA} - \nu_{ij}^{AV}$.

Note that under the first shell approximation, the effective interactions are restricted to the pair B-V at 1-NN. The term $\hat{\nu}_{ij}^{BV}$ can be estimated from the stationary condition of the kinetic equation of the two-point average $\langle n_i^B n_j^V \rangle$. As a result, $\hat{\nu}_{ij}^{BV}$ can be expressed as a function of the chemical potential gradient. Therefore, the atomic fluxes of solute atom and vacancy are also functions of $\nabla \mu^{VA}$ and $\nabla \mu^{BA}$, allowing us to identify the transport coefficients. Their expressions under first shell approximation are given in the following section (Eq. (2.25)–(2.28)).

2.3.4 SCMF theory under first shell approximation

Here, we focus on the diffusion properties of a dilute binary model alloy A(B): a host matrix of atoms A containing a single solute atom of species B and a single vacancy. The crystallographic structure is chosen to be a fcc crystal. As explained in Section 2.2.2, we consider the vacancy as the only type of PDs. Our purpose is to extend the SCMF theory to the athermal FAR mechanisms. In order to derive analytical transport coefficients, we start with a first shell approximation. This approximation consists in neglecting kinetic coupling and thermodynamic interactions between B and V if the distance between both species is beyond 1-NN. FAR-a and FAR-d are restricted to exchanges between 1-NN sites only. In such dilute alloy, there are five different atom-vacancy thermal exchange frequencies ($\omega_{i=0,1,2,3,4}$) which we designate after the Lidiard's nomenclature [194] (see Fig. 2.1), to which we add 4 FAR-a frequencies ($\Gamma_{i=0,1,3,4}^{AB}$) and 5 FAR-d frequencies ($\Gamma_{i=0,1,2,3,4}^{AV}$ and Γ_2^{BV}). The total B-V exchange frequency is noted W_2^{BV} . The total A-V and A-B exchanges conserving the 1-NN distance between B and V are respectively noted W_1^{AV} and W_1^{AB} . The total A-V and A-B exchanges dissociating the B-V pair are respectively noted W_3^{AV} and W_3^{AB} . The total A-V and A-B exchanges associating the B-V pair are respectively noted W_4^{AV} and W_4^{AB} , and all the other A-V and A-B exchanges far from the solute atom B are respectively noted W_0^{AV} and W_0^{AB} . Here we recall that:

$$\begin{aligned} W_i^{AV} &= \omega_i + \Gamma_i^{AV} = \omega_i + \Gamma^{\text{ad}}, \text{ for } i = 0, 1, 3, 4; \\ W_i^{AB} &= \Gamma_i^{AB} = \Gamma^{\text{aa}}, \text{ for } i = 0, 1, 3, 4; \\ W_2^{BV} &= \omega_2 + \Gamma_2^{BV} = \omega_2 + \Gamma^{\text{ad}}. \end{aligned} \quad (2.23)$$

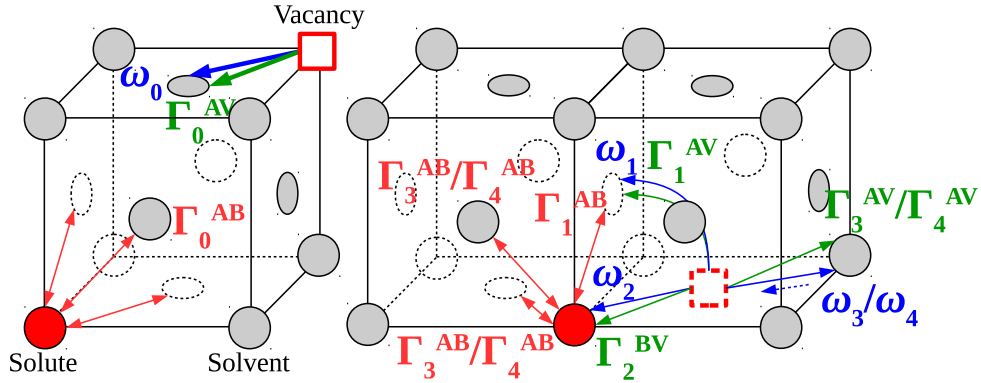


Figure 2.1: Illustration of all the possible transitions in dilute fcc alloys including 1-NN exchanges between atoms and between vacancy and atoms. Red hollow squares designate vacancies V, red filled circles designate solute atoms B, grey filled or hollow circles designate solvent atoms A.

Within the first shell approximation, two configurational probabilities are considered: P_1^{ness} for the configuration where B and V are located at 1-NN and P_0^{ness} for the dissociated configuration where B and V are beyond 1-NN. The analytical expression of the 1-NN-SRO is given

by:

$$\begin{aligned}\frac{P_1^{\text{ness}}}{P_0^{\text{ness}}} &= \frac{\omega_4 + \Gamma^{\text{ad}} + \Gamma^{\text{aa}}}{\omega_3 + \Gamma^{\text{ad}} + \Gamma^{\text{aa}}} \\ &= \frac{\exp(E_b/k_B T) + (\Gamma^{\text{ad}} + \Gamma^{\text{aa}})/\omega_3}{1 + (\Gamma^{\text{ad}} + \Gamma^{\text{aa}})/\omega_3},\end{aligned}\quad (2.24)$$

where E_b is the B-V 1-NN binding energy which is deduced from the ratio of thermal frequencies, with $\exp(E_b/k_B T) = \omega_4/\omega_3$. Note that $P_1^{\text{ness}}/P_0^{\text{ness}}$ is a SRO parameter revealing the binding tendency of B and V at the 1-NN. As Γ increases, the SRO parameter decreases towards 1. Note that the decrease in the above-threshold situation is larger than what is expected in the sub-threshold situation, just because two relocation frequencies contribute to the decrease in the above-threshold case.

The expressions of the phenomenological coefficients L_{BV} , L_{VB} , L_{VV} and L_{BB} in a dilute binary fcc alloy are given by

$$L_{\text{VB}} = -\frac{a_0^2}{4} C_{\text{BV}}^p \left[W_2^{\text{BV}} - \frac{\Lambda_4^{\text{B}}(\Lambda_3^{\text{V}} + \Lambda_4^{\text{V}})}{\Lambda} \right], \quad (2.25)$$

$$L_{\text{BV}} = -\frac{a_0^2}{4} C_{\text{BV}}^p \left[W_2^{\text{BV}} - \frac{\Lambda_4^{\text{V}}(\Lambda_3^{\text{B}} + \Lambda_4^{\text{B}})}{\Lambda} \right], \quad (2.26)$$

$$L_{\text{VV}} = \frac{a_0^2}{4} \left\{ C_{\text{V}}^{\text{m}} W_0^{\text{AV}} + C_{\text{BV}}^p \left[W_2^{\text{BV}} - \frac{\Lambda_4^{\text{V}}(\Lambda_3^{\text{V}} + \Lambda_4^{\text{V}})}{\Lambda} \right] \right\} \quad (2.27)$$

$$L_{\text{BB}} = \frac{a_0^2}{4} \left\{ C_{\text{B}}^{\text{m}} W_0^{\text{AB}} + C_{\text{BV}}^p \left[W_2^{\text{BV}} - \frac{\Lambda_4^{\text{B}}(\Lambda_3^{\text{B}} + \Lambda_4^{\text{B}})}{\Lambda} \right] \right\} \quad (2.28)$$

where $\Lambda = 7W_3 + 2W_1 + 2W_2^{\text{BV}}$, $\Lambda_3^\alpha = 3W_3^{\text{A}\alpha} - 2W_1^{\text{A}\alpha} - W_2^{\text{BV}}$ and $\Lambda_4^\alpha = 3W_4^{\text{A}\alpha} P_0^{\text{ness}}/P_1^{\text{ness}} - 2W_1^{\text{A}\alpha} - W_2^{\text{BV}}$ (for $\alpha = \text{B}, \text{V}$), with $W_i = W_i^{\text{AV}} + W_i^{\text{AB}}$ for $i = 0, 1, 3, 4$. C_{BV}^p is the concentration of B-V pair at 1-NN distance and C_{V}^{m} (resp. C_{B}^{m}) is the concentration of isolated V (resp. B). These concentrations can be deduced from the total concentrations of B and V (resp. C_{B} and C_{V}) by a low temperature expansion formalism [37–39]:

$$\begin{cases} C_{\text{BV}}^p = C_{\text{B}}^0 C_{\text{V}}^0 Z^{\text{ness}} \\ C_{\text{V}}^{\text{m}} = C_{\text{V}} - C_{\text{BV}}^p \\ C_{\text{B}}^{\text{m}} = C_{\text{B}} - C_{\text{BV}}^p, \end{cases} \quad (2.29)$$

with $C_{\text{B}}^0, C_{\text{V}}^0$ to be obtained by solving the following system of equations:

$$\begin{cases} C_{\text{B}} = C_{\text{B}}^0 + C_{\text{B}}^0 C_{\text{V}}^0 (Z^{\text{ness}} - Z_0) \\ C_{\text{V}} = C_{\text{V}}^0 + C_{\text{B}}^0 C_{\text{V}}^0 (Z^{\text{ness}} - Z_0), \end{cases} \quad (2.30)$$

where $Z^{\text{ness}} = 12P_1^{\text{ness}}/P_0^{\text{ness}}$ is the effective partition function at NESS and $Z_0 = 12$.

Note that the term $\Lambda_{m=3,4}^{\text{V}}$ (resp. $\Lambda_{m=3,4}^{\text{B}}$) is related to the vacancy (resp. solute atom) mobility since it contains all the vacancy (resp. solute atom) jump mechanisms including A-V (resp. A-B) and B-V (resp. V-B) exchanges. At equilibrium, $\Lambda_3^{\text{V}} = \Lambda_4^{\text{V}}$ and $\Lambda_3^{\text{B}} = \Lambda_4^{\text{B}}$ due to the microscopic detailed balance. Hence the two off-diagonal equilibrium coefficients L_{VB} and

L_{BV} are equal, according to the Onsager reciprocal relations. In addition, L_{VV} (resp. L_{BB}) can be separated into two parts: $C_V^m W_0^{AV}$ (resp. $C_B^m W_0^{AB}$) and the rest. The latter represents the exchanges of the B-V pair at 1-NN distance while the former represents the hops of the isolated V (resp. B).

In the case of sub-threshold irradiation for which there is no direct exchange between atoms (i.e. $\Gamma^{aa} = 0$), the off-diagonal coefficients are equal and, from Eq. (2.25), (2.26) we get:

$$L_{BV} = L_{VB} = -\frac{a_0^2 C_{BV}^p}{4} \frac{W_2^{BV} (13W_3^{AV} - 2W_1^{AV})}{7W_3^{AV} + 2W_1^{AV} + 2W_2^{BV}}. \quad (2.31)$$

Although the microscopic detailed balance is broken for the individual exchange frequencies ω_3 and Γ^{ad} , it still holds for the sum of the latter frequencies, that is $W_3 = W_3^{AV} = \omega_3 + \Gamma^{ad}$ (see Eq. (2.24)).

By replacing the total frequencies by the corresponding thermally activated jump frequencies, and replacing the dynamical SRO at NESS by the equilibrium SRO, the transport coefficients turn out to be equivalent to the Onsager coefficients L_{BV} of the five-frequency model within the first shell approximation [233].

The variation of L_{BV} with Γ^{ad} depends on the full set values of the thermal-activated jump frequencies. When Γ^{ad} is dominant before all ω_i : $L_{BV} \sim -C_B C_V \Gamma^{ad}$. Note that if $13\omega_3 > 2\omega_1$ ($L_{BV} < 0$), then L_{BV} remains negative whatever the magnitude of the relocation frequencies. Otherwise, a change of sign of L_{BV} can be observed when $\Gamma^{ad} \simeq -(13\omega_3 - 2\omega_1)/11$. Therefore, when a solute atom is dragged by a vacancy, FAR-d may change the sign of the solute-vacancy flux coupling and destroy the solute drag effect. In the opposite case, when L_{BV} is negative, FAR-d does not change the sign of the solute-vacancy flux coupling.

We consider now the case of above-threshold irradiation. Then FAR has two contributions: FAR-a and FAR-d, with $\Gamma^{aa} = \Gamma$ and $\Gamma^{ad} = \gamma\Gamma$. The off-diagonal terms L_{BV} and L_{VB} are not equal and their difference $\Delta L = L_{VB} - L_{BV}$ is given by:

$$\Delta L = \frac{3a_0^2 C_{BV}^p}{4} \frac{(1 - \omega_3/\omega_4)[\omega_a - (1 - \gamma)\Gamma] \omega_4 \Gamma}{(\omega_b + 11\gamma\Gamma + 9\Gamma)[\omega_4 + (1 + \gamma)\Gamma]}, \quad (2.32)$$

with

$$\begin{aligned} \omega_a &= 2\omega_2 + 2\omega_1 - 3\omega_3, \\ \omega_b &= 7\omega_3 + 2\omega_1 + 2\omega_2. \end{aligned} \quad (2.33)$$

Note that $\Delta L = 0$ in the two extreme cases when thermal jumps (ω) are dominant (i.e. $\Gamma/\omega \rightarrow 0$) or negligible ($\Gamma/\omega \rightarrow \infty$). The sign of ΔL is determined by the product $(1 - \omega_3/\omega_4)[\omega_a - (1 - \gamma)\Gamma]$. If $\gamma = 1$, this product involves thermal jump frequencies only. The first parenthesis is directly related to the equilibrium SRO parameter: $(1 - \omega_3/\omega_4)$ is positive if the vacancy and the solute atom attract each other and negative otherwise. The higher the thermodynamic attraction, the smaller the ratio ω_3/ω_4 , and the larger the difference ΔL .

2.3.5 Extension of the KineCluE code

For a more precise calculation beyond the first shell approximation, we consider each pair configuration where V and B are located at a distance lower than the kinetic radius R_k . At distances larger than R_k , B and V are considered as isolated monomers. Therefore, 3 cluster contributions are included: monomer B, monomer V as well as B-V pair. Note that the calculation under first shell approximation performed at Section 2.3.4 is a particular situation where the kinetic radius is set equal to the 1-NN distance. The calculation of the cluster transport coefficients is performed using the KineCluE code [167]. The latter accounts for all the kinetic paths within a pair cluster defined by radius R_k . Note that the kinetic radius can be set well beyond the 1-NN distance in KineCluE. This allows us to perform a converged calculation of cluster transport coefficients including long-distance FAR as well as long range kinetic correlations. In order to use NESS as reference state, a module is added to the code which calculates the NESS probability distribution by solving Eq. (2.9). Besides, the underlying principle of the microscopic detailed balance of the code is replaced by the global detailed balance condition (Eq. (2.10)). Models 1, 2 and 3 presented in Section 2.2.2 have been introduced into KineCluE. Note that the cluster radius R_c in Model 3 is set equal to R_k for simplicity.

2.3.6 Comparison between KineCluE results and Monte Carlo simulations

As mentioned in the introduction (Section 2.1), as soon as one of the microscopic diffusion mechanisms ($W_{\mathbf{n} \rightarrow \bar{\mathbf{n}}}^{AV}$ and $W_{\mathbf{n} \rightarrow \bar{\mathbf{n}}}^{AB}$) does not obey the microscopic detailed balance, we cannot use the Allnatt formulae [151, 152] to extract the phenomenological transport coefficients from atomistic kinetic Monte Carlo (AKMC) simulations. However, for a binary alloy with solute-point defect interactions restricted to 1-NN pairwise interactions, we have shown in Section 2.3.4 that detailed balance is fulfilled in the case of sub-threshold irradiation. Therefore, in this specific case, we may rely on the Allnatt formulae to obtain the Onsager matrix of the transport coefficients. As for the thermodynamic properties, we may apply AKMC to study the dynamical short range order characterizing a NESS from an average on the residential time, relying on the ergodic principle.

We choose here a model alloy with highly attractive vacancy-solute interactions because it emphasizes the effect of FAR on flux coupling. The migration barriers (in eV) are set to 0.95 for ω_0 and ω_3 , 0.75 for ω_1 and ω_4 , and 0.60 for ω_2 . The attempt frequency ν is chosen to be 10^{14} s^{-1} . As for the model of FAR, we choose Model 1, with r_m equal to the 1-NN distance r_1 .

The AKMC simulation box is a fcc crystal of 2048 sites. It contains one single solute atom and one vacancy. We apply periodic boundary conditions and use a residence-time algorithm. At each Monte Carlo step, we propose the whole set of the thermal jumps and FAR. We select one exchange from the proposed mechanisms. After every exchange, we compute the residence time increment. From the fluctuations of atomic positions, we compute the transport coefficients. Note that the corresponding off-diagonal coefficients given by the AKMC method

are by construction symmetric. As shown in Ref. [220, 221], they do not correspond to the transport coefficients L_{BV} and L_{VB} whenever one of the diffusion mechanism does not obey the detailed balance.

As for the KineCluE approach, the kinetic radius R_k of the cluster B-V is set to $4a_0$.

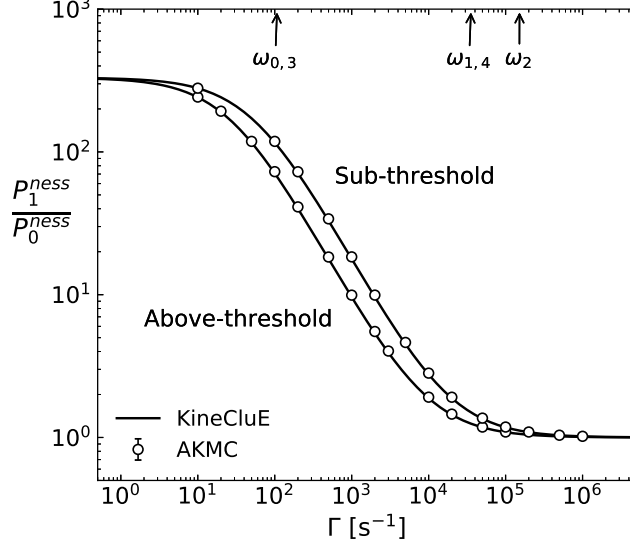


Figure 2.2: First nearest neighbor (1-NN) short range order as a function of FAR frequency Γ from KineCluE and AKMC simulations. Results are obtained for $\omega_4 = 3.55 \times 10^4 s^{-1}$ and $\omega_3 = 1.07 \times 10^2 s^{-1}$ at $T = 400K$. Model 1 is applied.

Fig. 2.2 shows the evolution of the dynamical 1-NN-SRO under sub- and above-threshold FAR. We obtain an excellent agreement between KineCluE and AKMC simulations on the SRO parameters. As expected, the dynamical SRO decreases with the relocation frequency with a higher rate in the case of an above-threshold irradiation.

Fig. 2.3 shows the variation of the transport coefficients with the frequency of FAR-d in the sub-threshold irradiation regime. Both KineCluE and AKMC methods give the same transport coefficients because the microscopic detailed balance holds for the total transition rates. However, when Γ is small compared with thermal jump frequencies, we observe a slight discrepancy between the coefficients. Yet the size of the AKMC simulation box is comparable with R_k . The discrepancy is due to the difference in the applied boundary conditions between KineCluE and the AKMC method. In KineCluE, configurations of solute and vacancy located at a distance larger than the kinetic radius are not included in the calculation, while the AKMC method relies on periodic boundary conditions. In the latter, atoms or PDs exiting from the simulation box enter back through another side and add a kinetic correlation contribution to the transport coefficients.

In the case of an above-threshold irradiation, we observe in Fig. 2.4 a similar behaviour of the diagonal transport coefficient L_{BB} , whereas the single off-diagonal coefficient measured in AKMC simulations does not correspond any more to the off-diagonal phenomenological transport coefficients obtained by KineCluE.

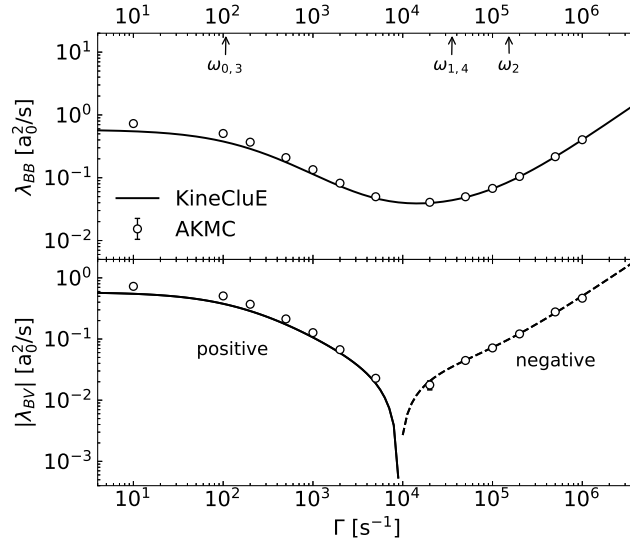


Figure 2.3: Solute atom diffusion coefficient and off-diagonal coefficients of transport matrix as a function of the FAR-d frequency Γ from KineCluE (solid and dashed lines) and AKMC (unfilled circles) simulations. Results are obtained for $\omega_{0,3} = 1.07 \times 10^2 s^{-1}$, $\omega_2 = 1.52 \times 10^5 s^{-1}$ and $\omega_{1,4} = 3.55 \times 10^4 s^{-1}$ at $T = 400K$. Model 1 is applied, with 1-NN FAR-d only.

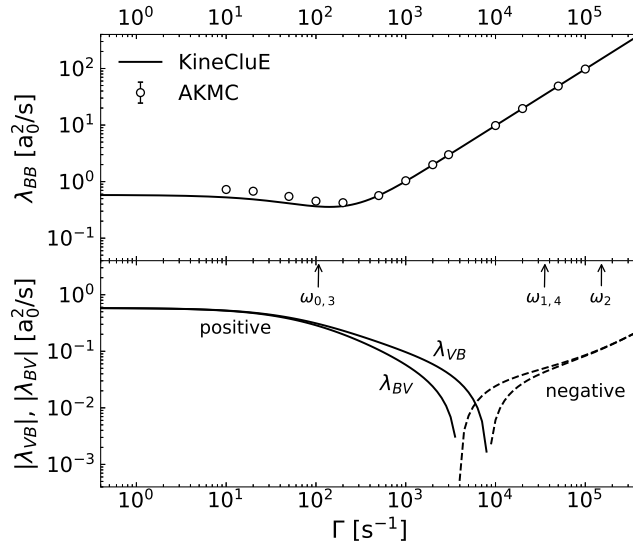


Figure 2.4: Solute atom diffusion coefficient and off-diagonal coefficients of transport matrix as a function of the above-threshold relocation frequency Γ from KineCluE (solid and dashed lines) and AKMC (unfilled circles) simulations. Results are obtained for $\omega_{0,3} = 1.07 \times 10^2 s^{-1}$, $\omega_2 = 1.52 \times 10^5 s^{-1}$ and $\omega_{1,4} = 3.55 \times 10^4 s^{-1}$ at $T = 400K$. Model 1 is applied, with 1-NN FAR-d and FAR-a.

2.4 Diffusion in far-from-equilibrium systems: beyond the linear response theory

The Onsager formulation of fluxes corresponds to a first-order Taylor expansion of the atomic fluxes in an equilibrium state, where chemical potential gradients are zero. This formulation yields a quantitative modeling of diffusion-controlled phenomena as long as the chemical potential gradients are not too large. Irradiation is an external force leading to gradients of concentrations of PDs and athermal reactions such as FAR, both affecting the chemical potential gradients. A higher-order expansion of fluxes could still be written as a linear combination of chemical potential gradients, provided the corresponding L -coefficients depend on the chemical potential gradients of a non-equilibrium reference state.

An external force inducing FAR exclusively, is a non-directional force. The incorporation of this force into the SCMF theory, requires two modifications: an expansion of the fluxes about a non-equilibrium state depending on FAR; and the account for the asymmetry of the PD-atom exchanges, as they do not obey the microscopic detailed balance. The resulting L -coefficients lose their symmetry and depend on the external force through the FAR frequencies. Hence, we may say fluxes written in function of these L -coefficients are far-from-equilibrium fluxes.

In this section, we tackle the far from equilibrium effects of both FAR and a large gradient of chemical potential on the kinetics of a simplified two-state model. Our developments rely on a molecular motor model [222]. In this model, dynamic events do not vary with the local environment. It mainly accounts for the asymmetry of jumps induced by a gradient of chemical potential. We extend the model to local concentration dependent jumps, and apply it to simplified atomic transport processes.

2.4.1 Two-state uni-dimensional model of vacancy-mediated atomic jumps

We consider a fictive four-frequency model of vacancy-mediated atomic jumps in a dilute binary alloy A(B) (cf. Fig. 2.5). Hops of vacancies and atoms are only possible along the axis (Oz). Moreover, we restrict the atomic jumps to the ones conserving the 1-NN distance between the vacancy and the solute atoms. Both thermally-activated vacancy jumps and FARs of solute atoms are considered. As indicated in Fig. 2.5, their transition rates are denoted by $\vec{\omega}_1$, $\overleftarrow{\omega}_1$, $\vec{\omega}_2$, and $\overleftarrow{\omega}_2$ for thermal jumps, and $\vec{\Gamma}_1$, $\overleftarrow{\Gamma}_1$, $\vec{\Gamma}_2$, and $\overleftarrow{\Gamma}_2$ for FARs. Therefore, only 1-NN solute-vacancy pair configurations are involved: we denote by ‘1⁻’ the one with the vacancy being on the left side of the solute atom, and by ‘1⁺’ the one with the vacancy being on the right side of the solute atom. The distribution function is noted $P_i(z_V, z_B, t)$ ($i = 1^-, 1^+$) where $z_V a_0$ and $z_B a_0$ are respectively the positions of the vacancy and solute atom at time t . The dynamics of

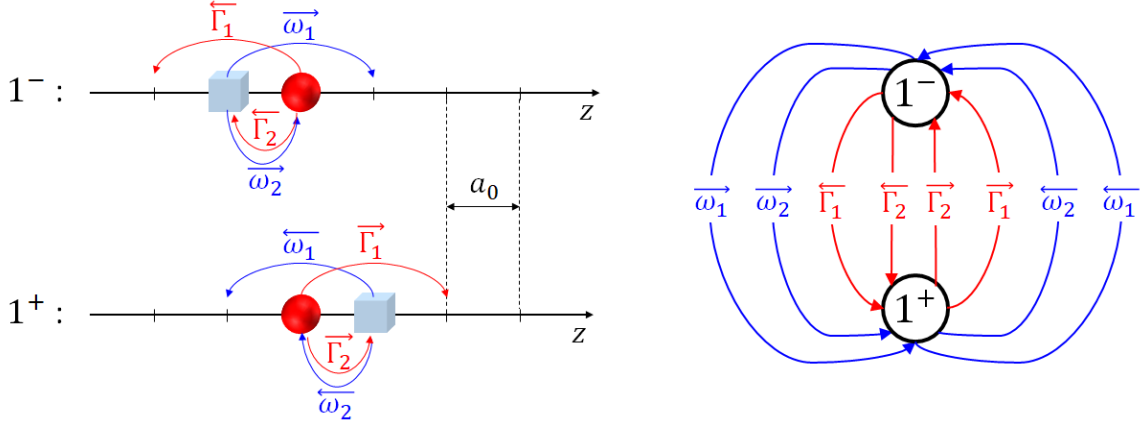


Figure 2.5: A schematic of the uni-dimensional atomic jumps along the axis (Oz). Only the vacancy (blue cubic) and the solute atom (red sphere) are presented. The other lattice sites are occupied by bulk atoms. Configuration 1^- corresponds to the solute-vacancy pair configuration with the vacancy located on the left side of the solute atom, and configuration 1^+ corresponds to the one with the vacancy located on the right side of the solute atom. The possible atomic jumps starting from configurations 1^- and 1^+ are presented in (a). The transitions between these two configurations are shown in (b).

the corresponding distribution function is governed by the following master equation,

$$\begin{aligned}
\frac{\partial P_{1^-}(z_V, z_B, t)}{\partial t} &= -(\overleftarrow{\omega}_1 + \overleftarrow{\omega}_2 + \overleftarrow{\Gamma}_1 + \overleftarrow{\Gamma}_2)P_{1^-}(z_V, z_B, t) \\
&\quad + \overleftarrow{\omega}_1 P_{1^+}(z_V + 2, z_B, t) + \overleftarrow{\Gamma}_1 P_{1^+}(z_V, z_B - 2, t) \\
&\quad + \overleftarrow{\omega}_2 P_{1^+}(z_V + 1, z_B - 1, t) + \overleftarrow{\Gamma}_2 P_{1^+}(z_V + 1, z_B - 1, t), \\
\frac{\partial P_{1^+}(z_V, z_B, t)}{\partial t} &= -(\overrightarrow{\omega}_1 + \overrightarrow{\omega}_2 + \overrightarrow{\Gamma}_1 + \overrightarrow{\Gamma}_2)P_{1^+}(z_V, z_B, t) \\
&\quad + \overrightarrow{\omega}_1 P_{1^-}(z_V - 2, z_B, t) + \overrightarrow{\Gamma}_1 P_{1^-}(z_V, z_B + 2, t) \\
&\quad + \overrightarrow{\omega}_2 P_{1^-}(z_V - 1, z_B + 1, t) + \overrightarrow{\Gamma}_2 P_{1^-}(z_V - 1, z_B + 1, t). \tag{2.34}
\end{aligned}$$

When no external force is applied, $\overleftarrow{\omega}_i = \overrightarrow{\omega}_i = \omega_i$ and $\overleftarrow{\Gamma}_i = \overrightarrow{\Gamma}_i = \Gamma_i$. Whereas, in the presence of external forces proportional to chemical potential gradients, $\overleftarrow{\omega}_i \neq \overrightarrow{\omega}_i$ and $\overleftarrow{\Gamma}_i \neq \overrightarrow{\Gamma}_i$. Under applied chemical potential gradients of vacancies (V), solute (B) and bulk atoms (A) along the (Oz)-direction, we write the transition rates as

$$\begin{aligned}
\overrightarrow{\omega}_1 &= \omega_1 e^{-2f_V}, \quad \overleftarrow{\omega}_1 = \omega_1 e^{+2f_V}, \quad \overrightarrow{\omega}_2 = \omega_2 e^{-f_V + f_B}, \quad \overleftarrow{\omega}_2 = \omega_2 e^{+f_V - f_B}, \\
\overrightarrow{\Gamma}_1 &= \Gamma_1 e^{-2f_B}, \quad \overleftarrow{\Gamma}_1 = \Gamma_1 e^{+2f_B}, \quad \overrightarrow{\Gamma}_2 = \Gamma_2 e^{-f_B + f_V}, \quad \overleftarrow{\Gamma}_2 = \Gamma_2 e^{+f_B - f_V}, \tag{2.35}
\end{aligned}$$

where $f_\alpha = a_0 \mathbf{e}_z \cdot (\nabla \mu_\alpha - \nabla \mu_A)/(k_B T)$ with a_0 the lattice parameter (i.e., 1-NN distance in our case) and \mathbf{e}_z the unit vector along the axis (Oz).

2.4.2 Description of the dynamics using generating functions

We investigate the long-time behaviors of the two-state diffusion model using generating functions. Let us introduce

$$F_i(n_V, n_B, t) = \sum_{z_V} \sum_{z_B} e^{-n_V z_V - n_B z_B} P_i(z_V, z_B, t), \quad (2.36)$$

whose time evolution is deduced from the Master Equation

$$\frac{\partial F_i}{\partial t} = \mathbf{M}_{ij} F_j, \quad (2.37)$$

where $\mathbf{M}(n_V, n_B)$ is a 2-dimension matrix obtained from the master equation—Eq. (2.34), and given by

$$\mathbf{M} = \begin{bmatrix} -(\overleftarrow{\omega}_1 + \overleftarrow{\omega}_2 + \overleftarrow{\Gamma}_1 + \overleftarrow{\Gamma}_2) & \overleftarrow{\omega}_1 e^{+2n_V} + \overleftarrow{\Gamma}_1 e^{-2n_B} + (\overleftarrow{\omega}_2 + \overleftarrow{\Gamma}_2) e^{+n_V - n_B} \\ \overleftarrow{\omega}_1 e^{-2n_V} + \overleftarrow{\Gamma}_1 e^{+2n_B} + (\overleftarrow{\omega}_2 + \overleftarrow{\Gamma}_2) e^{-n_V + n_B} & -(\overleftarrow{\omega}_1 + \overleftarrow{\omega}_2 + \overleftarrow{\Gamma}_1 + \overleftarrow{\Gamma}_2) \end{bmatrix} \quad (2.38)$$

By relying on the definition of the generating function Eq. (2.36), we write the following ensemble average as a sum of generating functions

$$\langle e^{-n_V z_V - n_B z_B} \rangle = \sum_i F_i(n_V, n_B, t), \quad (2.39)$$

where $\langle \cdot \rangle$ is the ensemble average over the distribution function P_i . When $t \rightarrow \infty$, one demonstrates the following equivalent relation

$$\sum_i F_i(n_V, n_B, t) \stackrel{t \rightarrow \infty}{\sim} e^{\lambda t}, \quad (2.40)$$

where λ is the largest eigenvalue of \mathbf{M} , which contains all the steady-state diffusion properties of the vacancy and solute atom [222].

From Eq. (2.40), we obtain that, for $\alpha \equiv V, B$,

$$\frac{\partial \lambda}{\partial n_\alpha}(n_V, n_B) = \frac{1}{t e^{\lambda t}} \frac{\partial e^{\lambda t}}{\partial n_\alpha} = -\frac{1}{t} \frac{\sum_i z_\alpha F_i(n_V, n_B, t)}{\sum_i F_i(n_V, n_B, t)}. \quad (2.41)$$

By definition of the generating function, the ensemble average of the position of species α at time t is equal to

$$\langle z_\alpha(t) \rangle = \frac{\sum_i z_\alpha F_i(0, 0, t)}{\sum_i F_i(0, 0, t)}, \quad (2.42)$$

and the average velocity of species α is given by

$$\bar{v}_\alpha = \frac{\langle z_\alpha(t) \rangle a_0}{t} = -a_0 \frac{\partial \lambda}{\partial n_\alpha}(0, 0). \quad (2.43)$$

From Eq. (2.43), we deduce the average flux of species α

$$J_\alpha = \frac{\bar{v}_\alpha}{\Omega} = -\frac{a_0}{\Omega} \frac{\partial \lambda}{\partial n_\alpha}(0, 0), \quad (2.44)$$

where Ω is the atomic volume.

The higher order derivatives of λ give access to higher moments of $z_\alpha(t)$. For instance, the second moments correspond to the second derivatives of λ . We first calculate the second derivatives of $e^{\lambda t}$

$$\frac{1}{t} \frac{\partial^2 e^{\lambda t}}{e^{\lambda t} \partial n_\alpha \partial n_\beta} = \frac{\partial^2 \lambda}{\partial n_\alpha \partial n_\beta} + t \frac{\partial \lambda}{\partial n_\alpha} \frac{\partial \lambda}{\partial n_\beta}. \quad (2.45)$$

Then, we relate the second-order partial derivatives of λ to the second moment of the generating function

$$\frac{1}{t} \frac{\partial^2 e^{\lambda t}}{e^{\lambda t} \partial n_\alpha \partial n_\beta}(0, 0) = \frac{1}{t} \frac{\sum_i z_\alpha z_\beta F_i(0, 0, t)}{\sum_i F_i(0, 0, t)} = \frac{\langle z_\alpha z_\beta \rangle}{t}. \quad (2.46)$$

From Eqs. (2.43), (2.45), and (2.46), we obtain the relation

$$\frac{\partial^2 \lambda}{\partial n_\alpha \partial n_\beta}(0, 0) = \frac{\langle z_\alpha z_\beta \rangle - \langle z_\alpha \rangle \langle z_\beta \rangle}{t}. \quad (2.47)$$

Therefore, the second moments of λ yield the diffusion matrix associated with the position fluctuations of the various species of the system

$$D_{\alpha\beta} = \frac{a_0^2}{2} \frac{\partial^2 \lambda}{\partial n_\alpha \partial n_\beta}(0, 0) \quad (2.48)$$

2.4.3 Far-from-equilibrium kinetic properties of the two-state model

From the transition matrix of the two-state model as defined in Eq. (2.38), we derive the exact expressions of λ , and its first and second derivatives

$$\lambda(n_V, n_B) = \frac{1}{2} [-(\omega_{\text{tot}} + \Gamma_{\text{tot}}) + \omega_\Delta], \quad (2.49)$$

$$\frac{\partial \lambda}{\partial n_\alpha}(n_V, n_B) = -\frac{c_1}{\omega_\Delta} \quad (2.50)$$

$$\frac{\partial^2 \lambda}{\partial n_\alpha \partial n_\beta}(n_V, n_B) = \frac{c_2 \omega_\Delta^2 - 2c_1^2}{\omega_\Delta^3}, \quad (2.51)$$

with

$$\omega_\Delta = \sqrt{(\omega_{\text{tot}} + \Gamma_{\text{tot}})^2 - 4c_0}, \quad (2.52)$$

where $\omega_{\text{tot}} = \overleftarrow{\omega}_1 + \overrightarrow{\omega}_1 + \overleftarrow{\omega}_2 + \overrightarrow{\omega}_2$, $\Gamma_{\text{tot}} = \overleftarrow{\Gamma}_1 + \overrightarrow{\Gamma}_1 + \overleftarrow{\Gamma}_2 + \overrightarrow{\Gamma}_2$, and

$$\begin{aligned} c_0(n_V, n_B) = & + \overleftarrow{\omega}_1 \overleftarrow{\Gamma}_1 (1 - e^{+2n_V+2n_B}) + \overrightarrow{\omega}_1 \overrightarrow{\Gamma}_1 (1 - e^{-2n_V-2n_B}) \\ & + \overrightarrow{\omega}_1 (\overleftarrow{\omega}_2 + \overrightarrow{\Gamma}_2) (1 - e^{-n_V-n_B}) + \overleftarrow{\omega}_1 (\overrightarrow{\omega}_2 + \overleftarrow{\Gamma}_2) (1 - e^{+n_V+n_B}) \\ & + \overrightarrow{\Gamma}_1 (\overrightarrow{\omega}_2 + \overleftarrow{\Gamma}_2) (1 - e^{-n_V-n_B}) + \overleftarrow{\Gamma}_1 (\overleftarrow{\omega}_2 + \overrightarrow{\Gamma}_2) (1 - e^{+n_V+n_B}), \end{aligned} \quad (2.53)$$

$$\begin{aligned} c_1(n_V, n_B) = & - 2 \overleftarrow{\omega}_1 \overleftarrow{\Gamma}_1 e^{+2n_V+2n_B} + 2 \overrightarrow{\omega}_1 \overrightarrow{\Gamma}_1 e^{-2n_V-2n_B} \\ & + \overrightarrow{\omega}_1 (\overleftarrow{\omega}_2 + \overrightarrow{\Gamma}_2) e^{-n_V-n_B} - \overleftarrow{\omega}_1 (\overrightarrow{\omega}_2 + \overleftarrow{\Gamma}_2) e^{+n_V+n_B} \\ & + \overrightarrow{\Gamma}_1 (\overrightarrow{\omega}_2 + \overleftarrow{\Gamma}_2) e^{-n_V-n_B} - \overleftarrow{\Gamma}_1 (\overleftarrow{\omega}_2 + \overrightarrow{\Gamma}_2) e^{+n_V+n_B}, \end{aligned} \quad (2.54)$$

$$\begin{aligned} c_2(n_V, n_B) = & - 4 \overleftarrow{\omega}_1 \overleftarrow{\Gamma}_1 e^{+2n_V+2n_B} - 4 \overrightarrow{\omega}_1 \overrightarrow{\Gamma}_1 e^{-2n_V-2n_B} \\ & - \overrightarrow{\omega}_1 (\overleftarrow{\omega}_2 + \overrightarrow{\Gamma}_2) e^{-n_V-n_B} - \overleftarrow{\omega}_1 (\overrightarrow{\omega}_2 + \overleftarrow{\Gamma}_2) e^{+n_V+n_B} \\ & - \overrightarrow{\Gamma}_1 (\overrightarrow{\omega}_2 + \overleftarrow{\Gamma}_2) e^{-n_V-n_B} - \overleftarrow{\Gamma}_1 (\overleftarrow{\omega}_2 + \overrightarrow{\Gamma}_2) e^{+n_V+n_B}. \end{aligned} \quad (2.55)$$

From Eq. (2.44) and Eq. (2.49), calculate the fluxes of vacancy V and solute B

$$J_V = J_B = \frac{a_0}{\Omega} \frac{c_1(0, 0)}{\omega_{\text{tot}} + \Gamma_{\text{tot}}}, \quad (2.56)$$

and from Eq. (2.48), the corresponding diffusion coefficients

$$D_{\alpha\beta} = \frac{c_2(0, 0) (\omega_{\text{tot}} + \Gamma_{\text{tot}})^2 - 2 [c_1(0, 0)]^2}{(\omega_{\text{tot}} + \Gamma_{\text{tot}})^3}. \quad (2.57)$$

We formulate the kinetic response to the applied chemical potential gradients, by means of a response matrix

$$\Lambda_{\alpha\beta} = k_B T \frac{\partial J_\alpha}{\partial \nabla \mu_{\beta A}}, \quad (2.58)$$

with $\mu_{\beta A} = \mu_\beta - \mu_A$. These coefficients around equilibrium, where f_B and f_V are set to zero, the response matrix corresponds to the Onsager matrix

$$L_{\alpha\beta} = k_B T \left. \frac{\partial J_\alpha}{\partial \nabla \mu_{\beta A}} \right|_{f_\alpha=0, f_\beta=0}. \quad (2.59)$$

From Eq. (2.35), the exact expressions of the Onsager coefficients write

$$L_{VV} = L_{BB} = L_{VB} = L_{BV} = \frac{a_0^2}{\Omega} \frac{4\omega_1\Gamma_1 + (\omega_1 + \Gamma_1)(\omega_2 + \Gamma_2)}{\omega_1 + \omega_2 + \Gamma_1 + \Gamma_2}. \quad (2.60)$$

Note that $L_{BV} = L_{VB}$, as demonstrated by the Onsager theorem [217, 218]. From Eq. (2.57), we may demonstrate that, if $f_B = 0$ and $f_V = 0$, the L -coefficients are directly related to the fluctuation-related diffusion coefficients: $L_{\alpha\beta} = D_{\alpha\beta}/\Omega$. These relationships are similar to the Einstein-Allnatt relations [151]. Note that, the generalized SCMF theory including FAR [40] leads to the same expressions of the transport coefficients as Eq. (2.60). The Onsager relation is still valid in the presence of athermal mechanism (FAR) because in this particular atomic jump process, the microscopic detailed balance is not broken by FAR.

Away from equilibrium, Onsager and generalized Einstein-Allnatt relations are no longer valid, i.e., $\Lambda_{\text{BV}} \neq \Lambda_{\text{VB}}$ and $\Lambda_{\alpha\beta} \neq D_{\alpha\beta}/\Omega$.

It is possible to apply this approach to a more complex diffusion model with more solute-vacancy pair configurations beyond the 1-NN pair configuration. When the dimension of the corresponding transition matrix \mathbf{M} is larger than 4, it is, in general, impossible to give the analytical expression of λ ; thus, we need to perform a numerical calculation of λ and its partial derivatives.

2.5 Diffusion properties in model alloys

Here we focus on the above-threshold irradiation case. We consider a model alloy with relatively high migration barriers. Hence the alloy is potentially sensitive to FAR effects, just because the thermal jump frequencies are small with respect to the relocation frequency deduced from realistic dose rate. The energy interaction between B and V is restricted to a pairwise 1-NN interaction. The migration barriers (in eV) are set to 1.10 for ω_0 , ω_1 and ω_3 , 0.90 for ω_4 , and 0.80 for ω_2 . The attempt frequency ν is chosen to be equal to $5 \times 10^{12} \text{ s}^{-1}$. The three relocation models indicated in the Section 2.2.2 are considered. We use KineCluE to calculate the transport coefficients.

The parameter values that we set to estimate the vacancy concentration under irradiation are shown in Tab. 2.2. Here the mean relocation range r_m and the cut-off distance L for Models 2 and 3 are respectively set to 1-NN ($\sqrt{1/2} a_0$) and 5-NN ($\sqrt{5/2} a_0$) distances. The kinetic radius is set to $2a_0$.

Table 2.2: List of the parameters needed to estimate the vacancy concentration and their set values.

Parameter	Value
Lattice parameter a_0	0.35 nm
Vacancy formation enthalpy H_{V}^{f}	1.65 eV
Vacancy formation entropy S_{V}^{f}	$1.82 k_{\text{B}}$
Number of FARs per dpa n_{FAR}	100
Sink strength k^2	10^{15} m^{-2}

2.5.1 Dynamical short range order

Fig. 2.6 shows the profile of dynamical SRO as a function of Γ for Models 1, 2 and 3. The probability for B and V at 1-NN distance is reduced by FAR leading to an effective B-V interaction smaller than the thermodynamic one. The decrease of 1-NN-SRO with the relocation frequency in Model 1 starts when Γ is around 10^{-2} s^{-1} . The decrease starts earlier in Models 2 and 3: respectively around 10^{-4} s^{-1} and 10^{-3} s^{-1} . However, the 1-NN-SRO of Model

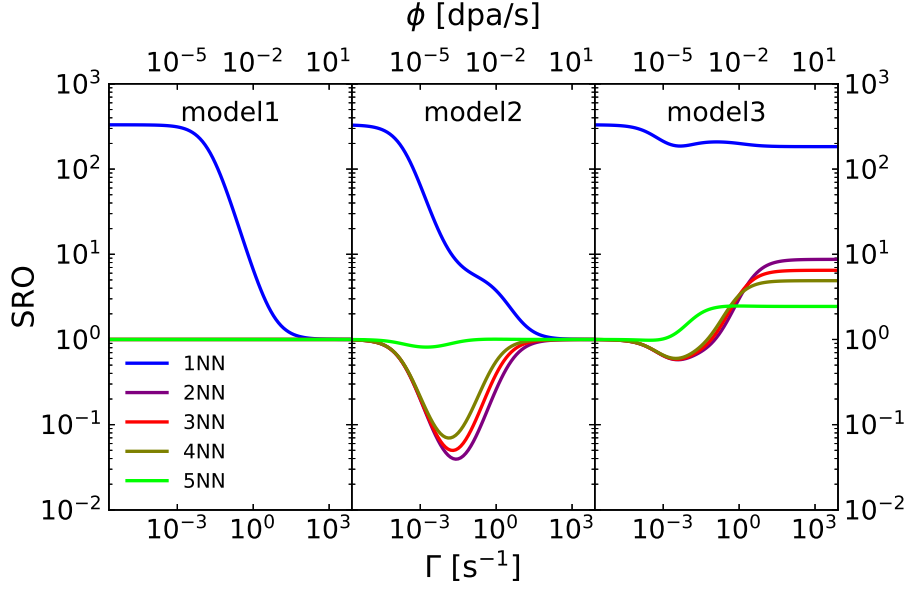


Figure 2.6: Steady-state short range order as a function of the relocation frequency in the above-threshold radiation regime. Results are obtained by KineCluE for $\omega_{0,1,3} = 6.9 \times 10^{-2} s^{-1}$, $\omega_2 = 4.2 \times 10^2 s^{-1}$ and $\omega_4 = 2.3 \times 10^1 s^{-1}$ at $T = 400K$. The mean relocation range r_m is set 1-NN. The cut-off relocation distance and the kinetic radius of the cluster B-V are set to $3a_0$.

3 converges towards non-zero value at large Γ . In Model 1, there is no interaction between B and V beyond the 1-NN distance, whatever the relocation frequency. However, in Models 2 and 3, we observe that the effective B-V interaction extends beyond the range of the thermal one (i.e. beyond the 1-NN). The effective interaction remains up to 5-NN distance when Γ is comparable to one of the thermal jump frequencies. This is due to the relatively long range of FAR. In the extreme case when Γ is dominant before the thermal jump frequencies, the B-V interactions are dropping in Models 1 and 2 whereas in Model 3 the 1-NN attraction is slightly decreasing and the 2-, 3-, 4-, and 5-NN are slightly increasing. The binding tendency of a vacancy around the solute atom is still high ($P_1^{\text{ness}}/P_0^{\text{ness}} \simeq 10^2$) due to the introduction of the biased FAR-d with the 1-NN atoms of the solute atom in Model 3.

2.5.2 Tracer diffusion coefficient

In the dilute limit, the tracer diffusion coefficient of solute B is written as

$$D_B^* = \frac{L_{BB}}{C_B}. \quad (2.61)$$

Phenomenological models of diffusion under irradiation systematically rely on the assumption that the thermally activated diffusion and FAR take place in parallel [69, 144]. The tracer diffusion coefficient is then written as a sum of two diffusion coefficients:

$$D_{B,\text{add}}^* = D_{B,\text{th}}^* C_V^{\text{ness}} / C_V^{\text{eq}} + D_{B,\text{far}}^*, \quad (2.62)$$

where $D_{B,\text{th}}^*$ is the thermal diffusion coefficient commonly deduced from diffusion experiments or atomic based diffusion models and $D_{B,\text{far}}^*$ is the diffusion coefficient of solute atom B resulting

from FAR only. Note that both coefficients can be calculated by KineCluE. Unless one diffusion mechanism is dominant over the other, we expect a non-additive contribution to the solute tracer diffusion coefficient because of the kinetic correlations. In order to quantify the non-additive contribution, we define the relative difference:

$$\Delta D_B = \frac{D_{B,\text{add}}^* - D_B^*}{D_B^*}. \quad (2.63)$$

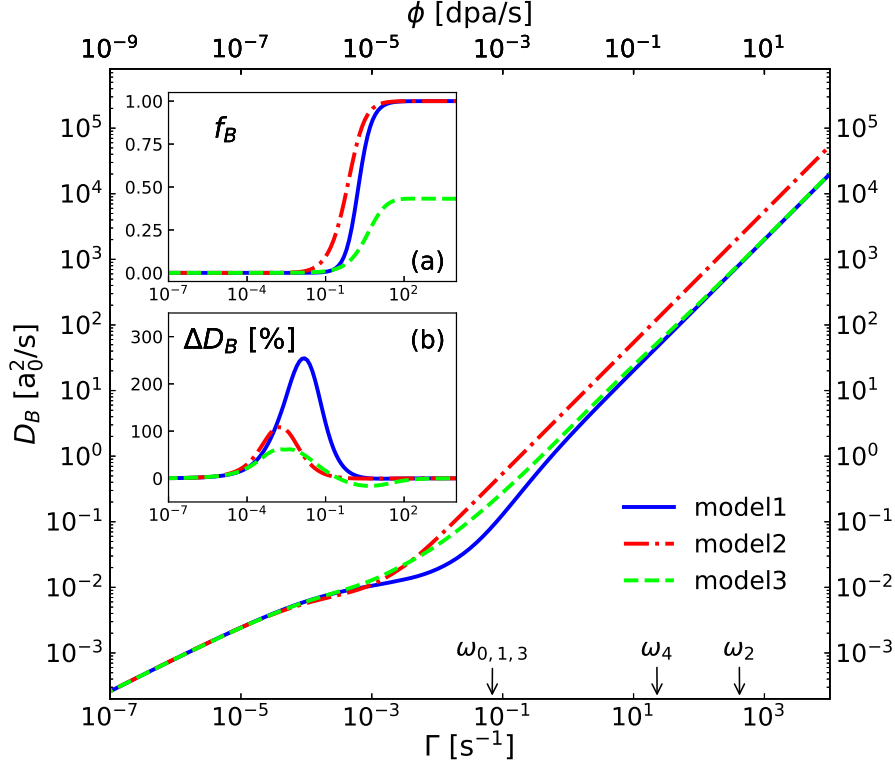


Figure 2.7: Solute atom diffusion coefficient as a function of the relocation frequency Γ in the above-threshold radiation regime. Results are obtained by KineCluE for $\omega_{0,1,3} = 6.9 \times 10^{-2} s^{-1}$, $\omega_2 = 4.2 \times 10^2 s^{-1}$ and $\omega_4 = 2.3 \times 10^1 s^{-1}$ at $T = 400K$. C_B is set 0.1 at.%. The mean relocation range r_m is set 1-NN. The cut-off relocation distance and the kinetic radius of the cluster B-V are set to $3a_0$. The insets (a) and (b) show the variations of correlation factor f_B and the relative difference ΔD_B with the relocation frequency.

Fig 2.7 shows the variation of the solute diffusion coefficient with the relocation frequency. We observe that the global tendencies of the diffusion coefficients obtained with the three models are similar. However, the three curves do not have the same asymptote at large Γ . The largest difference occurs when the correlation factor f_B is increased by FAR. With Models 1 and 2, this factor tends to 1 when Γ is dominant over the thermal jump frequencies, meaning that there are no kinetic correlations. However, in Model 3, the correlation factor tends to 0.46. The remaining kinetic correlations are due to the thermodynamic bias of FAR-d. Besides, ΔD_B is high when Γ is in the range of the thermal jump frequencies because then, there is a strong competition between the thermal mechanisms and FAR. In this example, ΔD_B spans from 100 % to 300 % depending on the relocation model.

2.5.3 Flux coupling

We characterize the flux coupling between solute B and vacancy V by computing the wind factors [13, 16, 169]

$$\delta_{B \rightarrow V} = \frac{L_{BV}}{L_{VV}} \quad (2.64)$$

and

$$\delta_{V \rightarrow B} = \frac{L_{VB}}{L_{BB}}. \quad (2.65)$$

Both wind factors describe the B-V flux coupling related to two different situations. The wind factor $\delta_{B \rightarrow V}$ gives the number of solute atoms following a vacancy under the driving force $\nabla\mu_V$ and the wind factor $\delta_{V \rightarrow B}$ indicates the number of vacancies dragged by a solute atom under the driving force $\nabla\mu_B$. If the wind factors are positive, a drag of B by V (or vice versa) may occur. As shown in Section 2.5.1, the interactions between the solute atom and the vacancy are reduced or even destroyed by FAR. Since the drag effect is highly related to this interaction, we study the effect of the relocation frequency Γ on the wind factors.

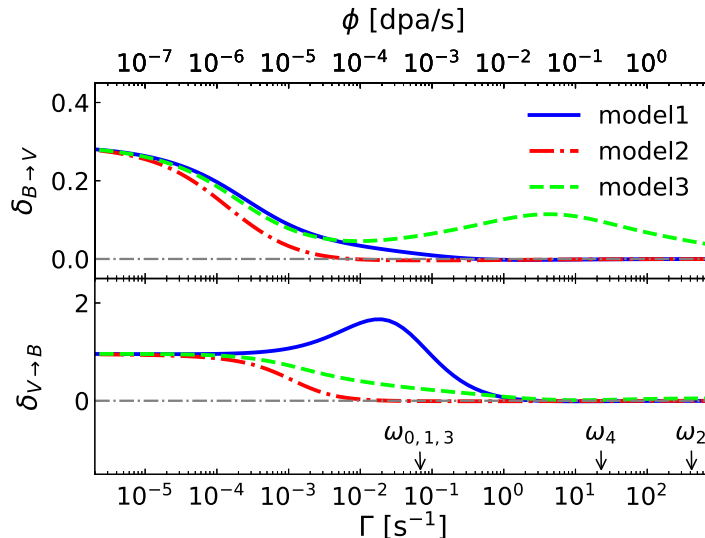


Figure 2.8: Drag factors $\delta_{B \rightarrow V}$ and $\delta_{V \rightarrow B}$ as a function of the relocation frequency Γ in the above-threshold radiation regime. Results are obtained by KineCluE for $\omega_{0,1,3} = 6.9 \times 10^{-2} s^{-1}$, $\omega_2 = 4.2 \times 10^2 s^{-1}$ and $\omega_4 = 2.3 \times 10^1 s^{-1}$ at $T = 400K$. C_B is set 0.1 at.%. The mean relocation range r_m is set 1-NN. The cut-off relocation distance and the kinetic radius of the cluster B-V are set to $3a_0$. The dashed lines are eye-guides for $\delta_{B \rightarrow V} = 0$ or $\delta_{V \rightarrow B} = 0$.

Fig. 2.8 shows the variation of the wind factors with the relocation frequency. Whatever the relocation models, $\delta_{B \rightarrow V}$ and $\delta_{V \rightarrow B}$ globally decrease with Γ . However, $\delta_{V \rightarrow B}$ of Model 1 has a surprising non-monotonous behaviour: the drag effect is enhanced before being destroyed by FAR. $\delta_{B \rightarrow V}$ of Model 3 has also an atypical behaviour: it slightly increases and tends to a non-zero value at large Γ , meaning that the solute drag and vacancy drag effects are not totally destroyed. This is because the biased FAR-d maintains a flux coupling between B and V. This persistent flux coupling at high radiation flux should be very sensitive to the details of the relocation mechanism.

2.6 Sensitivity study with respect to the model and alloy parameters

FAR models depend on the values of the mean relocation range r_m , the kinetic radius R_k of the cluster B-V and the truncation distance. However, the latter parameter is not a physical parameter. Since the relocation frequency exponentially decreases with the distance between B and V (see Eq. (2.4)), the value of L in Eq. (2.4) does not affect the diffusion properties as long as it is large enough. Therefore, we focus here on the sensitivity of the results to the other two parameters: r_m and R_k .

2.6.1 Kinetic radius

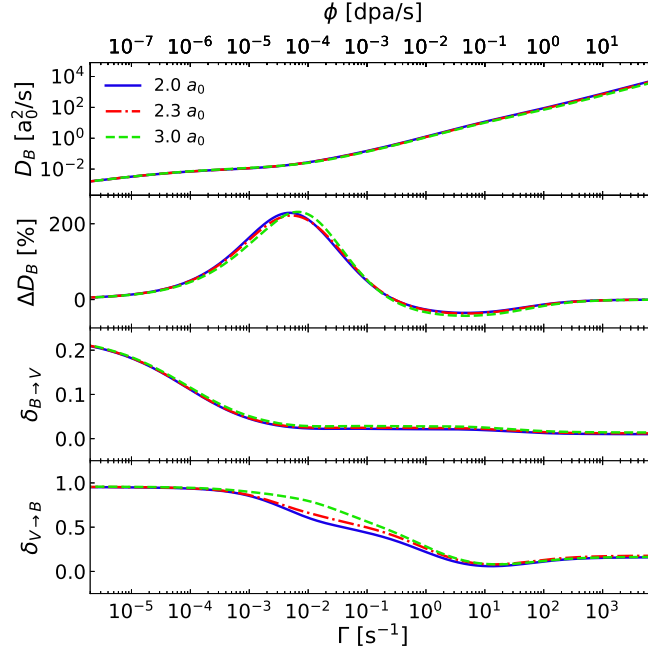


Figure 2.9: Diffusion properties as functions of the relocation frequency Γ in the above-threshold radiation regime. Results are obtained by KineCluE for $\omega_{0,1,3} = 6.9 \times 10^{-2} s^{-1}$, $\omega_2 = 4.2 \times 10^2 s^{-1}$ and $\omega_4 = 2.3 \times 10^1 s^{-1}$ at $T = 400K$ with three different kinetic radius $R_k = 2a_0$, $2.3a_0$ and $3a_0$. C_B is set 0.05 at.%. Model 3 is used as the relocation model. The mean and cut-off relocation distances are respectively set to $(\sqrt{2}/2)a_0$ and $2a_0$.

In general, the results given by KineCluE code converge with the kinetic radius R_k [167]. However, because $R_c = R_k$ in Model 3, the FAR-d models for a monomer vacancy and for a vacancy within the B-V pair are different. In this case, the results obtained with Model 3 may depend on the values of R_k . However, Fig. 2.9 shows that D_B^* , ΔD_B and $\delta_{B \rightarrow V}$ are not very sensitive to the change of the kinetic radius. Although, the decrease rate of $\delta_{V \rightarrow B}$ with Γ is

slower with $R_k = 3a_0$ than $2a_0$. This is because the vacancy performs biased FAR-d with the 1-NN atoms of the solute atom from longer distances.

2.6.2 Mean relocation range

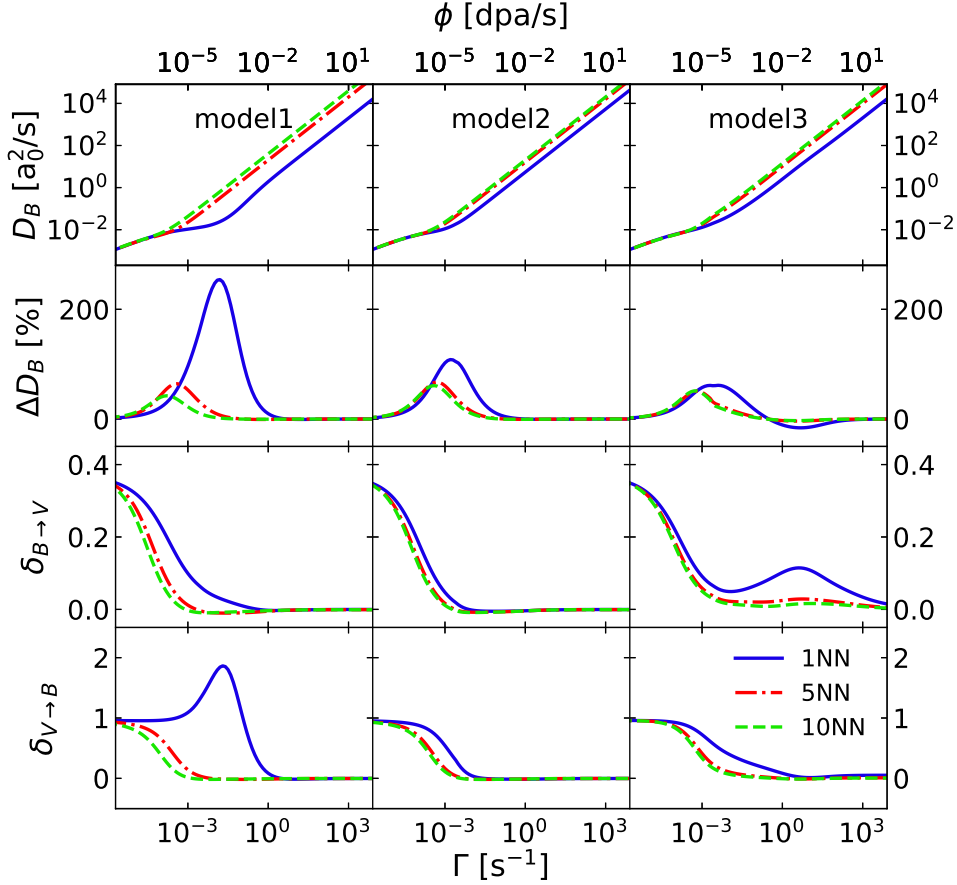


Figure 2.10: Diffusion properties as functions of the relocation frequency Γ in the above-threshold radiation regime. Results are obtained by KineCluE for $\omega_{0,1,3} = 6.9 \times 10^{-2} s^{-1}$, $\omega_2 = 4.2 \times 10^2 s^{-1}$ and $\omega_4 = 2.3 \times 10^1 s^{-1}$ at $T = 400K$ with three different values of r_m : 1-, 5-, and 10-NN. C_B is set 0.1 at.%. The cut-off relocation distance and the kinetic radius of the cluster B-V are set to $3a_0$.

Fig. 2.10 shows the effect of the mean relocation distance r_m on the solute diffusion and flux coupling. First we focus on Model 1. Since the solute mobility is enhanced when increasing the relocation distance, the corresponding solute diffusion coefficient increases with r_m . Besides, according to the plot of ΔD_B , the interaction between thermal jumps and FAR decreases with r_m . The thermally-activated jump distance and the thermal interaction between B and V are both restricted to 1-NN. The larger the relocation distance, the smaller the B-V interaction. Thus B and V are more likely to diffuse as monomers, a kinetic regime where the diffusion

properties related to the thermal jumps and FAR become additive. As for the flux coupling, the decreasing rate of $\delta_{B \rightarrow V}$ with Γ increases with r_m . Thus the solute drag effect is destroyed more easily. Besides, the variation tendency of $\delta_{V \rightarrow B}$ with Γ become qualitatively different when $r_m > 1$ -NN. The vacancy drag effect is not enhanced when r_m equals to 2- and 3-NN. This may be due to the same reason mentioned before: B and V have many more paths to escape from each other. As for the results obtained with Models 2 and 3, they have similar profiles as the ones in Model 1.

2.6.3 Atomic mixing rate

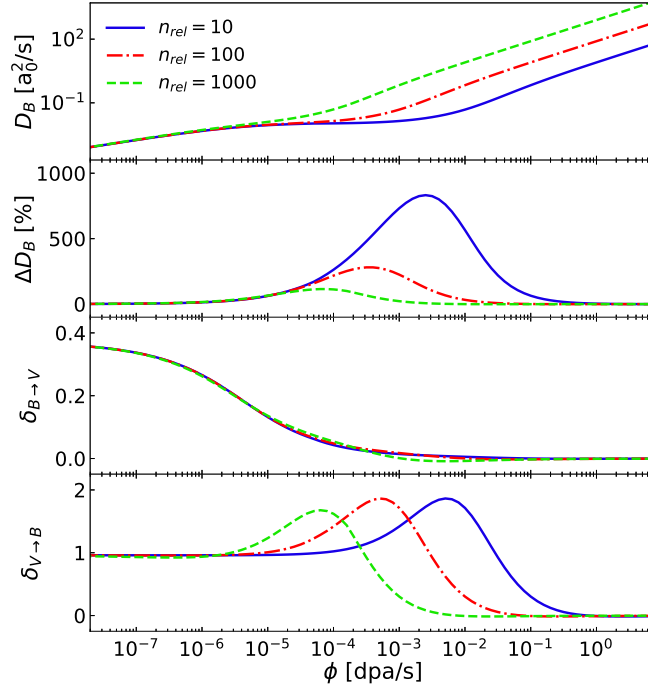


Figure 2.11: D_B , and wind factors $\delta_{B \rightarrow V}$, $\delta_{V \rightarrow B}$ as a function of relocation frequency Γ from KineCluE simulations. Results are obtained for $\omega_{0,1,3} = 6.9 \times 10^{-2} s^{-1}$, $\omega_2 = 4.2 \times 10^2 s^{-1}$ and $\omega_4 = 2.3 \times 10^1 s^{-1}$ with different values of n_{FAR} at $T = 400K$. C_B is set 0.1 at. %.

Since the previous section has shown that the effects of FAR are roughly the same in terms of the global tendency whatever the relocation model and the mean relocation distance, we choose the simplest model, Model 1 with $r_m = r_1$. As stated in Section 2.2.3, the number of relocations per Frenkel pair created (i.e. n_{FAR}) should be alloy specific due to the thermal effect on heat spike mixing. Fig. 2.11 shows the variation of the diffusion properties in function of radiation dose rate with different values of n_{FAR} . The effect of FAR on the flux coupling and tracer diffusion occurs at a smaller dose rate when n_{FAR} increases. Moreover, we observe that ΔD_B decreases with n_{FAR} . These results show the importance of n_{FAR} in the prediction of a critical dose rate when the effects of FAR on the flux coupling and tracer diffusion is paramount.

2.6.4 FAR-d frequencies

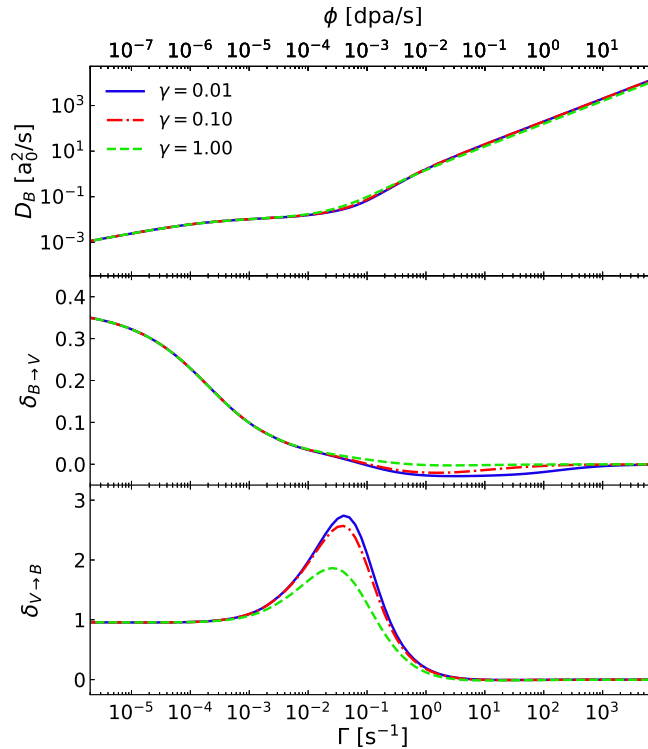


Figure 2.12: D_B , and wind factors $\delta_{B \rightarrow V}$, $\delta_{V \rightarrow B}$ as a function of relocation frequency Γ from KineCluE simulations. Results are obtained for $\omega_{0,1,3} = 6.9 \times 10^{-2} s^{-1}$, $\omega_2 = 4.2 \times 10^2 s^{-1}$ and $\omega_4 = 2.3 \times 10^1 s^{-1}$ with different values of $\gamma = \Gamma^{ad}/\Gamma^{aa}$ at $T = 400K$. C_B is set 0.1 at.%.

For the reason stated in Section 2.6.3, Model 1 with $r_m = r_1$ is chosen for the sake of simplicity. Note that FAR-a and FAR-d are due to different phenomena in the displacement cascade: FAR-a describes the recoil mixing due to PKA while FAR-d models the lattice site change of PD during the quenching process. There is no guarantee that the frequencies of FAR-a (Γ^{aa}) and FAR-d (Γ^{ad}) are equal. Fig. 2.12 shows the plot of D_B , $\delta_{B \rightarrow V}$ and $\delta_{V \rightarrow B}$ as a function of relocation frequency $\Gamma^{aa} = \Gamma$ with different ratios $\gamma = \Gamma^{ad}/\Gamma^{aa}$. The global tendencies of the above quantities are not affected by the variation of the ratio γ . Besides, the tracer diffusion coefficient D_B is not sensitive to the variation of the ratio γ . However, $\delta_{B \rightarrow V}$ decreases with γ while the variation of $\delta_{V \rightarrow B}$ has the opposite tendency. For $\gamma \neq 1$, FAR-a and FAR-d effects on the solute atom and PD diffusion occurs at different dose rate. It respectively happens when Γ^{aa} (i.e. Γ) and Γ^{ad} (i.e. $\gamma\Gamma$) are of the same order of magnitude compared with thermal jump frequencies. In brief, the smaller the γ value, the larger the difference between the frequencies for FAR-a and FAR-d, and the more important the strength of the flux coupling.

2.6.5 Thermal jump frequencies

The effects of FAR depend on the radiation dose rate and the intrinsic thermal jump frequencies of the alloy. We use KineCluE to perform a sensitive study of the radiation kinetic

properties with respect to the thermal jump frequencies. Fig. 2.13 shows the variation of ΔD_B and the wind factors $\delta_{B \rightarrow V}$, $\delta_{V \rightarrow B}$ with respect to Γ , for various values of ω_4 . The values of the other thermal jump frequencies are fixed. Model 1, with $r_m = r_1$, is chosen for the following discussion. The interactions between thermal jumps and FAR are emphasized in this case because the hop distances are both 1-NN. The ratio ω_4/ω_3 directly affects the binding energy E_b between solute atom and vacancy at 1-NN. We observe that ΔD_B and wind factors increase with the binding energy. Besides, the larger the binding energy, the larger the enhancement of the wind factor $\delta_{V \rightarrow B}$ by FAR. This can be explained by noting that the solute atom and vacancy tend to be closer to each other with a larger binding energy. Therefore, the interaction between FAR and thermally activated diffusion of solute atom is more important, leading to a larger difference from what we would expect with an additive model, i.e. Eq. (2.62). Moreover, the binding tendency of the vacancy and the solute atom increases, causing an enhancement of the wind factor δ_V . As well, ω_1 and ω_2 have a non-negligible effect on the profile of ΔD_B and wind factors in function of Γ . Here we set ω_4 to its initial value $2.3 \times 10^1 s^{-1}$ and we perform calculations with different values of ω_1 and ω_2 . Fig. 2.14 shows that if ω_2 is large compared to ω_1 (more than 1 order of magnitude), ΔD_B and $\delta_{B \rightarrow V}$ increase with ω_1 whereas the enhancement of $\delta_{V \rightarrow B}$ by FAR decreases with ω_1 . If the amplitudes of ω_2 and ω_1 are comparable (within 1 order of magnitude), the trends are opposite: ΔD_B and $\delta_{B \rightarrow V}$ decrease with ω_1 whereas the enhancement of $\delta_{V \rightarrow B}$ by FAR increases with ω_1 . However, we observe that if the values of ω_1 and ω_2 are close (within 1 order of magnitude), the variations of ΔD_B and wind factors with Γ are not sensitive to ω_1 .

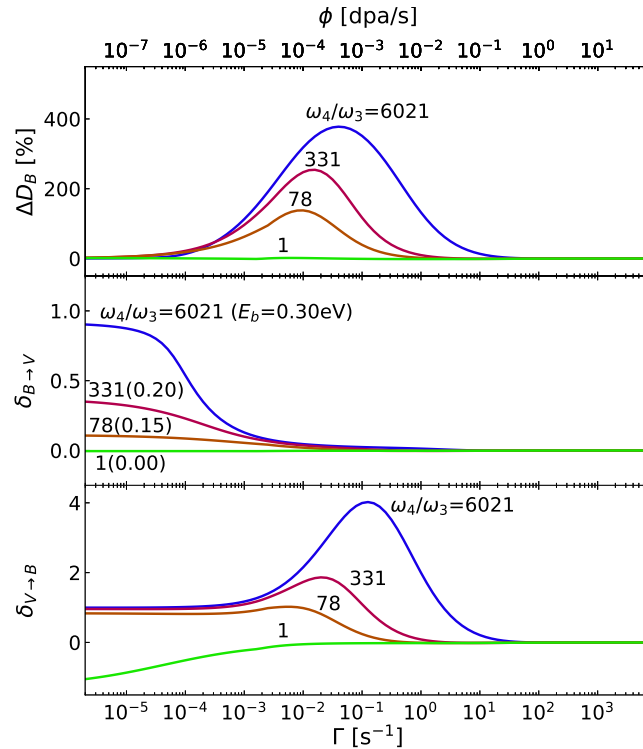


Figure 2.13: ΔD_B , and wind factors $\delta_{B \rightarrow V}$, $\delta_{V \rightarrow B}$ as a function of relocation frequency Γ from KineCluE simulations. Results are obtained for $\omega_{0,1,3} = 6.9 \times 10^{-2} s^{-1}$ and $\omega_2 = 4.2 \times 10^2 s^{-1}$ with different values of ω_4 at $T = 400K$. C_B is set 0.1 at.%.

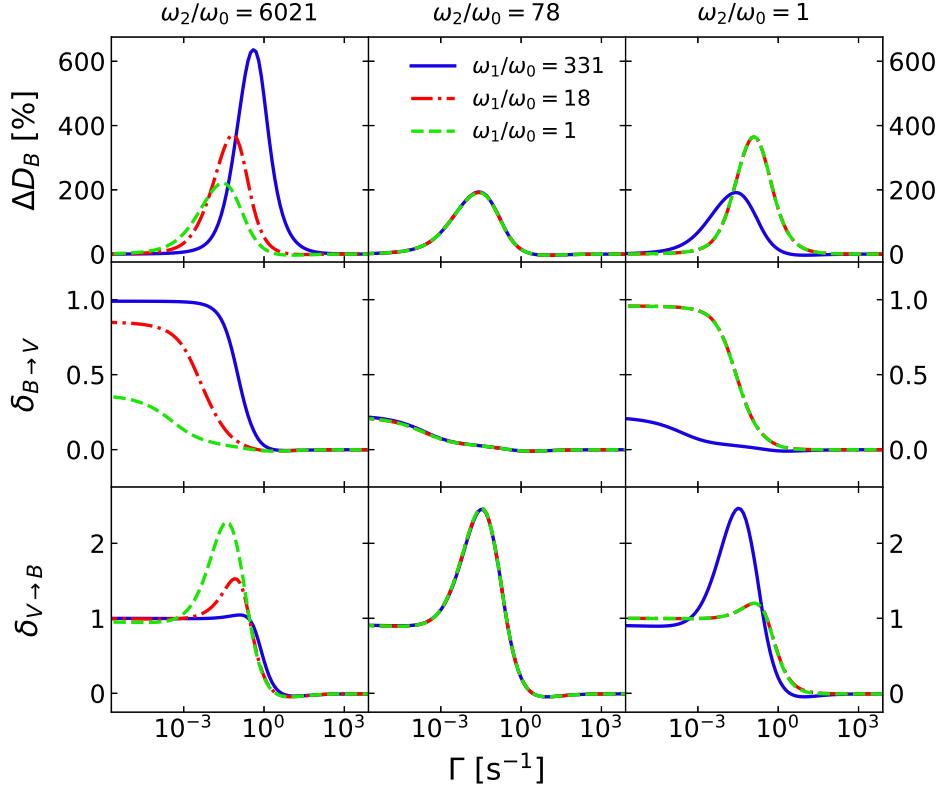


Figure 2.14: ΔD_B , and wind factors $\delta_{B \rightarrow V}$, $\delta_{V \rightarrow B}$ as a function of relocation frequency Γ from KineCluE simulations. Results are obtained for $\omega_{0,3} = 6.9 \times 10^{-2} s^{-1}$, $\omega_2 = 4.2 \times 10^2 s^{-1}$ and $\omega_4 = 2.3 \times 10^1 s^{-1}$ with different values of ω_1 and ω_2 at $T = 400K$. C_B is set 0.1 at.%.

2.7 Summary and concluding remarks

Neutron or ion irradiation in metals generates displacement cascades. We present a simplified model of this complex phenomenon by introducing FAR mechanisms, and an average creation rate of PD uniform in time and space. To calculate the energetic and kinetic properties, we write a Master Equation for the evolution of the distribution function which includes both the thermal jumps and FAR. We extend the SCMF theory to solve and compute the SRO parameters and the phenomenological transport coefficients at the NESS reached under irradiation. The main difficulty lies in the loss of the microscopic detailed balance when considering FAR mechanisms. Relying on Model 1 including FAR between 1-NN sites only and a first shell approximation of the kinetic correlations, we derive analytical expressions of the phenomenological transport coefficients. We demonstrate that FAR does not produce a simple additive term to the transport coefficients. When the magnitude of the relocation frequency is in the range of the thermal frequencies, FAR interacts with the thermal diffusion mechanism, yielding non-symmetric off-diagonal transport coefficients and a solute tracer diffusion coefficient deviating from a direct sum of a thermal and FAR diffusion coefficients. This deviation increases with the solute kinetic correlations. We use the automated code KineCluE to yield a more systematic study of the effect of the range and magnitude of FAR on the kinetic properties, including a sensitivity study with respect to the alloy thermodynamics and the models of

relocation and PD production.

Due to the lack of data on the detailed mechanisms of FAR and PD production, we introduce Models 2 and 3 representing two extreme situations, expecting the real situation to be in-between. In Model 2, we assume that FAR is a fully random process while in Model 3, we introduce a thermodynamic bias of FAR-d with the 1-NN atoms of the solute atoms, in order to reproduce the fact that the vacancy creation within a cascade is partially driven by the vacancy-solute thermodynamic attraction. As a result, part of the vacancy-solute SRO remains which in turns leads to a higher resistance of the vacancy-solute flux coupling to irradiation. Positive solute-vacancy flux coupling is the result of strong kinetic correlations, which can be modified by introducing FAR mechanisms. Our sensitivity study shows that the magnitude of the surviving kinetic correlations strongly depends on the details of the biased FAR-d mechanism, while the reduction of correlations and flux coupling due to the randomizing processes are less sensitive to the details of the relocation events unless the distance of FAR is close to the thermodynamic range. A persistent vacancy-solute flux coupling at low temperature and high radiation flux may play an important role on the solute redistribution in irradiated materials. Therefore, the mechanism of PD production with respect to the solute atom spatial distribution within the displacement cascade should be analyzed more precisely.

Eventually, the effect of the interplay between thermal jumps and FAR on vacancy-solute positive flux coupling is important when the solute-vacancy thermodynamic attraction is large, the magnitude of the thermal jump frequencies compared with the relocation frequency and the range of thermodynamic interactions is close to the relocation distances. As for the tracer diffusion coefficients, their non-additivity property with respect to FAR and thermal jumps follows the same trend as the flux coupling phenomena in systems featuring positive flux coupling but may also arise in case of no positive flux coupling but strong correlated solute migration paths. For instance, the additive expression of Eq. (2.62) reproduces correctly the diffusion coefficient of Au in Al measured under irradiation [146]. This is because the vacancy-jump barrier in Al is around 0.58 eV [234], hence the thermal jump frequencies are dominant over the relocation frequencies under realistic experimental conditions. However, we expect a non-negligible effect of FAR in Ni-based alloys because the vacancy-mediated migration barrier in pure Ni is high (around 1.09 eV [234]).

Chapter 3

Analytical modeling of RIS: application to Ni- and Fe-based alloys

Contents

3.1	Introduction	82
3.2	Modeling of RIS	84
3.2.1	RIS of point defects	85
3.2.1.1	Steady-state RIS profile of PDs	85
3.2.1.2	Vacancy segregation amount	87
3.2.2	RIS of solute atoms	88
3.2.2.1	RIS factors	89
3.2.2.2	RIS of solute atoms with α independent of local concentration C_B	89
3.2.2.3	RIS of solute atoms with α proportional to local concentration C_B	91
3.3	DFT energy database of Ni- and Fe-based alloys	93
3.3.1	PDs in pure nickel and iron	93
3.3.2	Solute-PD interactions in dilute Fe-based alloys	94
3.3.2.1	Solute-vacancy pair	94
3.3.2.2	Solute-SIA pair	94
3.3.2.3	Prospects on kinetics of Fe-based alloys from their PD properties	96
3.3.3	Solute-PD interaction in dilute Ni-based alloys	96
3.3.3.1	Solute-vacancy pair	96
3.3.3.2	Solute-SIA pair	97
3.3.3.3	Remarks on the DFT energy database of Ni-based alloys	97
3.4	Diffusion properties in Ni- and Fe-based alloys	98

3.4.1	Bulk vacancy concentration	98
3.4.2	Solute diffusion coefficient	99
3.4.3	Flux coupling between atoms and point defects	99
3.4.3.1	Solute-vacancy flux coupling	100
3.4.3.2	Solute-SIA flux coupling	101
3.5	RIS in Ni- and Fe-based alloys	103
3.5.1	RIS of vacancies	103
3.5.1.1	Analytical RIS profiles of vacancies versus the reference solution	103
3.5.1.2	Vacancy segregation profile	103
3.5.1.3	The amount of vacancy segregation S_V	104
3.5.2	RIS of solute atoms	106
3.5.2.1	Calculation of α_1 and α_2 in Ni- and Fe-based alloys	107
3.5.2.2	Comparison between analytical results and reference solutions	111
3.5.2.3	Solute segregation profile	112
3.5.2.4	Solute segregation amount in Ni- and Fe-based alloys	113
3.5.2.5	FAR effects on the solute segregation	116
3.5.3	Dose rate compensation by a temperature shift	117
3.6	Comparison between experimental measurement and analytical results	121
3.6.1	Ni-0.4Ti alloy	121
3.6.2	Fe-3.3Ni alloy	123
3.7	Summary and concluding remarks	126

3.1 Introduction

As reviewed in Section 1.3.3, RIS is largely controlled by the kinetic coupling between fluxes of PDs and atomic fluxes. In this chapter, we ignore the effect of the segregation thermodynamic driving forces on RIS. The sign of solute RIS, positive for solute enrichment and negative for solute depletion, is directly related to the relative magnitude of solute-vacancy and solute-SIA flux coupling [224]. In Chapter 2, we have shown that when the FAR frequency is close to the thermal PD jump frequency, FAR may enhance or reduce the PD-solute flux coupling. Calculation methods of flux coupling coefficients rely on the Onsager formulation of solute and PDs fluxes within the framework of the thermodynamics of irreversible processes [217], where these fluxes are expressed as linear combinations of chemical potential gradients. The constants of proportionality are the phenomenological transport coefficients L_{ij} .

At steady state, one relates the solute local concentration gradients (∇C_B) to the PD local concentration gradient normalized by the PD local concentration ($\nabla C_d/C_d$) as

$$\nabla C_B = \alpha \frac{\nabla C_d}{C_d}. \quad (3.1)$$

In this equation, α is the RIS factor, which is essentially a function of the phenomenological coefficients L_{ij} , the concentration derivatives of chemical potentials, and the solute and PD local concentrations [19, 20]. When FAR is taken into account, the RIS factor also varies with the FAR frequency. When the RIS factor is assumed to be uniform, the amplitude of the solute concentration gradient is proportional to the normalized local PD concentration gradients [30]. Therefore, the amplitude and shape of the stationary RIS profile depends not only on the RIS factor, but also on the local concentration of PDs [19, 30]. The evolution of the PD concentration fields depends on their mobility, on the radiation flux, on their mutual interaction, and on their interaction with the microstructure and solutes. Among PD reactions, let us mention the mutual recombination of vacancy and SIA, the clustering of PDs leading to the formation of dislocation loops and voids, and the elimination of PDs at sinks. The analysis of PD-microstructure interactions may be simplified by introducing an effective PD sink strength governing the average PD elimination rate at all PD sinks.

Experimental studies investigating the dependence of RIS on the microstructure of the irradiated sample and the irradiation conditions are reviewed in Section 1.3.3. However, it is still very difficult to obtain an accurate estimation of the PD sink strength from the observation of the microstructure due to the limitations of resolution, even for nanoscale experimental techniques. In order to obtain an accurate estimation of the sink strength, experimental measurements need to be complemented with modeling [235]. Predicting the evolution of RIS in materials of a nuclear power plant from a direct observation of neutron irradiated materials is difficult, mainly because neutron irradiation activates the sample and the radiation exposure times of several years needed to reach a few dpas are rarely available [11]. Radiation fluxes of electrons and heavy ions can be high, which allows radiation doses to reach up to hundreds of dpas in a much shorter time. However, most of the phenomena occurring under irradiation are sensitive to the radiation flux. According to simple mean-field rate theories, the PD concentrations obtained at a low radiation flux and given temperature are identical to the ones obtained at a higher flux provided the temperature is increased by a specific amount, which suggests that a difference in radiation flux can be compensated by a temperature shift [11, 183, 184]. This theory has been first applied to investigate the swelling phenomena, but it relies on the assumption that solute atoms do not interfere with the kinetics of PDs and the overall PD sink strength is fixed by the initial microstructure. According to this theory, there are three kinetic domains: (i) at low temperature and high radiation flux, the recombination domain in which the PD concentration is controlled by the PD recombination reaction, (ii) at intermediate temperature and low radiation flux, the sink domain controlled by the elimination of PDs at sinks, and (iii) at high temperature and low radiation flux, thermal domain in which the PD concentration are close to thermal equilibrium concentrations [183]. Estimations of the temperature shift required to compensate for a large radiation flux depend on the kinetic domains and whether the system is at steady state or in a transient state. These temperature shifts require the definition of an invariant quantity, either the bulk concentration of PDs at steady state [11], or the amount of PDs absorbed by sinks [184]. Attempts have been made to apply Mansur's invariant PD-absorption relation to the study of solute RIS [11, 22, 23]. The

estimation of the temperature shift was good enough to yield similar RIS profiles of Cr and Ni in 304L stainless steels, respectively irradiated with neutrons and self ions [23]. Nevertheless, in the same publication, the authors observe that the temperature shift predicted by Mansur’s invariant relation is not accurate for alloys with a high dislocation density. Yet, a material with an initial high dislocation density seems to be more appropriate to test Mansur’s invariant relation, because the high PD sink strength of a microstructure full of dislocations is less sensitive to the radiation flux and dose, and can be considered to be fixed as assumed in Mansur’s theory. A recent analytical model of steady-state RIS in the sink domain precisely predicts that solute RIS does not depend on the radiation flux, whereas PD concentration does [30]. However, as explained by the authors, we should not ignore that an increase of the dislocation density may induce a transition from the recombination domain to the sink domain, hence, shift the system from a radiation-flux dependence to another. Therefore, there is a need for a PD-RIS model accounting for both the transitions between the various PDs kinetic domains, and the effect of the irradiation conditions and the microstructure on the RIS profile within each PDs kinetic domain.

We derive, in this chapter, an analytical RIS model, aimed at (i) taking into account the complete PD reactions, solute-PD interactions, and FAR mechanisms; (ii) quantitatively studying the effect of a variation of either the sink strength, the radiation flux, or the temperature on the RIS properties; and (iii) helping addressing the flux-temperature effects in experiments in each kinetic domain (recombination/sink/thermal).

In Section 3.2, we rely on a simple mean-field rate theory to deduce the variation of the steady-state bulk concentration of PDs with respect to the radiation flux and the overall effective sink strength. Then we introduce a discretization method of the PDs concentration profile in order to obtain an analytical expression of the steady-state PDs concentration profile. From the RIS profile of PDs, and the RIS factor relating the solute concentration gradient to the PDs concentration gradient [188], we deduce an analytical expression of the solute steady-state RIS profile. Then, we discuss the role of the PDs-microstructure interaction on the RIS concentration profiles. In Section 3.3, we briefly present the Ni- and Fe-based alloys from a perspective of their PD energy properties. In Section 3.4, we present a parametric study of the stationary vacancy concentration, the solute diffusion coefficient, and the flux couplings in the form of temperature-radiation flux–sink strength maps. Then, in Section 3.5, we extend this parametric approach to the studies of RIS factors, and the vacancy and solute RIS profiles. Finally, in Section 3.6, we present comparisons between the simulated and experimental RIS profiles in dilute Ni-Ti and Fe-Ni alloys.

3.2 Modeling of RIS

In this section, we derive analytical solutions of the uni-dimension profiles of PD and solute atom concentrations for planar PD sinks (representing e.g. grain boundaries, surfaces, and planar interfaces) as presented in Fig. 1.5(a).

3.2.1 RIS of point defects

A sustained flux of PDs towards sinks leads to a steady-state depleted RIS profile of PDs at sinks. We introduce an analytical calculation method of this profile. First, we compute the bulk mean-field PD concentration from a mean-field rate theory. Then, we calculate the steady-state profile from the flux of PDs. We relate both calculations through the boundary conditions.

3.2.1.1 Steady-state RIS profile of PDs

We start from a modeling of PD diffusion towards sinks in terms of the divergences of PD fluxes \mathbf{J}_V and \mathbf{J}_I .

$$\frac{\partial C_V}{\partial t} = \phi - K_R C_V C_I - \nabla \cdot \mathbf{J}_V, \quad (3.2)$$

$$\frac{\partial C_I}{\partial t} = \phi - K_R C_V C_I - \nabla \cdot \mathbf{J}_I, \quad (3.3)$$

where K_R is a parameter characterizing the recombination rate, which is defined in Section 1.2.2.1. To compute \mathbf{J}_V and \mathbf{J}_I , we assume $\nabla\mu_V$ and $\nabla\mu_I$ to be the dominant driving force compared to $\nabla\mu_A$ and $\nabla\mu_B$. Thus, we have

$$\mathbf{J}_V = -L_{VV} \nabla\mu_V = -D_V \nabla C_V, \quad (3.4)$$

$$\mathbf{J}_I = -L_{II} \nabla\mu_I = -D_I \nabla C_I, \quad (3.5)$$

where $D_d = L_{dd}/D_d$ for $d = V, I$.

We consider the vacancy concentration profile along the direction (coordinate z) normal to the surface of planar PD sinks. After Eqs. (3.2) and (3.3), the chemical rate equations for SIAs and vacancies near the PD sinks under stationary-state conditions are given by

$$0 = \phi - K_R C_V C_I + D_V \frac{\partial^2 C_V}{\partial z^2}, \quad (3.6)$$

$$0 = \phi - K_R C_V C_I + D_I \frac{\partial^2 C_I}{\partial z^2}, \quad (3.7)$$

where $C_V(z)$ and $C_I(z)$ are respectively the concentrations of vacancies and SIAs at positions along axis (Oz).

After Eq. (3.6) and (3.7), we have:

$$\begin{aligned} 0 &= D_V \frac{\partial^2 C_V}{\partial z^2} - D_I \frac{\partial^2 C_I}{\partial z^2} \\ &= \frac{\partial^2}{\partial z^2} (D_V C_V - D_I C_I). \end{aligned} \quad (3.8)$$

Therefore, $D_V C_V(z) - D_I C_I(z) = K_2 z + K_3$, with K_2 and K_3 two integration constants to be determined. By symmetry, the PD flux at the mid-point between two successive sinks ($z = 0$) is zero, hence we have:

$$\frac{\partial C_V}{\partial z}(z = 0) = 0, \quad \frac{\partial C_I}{\partial z}(z = 0) = 0. \quad (3.9)$$

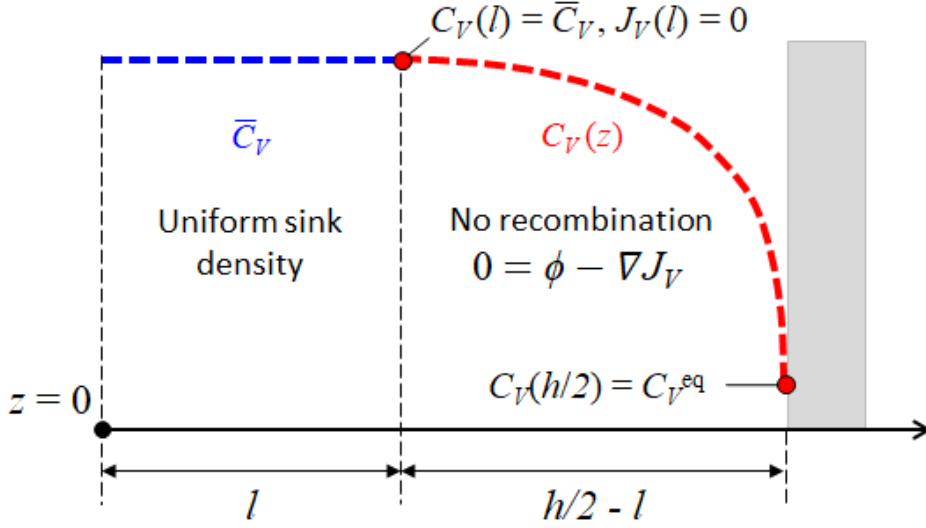


Figure 3.1: Schema of vacancy concentration profile divided into two parts.

According to Eq. (3.9), $K_2 = 0$. Moreover, the PD concentrations at sink ($z = h/2$) are assumed to be the equilibrium concentrations. Therefore, we have:

$$C_V(z = h/2) = C_V^{\text{eq}}, \quad C_I(z = h/2) = C_I^{\text{eq}}. \quad (3.10)$$

After Eq. (3.10), $K_3 = D_V C_V^{\text{eq}} - D_I C_I^{\text{eq}}$. By assuming that $D_I C_I^{\text{eq}} \ll D_V C_V^{\text{eq}}$, we have $K_3 \simeq D_V C_V^{\text{eq}}$. Accordingly, $C_V(z)$ and $C_I(z)$ are related by the following equation

$$D_V [C_V(z) - C_V^{\text{eq}}] = D_I C_I(z). \quad (3.11)$$

Since C_V and C_I are not independent variables, in the following, we replace C_I by its variation with C_V . By assuming that $D_I \gg D_V$, Eq. (3.6) can be rewritten as:

$$\frac{\partial^2 C_V(z)}{\partial z^2} = -\frac{\phi}{D_V} + \frac{4\pi r_{\text{rec}}}{\Omega} C_V(z) [C_V(z) - C_V^{\text{eq}}]. \quad (3.12)$$

Note that, as far as we know, a general analytical solution of Eq. (3.12) does not exist [236–238]. Close to a planar sink and if we neglect the mutual recombination reactions between PDs (i.e. $r_{\text{rec}} = 0$), there is a simple analytical solution of the PD concentration profile [30]. As explained in Ref. [30], the solution of Eq. (3.12) with $r_{\text{rec}} = 0$, reads:

$$C_V(z) = -a\left(z^2 - \frac{h^2}{4}\right) + C_V^{\text{eq}}, \quad (3.13)$$

where $a = \phi/(2D_V)$, h is the average spacing between planar sinks. and the position of the origin of axis ($0z$) is chosen to be at the mid-point between two planar sinks (see Fig. 3.1).

Close to a PD sink, ignoring the recombination reactions should be a reasonable hypothesis, because locally concentrations of PDs are very low. Hence their probability of recombination, that is proportional to the square of the PD concentrations, should be very low as well. Therefore, we split the PD concentration profiles in two regions: a bulk region far from sinks in which

concentrations are uniform, and a sink region in which we account for the z -variation of the PD concentration profile (cf. Fig. 3.1). The z coordinate of the bulk region ranges between 0 and l , whereas the z -coordinate of the sink region ranges from l to $h/2$, h being the distance between the planar sinks. In the bulk region, $C_V(z)$ is uniform and equal to the steady-state bulk concentration C_V^b (see Eq. (1.23)). From Eq. (3.13), we deduce the vacancy concentration profile $C_V(z)$, with $l \leq z \leq h/2$. In order to ensure the continuity of the vacancy concentration and its spatial derivative (i.e., the vacancy flux), we apply the boundary conditions

$$C_V(l^-) = C_V(l^+), \quad \frac{\partial C_V}{\partial z}(l^-) = \frac{\partial C_V}{\partial z}(l^+) = 0. \quad (3.14)$$

At PD sinks, the vacancy concentration corresponds to the equilibrium one:

$$C_V\left(\frac{h}{2}\right) = C_V^{\text{eq}}. \quad (3.15)$$

The solution is then given by

$$C_V(z) = \begin{cases} C_V^b, & 0 \leq z < l; \\ -a(z-l)^2 + C_V^b, & l \leq z \leq h/2, \end{cases} \quad (3.16)$$

where the characteristic distance l is defined as

$$l = \frac{h}{2} - \sqrt{\frac{C_V^{\text{exc}}}{a}}, \quad (3.17)$$

where $C_V^{\text{exc}} = C_V^b - C_V^{\text{eq}}$ corresponds to the vacancy excess concentration with respect to the equilibrium one. Note that the characteristic distance l depends on the interplanar distance h and C_V^{exc} . Both quantities are related to the microstructure. The interplanar distance h determines the sink strength of the parallel planar sinks [119]:

$$k^2 = \frac{8}{h^2}. \quad (3.18)$$

In case there is no other PDs sinks in the system, this sink strength fully determines the bulk concentration of vacancy, C_V^b . Note that in case there are other sinks, in addition to the local sink strength of the planar sinks, C_V^b depends on the overall sink strength of the other PDs sinks of the microstructure. If $l < 0$, Eq. (3.16) is no longer appropriate, because the PDs planar sinks are so close that it is not possible to introduce a bulk region with uniform concentrations. In this case, we set $l = 0$, and the obtained PD concentration profile is given by Eq. (3.13).

3.2.1.2 Vacancy segregation amount

By analogy with the Gibbs formalism of interface excess quantities, we define the vacancy concentration excess at sinks by the following integral:

$$S_V = \int_0^{h/2} [C_V(z) - C_V(0)] dz. \quad (3.19)$$

We obtain from Eq. (3.16) and Eq. (3.19) that:

$$S_V = -\frac{(C_V^b - C_V^{\text{eq}})^{\frac{3}{2}}}{3\sqrt{a}}. \quad (3.20)$$

As expected, S_V is always negative. Note that the latter depends on the PD recombination reactions. Therefore, as stated in Section 1.2.2.1, we cannot ignore the recombination reactions, unless the recombination rate ($R = K_R C_V^b C_I^b$) is negligible with respect to the PD elimination rate at sinks ($K = k^2 D_V (C_V^b - C_V^{\text{eq}})$).

In the sink domain, i.e., $K \gg R$, we have

$$S_V = -\frac{\sqrt{2}}{3(k^2)^{3/2}} \left(\frac{\phi}{D_V} \right). \quad (3.21)$$

Therefore, S_V is proportional to the ratio ϕ/D_V , and it decreases with the sink strength k^2 .

In the recombination domain, i.e. $R \gg K$, we have

$$S_V = -\frac{1}{6} \left(\frac{\Omega}{\pi r_{\text{rec}}} \right)^{3/4} \left(\frac{\phi}{D_V} \right)^{1/4}. \quad (3.22)$$

Thus, S_V is proportional to $(\phi/D_V)^{\frac{1}{4}}$, and it is independent of k^2 .

3.2.2 RIS of solute atoms

As stated in Section 1.3.3, the concentration profiles of PDs and solute atoms are related by the RIS factor α of the Wiedersich's approach [188]. First, we investigate the variation of α with the local concentrations. Then, we deduce the solute concentration profile from the RIS factor and the PD concentration profile.

Note that in this study we neglect the equilibrium segregation of solutes resulting from the interaction of solutes with the sink [239–241]. This thermodynamic property may strongly modify the solute concentration over the first two or three atomic planes of the sink [239, 240]. Its amplitude and width (generally less than 1 nm) vary with the temperature, the chemical nature of solute atoms and the nature of the sink. A quantitative investigation of this phenomenon would require a detailed knowledge of the structure of the sink as well as the solute segregation energies at different atomic sites near the sink. Nevertheless, the total amount of solute RIS segregation as well as the average width of the RIS profiles spreading over a few tens of nanometers [11] should not be much affected by the equilibrium segregation. Besides, alloys with an ordering tendency may exhibit an oscillating segregation profile along specific orientations [19]. Since we rely on a dilute alloy approximation, we cannot reproduce such RIS behaviors, for instance, the formation of a W-shaped RIS profile in austenitic steels [242].

3.2.2.1 RIS factors

After Eq. (1.71), the local RIS factor is a function of the phenomenological L -coefficients. It depends on the coordinate z through the variation of the local concentration C_B and C_V with z (see Eq. (1.71)). In order to analyze the variation of α with the local concentrations of vacancies and solute atoms, we rewrite α by making explicit its variation with C_V and C_B . We deduce from Eqs. (1.71), (1.73), and (3.11) that:

$$\alpha(z) = \frac{\alpha_1 C_B(z)}{C_V(z) + \alpha_2}, \quad (3.23)$$

where

$$\alpha_1 = \frac{\alpha_s (1 - C_B) d_{AI} d_{AV}}{(1 - C_B) d_{AI} d_{BV}^c + C_B d_{BI} + [(1 - C_B) d_{AI} d_{BI}^c + C_B d_{BI} d_{AI}^c] D_V / D_I}, \quad (3.24)$$

$$\alpha_2 = \frac{[(1 - C_B) d_{AI} + C_B d_{BI}] L_{BB}^{\text{mono}} - C_V^{\text{eq}} [(1 - C_B) d_{AI} d_{BI}^c + C_B d_{BI} d_{AI}^c] D_V / D_I}{(1 - C_B) d_{AI} d_{BV}^c + C_B d_{BI} + [(1 - C_B) d_{AI} d_{BI}^c + C_B d_{BI} d_{AI}^c] D_V / D_I}. \quad (3.25)$$

Therefore, α decreases with $C_V(z)$. The RIS factors α_1 and α_2 are independent of the PDs concentrations. Instead, they vary with $C_B(z)$, and so do the partial diffusion coefficients d_{ij} and d_{ij}^c . However, along an RIS profile, the relative variation of the solute concentration is a lot smaller than that of the PD concentration. In Ref. [30], α is assumed to be uniform, depending on the nominal composition of the concentrated Fe-Cr alloy only. This assumption leads to a good agreement with direct Monte Carlo simulation of RIS. In dilute alloys, accounting for a linear variation of α with local concentration, $C_B(z)$, as emphasized by Eq. (3.23), might be a better approximation. In the following, we calculate the solute RIS profile using both approximations of α . Then, we choose the most appropriate one by a comparison between the solute RIS profiles obtained from these two approximations and the exact solution (see Section 3.5.2.2).

3.2.2.2 RIS of solute atoms with α independent of local concentration C_B

First, we consider the simplified case where the RIS factors α is supposed to be independent of the local concentration of solute atoms. We determine α at the nominal composition \bar{C}_B . After Eq. (3.16), we deduce the vacancy concentration gradient ∇C_V , and from Eqs. (1.70) and (3.23), we write the solute concentration gradient as follows.

$$\nabla C_B(z) = \begin{cases} 0, & 0 \leq z < l; \\ -\frac{2\alpha_3(z-l)}{(z-l)^2 - b^2}, & l \leq z \leq h/2, \end{cases} \quad (3.26)$$

with $b^2 = (C_V^b + \alpha_2)/a$ and $\alpha_3 = \alpha_1 \bar{C}_B$. We derive the concentration profile of the solute atoms by integrating Eq. (1.70) and applying the following boundary conditions

$$C_B(l^-) = C_B(l^+), \quad (3.27)$$

$$\int_0^{h/2} C_B(z) dz = \frac{h}{2} \bar{C}_B, \quad (3.28)$$

in order to ensure the continuity of the solute profile $C_B(z)$ at $z = l$ and the mass conservation of the solute atoms, respectively. Hence, we obtain

$$C_B(z) = \begin{cases} -2\alpha_3 \ln(b) + K_0, & 0 \leq z < l; \\ -\alpha_3 \ln [b^2 - (z - l)^2] + K_0, & l \leq z \leq h/2, \end{cases} \quad (3.29)$$

where K_0 is equal to

$$K_0 = \bar{C}_B + \frac{4\alpha_3 l}{h} [\ln(b) + 1] + \frac{4\alpha_3 b}{h} \operatorname{arctanh} \left[\frac{(h/2) - l}{b} \right] - 2\alpha_3 + \alpha_3 \left[\frac{(h/2) - l}{h/2} \right] \ln \left[b^2 - \left(\frac{h}{2} - l \right)^2 \right]. \quad (3.30)$$

Similarly to Eq. (3.20), we define the total amount of solute atoms segregated at sink as $S_B = (h/2) (\bar{C}_B - C_B(0))$. It writes

$$S_B = \alpha_3 (h - 2l) - \alpha_3 \left(\frac{h}{2} - l \right) \ln \left\{ \frac{b^2 - [(h/2) - l]^2}{b^2} \right\} - 2b\alpha_3 \operatorname{arctanh} \left[\frac{(h/2) - l}{b} \right]. \quad (3.31)$$

In case we ignore C_V^{eq} , we have $(h/2) - l = C_V^b/a$, and from Eq. (3.31), we obtain

$$S_B = 2\alpha_3 \sqrt{\frac{C_V^b}{a}} - \alpha_3 \sqrt{\frac{C_V^b}{a}} \ln \left(\frac{\alpha_2}{C_V^b + \alpha_2} \right) - 2\alpha_3 \sqrt{\frac{C_V^b + \alpha_2}{a}} \operatorname{arctanh} \left[\sqrt{\frac{C_V^b}{C_V^b + \alpha_2}} \right]. \quad (3.32)$$

In case we may not ignore the FAR mechanism, the diffusion of isolated solute atoms, $L_{\text{BB}}^{\text{mono}}$, and in turn α_2 are non negligible. α_2 increases with the FAR frequency, which in turn decreases the RIS of solute atoms. In the extreme case, $\alpha_2 \gg C_V^b$, and the amount of solute RIS is zero ($S_B = 0$).

On the contrary, if we ignore FAR, $\alpha_2 \ll C_V^b$. Then, we may approximate S_B as follows

$$S_B = 2(1 - \ln 2) \alpha_3 \sqrt{\frac{C_V^b}{a}}. \quad (3.33)$$

After Eqs. (3.20) and (3.33), we obtain a direct relationship between S_B and S_V

$$S_B = 6(\ln 2 - 1) \alpha_3 \frac{S_V}{C_V^b}. \quad (3.34)$$

We observe the amount solute RIS, S_B , is directly related to α_1 and S_V/C_V^b . In the denominator, C_V^b is the signature of the backward diffusion opposing to the RIS solute concentration

gradient. This backward diffusion is the reason why solute RIS (S_B), unlike PD RIS (S_V), is not systematically governed by the ratio ϕ/D_V .

In the sink domain ($K \gg R$), we obtain from Eq. (1.24) and Eq. (3.33) that

$$S_B = 2(1 - \ln 2) \alpha_3 \sqrt{\frac{2}{k^2}}. \quad (3.35)$$

We recover the same expression published in Ref. [30]. The solute segregation amount is independent of the ratio ϕ/D_V , whereas it decreases with k^2 . Thus, at fixed k^2 , if we neglect the variation of α_3 with the dose rate ϕ , the solute segregation amount is independent of ϕ [30]. Besides, S_B varies with temperature through the variation of α_3 with temperature.

In the recombination domain ($K \ll R$), we obtain from Eq. (1.25) and Eq. (3.33) that

$$S_B = 2(1 - \ln 2) \alpha_3 \left(\frac{\Omega}{\pi r_{\text{rec}}} \right)^{1/4} \left(\frac{\phi}{D_V} \right)^{-1/4}. \quad (3.36)$$

S_B is governed by the ratio ϕ/D_V as well as by the RIS factor α_3 . Moreover, it decreases with the dose rate ϕ , whereas it is k^2 -independent.

3.2.2.3 RIS of solute atoms with α proportional to local concentration C_B

Here we assume that α_1 and α_2 do not vary with $C_B(z)$. Thus α is proportional to $C_B(z)$ so that:

$$\frac{\nabla C_B}{C_B} = \alpha_1 \frac{\nabla C_V}{C_V + \alpha_2} \quad (3.37)$$

By integrating Eq. (3.37) and applying the boundary conditions as Eq. (3.27) and Eq. (3.28), we obtain that:

$$C_B(z) = \begin{cases} K_1 b^{-2\alpha_1}, & 0 \leq z < l; \\ K_1 [b^2 - (z - l)^2]^{-\alpha_1}, & l \leq z \leq h/2, \end{cases} \quad (3.38)$$

with

$$K_1 = \frac{h}{2} \frac{\overline{C}_B}{lb^{-2\alpha_1} + \int_0^{(h/2)-l} (b^2 - z^2)^{-\alpha_1} dz}. \quad (3.39)$$

Note that there is no simple analytical expression of the integral $I = \int_0^{(h/2)-l} (b^2 - z^2)^{-\alpha_1} dz$. Nevertheless, we can calculate it from the hypergeometric function ${}_2F_1$ [243] or by numerical integration.

Therefore, the solute segregation amount is given by

$$S_B = \frac{h}{2} (\overline{C}_B - K_1 b^{-2\alpha_1}). \quad (3.40)$$

In the extreme case where FAR is dominant, i.e., $\alpha_2 \gg C_V^b$, we obtain for $0 < z < (h/2) - l$:

$$z^2 < \left(\frac{h}{2} - l \right)^2 < C_V^b/a \ll b^2. \quad (3.41)$$

In this case, $I = [(h/2) - l]b^{-2\alpha_1}$, $K_1 = \bar{C}_B b^{2\alpha_1}$, and the amount of solute RIS is zero ($S_B = 0$).

On the contrary, if we ignore FAR, we have $\alpha_2 \ll C_V^b$. If we also neglect C_V^{eq} , $b = (h/2) - l$ and

$$I = \int_0^b (b^2 - z^2)^{-\alpha_1} dz = b^{-2\alpha_1+1} I_{\alpha_1}, \quad (3.42)$$

with

$$I_{\alpha_1} = \int_0^1 (1 - z^2)^{-\alpha_1} dz. \quad (3.43)$$

Note that I_{α_1} is positive and only depends on the RIS factor α_1 . Moreover, it is larger than 1 if the solute RIS is positive (i.e., $\alpha_1 > 0$), and smaller than 1 in the opposite case. Then, after Eqs. (3.39), (3.40), and (3.42), we may approximate S_B as follows

$$S_B = \frac{h}{2} \bar{C}_B \frac{I_{\alpha_1} - 1}{I_{\alpha_1} + \frac{l}{(h/2)-l}}, \quad (3.44)$$

$$= \frac{h}{2} \bar{C}_B \frac{I_{\alpha_1} - 1}{I_{\alpha_1} - 1 + \frac{h}{2} \sqrt{\frac{a}{C_V^b}}}. \quad (3.45)$$

According to Eq. (3.44), S_B is positive if α_1 is positive and negative otherwise.

Besides, after Eqs.(3.20) and (3.45), we obtain a direct relationship between S_B and S_V

$$S_B = \frac{h}{2} \bar{C}_B \frac{I_{\alpha_1} - 1}{I_{\alpha_1} - 1 - \frac{h}{2} \frac{C_V^b}{S_V}}. \quad (3.46)$$

Similarly to the situation where α is independent of C_B , we observe that the amount of solute RIS, S_B , is directly related to α_1 and S_V/C_V^b .

In the sink domain ($K \gg R$), we obtain from Eq. (1.24) and Eq. (3.45) that

$$S_B = \frac{h}{2} \bar{C}_B \frac{I_{\alpha_1} - 1}{I_{\alpha_1} - 1 + \frac{h}{2} \sqrt{\frac{k^2}{2}}}. \quad (3.47)$$

The solute segregation amount is independent of the ratio ϕ/D_V , whereas it decreases with k^2 . Thus, at fixed k^2 , if we neglect the small variation of α_1 with the dose rate ϕ , the solute RIS amount is ϕ -independent. Besides, S_B varies with temperature through the variation of α_1 with temperature. Note that the present expression of S_B is not the same as the published one in Ref. [30], because here we do not assume that the RIS factor is independent of solute and PD concentrations.

In the recombination domain ($K \ll R$), we obtain from Eq. (1.25) and Eq. (3.45) that

$$S_B = \frac{h}{2} \bar{C}_B \frac{I_{\alpha_1} - 1}{I_{\alpha_1} - 1 + \frac{h}{2} \left(\frac{\Omega}{\pi r_{\text{rec}}} \right)^{-1/4} \left(\frac{\phi}{D_V} \right)^{1/4}} \quad (3.48)$$

The solute RIS amount is governed by the ratio ϕ/D_V as well as by the RIS factor α_1 . Besides, it decreases with the dose rate ϕ .

3.3 DFT energy database of Ni- and Fe-based alloys

We calculate of the phenomenological L -coefficients rely on DFT-computed atomic jump frequencies. The computation of the RIS factors in Fe-based dilute alloys has shown that the general flux coupling behavior is largely governed by the short-range interaction energy between PDs and solute atoms [181]. Therefore, in order to understand the diffusion behaviors of the solute atoms in Ni- and Fe-based alloys, it is interesting to review their energy database of PD migration and PD-solute interaction. We present in this section selected results extracted from *ab initio* studies of Ni-based [244] and Fe-based alloys [41, 181]. In these calculation, the Vienna *ab initio* Simulation Package (VASP) [245–247] is applied. The VASP full-core pseudopotentials developed within the projector augmented wave (PAW) method [248, 249] are employed for all elements. The Perdew-Burke-Ernzerhof (PBE) parameterization [250] of the generalized gradient approximation (GGA) is used to describe the exchange-correlation function. Calculations are spin-polarized, and make use of the Vosko-Wilk-Nusair (VWN) interpolation scheme of the correlation potential.

3.3.1 PDs in pure nickel and iron

Table 3.1: Thermodynamic and kinetic properties of PDs in pure Ni and Fe.

Material	H_V^f	S_V^f	ν_V	E_V^{mig}	H_I^f	S_I^f	ν_I	E_I^{mig}
Ni	1.65 eV ^a	1.82 k_B ^a	4.48THz ^a	1.09 eV ^a	4.07 eV ^a	12.7 k_B ^a	4.48THz ^a	0.14 eV ^a
Fe	2.18 eV ^b	4.1 k_B ^b	6.00THz ^b	0.70 eV ^b	4.08 eV ^c	0.05 k_B ^c	4.44THz ^c	0.34 eV ^c

^a Ref. [193], ^b Ref. [181], ^c Ref. [41].

In this table, H_d^f and S_d^f are formation enthalpy and entropy of defect d , respectively. ν_d and E_d^{mig} are attempt frequency and migration barrier of defect d , respectively. $d \equiv V$ for vacancy and $d \equiv I$ for dumbbell-type SIA.

We summarize in Tab. 3.1 the DFT data related to the formation and migration of PDs in pure Ni and Fe.

The formation energy differences between SIA and vacancy are up to 1.9 eV and 2.4 eV in pure Ni and Fe, respectively. These significant differences justify that we neglect the equilibrium concentration of SIAs in comparison to the one of vacancies in both dilute Ni- and Fe-based alloys.

Moreover, the migration barrier of SIA is much lower than that of vacancy. The difference is 0.95 eV and 0.36 eV in pure Ni and Fe, respectively. It is worth noting that the vacancy migration barrier in Ni is higher than that in Fe with a difference of 0.39 eV, meaning that vacancy diffusion in Ni is much slower than that in Fe. However, concerning the SIA diffusion, the situation is opposite because the SIA migration barrier in Ni is 0.20 eV lower than that in Fe.

For a complete investigation of PD diffusion properties in dilute Ni- and Fe-based alloys, we need to look at properties of the solute-PD pairs. We present in the following sections a few

selected DFR binding energies of solute-PD pairs in Fe and Ni.

3.3.2 Solute-PD interactions in dilute Fe-based alloys

Vacancy energy and migration with respect to the local solute environment in Fe-P, Fe-Mn, Fe-Cr, Fe-Si, Fe-Ni and Fe-Cu alloys is investigated in Ref. [181] by DFT calculations. The SIA properties in the same alloys are studied in Ref. [41]. Below, we choose to present the solute-PD binding energies only.

3.3.2.1 Solute-vacancy pair

Table 3.2: *Ab initio* solute-vacancy binding energies (in eV) taken from Ref. [181]. Negative energies stand for attractive interactions.

Distance	Fe-P	Fe-Si	Fe-Cu	Fe-Ni	Fe-Mn	Fe-Cr
1-NN	-0.38	-0.30	-0.26	-0.10	-0.17	-0.06
2-NN	-0.28	-0.12	-0.17	-0.21	-0.11	-0.01
3-NN	0.02	0.01	-0.03	-0.04	-0.03	0.00
4-NN	-0.01	0.01	0.00	0.00	0.00	0.00
5-NN	0.01	-0.03	-0.10	-0.06	-0.07	-0.03
6-NN	0.03	0.01	-0.01	-0.03	-0.01	0.00

The binding energies between solute and vacancy of Tab. 3.2 are taken from Ref. [181]. In this table, we order the solutes according to the magnitude of their interaction energy with the vacancy—from the strongest binding (P) to the weakest (Cr). All solutes, except Cr, present a strong binding character with vacancies. Besides, the attractive interaction is strong up to the 2-NN distance, beyond which it drops to zero. Although in case of Cu, Mn, and Ni, there exists a non-negligible attraction between solute and vacancy at the 5-NN distance. Therefore, in Ref. [181], the kinetic paths of vacancy includes every vacancy jump sequences connecting lattice sites up to the 10-NN of the solute atom, resulting in a network of in total 14 vacancy jump frequencies.

3.3.2.2 Solute-SIA pair

We present in Tab. 3.3 and Fig. 3.2 all the solute-dumbbell binding energies taken from Ref. [41]. In most cases, the binding energies fade already at the 2-NN shell. The striking exception is the 5b configuration in Fe-P, with a binding energy equal to 0.21 eV. Standard strain-relief discussion [20] suggest that undersized impurities (P, Si) should hold an attractive interaction in M and 1b configurations (Fig. 3.2), and a repulsive one in 1a, whereas we expect the opposite trends for oversized impurities (Cu, Ni, Mn, Cr). These trends are indeed true for P, and to a certain extent for Cu, Ni, and Si, but does not apply to Cr and Mn, where the

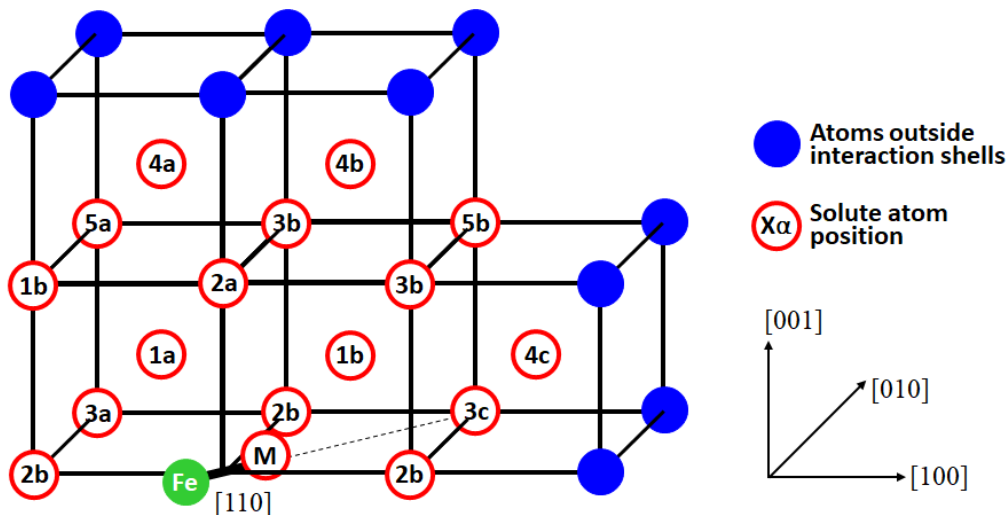


Figure 3.2: Solute-dumbbell equilibrium configurations of bcc Fe-based alloys as defined in Ref. [41]. The red circles mark the solute position relative to the dumbbell defect: ‘X’ is the solute nearest-neighbor shell with respect to the dumbbell position, and ‘ α ’ the symmetry class within the same shell. The blue circles represent the atoms located outside the interaction shells. ‘M’ marks the mixed-dumbbell configuration.

Table 3.3: *Ab initio* solute-dumbbell binding energies (in eV) of Fe-based alloys taken from Ref. [181]. Negative energies stand for attractive interactions.

Configuration	Fe-P	Fe-Si	Fe-Cu	Fe-Ni	Fe-Mn	Fe-Cr
M	+1.025	+0.555	+0.045	-0.002	-0.191	-0.380
1a	-0.331	+0.107	-0.065	-0.173	+0.016	+0.188
1b	+0.855	+0.305	+0.038	+0.274	+0.065	+0.065
2a	-0.012	-0.006	-0.082	-0.064	-0.047	+0.099
2b	^a	+0.083	+0.081	+0.045	+0.027	+0.064
3a	-0.05	-0.06	-0.06	-0.01	-0.03	+0.02
3b	+0.04	+0.01	-0.03	-0.02	-0.00	+0.06
3c	-0.12	+0.01	-0.03	-0.07	-0.04	+0.10
4a	-0.01	-0.03	-0.04	-0.01	-0.02	+0.01
4b	+0.04	+0.02	-0.05	+0.08	+0.03	+0.07
4c	-0.02	-0.00	-0.03	+0.02	+0.01	+0.05
5a	-0.031	-0.004	-0.023	-0.000	+0.011	+0.052
5b	+0.212	+0.013	-0.033	+0.038	-0.024	+0.017

^a Configuration 2b in Fe-P is unstable because it relaxes into a mixed dumbbell.

corresponding M and 1b configurations are stable. In fact many studies suggest that solute-defect interaction energies cannot be explained based on size-related arguments only and are mainly determined by electronic interactions [251, 252]. According to the binding energies in M configuration, mixed Fe-Si, Fe-Ni, and Fe-Cu dumbbells are less stable than pure Fe-Fe dumbbells, whereas P, Mn, and Cr are likely to form a mixed dumbbell interstitial in iron alloys.

In addition to the translation-rotation mechanism of dumbbell migration, Messina et al. [41] also calculated the migration barriers of translation and on-site rotation mechanisms. They are much higher than those of the translation-rotation mechanism. Therefore, we consider only the latter mechanism for SIA diffusion.

3.3.2.3 Prospects on kinetics of Fe-based alloys from their PD properties

In the six binary iron alloys, the 1- and 2-NN solute-vacancy binding energies are negative, i.e., the solute atoms are attracted by the vacancy. Moreover, Cr has a very weak interaction with vacancies compared with the other solute atoms. Concerning the SIAs, their most stable configuration is the dumbbell one. Regarding the dumbbell, we can classify the Fe-based dilute alloys into two groups: the alloys containing stable (P, Mn, Cr) and non-stable (Si, Ni, Cu) mixed dumbbells.

Note that the kinetic behaviors of the solute atoms forming non-stable mixed dumbbells (Si, Ni, Cu) are predominantly controlled by the vacancy mechanism [41]. In addition, the values of the 1-NN and 2-NN solute-vacancy binding energies in Fe-Si, Fe-Ni, and Fe-Cu alloys are close. Therefore, the kinetic properties of the solute atoms are expected to be similar in these alloys. Regarding the alloys with stable mixed dumbbells (Fe-P, Fe-Mn, Fe-Cr), solute-PD binding energies show significant differences, suggesting that the kinetic properties can be very different in Fe-P, Fe-Mn, and Fe-Cr alloys.

3.3.3 Solute-PD interaction in dilute Ni-based alloys

Ab initio study on both vacancy and SIA thermodynamic and kinetic properties in dilute Ni-Ti and Ni-Cr alloys has recently been published in Ref. [244].

3.3.3.1 Solute-vacancy pair

Table 3.4: *Ab initio* solute-vacancy binding energies (in eV) of Ni-based alloys taken from Ref. [244]. Negative energies stand for attractive interactions.

Alloy	1-NN	2-NN	3-NN	4-NN	5-NN	6-NN
Ni-Cr	+0.04	-0.02	+0.03	-0.02	+0.004	+0.004
Ni-Ti	-0.05	+0.06	+0.03	-0.07	+0.01	+0.001

The solute-vacancy binding energies versus nearest neighbour position obtained in Ref. [244] are summarized in Tab. 3.4. Ti displays an attractive binding in the 1-NN. Hence, we may expect a drag of Ti by vacancy. On the contrary, Cr displays a repulsive 1-NN interaction with vacancies, indicating that a positive Cr-vacancy coupling is less likely in this case. The interaction range of the vacancy-solute pairs is small. To this work, we consider this interaction to be equal to zero beyond the 4-NN distance. Such set of interactions leads to a network of 9 different vacancy jump frequencies [244].

3.3.3.2 Solute-SIA pair

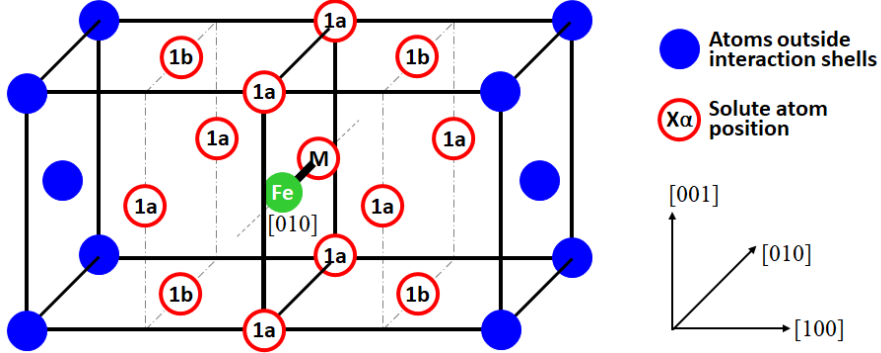


Figure 3.3: Solute-dumbbell equilibrium configurations of fcc Ni-based alloys considered in Ref. [244]. The red circles mark the solute position relative to the dumbbell defect: ‘X’ is the solute nearest-neighbor shell with respect to the dumbbell position, and ‘ α ’ the symmetry class within the same shell. The blue circles represent the atoms located outside the interaction shells. ‘M’ marks the mixed-dumbbell configuration.

Table 3.5: *Ab initio* solute-dumbbell binding energies (in eV) of Fe-based alloys obtained in Ref. [244]. Negative energies stand for attractive interactions.

Alloy	M	1a, 1b
Ni-Cr	-0.38	-0.10, -0.002
Ni-Ti	+0.33	+0.07, -0.024

As presented in Tab. 3.5, Ti shows repulsive interactions with dumbbell in M and 1b configurations, and attractive interaction in 1a configuration. Notably, the mixed dumbbell Ni-Ti is strongly repulsive and the energy landscape of Ti around the dumbbell Ni-Ni is flat. Therefore, SIA-mediated diffusion of this species is very unlikely. Regarding Cr, the mixed dumbbell is stable as it is in bcc Fe, which indicates that the SIA-mediated migration plays an important role in Cr diffusion in Ni. Interactions of solute-SIA at distances beyond 1-NN are negligible, leading to a network of 12 different jump frequencies Ref. [244].

3.3.3.3 Remarks on the DFT energy database of Ni-based alloys

Compared with the solute-vacancy interactions in Fe-based alloys, both Cr and Ti solute atoms have relatively small interactions with vacancies in Ni-based alloys. Therefore, solute drag by vacancy is unlikely to happen in these alloys. Besides, the solute-SIA interactions in the two alloys are very different: Ti shows a strong repulsive interaction with dumbbells, whereas Cr displays a strong attractive interaction with them. Therefore, we expect the kinetic properties to be very different in Ni-Ti and Ni-Cr alloys.

3.4 Diffusion properties in Ni- and Fe-based alloys

As shown in Section 3.2, the RIS of PDs and solute atoms depends on the diffusion properties of the alloys, including the PD and solute diffusion coefficients, together with the solute-PD flux coupling and bulk concentrations of vacancies. In this section, we compute the bulk vacancy concentration and the alloy diffusion properties of Ni- and Fe-based alloys, at different irradiation conditions.

3.4.1 Bulk vacancy concentration

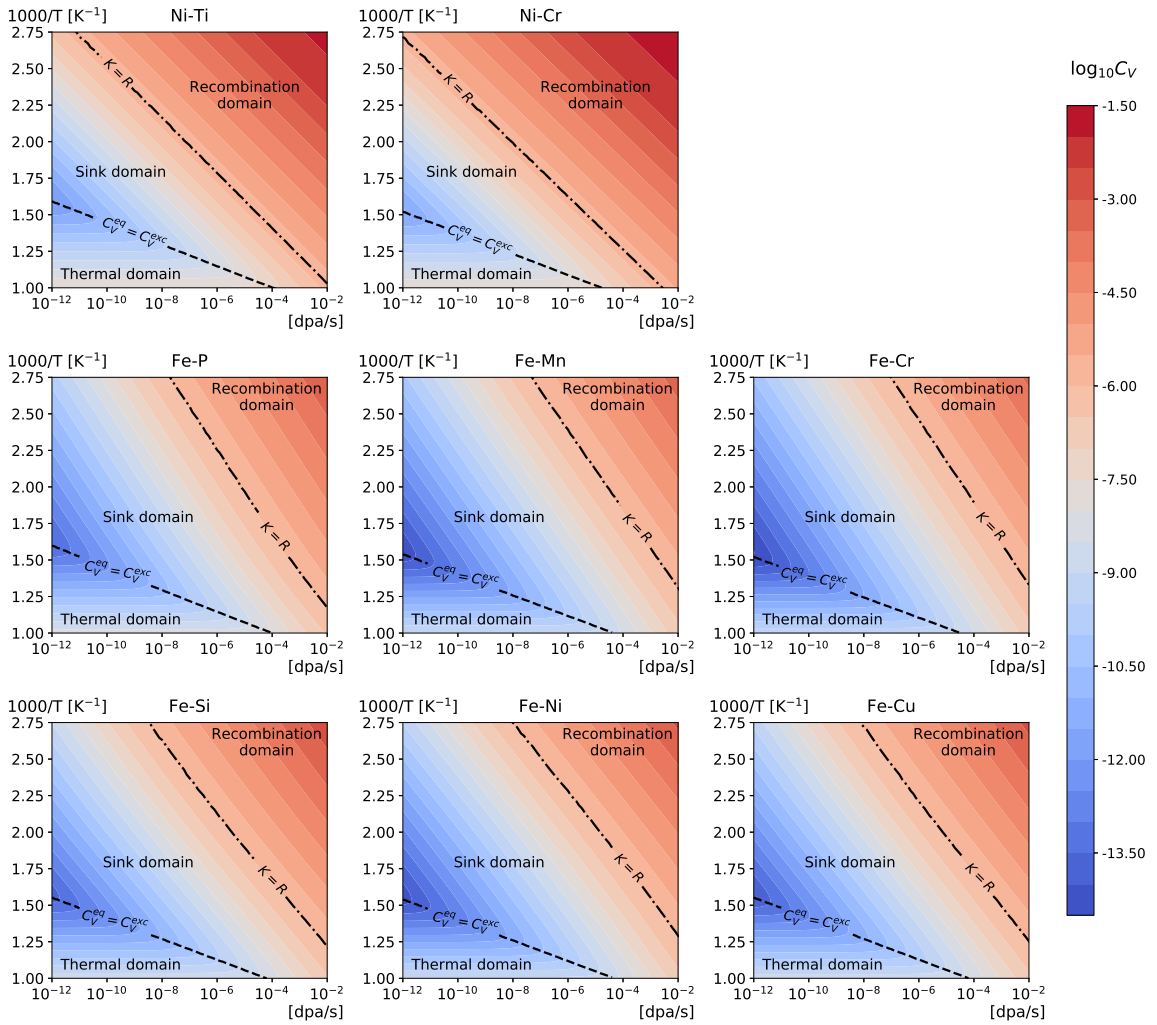


Figure 3.4: Bulk vacancy concentration C_V^b in function of dose rate (in dpa/s) and inverse of temperature (in K^{-1}) in different Ni- and Fe-based alloys. The nominal solute concentration \bar{C}_B is set to 1 at.% and the sink strength k^2 is set to $5 \times 10^{14} \text{ m}^{-2}$.

First, we investigate the variation of the bulk vacancy concentration C_V^b with temperature T and dose rate ϕ . This concentration deduced from Eq. (1.23) is plotted in form of ϕ - T maps in Fig. 3.4 for the dilute binary Ni- and Fe-based alloys at different T and ϕ .

ϕ - T maps of Fig. 3.4 can be divided into three domains according to the dominant PD reaction: the thermal domain when the bulk vacancy concentration is lower than twice the equilibrium vacancy concentration, i.e., the effect of irradiation is negligible; the sink domain for $K > R$; the recombination domain for $R > K$.

As expected from Eqs. (1.24) and (1.25), C_V^b decreases with T , whereas it increases with ϕ . In both the recombination and sink domains, the level lines correspond to a fixed value of ϕ/D_V . In the thermal domain, the level lines are horizontal lines with slope equal to 0 because C_V^b is close to the equilibrium vacancy concentration C_V^{eq} , and independent of ϕ .

We find that the main trends of C_V^b with T and ϕ are similar for the six investigated Fe-based alloys, with only slight variations of the extent of the kinetic domains. This is also true for the two Ni-based alloys. Therefore, the solute effect on the bulk concentration of vacancies is negligible. Regarding the effect of the host matrix between Fe and Ni, the variation tendencies with T and ϕ are similar, even though the sizes of the kinetic domains are different. The recombination domain in Ni-based alloys is larger than the one in Fe-based alloys, while the sink domain in Ni-based alloys is smaller than that in Fe-based alloys. These differences are due to the large difference of the vacancy migration energies in Fe ($\simeq 0.7$ eV) and Ni ($\simeq 1.1$ eV).

3.4.2 Solute diffusion coefficient

Here, we compute the intrinsic diffusion coefficient of solute B, D_B , which is equal to the solute tracer diffusion coefficient in a dilute alloy. The ϕ - T maps of D_B are presented in Fig. 3.5. We set the nominal solute concentration, \bar{C}_B , to 1 at.%. Over most irradiation conditions of interest, $C_B \gg C_V^b$. In this case, the solute diffusion coefficient varies linearly with the bulk vacancy concentration (cf. Eq. (1.73)), provided the effect of FAR is negligible. As expected, we recover the three kinetic domains of C_V^b , except in the low-temperature and high-flux domain of Ni-based alloys where FAR may affect the solute diffusion properties.

D_B increases with temperature in the recombination and thermal domains, though the increasing rate is different in the two domains. In the sink domain, D_B is nearly T -independent. As for the effect of the radiation flux, D_B increases with ϕ except in the thermal domain. Similarly to C_V^b , there is a weak effect of solute on the main trends.

At low temperature ($1000/T > 2.25$) and high dose rate ($\phi > 10^{-5}$ dpa/s), D_B in Ni-based alloys is nearly temperature-independent because the FAR mechanism is dominant over the thermal diffusion. However, this is not observed in Fe-based alloys under the same irradiation conditions because the PD migration barriers are relatively low and the thermally-activated diffusion mechanism is still significant compared with the FAR mechanism.

3.4.3 Flux coupling between atoms and point defects

We investigate the solute-PD flux couplings by computing the flux coupling factors δ_V and δ_I , given respectively by Eq. (1.64) and Eq. (1.65), in Ni- and Fe-based alloys at different

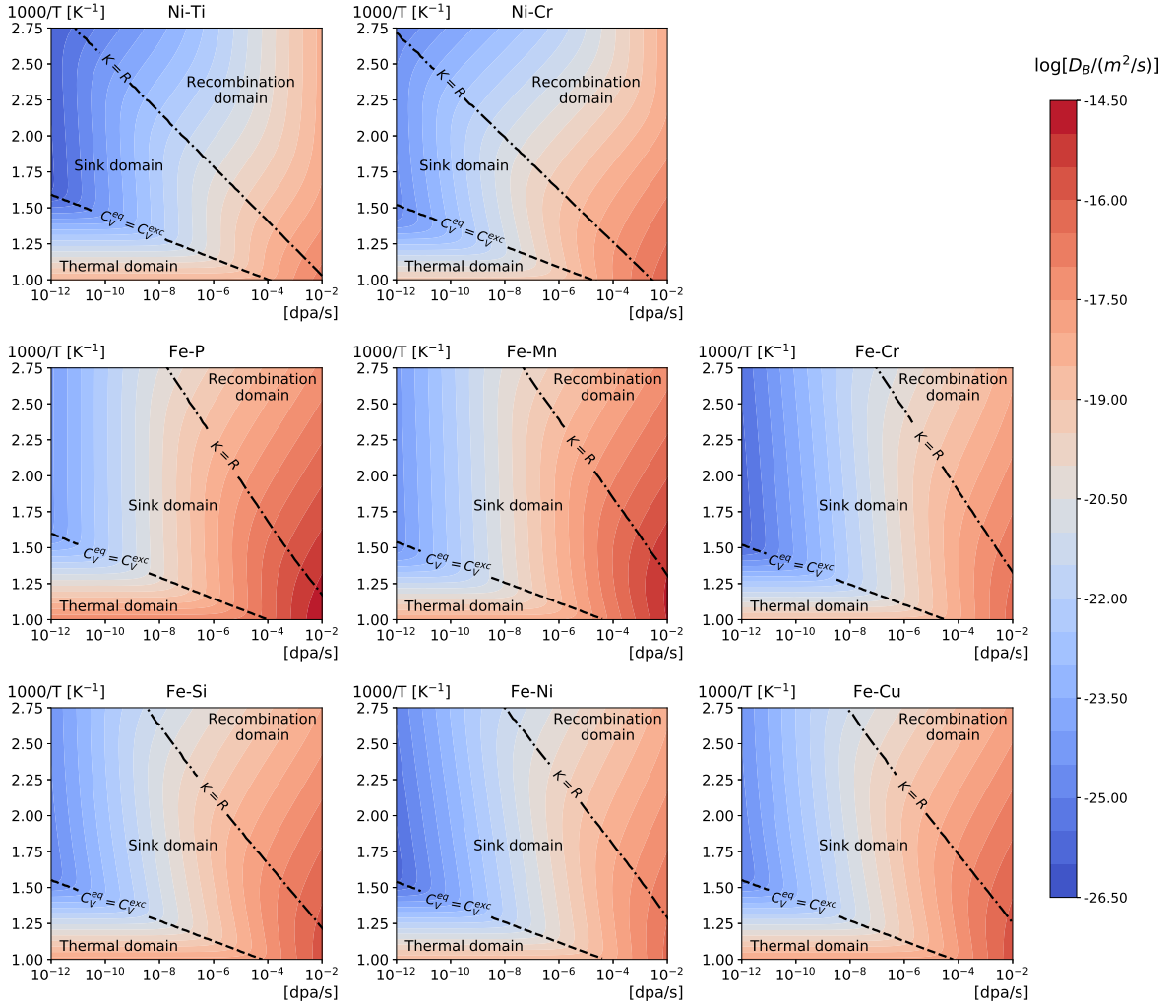


Figure 3.5: Solute diffusion coefficient D_B in function of dose rate (in dpa/s) and temperature (in $1000/T$ [K⁻¹]) of different Ni- and Fe-based alloys. The nominal solute composition \bar{C}_B is set to 1 at.% and the sink strength k^2 is set to $5 \times 10^{14} \text{ m}^{-2}$.

irradiation conditions.

3.4.3.1 Solute-vacancy flux coupling

The ϕ - T maps of normalized δ_V in Ni- and Fe-based alloys are plotted in Fig. 3.6. δ_V indicates the direction of solute flux with respect to the vacancy one. At all investigated temperatures, δ_V is negative in Ni-Ti and Fe-Cr alloys, while it is positive in Fe-P, Fe-Mn, Fe-Si, Fe-Ni, and Fe-Cu alloys. As for Ni-Cr alloy, δ_V is positive when the temperature is below about 525 K, and negative if not. Therefore, solute drag occurs in most of the investigated alloys except in Ni-Ti and Fe-Cr systems.

The strength of solute drag in Fe-P, Fe-Mn, Fe-Si, Fe-Ni, Fe-Cu, and Ni-Cr alloys decreases with temperature. In addition, the solute drag cancels out at $T = 525 \text{ K}$ in Ni-Cr. Besides, a

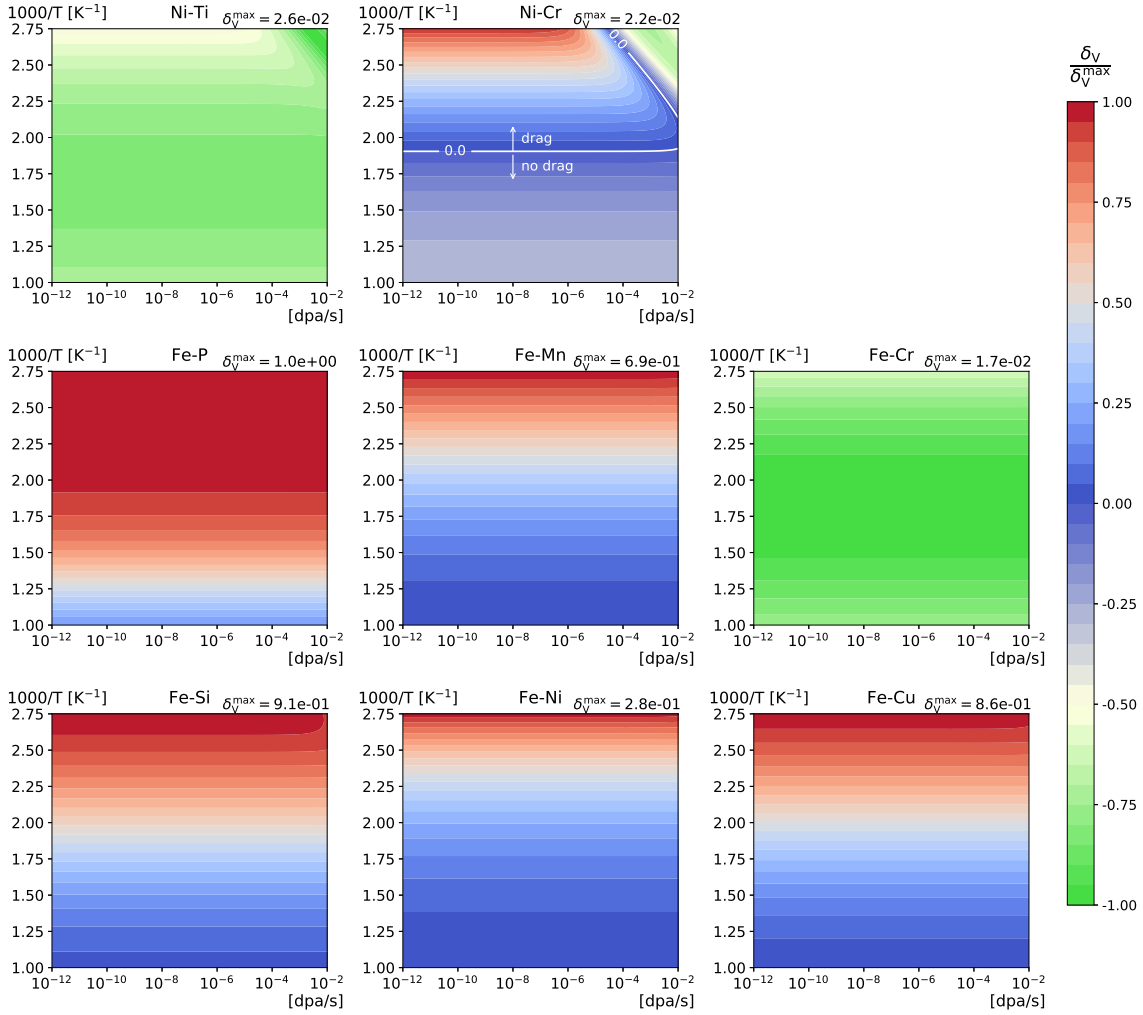


Figure 3.6: Solute-vacancy flux coupling factor δ_V normalized by its maximum absolute value δ_V^{\max} in function of dose rate (in dpa/s) and temperature (in 1000/K) of different Ni- and Fe-based alloys. The nominal solute composition \bar{C}_B is set to 1 at.% and the sink strength k^2 is set to $5 \times 10^{14} \text{ m}^{-2}$.

change of dose rate does not affect the solute drag behaviors in Fe-based alloys. Whereas, in Ni-based alloys, δ_V is reduced at large dose rate ($> 10^{-4}$ dpa/s) and low temperature (< 450 K). In particular, in Ni-Cr alloy, the increase of dose rate changes the sign of δ_V and destroys the solute drag, which is due to the increasing relative contribution of FAR with respect to thermal solute diffusion.

3.4.3.2 Solute-SIA flux coupling

We present in Fig. 3.7 the ϕ - T maps of normalized δ_I in Ni- and Fe-based alloys.

The factor δ_I is systematically positive due to the fact that SIAs and atoms diffuse in the same direction. δ_I is relatively small in Ni-Ti, Fe-Si, Fe-Ni, and Fe-Cu alloys because the

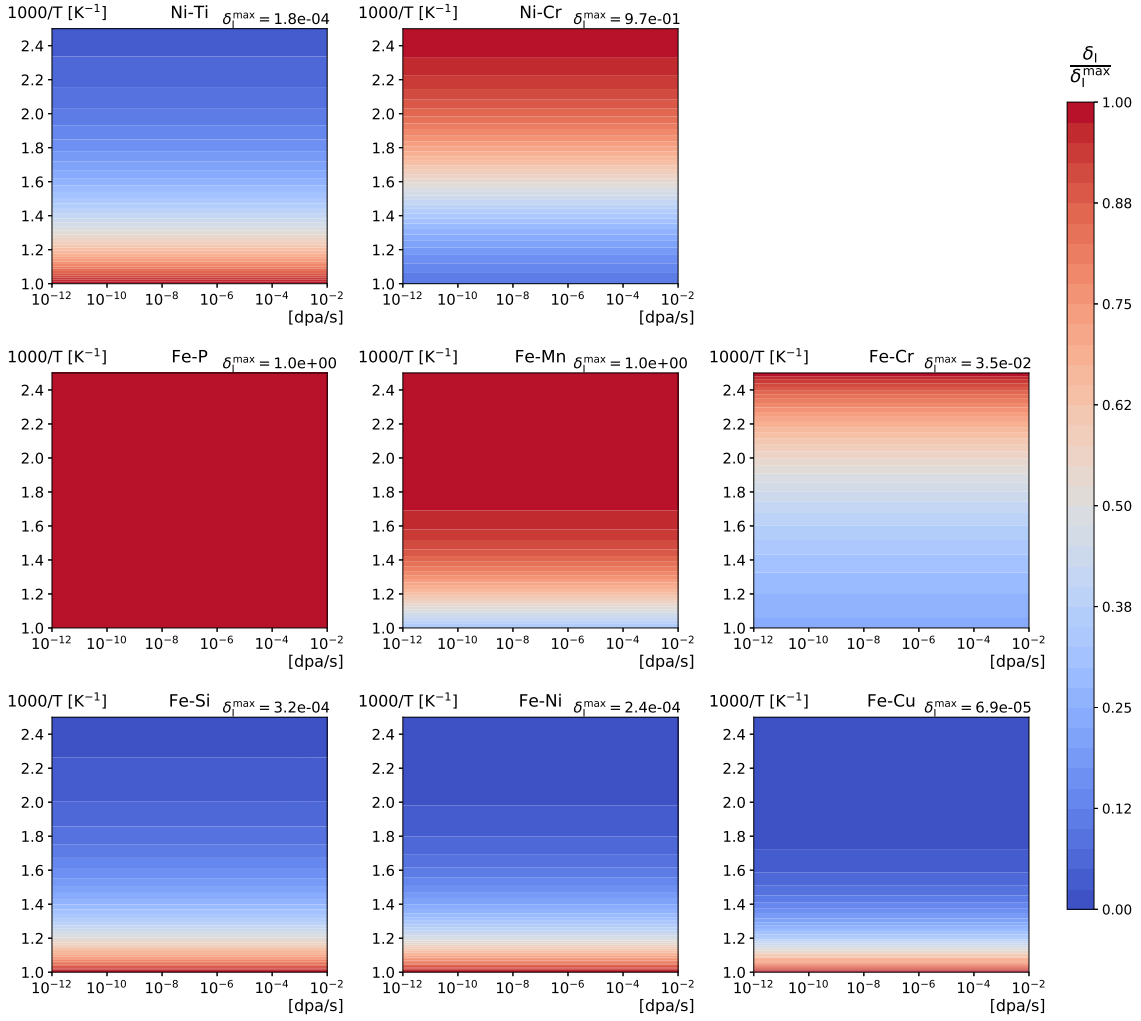


Figure 3.7: Solute-SIA flux coupling factor δ_I normalized by its maximum absolute value δ_I^{\max} in function of dose rate (in dpa/s) and temperature (in 1000/K) of different Ni- and Fe-based alloys. The nominal solute composition \bar{C}_B is set to 1 at.% and the sink strength k^2 is set to $5 \times 10^{14} \text{ m}^{-2}$.

stability of the solute-SIA complex is low. In Fe-P and Fe-Mn alloys, δ_I is close to 1 for almost all irradiation conditions, because mixed dumbbells Fe-P and Fe-Mn are very stable.

δ_I in Fe-Mn and Fe-Cr alloys decreases with temperature, while δ_I in Ni-Ti, Ni-Cr, Fe-Si, Fe-Ni, and Fe-Cu alloys increases with temperature. There is no effect of dose rate in Ni- and Fe-based alloys because the relative contribution of FAR with respect to SIA thermal diffusion is much smaller than that of vacancy.

3.5 RIS in Ni- and Fe-based alloys

Relying on the RIS models developed in Section 3.2, we calculate the RIS profiles of PDs and solute atoms in the various Ni- and Fe-based alloys.

3.5.1 RIS of vacancies

First, we assess the accuracy of our analytical RIS model by proceeding to a comparison between a numerical application of the analytical model and a full numerical integration of the diffusion equation (Eq. (3.12)). Then, we investigate the shape of vacancy concentration profile and the amount of vacancy segregation at different temperatures, dose rates, and sink strengths.

3.5.1.1 Analytical RIS profiles of vacancies versus the reference solution

The concentration profiles of vacancies at different temperatures and sink strengths are respectively given in Fig. 3.8. In order to assess the accuracy of the analytical approximations, we plot as well the reference profile obtained from the exact solution of Eq. (3.12) computed by a finite-difference method. We observe that the concentration profiles obtained from the present analytical approach are in good agreement with the reference profiles.

In order to investigate the effect of PD recombination on the RIS profiles, we compare the profiles given by two different methods: (i) the analytical approximation proposed in this work (Eq. (3.16) for $C_V(z)$), and (ii) the one proposed in Ref. [30] where the recombination rate is set to zero.

When recombination reactions are neglected, the vacancy concentration along the RIS profile is overestimated, especially at low temperatures (e.g., 600 K) and small sink strength (e.g., $5 \times 10^{13} \text{ m}^{-2}$), because the ratio K/R . Therefore, the recombination effect is non-negligible.

3.5.1.2 Vacancy segregation profile

In order to investigate the shape of the vacancy RIS profile at different irradiation conditions, we define an effective width l_V^e of the vacancy concentration profile as follows

$$l_V^e = \sqrt{\frac{\int_0^{h/2} [(h/2) - z]^2 [C_V(z) - C_V(0)] dz}{\int_0^{h/2} [C_V(z) - C_V(0)] dz}}. \quad (3.49)$$

This parameter represents the average distance between the vacancy and the PD sink. It is also related to the width of the vacancy depleted zone near sinks [253]. In Fig. 3.9, we plot the maps of l_V^e as a function of the inverse of temperature ($1000/T$ in K^{-1}) and dose rate in dpa/s for the various Ni- and Fe-based alloys. In the sink domain, the width of the vacancy profile does

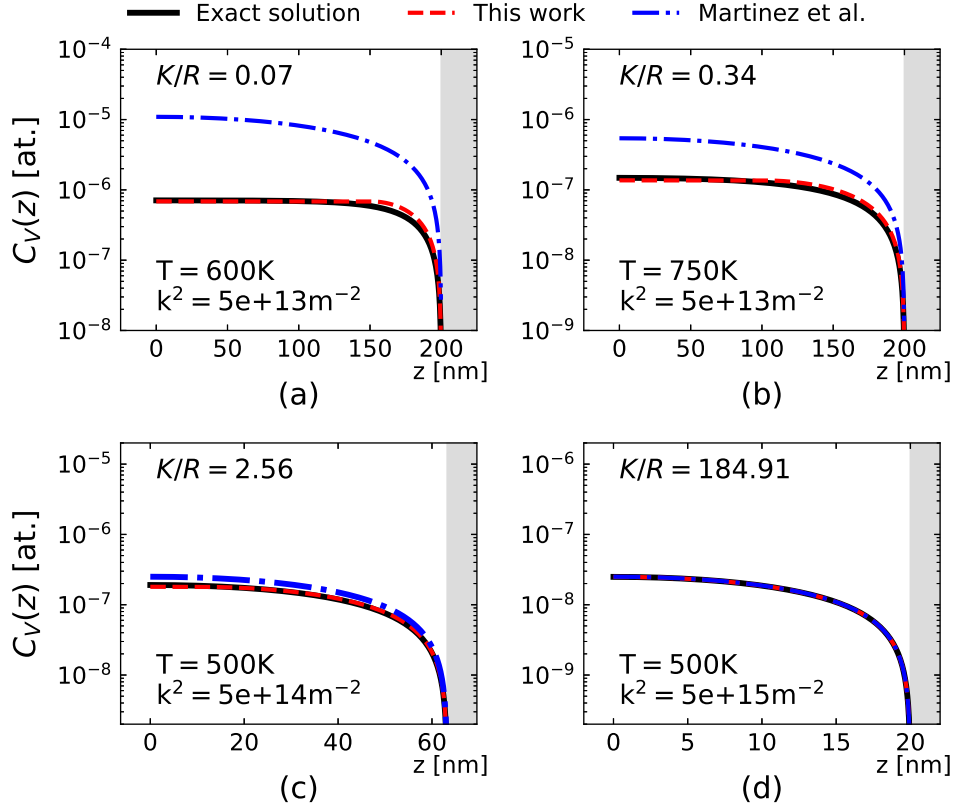


Figure 3.8: Concentration profiles of vacancies under irradiation. The solid lines are the reference solutions of Eq. (3.12). The dashed and dash-dotted lines are the analytical approximations of Eq. (3.12), obtained from Eq. (3.16) (this work) and Eq. (3.13) (cf. Ref. [30]), respectively. The shaded area indicates the interface. The results (a) and (b) are respectively given for $T = 600$ K and 750 K, with $\phi = 10^{-4}$ dpa/s and $k^2 = 5 \times 10^{13} \text{ m}^{-2}$ (i.e. $h = 400$ nm). The results (c) and (d) are respectively given for $k^2 = 5 \times 10^{14} \text{ m}^{-2}$ and $5 \times 10^{15} \text{ m}^{-2}$, with $\phi = 10^{-6}$ dpa/s and $T = 500$ K.

not vary with the irradiation conditions. According to the analytical solution of Eq. (3.49), l_V^e increases with h . Therefore, the smaller the sink density, the larger the distance between sinks, and the wider the vacancy depleted zone. In the recombination domain, l_V^e decreases with dose rate, while it increases with temperature.

3.5.1.3 The amount of vacancy segregation S_V

Here we apply Eq. (3.20) to the calculation of the vacancy segregation amount in specific Ni- and Fe-based alloys. We investigate the effects of temperature, dose rate and sink strength on vacancy segregation. Note that, after Eq. (3.21) and Eq. (3.22), $\log |S_V|$ is given by:

$$\log |S_V| = \begin{cases} \log \phi - \log D_V - \frac{3}{2} \log k^2 + K_2, & K \gg R; \\ \frac{1}{4} \log \phi - \frac{1}{4} \log D_V + K_3, & K \ll R, \end{cases} \quad (3.50)$$

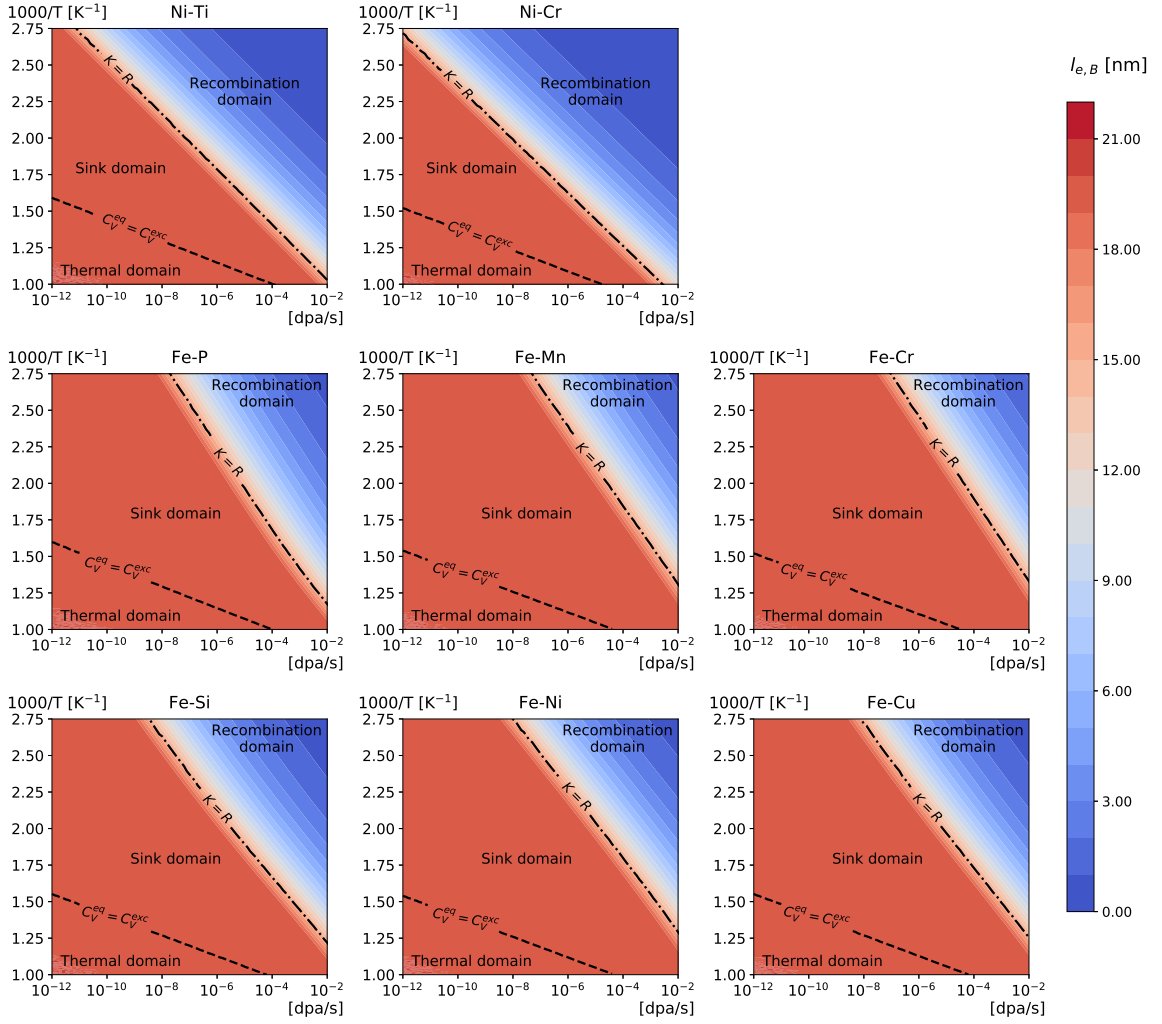


Figure 3.9: The effective width of RIS profiles of vacancies in function of dose rate (in dpa/s) and temperature (in K^{-1}) of various dilute binary Ni- and Fe-based alloys. The nominal solute composition \bar{C}_B is set to 1 at.% and the sink strength k^2 is set to $5 \times 10^{14} \text{ m}^{-2}$. The corresponding distance between planar sinks h is 126 nm.

with $K_2 = \log(\sqrt{2}/3)$ and $K_3 = \log\left[(\Omega/\pi r_{\text{rec}})^{3/4}/6\right]$.

Fig. 3.10 shows the maps of $\log |S_V|$ in function of the inverse of temperature ($1000/T$ in K^{-1}) and dose rate in dpa/s. The maps are divided into two domains corresponding to the two limit cases of Eq. (3.50): the first one is dominated by the PD recombination reactions ($K < R$), and the second one is dominated by the PD elimination at sinks ($K > R$). $\log |S_V|$ increases linearly with $\log \phi$ and $1/T$. However, the slopes are different in the two domains.

Fig. 3.11 shows temperature-sink strength maps of the segregation amount of vacancies ($\log |S_V|$). These maps are also divided into two domains, corresponding to the PD recombination ($K < R$) and PD elimination at sinks ($K > R$), respectively. $\log |S_V|$ decreases linearly with $\log k^2$ in the sink domain, whereas it is nearly k^2 -independent in the recombination domain.

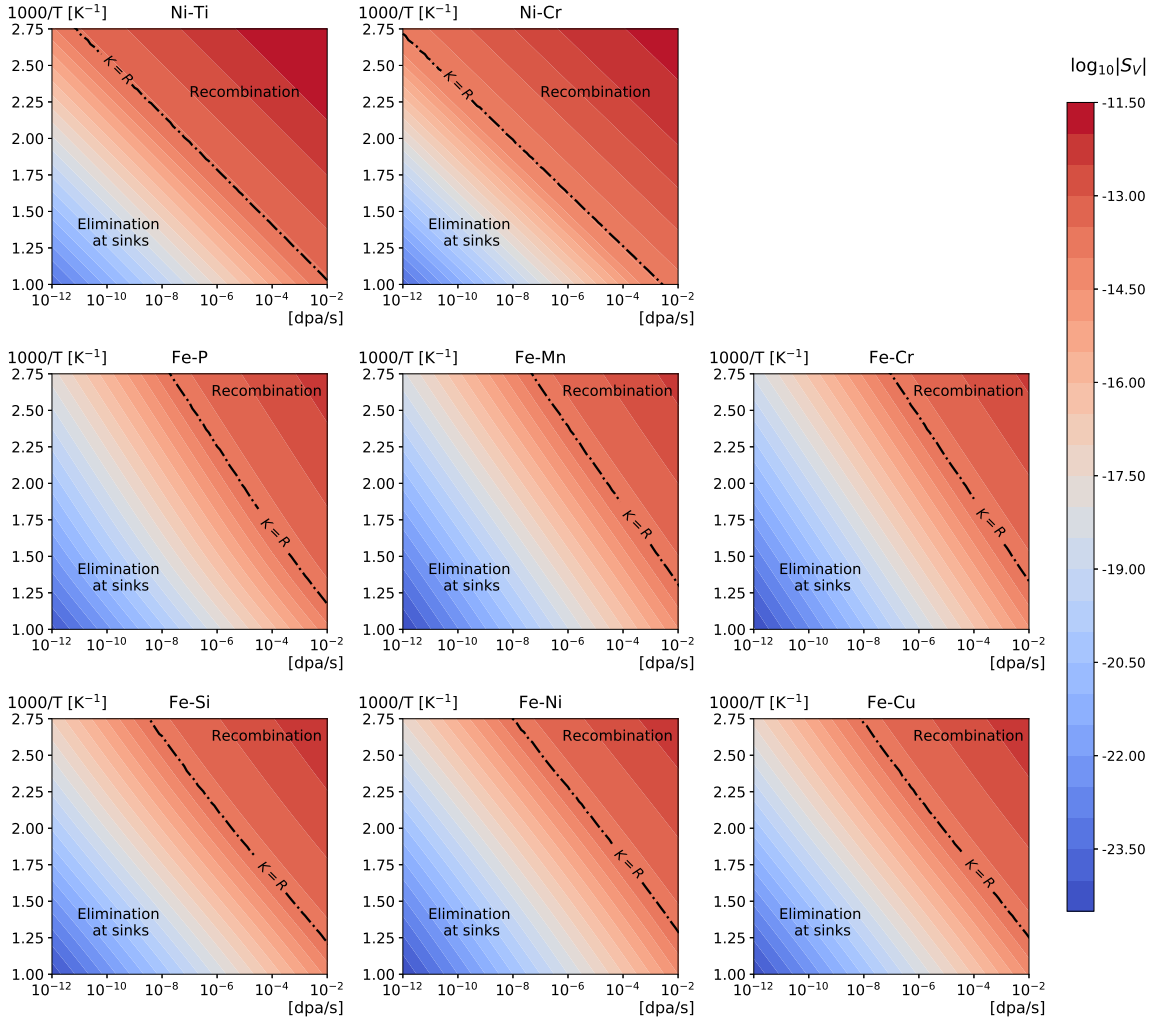


Figure 3.10: Vacancy segregation amount S_V in function of dose rate (in dpa/s) and temperature (in K^{-1}) of different Ni- and Fe-based alloys. The nominal solute composition \bar{C}_B is set to 1.0 at.% and the sink strength k^2 is set to $10^{14} m^{-2}$.

The variations of S_V with ϕ and k^2 are similar in the various Ni- and Fe-based alloys, whereas the variations with $1000/T$ are slightly different because the vacancy diffusion coefficient D_V is alloy-specific. Moreover, the absolute value of the vacancy segregation amount is more important in Ni-based alloys than in Fe-based alloys at the same irradiation conditions and microstructures. Note that in Section 4.5.4, we show that the solute effects on the PD RIS give rise to the biased PD absorption at sinks.

3.5.2 RIS of solute atoms

We calculate the L -coefficients for the various Ni- and Fe-based alloys and deduce the RIS factors α_1 and α_2 from these coefficients. From the solute concentration variation of α_1 and α_2 , we choose the appropriate analytical RIS models to calculate the solute RIS profiles of the

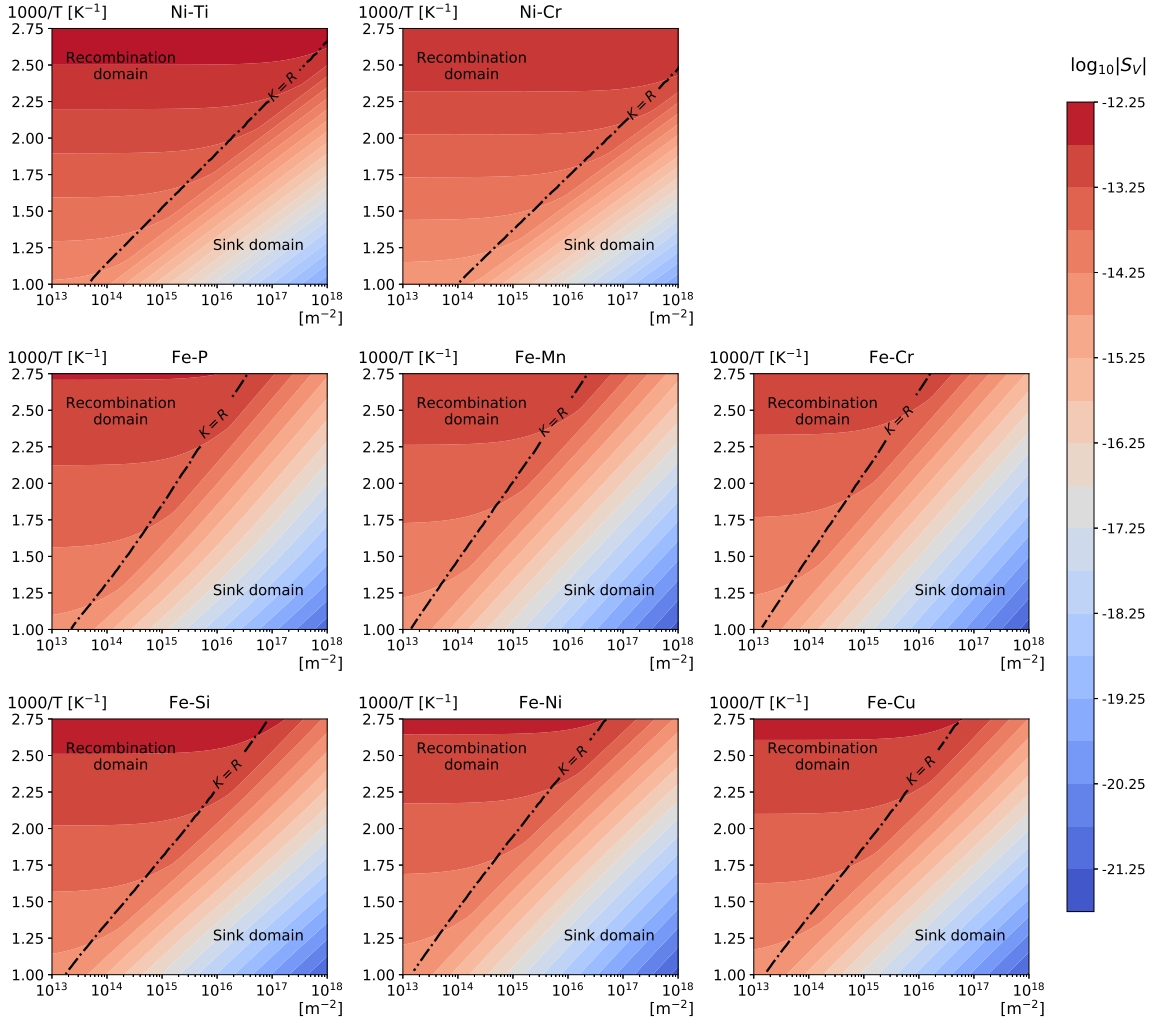


Figure 3.11: Vacancy segregation amount S_V in function of the sink strength (in m^{-2}) and temperature (in K^{-1}) of Ni- and Fe-based alloys. The nominal solute composition \bar{C}_B is set to 1.0 at.% and the dose rate ϕ is set to 2×10^{-4} dpa/s.

various alloys.

3.5.2.1 Calculation of α_1 and α_2 in Ni- and Fe-based alloys

First, we consider the RIS factor α_1 , which is directly related to the flux couplings after Eq. (3.24). We show in Fig. 3.12 the maps of the RIS factor α_1 in function of temperature and dose rate.

The sign of α_1 indicates the overall segregation tendency of the solute atoms, resulting from both V and SIA fluxes. Whatever the irradiation conditions, α_1 is positive in Ni-Cr, Fe-P, Fe-Mn, Fe-Si, Fe-Ni, and Fe-Cu alloys, indicating an enrichment of the solute atoms in these systems. Whereas, α_1 is negative in Ni-Ti alloy, leading to a solute depletion. As for the Fe-Cr alloy, the sign of the RIS factor changes around 530 K. At lower temperatures, an enrichment

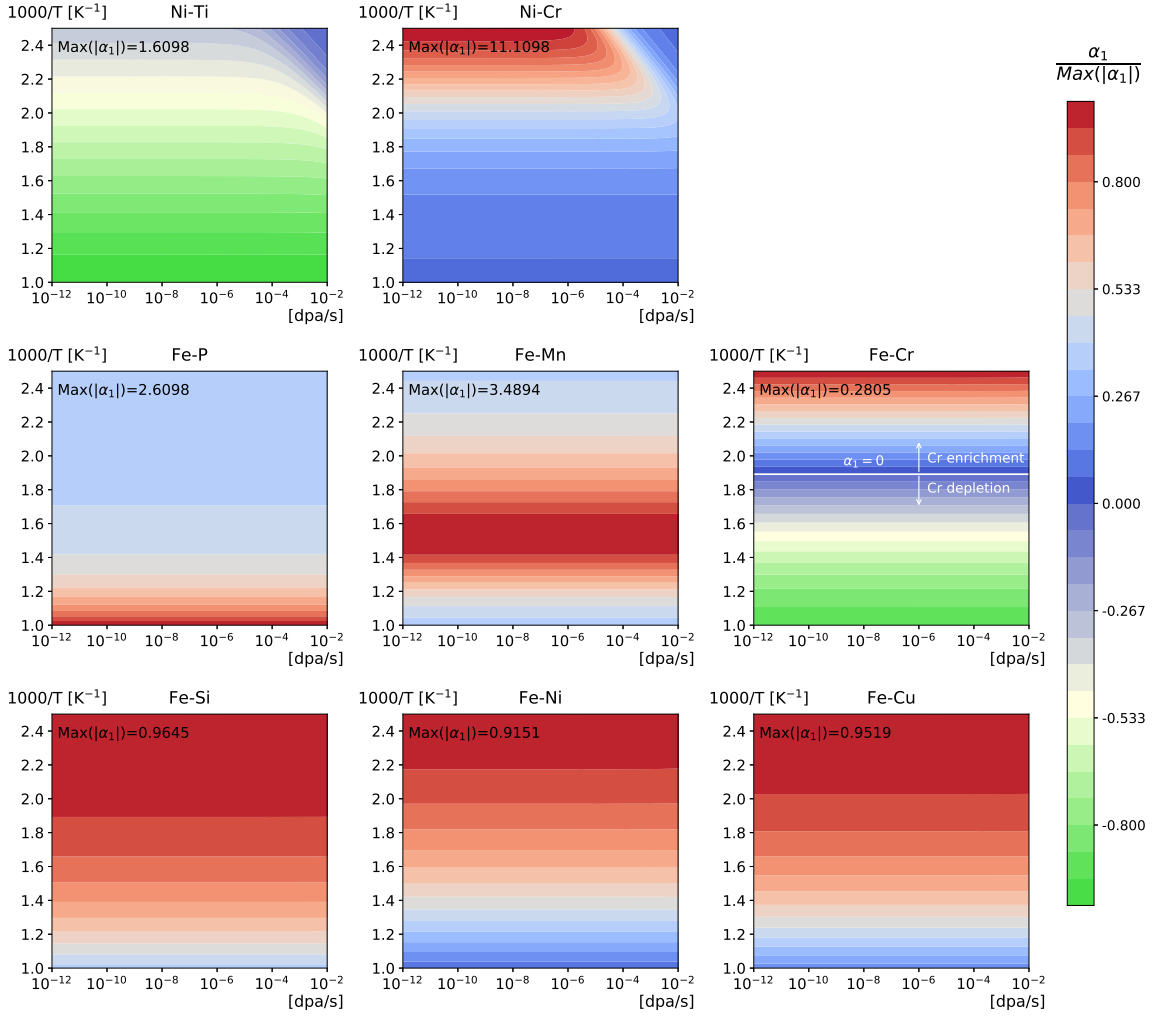


Figure 3.12: RIS factor α_1 normalized by its maximum in absolute value $\text{Max}(|\alpha_1|)$ in function of dose rate (in dpa/s) and temperature (in K^{-1}) in different Ni- and Fe-based alloys. The solid line in Fe-Cr system is an eye guide indicating $\alpha_1 = 0$. The nominal solute composition \bar{C}_B is set to 1 at.% and the sink strength k^2 is set to $5 \times 10^{14} \text{m}^{-2}$.

of Cr is predicted, while at higher temperatures, a depletion of Cr is expected.

The variation of α_1 with temperature in Fe-Si, Fe-Ni and Fe-Cu is similar. The value of α_1 decreases with temperature because of the drop of vacancy-solute interaction [181]. Therefore, the enrichment tendency is reduced when temperature is increased. In Fe-P, Fe-Mn, and Fe-Cr alloys, the variation of α_1 with temperature is quite different. α_1 in Fe-P increases with temperature, increasing the enrichment in P at sinks. As for the Fe-Mn alloy, $|\alpha_1|$ increases up to around 650 K. The binding of the Fe-Mn dumbbell is lower than that of the Fe-P dumbbell. As a consequence, $|\alpha_1|$ decreases after 650 K due to a reduction of the Fe-Mn dumbbell stability. Regarding the Fe-Cr alloy, we observe a change of sign of α_1 around 530 K. In Ni-Ti alloy, α_1 remains negative and decreases with temperature, meaning that the depletion tendency of Ti increases with temperature. As for Ni-Cr alloy, α_1 is positive and decreases with temperature, which is similar to Fe-Si, Fe-Ni, and Fe-Cu alloys.

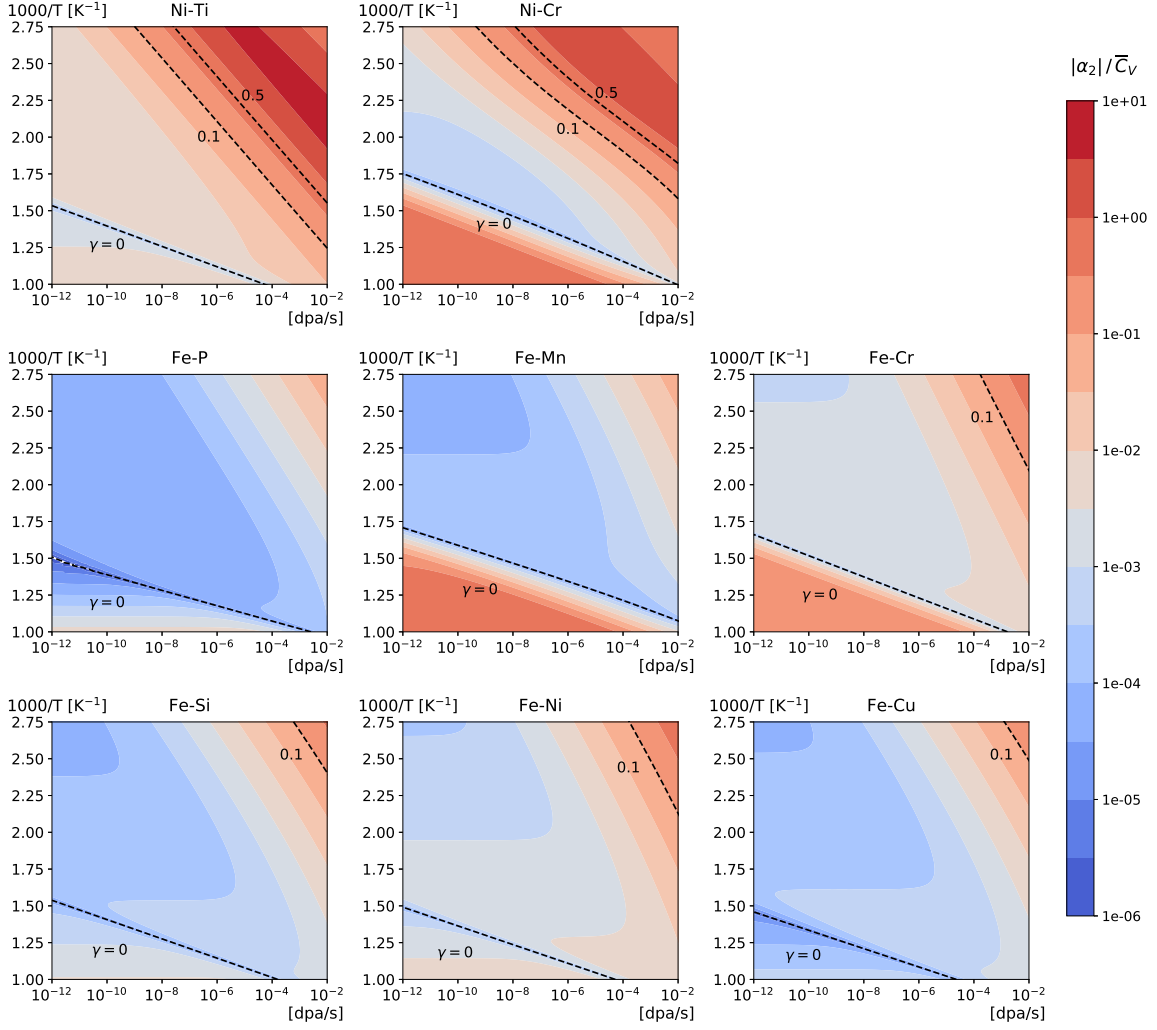


Figure 3.13: The relative FAR contribution $\gamma = |\alpha_2|/C_V^b$ in function of dose rate (in dpa/s) and temperature (in K^{-1}) in different Ni- and Fe-based alloys. The nominal solute composition \bar{C}_B is set to 1 at.‰ and the sink strength k^2 is set to $5 \times 10^{14} \text{ m}^{-2}$.

The factor α_1 in Fe-based alloys is ϕ -independent at the considered irradiation conditions. However, this is not the case in Ni-based alloys. When the temperature is lower than about 600 K, α_1 decreases with dose rate. In the extreme case when $T = 300 \text{ K}$ and $\phi = 10^{-2} \text{ dpa/s}$, α_1 in Ni-based alloys is close to 0 because the flux coupling is destroyed by FAR. Above 600 K or at low dose rate (less than about 10^{-5} dpa/s), there is no FAR effects on the RIS factor α_1 . Note that even though FAR may reduce α_1 in Ni-based alloys, it does not qualitatively change the segregation tendency (i.e. the sign of α_1 remains unchanged).

In addition to α_1 , the RIS amount depends also on the RIS factor α_2 , which is directly related to the FAR mechanism (i.e. L_{BB}^{mono}). As stated in Section 3.2.2.2, the ratio $\gamma = \alpha_2/C_V^b$ indicates how important the FAR effect on the RIS amount of solute atoms. If $\gamma \gg 1$, S_B is equal to 0. We plot in Fig. 3.13 the ϕ - T maps of $|\gamma| = |\alpha_2|/C_V^b$. Dashed lines represent level lines of γ . We observe that over most flux-temperature conditions, γ is smaller than 0.1. γ is close to or larger than 1 only when ϕ is large and T is low. The results show that γ decreases

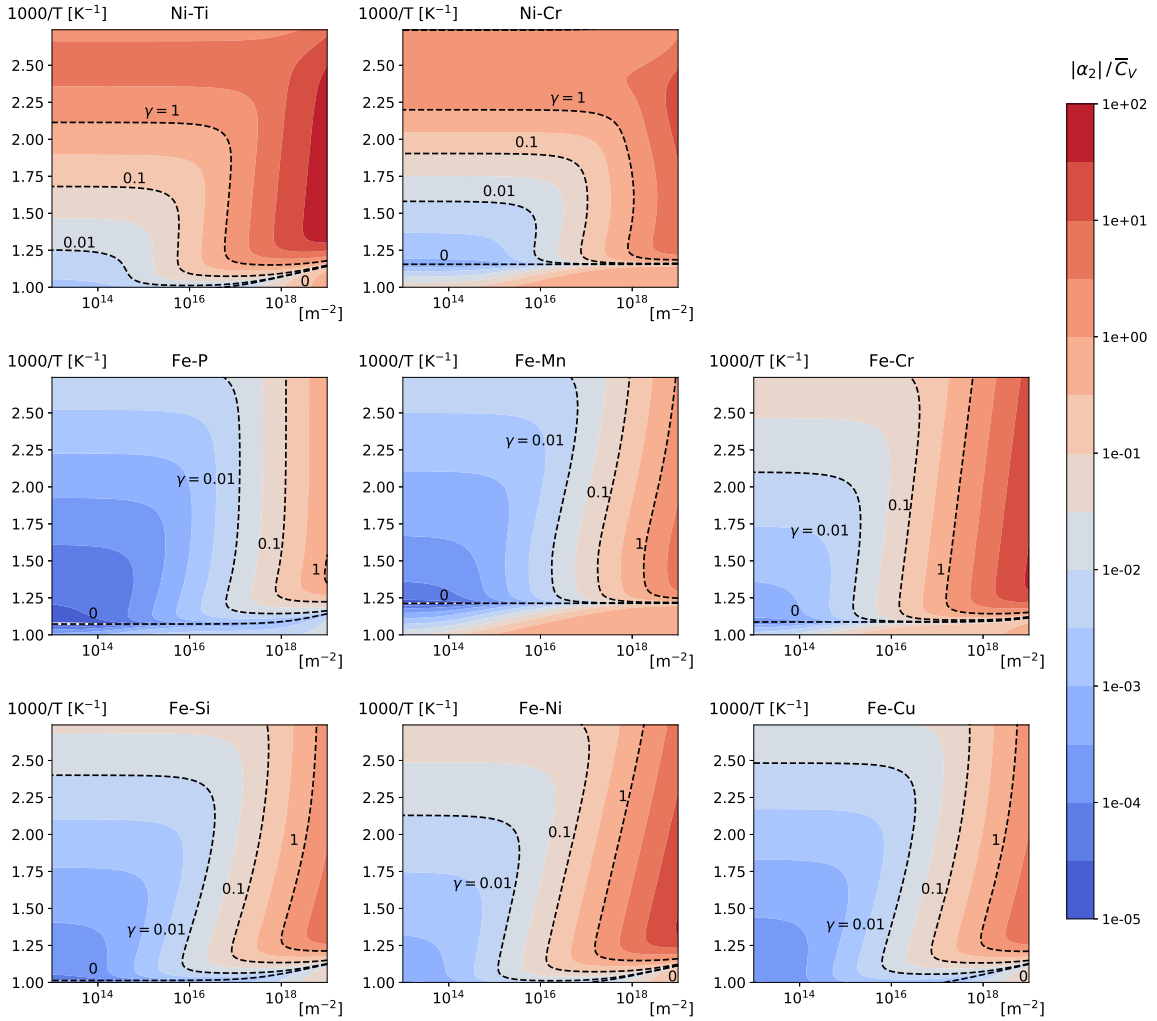


Figure 3.14: The relative FAR contribution $\gamma = |\alpha_2|/C_V^b$ in function of sink strength (in m^{-2}) and temperature (in K^{-1}) in different Ni- and Fe-based alloys. The nominal solute composition \bar{C}_B is set to 1 at.% and ϕ is set to 2×10^{-4} dpa/s.

with temperature, and at high temperatures, it becomes negative. The domain where $\gamma < 0$ coincides with the thermal regime domain of Fig. 3.4, meaning $C_V \simeq C_V^{\text{eq}}$. Moreover, γ increases with the dose rate.

We observe that over most irradiation conditions, γ is smaller than 0.1 in Fe-based alloys. However, in Ni-based alloys, the value of γ is larger than that in Fe-based alloys. At large dose rates and low temperatures, γ is close to or larger than 1 in Ni-based alloys. Therefore, the FAR effect on the RIS of solute atoms in Ni-based alloys should be more important than that in Fe-based alloys.

In order to highlight the effect of the sink strength on γ , we plot in Fig. 3.14 the k^2 - T maps of $|\gamma|$. γ increases with k^2 . Hence, the FAR effect on RIS should be significant at large values of k^2 .

Note that the variation of γ with T , ϕ and k^2 is very alloy-specific. For instance, in Fe-based alloys, at the same values of T , ϕ and k^2 , γ is relatively high in Fe-Ni and Fe-Cr alloys whereas it is small in Fe-P and Fe-Mn alloys. The values of γ in Fe-Si and Fe-Cu are between them. Therefore, the solute segregation in Fe-P and Fe-Mn alloys is more resistant to the FAR effect than that in the other four Fe-based alloys.

3.5.2.2 Comparison between analytical results and reference solutions

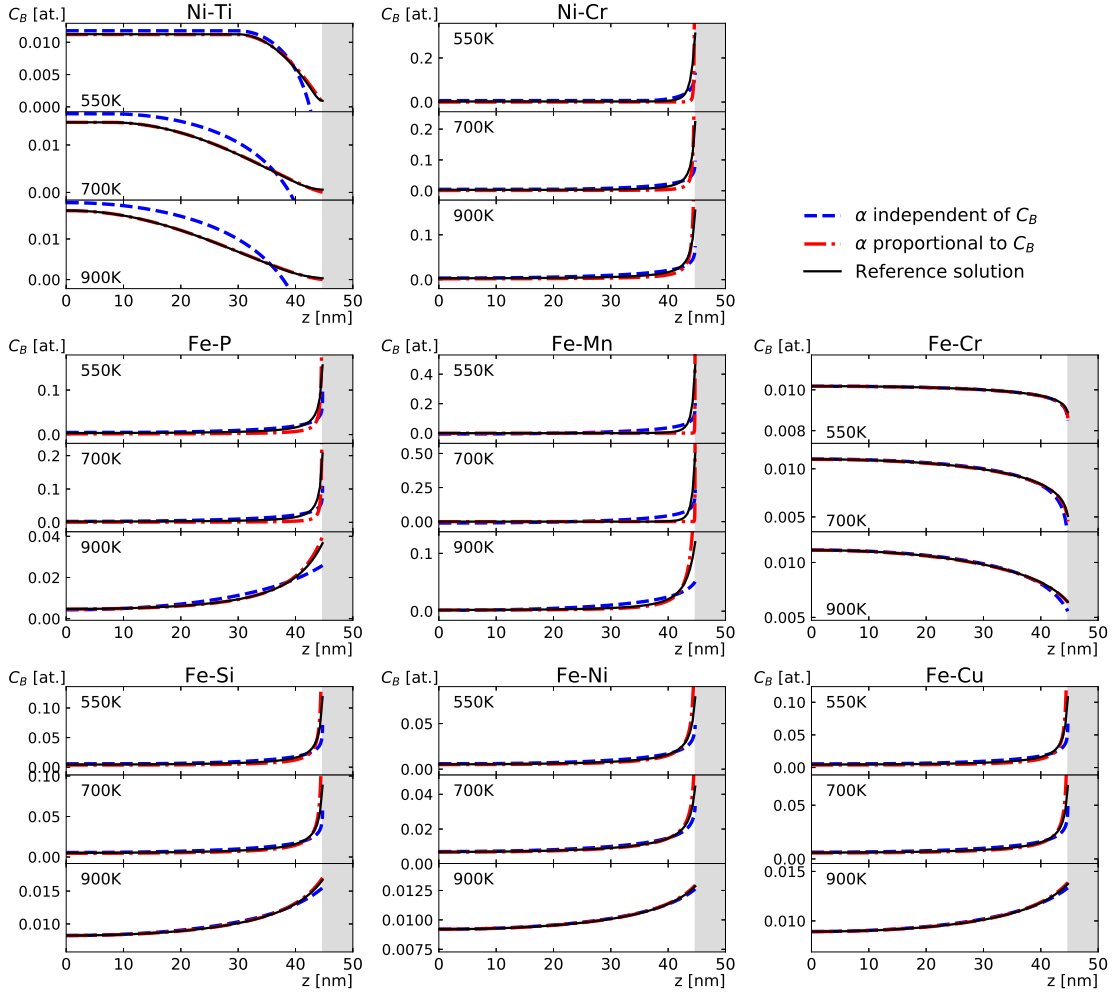


Figure 3.15: The solute RIS profiles deduced from the analytical calculations in several dilute Ni- and Fe-based alloys using Eq. (3.29) (dashed lines) and Eq. (3.38) (dash-dotted lines). The profiles obtained by the exact solution of Eq. (1.70) are plotted as reference. The nominal solute composition \bar{C}_B is set to 1 at.% and the sink strength k^2 is set to 10^{15} m^{-2} .

As stated in Section 3.2.2.1, different assumptions are made with respect to the solute concentration dependence of α . In Approximation 1, the factor α is assumed to be independent of C_B . In Approximation 2, α_1 and α_2 are assumed to be independent of C_B so that α is proportional to C_B . In order to investigate which assumption is more appropriate to calculate

the solute RIS, we compare the RIS profiles given by the analytical model (Eq. (3.29) and Eq. (3.38)) and the exact solution of Eq. (1.70) by numerical integration. The variation of α with C_B is systematically accounted for in the exact solution. The solute RIS profiles at different temperatures are plotted in Fig. 3.15.

In Approximation 2, we have a good agreement between the analytical profiles and the reference results in the various Ni- and Fe-based alloys at every temperature. In Ni-Cr, Fe-P, and Fe-Mn alloys, we observe slightly different profile shapes between the analytical and reference results at 550 and 700 K. However, we systematically obtain a very good agreement on the solute bulk concentration and the solute segregation amount.

In Approximation 1, in Fe-Si, Fe-Ni, Fe-Cu, and Fe-Cr alloys, the analytical profiles are in relatively good agreement with the reference profiles. However, in Ni-Ti, Ni-Cr, Fe-P, and Fe-Mn alloys, the shape of the analytical profiles are quite different from the reference solutions. Especially in the Ni-Ti alloy, the analytical profile is negative near the PD sink. The tendency of the depletion of Ti solute atom is so important that C_B tends to zero near the sink, and so does α . Therefore, the magnitude of α at sink should be much smaller than that in the bulk area. However, in Approximation 1, α is supposed to be constant. Thus, the depletion tendency near sink is overestimated, leading to a negative profile.

To conclude, compared with the analytical profiles obtained in Approximation 1, the ones obtained in Approximation 2 are in better agreement with the reference solutions. In the following, we investigate the solute RIS profile by relying on approximation 2: α is proportional to C_B , and α_1 and α_2 are independent of C_B .

3.5.2.3 Solute segregation profile

As for the vacancy concentration profile, we introduce an effective width, l_B^e , of the concentration profile of solute atoms in order to characterize the shape of the solute RIS profile. Its definition is similar to that of the vacancies (Eq. (3.49)), though letter V is replaced by letter B . Fig. 3.16 shows the ϕ - T maps of l_B^e .

l_B^e is large and almost uniform in the thermal domain. In the recombination domain, l_B^e decreases with dose rate and increases with temperature. These trends are very similar to the ones of l_V^e . As a result, we expect the RIS profiles of vacancies and solute atoms to have almost the same width in the thermal and recombination-dominated domains. Instead, in the sink domain, the larger the solute RIS amount, S_B , the smaller the width of the RIS profile, l_B^e . Moreover, in this domain, l_B^e is smaller than l_V^e , especially in Ni-Cr, Fe-P, and Fe-Mn alloys, where the tendency of positive RIS is significant.

Note that the width of the solute RIS profile in the Ni-Ti alloy is the largest among the various alloys. This is because the negative RIS of the solute Ti is so important that the solute concentration at sinks is very close to zero. In this case, the decrease of Ti concentration near sinks is intrinsically limited since the solute concentration cannot be negative. To compensate this limitation, the RIS profile gets wider.

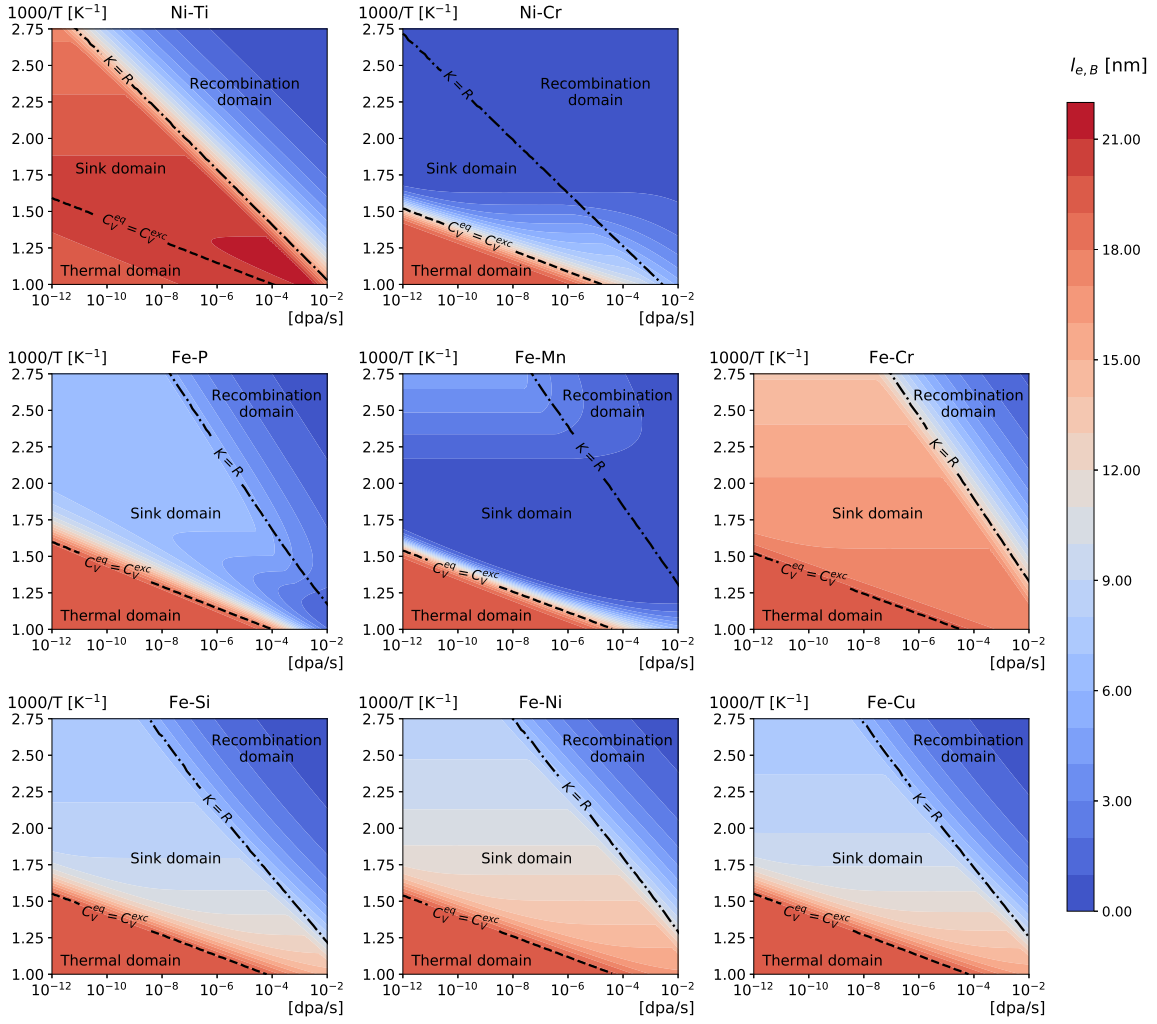


Figure 3.16: The effective width of RIS profiles of solute atoms in function of dose rate (in dpa/s) and temperature (in K^{-1}) of various dilute binary Ni- and Fe-based alloys. The nominal solute composition \bar{C}_B is set to 1.0 at.%. The distance between planar sinks h is set to 126 nm, leading to a sink strength $k^2 = 5 \times 10^{14} \text{ m}^{-2}$.

3.5.2.4 Solute segregation amount in Ni- and Fe-based alloys

We calculate the solute segregation amount S_B at different temperatures T , dose rates ϕ , and sink strengths k^2 in the various Ni- and Fe-based alloys. S_B of Ni-Cr, Fe-P, and Fe-Mn alloys are deduced from Eq. (3.31). S_B of Ni-Ti, Fe-Cr, Fe-Si, Fe-Ni, and Fe-Cu alloys are obtained from Eq. (3.40).

First, we investigate the effect of temperature T and dose rate ϕ on the segregation amount of solute atoms, with a fixed sink strength k^2 set to 10^{14} m^{-2} . The corresponding ϕ - T maps are presented in Fig. 3.17. As expected, we observe that S_B is great in the sink domain, and relatively small in the recombination and thermal domains.

The variations of S_B with T and ϕ in the various alloys are similar. As expected, S_B is

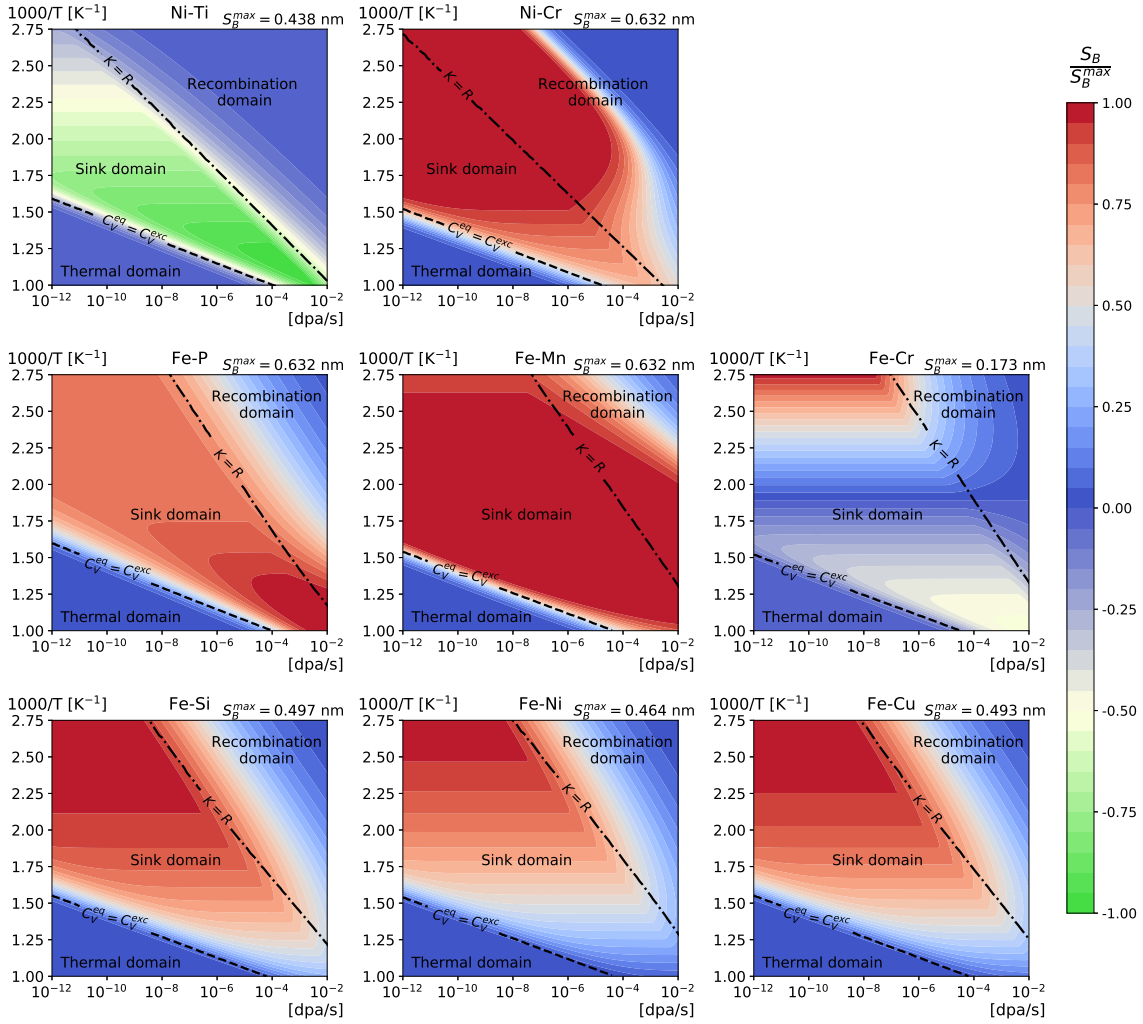


Figure 3.17: Solute atom segregation amount S_B normalized by its maximum over all considered irradiation conditions S_B^{\max} in function of dose rate (in dpa/s) and temperature (in K) of different Ni- and Fe-based alloys. The nominal solute composition \bar{C}_B is set to 1 at.%, and the sink strength k^2 is set to $5 \times 10^{14} \text{ m}^{-2}$.

ϕ -independent in the sink domain (cf. Eq. (3.47)), and decreases with the dose rate in the recombination domain (cf. Eq. (3.48)).

The variations of S_B with T and ϕ strongly depend on the chemical nature of the solute atoms because α_1 and α_2 are alloy-specific (see Fig. 3.12 and Fig. 3.13). In addition, the maximum of S_B occurs at different irradiation conditions. In Ni-Cr, Fe-Si, Fe-Ni, and Fe-Cu alloys, the highest solute enrichment tendency is at low temperatures (about 400 K) and dose rates (about 10^{-12} dpa/s), whereas the highest enrichment tendency in Fe-P is at high temperatures (> 1000 K) and dose rates (around 10^{-3} dpa/s). As for the solute atom Mn, the peak of RIS occurs at intermediate temperatures (about 650 K) and dose rates (from 10^{-10} to 10^{-6} dpa/s). Concerning the segregation of Cr in Fe, the peak of positive RIS occurs at low temperatures (about 300 K) and dose rates (about 10^{-11} dpa/s), whereas the peak of the negative RIS occurs at high temperatures (> 800 K) and dose rates ($> 10^{-6}$ dpa/s). Similarly, in the Ni-Ti alloy,

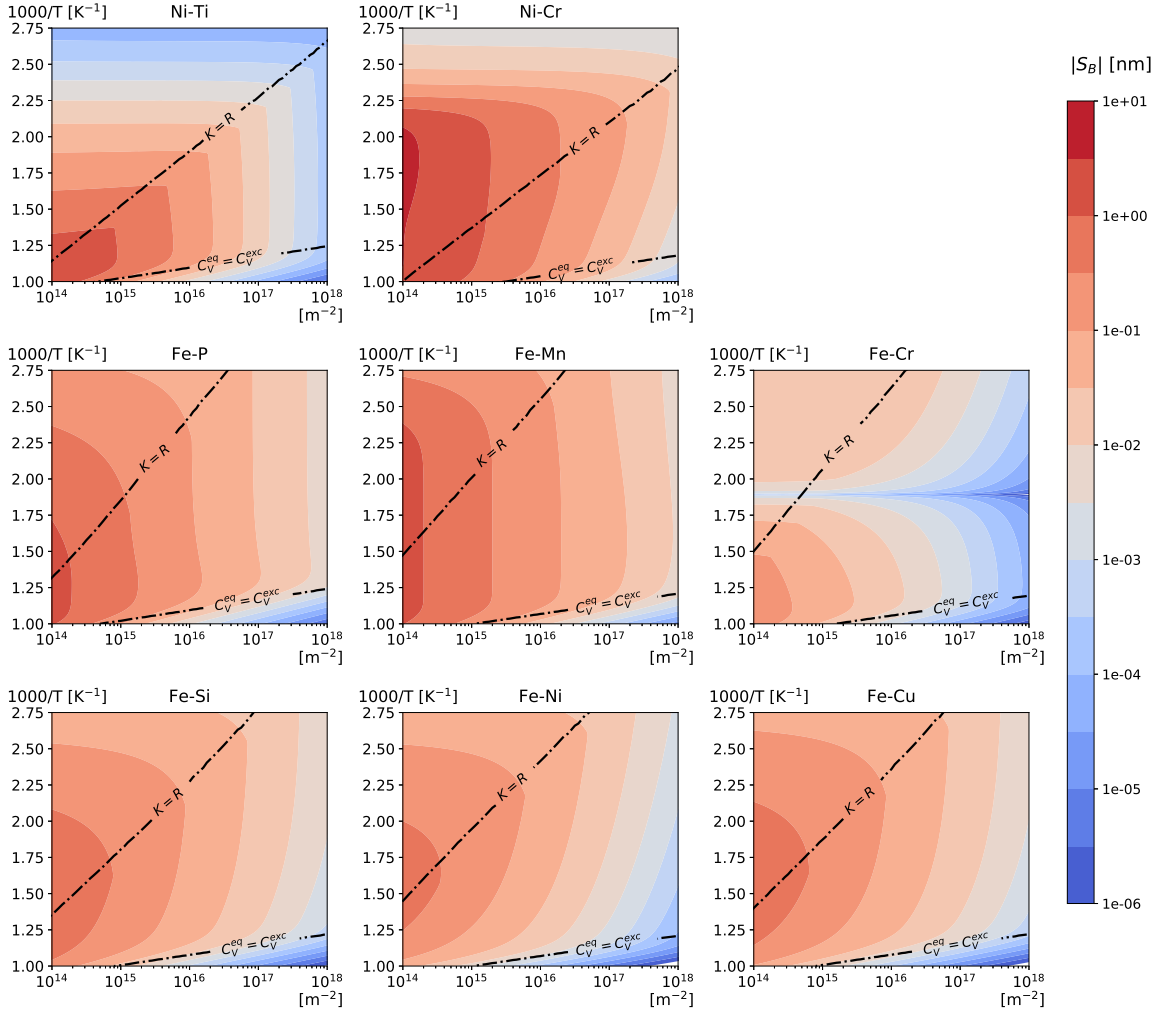


Figure 3.18: Solute atom segregation amount S_B in function of sink strength (in m^{-2}) and temperature (in K) of different Ni- and Fe-based alloys. The nominal solute composition \bar{C}_B is set to 1 at.% and the dose rate $\phi = 2 \times 10^{-4}$ dpa/s.

the peak of the negative RIS occurs at high temperatures and dose rates.

In Fig. 3.18, we represent the T - k^2 maps of S_B at fixed irradiation flux $\phi = 2 \times 10^{-4}$ dpa/s. With different models to calculate S_B , the evolution of S_B with k^2 is similar in different alloys. In the recombination domain ($K < R$), S_B is shown to be k^2 -independent (cf. Eq. (3.48)). In the domain of PD elimination ($K > R$), S_B decreases with k^2 , as shown by Eq. (3.47).

Further, we take Fe-Cr alloy as an example to investigate the effect of sink strength on the maximum of the solute segregation amount and on the size of the kinetic domains. Fig. 3.19 shows the Cr solute segregation maps with different sink strength k^2 . Note that the sink domain is enlarged with k^2 . Therefore, the higher the sink strength, the bigger the RIS domain. However, the total amount of segregated solutes summed up over the sink population is constant. As a result, the maximum of the Cr segregation amount ($S_{\text{Cr}}^{\text{max}}$) decreases with k^2 , meaning that the Cr enrichment/depletion of a single sink is higher when the sink strength is smaller.

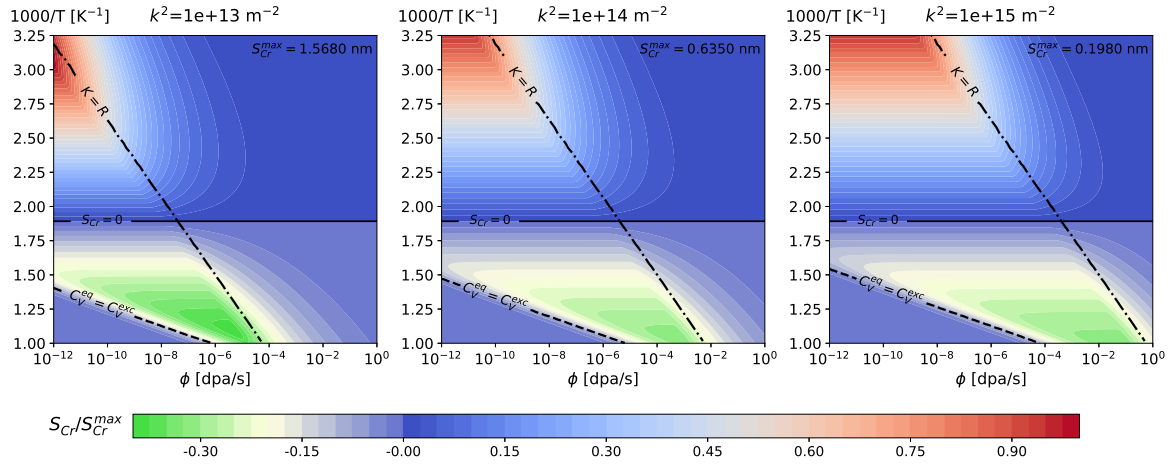


Figure 3.19: Cr segregation amount S_{Cr} in function of dose rate (in dpa/s) and temperature (in K) obtained with different sink strengths: 10^{13} m^{-2} , 10^{14} m^{-2} and 10^{15} m^{-2} . The results are factorized by the maximum segregation amount S_{Cr}^{max} . The nominal solute composition \bar{C}_B is set to 1 at. %.

Though not represented, we obtain the same trends for the other Ni- and Fe-based alloys.

3.5.2.5 FAR effects on the solute segregation

As stated in Section. 3.2.2.1, the FAR effect on the solute RIS should be significant at large k^2 because then, γ is close to or larger than 1. We take Ni-Ti and Fe-Ni alloys as examples to investigate the FAR effect on the RIS profile of solute atoms. In order to identify the FAR effect, we calculate and compare the solute concentration profiles and segregation amounts at different values of the FAR efficiency n_{FAR} (i.e., the number of FARs per dpa). Note that $n_{\text{FAR}} = 0$ indicates that FAR is ignored. The solute RIS profiles are plotted in Fig. 3.20 (a) and (b) with two different sink strengths and n_{FAR} equal to 0, 40, 100, and 400. When $k^2 = 10^{15} \text{ m}^{-2}$, the segregation profiles are almost insensitive to FAR, because γ is less than 0.01, and the FAR effect is negligible. However, when $k^2 = 5 \times 10^{16} \text{ m}^{-2}$, the RIS profiles strongly depend on the FAR efficiency n_{FAR} . In Ni-Ti alloy, the concentration of solute atoms at sink increases with n_{FAR} . Moreover, the amount of depleted Ti atoms decreases with n_{FAR} (Fig. 3.20 (c)). For $k^2 = 5 \times 10^{16} \text{ m}^{-2}$ and $n_{\text{FAR}} = 500$, S_{Ti} is only about a half of the one without FAR (i.e. $n_{\text{FAR}} = 0$). In Fe-Ni, solute atoms are enriched near sinks. The solute concentration at sink and the amount of enriched Ni atoms decrease with n_{FAR} (Fig. 3.20 (f)). Though not represented, we observe similar tendencies in Ni-Cr and the other Fe-based alloys. To conclude, RIS calculations ignoring the FAR mechanisms overestimates the RIS tendencies in the Ni- and Fe-based alloys.

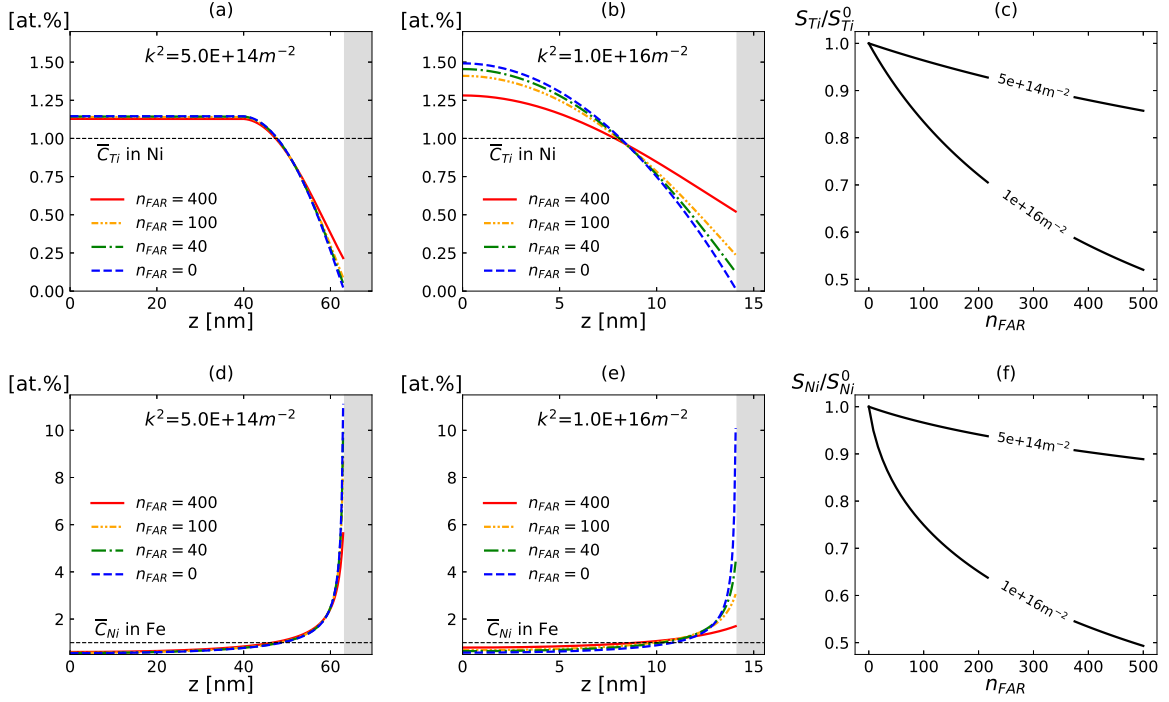


Figure 3.20: Solute concentration profile near an interface (indicated by the shaded) and the corresponding solute segregation amount. Figures (a) and (b) represent concentration profiles in Ni-Ti alloys with $k^2 = 10^{15} \text{ m}^{-2}$ and $k^2 = 5 \times 10^{16} \text{ m}^{-2}$, respectively. Figure (c) is the corresponding Ti segregation amount calculated with different FAR efficiencies. Figures (d) and (e) represent concentration profiles in Fe-Ni alloys with $k^2 = 10^{15} \text{ m}^{-2}$ and $k^2 = 5 \times 10^{16} \text{ m}^{-2}$, respectively. Figure (f) is the corresponding Ti segregation amount calculated with different FAR efficiencies. S_B^0 is the segregation amount obtained with $n_{\text{FAR}} = 0$. The nominal solute composition \bar{C}_B is set to 1 at.%. The temperature T and the dose rate ϕ are respectively set to 600 K and 10^{-5} dpa/s .

3.5.3 Dose rate compensation by a temperature shift

One objective of this work is to provide quantitative temperature-shift criteria for ion-irradiation experiments aimed at emulating RIS generated by neutron irradiation. We ascribe the difference of structural evolution between neutron and ion irradiations to a difference of radiation flux. A change of temperature may compensate the effect of a change of the radiation flux on the vacancy profile or on the solute RIS. With this work, we can suggest temperature shifts that should be applied depending on the (evolving) microstructure and the RIS quantity that one wants to reproduce (S_V or S_B). Even though S_B and S_V are inter-dependent quantities (cf. Eq. (3.46)), the behavior of solute RIS is very different from that of PDs, mainly because solute RIS results from a balance between the solute flux triggered by a PD driving force and the backward solute flux triggered by a solute concentration gradient, whereas such backward flux does not occur for PDs. Another difficulty is that the behavior of both PDs and solutes depends not only on the radiation flux and temperature, but also on the evolving microstructure sink

Table 3.6: Definition of cases in which quantitative criteria of temperature shift ΔT can be proposed.

Cases	Assumptions	Criteria for S_V	Criteria for S_B
(i)	k^2 independent of ϕ and T	Invariant ϕ/D_V	<ul style="list-style-type: none"> • $K \ll R^1$: invariant $\frac{I_{\alpha_1}-1}{I_{\alpha_1}-1+\frac{h}{2}\left(\frac{\Omega}{\pi r_{\text{rec}}}\right)^{-1/4}\left(\frac{\phi}{D_V}\right)^{1/4}}$ • $K \gg R^1$: no temperature shift ($\Delta T = 0$) • $K \simeq R$: use of ϕ-T maps (e.g., Tab. 3.7)
(ii)	$K \ll R^1$	Invariant ϕ/D_V	Invariant $\frac{I_{\alpha_1}-1}{I_{\alpha_1}-1+\frac{h}{2}\left(\frac{\Omega}{\pi r_{\text{rec}}}\right)^{-1/4}\left(\frac{\phi}{D_V}\right)^{1/4}}$
(iii)	$K \gg R^1$	Invariant $\frac{1}{(k^2)^{3/2}}\left(\frac{\phi}{D_V}\right)$	<ul style="list-style-type: none"> • If ΔT is sufficiently small such that the variation of α_1 is negligible (e.g., within about ± 50 K from Fig. 3.12): invariant k^2 • Else: invariant $\frac{h}{2}\frac{I_{\alpha_1}-1}{I_{\alpha_1}-1+\frac{h}{2}\sqrt{\frac{k^2}{2}}}$
(iv)	$k^2(\phi, T)$ is given	We use our models to calculate S_V and S_B with k^2 varying with ϕ and T . We search for at which temperature (T_2), the ion irradiation at $\phi = \phi_2$ reproduces the same S_V or S_B obtained from the neutron irradiation at $T = T_1$ and $\phi = \phi_1$ (e.g., Fig. 3.21).	

strength. The latter is a complex function of temperature, radiation dose rate, and radiation dose (i.e., dose rate \times time), as shown in Fig. 3.21. Besides, the evolution of S_V and S_B as a function of sink strength, radiation flux and temperature differs from one kinetic domain to another, and the extent of each kinetic domain in terms of temperature and radiation flux depends itself on the sink strength which evolves over time. Nevertheless, there are a few limiting cases (defined in Tab. 3.6) which provide some insights in this rather complex interplay and from which some quantitative temperature-shift criteria can be proposed.

In case (i), the sink strength is assumed to be constant during irradiation. This is a good approximation for alloys with initially high dislocation density, for instance, cold-worked materials. At fixed sink strength, the amount of vacancy RIS, S_V , increases linearly with the ratio ϕ/D_V in the sink domain, and with $(\phi/D_V)^{1/4}$ in the recombination domain. On the other hand, S_B is independent of ϕ in the sink domain, whereas, in the recombination domain, it decreases with ϕ/D_V . Thus, if the vacancy RIS is to be conserved from a neutron to a higher flux ion irradiation, we prescribe a shift of temperature such as to keep the ratio ϕ/D_V constant. Concerning the RIS of PDs, we recover the Mansur's invariant relation, which has been established in the recombination domain for swelling phenomena [184]. However, for the solute RIS in the sink domain, there is no need for a change of temperature to keep the amount of solute RIS constant. In the recombination domain, a temperature shift conserving the ratio

ϕ/D_V does not necessarily ensure a correct emulation of a neutron radiation-induced solute RIS. Therefore, one temperature shift only enables to reproduce one RIS quantity. Indeed, the solute-PDs flux couplings leading to RIS are strongly non-linear and alloy specific functions of temperature. Nevertheless, we may use our temperature-flux maps to obtain an estimation of the temperature shift leading to the same amount of solute RIS. According to the maps of Fig. 3.10 and Fig. 3.17, for $k^2 = 5 \times 10^{14} \text{ m}^{-2}$, an emulation of neutron irradiation with a flux of 10^{-7} dpa/s at $T = 360 \text{ K}$ (i.e., $1000/T = 2.75$) by means of an ion irradiation of 10^{-5} dpa/s would require a shift of temperature $\Delta T \simeq +90 \text{ K}$ for the PDs, and alloy dependent ΔT for solute RIS as listed in Table 3.7. Note that no temperature shift is proposed for Fe-Cr alloy because S_{Cr} at $\phi = 10^{-5} \text{ dpa/s}$, at any temperature, is systematically smaller than that at $\phi = 10^{-7} \text{ dpa/s}$ and $T = 360 \text{ K}$.

Table 3.7: Temperature shift required to simulate the solute RIS from the neutron irradiation with a flux of 10^{-7} dpa/s at 400 K by means of an ion irradiation of 10^{-5} dpa/s . The sink strength is assumed to be constant during irradiation (case (i)).

	Fe-P	Fe-Mn	Fe-Cr	Fe-Si	Fe-Ni	Fe-Cu
ΔT [K]	+95	+40	—	+90	+105	+100

In case (ii), both neutron and ion irradiations take place in the recombination domain, our results suggest that S_V and S_B are nearly independent of k^2 (cf. Figs. 3.11 and 3.18). The temperature-shift criterion for S_V is the same as the one in case (i). To estimate the temperature shift for S_B , we use the ϕ - T maps of S_B in the same way as presented in case (i).

In case (iii), both neutron and ion irradiations take place in the sink domain. We assume that the temperature shift is sufficiently small such that the variation of α_1 can be neglected. Thus, S_B only depends on the microstructure (cf. Eq. (3.35)). We assume that the time for the establishment of PD and solute RIS is much shorter than the characteristic time of the evolving microstructure. In this case, the temperature-shift criterion for S_B is the one ensuring an invariant sink strength. Therefore, given the variations of k^2 with temperature and dose rate, the variations of S_B should have the same trends. This is consistent with the experimental observation in Ref. [23]. In this experiment, the authors attempted to emulate the microstructure of a cold-worked 316-stainless steel produced by a neutron irradiation at 320°C by a self-ion irradiation at higher temperatures. In such cold-worked material, the sink density was relatively high; thereby the irradiation must take place in the sink domain. Authors in this study observed that self-ion irradiation at 380°C produces dislocation loop size and density which matched well with those obtained with neutron irradiation. In the same study, they showed that the RIS behaviors from these two irradiation conditions coincided as well. Therefore, this experiment shows that a relatively small temperature shift ($+60^\circ\text{C}$ in this experiment) ensuring an invariant microstructure (i.e., sink strength) is able to reproduce as well the RIS behaviors for materials irradiated in the sink domain.

In case (iv), we assume that the evolution of the sink strength is not affected by the RIS of solutes. In this case, there are simulation methods and/or experimental studies yielding the evolution of the PDs microstructure with respect to the irradiation conditions and the radiation dose [104, 254]. Authors in Ref. [104] simulated the microstructural evolution of a

Fe-Cr alloy irradiated by neutrons (3.4×10^{-7} dpa/s) and ions (5.2×10^{-5} dpa/s) at similar temperatures using cluster dynamics and atomic kinetic Monte Carlo simulations. Relying on their results, we can predict the evolution of the RIS behaviors. Note that their results indicate that the PD clusters are the major sinks. Due to the lack of information on cluster densities, we estimate the average distance between sinks directly from the sink strength by Eq. (3.18). In Fig. 3.21, we plot k^2 (from Ref. [104]), S_V and S_B (from our calculation) as a function of the radiation dose. The evolution of k^2 indicates that, up to 0.01 dpa for neutron irradiation and 0.1 dpa for ion irradiation, the system is at the frontier between the recombination and sink domains. After these doses, the system is in the sink domain and the sink strengths of both neutron and ion irradiation conditions are close to each other. The calculated S_B in the two irradiation conditions are as well very similar after 0.1 dpa. This is because, in the sink domain, S_B depends only on α_1 and k^2 (as presented in case (iii)); since the temperatures are close in the two irradiation conditions, the calculated S_B is nearly the same whenever the sink strengths are very close to each other. Below 0.01 dpa, both S_V and S_B in the two irradiation conditions are different. Given the variation trends of the sink strength with the irradiation conditions, we propose a temperature-shift that would reproduce either the same S_V or the same S_B as in neutron irradiation from an ion irradiation experiment. As a qualitative approach, we assume that the sink strength k^2 is proportional to S_V . This approach should be reasonable because PD clusters are major sinks and their growth should be proportional to the PD segregation amount. Thus, by assuming that the ion irradiation is in the recombination domain, we set k^2 as a linear function of $(\phi/D_V)^{0.25}$. Hence, from the simulated $k^2(\phi)$ resulting from an ion irradiation [104], we can deduce the sink strength evolution at different temperatures. Relying on our model, we calculate the evolution of S_V and S_B from the ion irradiation at different temperatures. From these results, we find out at which temperature the evolution of S_V or S_B matches well with that obtained by neutron irradiation. By this approach, we obtain the temperature shifts of an ion irradiation (5.2×10^{-5} dpa/s) required to emulate the RIS behaviors from neutron irradiation (3.4×10^{-7} dpa/s) (cf. Fig. 3.21-(d)). For a dose below 0.01 dpa, the temperature shift (ΔT) required for an invariant S_V is about $+90^\circ\text{C}$ and the one for an invariant S_B is about $+110^\circ\text{C}$. After 0.01 dpa, ΔT for S_V increases up to $+200^\circ\text{C}$, whereas ΔT for S_B notably decreases.

Apart from the simulation methods, direct observations of the microstructure may inform on the sink strength evolution. However, a precise estimation of the latter is difficult because small PD nano-clusters forming under irradiation are not detectable by current microscopy techniques. Nevertheless, investigating the variation of the solute RIS profiles with radiation flux and radiation dose should give an insight on the sink strength, provided the time scale of RIS is smaller than that of the microstructure evolution, so that we may assume steady-state solute RIS. For instance, we have shown that the RIS amount of solute atoms is directly related to the bulk concentration of vacancies. Therefore, measuring the solute RIS provides a way to estimate the bulk concentration of vacancies—thereby the global sink strength of the microstructure—provided the diffusion properties of PDs are known.

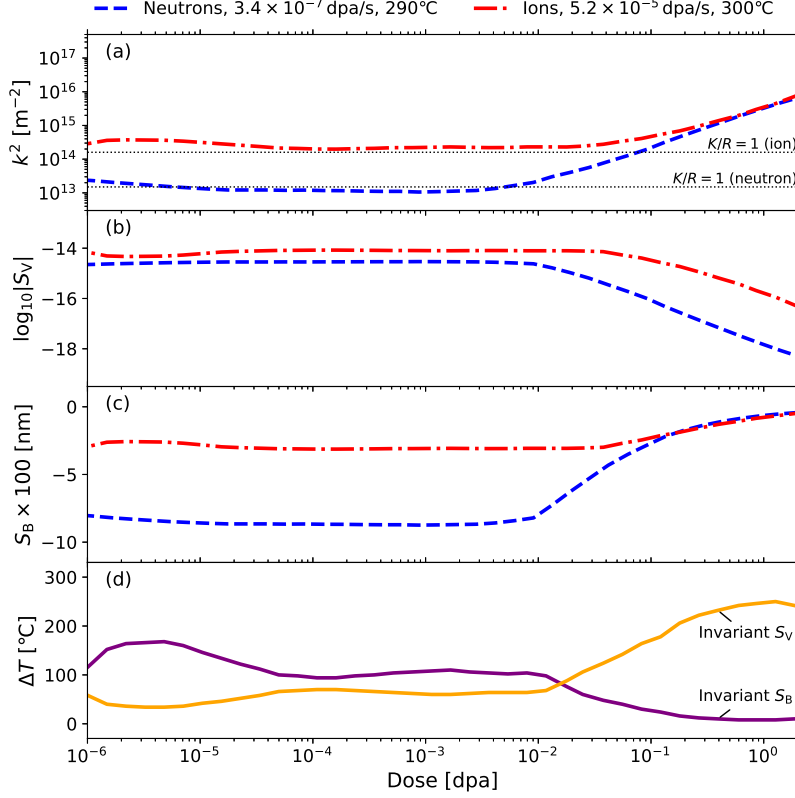


Figure 3.21: The evolution of (a) the sink strength k^2 , (b) the amount of vacancy RIS S_V , and (c) the amount of solute RIS S_B in the Fe-Cr alloy irradiated by neutrons and ions. The evolution of the temperature shift for ion irradiation that is required to emulate the neutron RIS is plotted in (d). The plots of k^2 are reproduced from the results in Ref. [104]. The dotted guiding lines obtained from $K/R = 1$ are plotted in (a) to help identifying the kinetic domain.

3.6 Comparison between experimental measurement and analytical results

3.6.1 Ni-0.4Ti alloy

Table 3.8: Estimated average sink strength of the major defects in irradiated Ni-0.4 at.% Ti.

Defect	Dislocation loops	Dislocation lines	Cavities	Total
Average sink strength [m^{-2}]	7.23×10^{13}	4.86×10^{13}	2.29×10^{13}	1.44×10^{14}

Ma et al. [255] measured the RIS profiles of Ti in Ni-0.4 at.% Ti near a dislocation loop by atom probe tomography (APT). This alloy was irradiated at 450°C with a dose rate of around 6.5×10^{-5} dpa/s (estimated by SRIM). According to a full characterization of the microstructure by transmission electron microscopy (TEM), the three defects—cavities, dislocation lines, and loops—are the major defect sinks in this alloy. From the measured size distribution and density

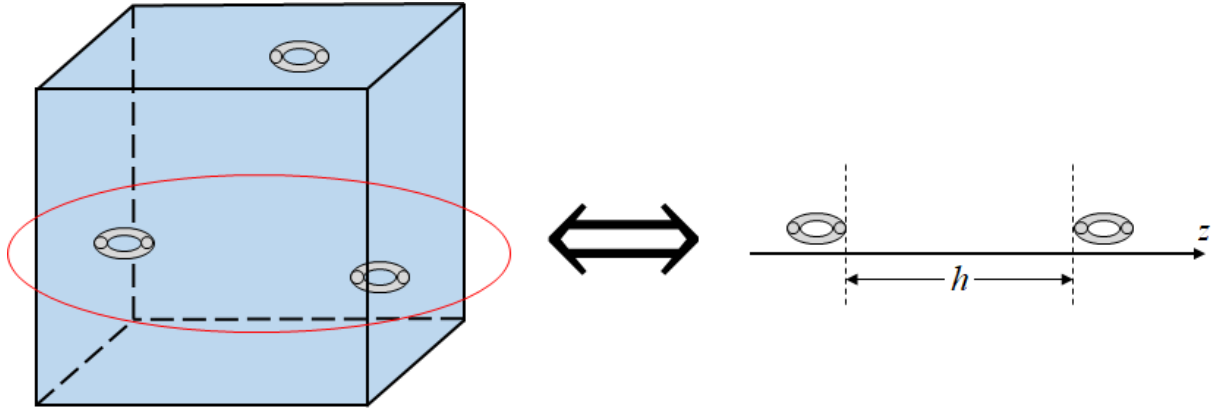


Figure 3.22: Uni-dimensional approximation of dislocation loop geometry.

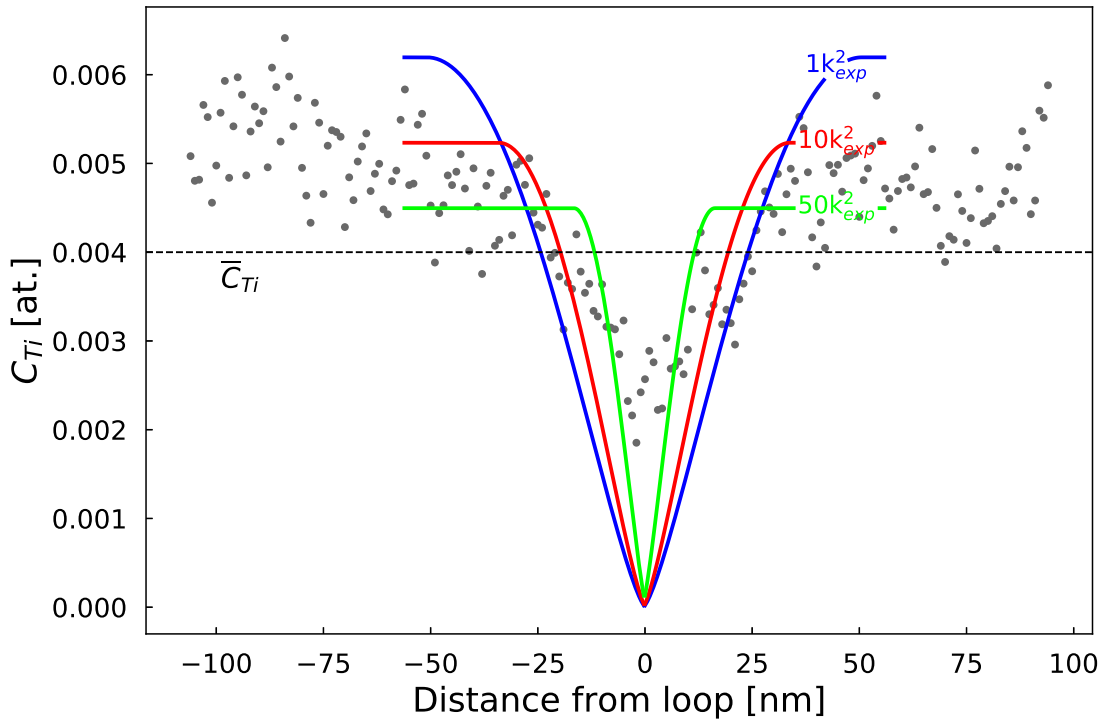


Figure 3.23: RIS profiles of Ti in Ni-0.4at.% Ti. Solid lines are analytical results given by Eq. (3.40). Solid dots are experimental data measured by Atom Probe Tomography.

of defects, we estimate the sink strengths of the three defects by relying on the analytical models presented in Section 1.2.2.2. The obtained values are given in Tab. 3.8. As presented in this table, the dislocation loops have the most significant contribution to the total sink strength, followed by dislocation lines and cavities. However, they are all of the same order of magnitude. Thus their contributions should be all considered into the calculation of the RIS profile. Note that our estimation of the total sink strength may be an underestimated value because contributions of the small PD clusters are ignored due to the resolution limit of the microscope.

The investigation of RIS near a dislocation loop requires the solution of the diffusion equation in 3 dimensions (see Section 1.2.2.2). As the distance between loops is much larger than the loop size, we transform pairs of dislocation loops into parallel planar sinks (Fig. 3.22). This way, we approximate the 3-dimension RIS problem by our uni-dimensional RIS analytical model of Section 3.2. The average spacing \bar{h} between two loops is deduced from the average loop density $\bar{\rho}_L$:

$$\bar{h} = \left(\frac{6}{\pi \bar{\rho}_L} \right)^{\frac{1}{3}}. \quad (3.51)$$

In Fig. 3.23, we compare the resulting RIS profiles from Eq. (3.40) with the experimental one.

Table 3.9: Simulated and measured bulk solute concentration in irradiated Ni-0.4 at.% Ti.

Case	Experiment	$k^2 = k_{\text{exp}}^2$	$k^2 = 10 k_{\text{exp}}^2$	$k^2 = 50 k_{\text{exp}}^2$
Bulk solute concentration [at.%]	0.49	0.61	0.51	0.44

Calculations are done with three different values of the sink strength: k_{exp}^2 , $10k_{\text{exp}}^2$, and $50k_{\text{exp}}^2$, where k_{exp}^2 is the total sink strength estimated from the microstructural data (in Tab. 3.8). The predicted width and bulk solute concentration of the segregation domain are in satisfying agreement with the experimental profile. The simulated and measured bulk solute concentrations are presented in Tab. 3.9. The increase of the bulk solute concentration resulting from the solute depletion at sinks is very sensitive to the sink strength. The analytical profile with $k^2 = 10k_{\text{exp}}^2$ is the closest one to the experimental one. Note that there is significant difference between the predicted and measured Ti concentration at the dislocation loop (distance = 0). The latter is certainly due to the resolution limits of the experimental technique, and to the neglect of the equilibrium segregation tendency in the present RIS model. To conclude, our simulations predict the right sign of Ti RIS and the simulated bulk solute concentrations are within 20 % of relative error. Moreover, we show how measuring the non-equilibrium bulk solute concentration is an efficient way to estimate the effective sink strength of a microstructure.

3.6.2 Fe-3.3Ni alloy

Belkacemi et al. measured [256] the RIS profiles of Ni in Fe-3.3 at.% Ni near a dislocation loop by atom probe tomography (APT). This alloy is irradiated at 400°C at two different irradiation fluxes: 8.7×10^{10} and 8.6×10^{11} ions · cm⁻² · s⁻¹. A full characterization of the microstructure by TEM indicates that the dislocation loops are the major PD sinks. The obtained average size and density of the loops in the two different samples respectively irradiated at 4.9×10^{-4} and 7.5×10^{-6} dpa/s (estimated by SRIM) are given in Tab. 3.10.

Table 3.10: Average loop radius and density in Fe-3.3 at.% Ni samples respectively irradiated at low (7.5×10^{-6} dpa/s) and high flux (4.9×10^{-4} dpa/s).

Conditions	Low flux	High flux
Average loop radius [nm]	19	1.4
Average loop density [loops/m ³]	5.1×10^{20}	2.6×10^{22}

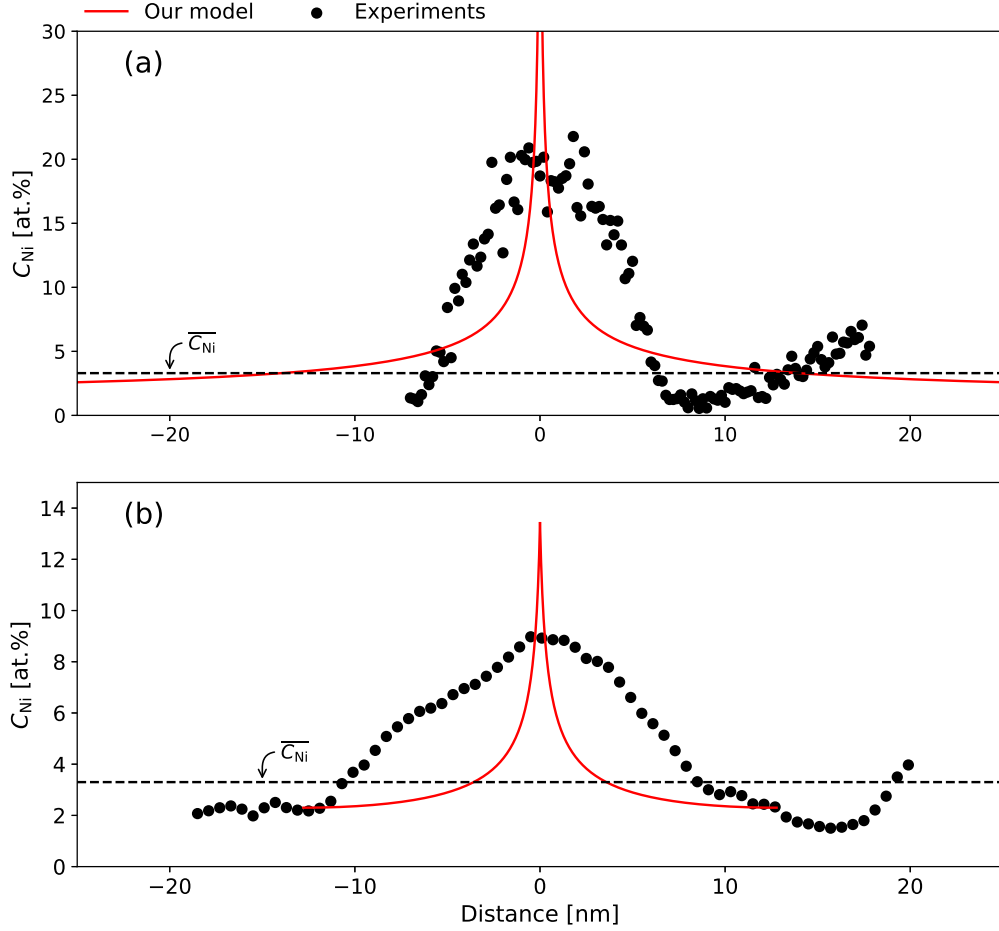


Figure 3.24: RIS profiles of Ni in Fe-3.3 at.% Ni at (a) low flux and (b) high flux. Solid lines are analytical results given by Eq. (3.40). Solid dots are experimental data measured by Atom Probe Tomography.

We use the same uni-dimensional approach of the dislocation loop geometry (Fig. 3.22) to calculate the solute RIS profile. From the average microstructure (listed in Tab. 3.10), we deduce an average spacing \bar{h} between two loops (Eq. (3.51)). From this average spacing, we calculate the steady-state RIS profile in Fe-Ni. In Fig. 3.24, we compare the obtained profiles with the experimental ones at low and high flux. The simulated profiles are narrower than the experimental ones. Moreover, the predicted solute concentration at the loop is higher than the experimental one. However, at low flux, the integrated segregation amount ($S_{\text{Ni}}^{\text{sim}}$) is in good agreement with the measured one ($S_{\text{Ni}}^{\text{exp}}$): $S_{\text{Ni}}^{\text{sim}} = 140 \text{ nm} \cdot \text{at.}\%$ and $S_{\text{Ni}}^{\text{exp}} = 159 \text{ nm} \cdot \text{at.}\%$. At high flux, $S_{\text{Ni}}^{\text{sim}} (= 25 \text{ nm} \cdot \text{at.}\%)$ is about one third of $S_{\text{Ni}}^{\text{exp}} (= 81 \text{ nm} \cdot \text{at.}\%)$. Note that, at low flux, the radius of the investigated loop, where the RIS profile is measured, is almost equal to the average one; while, at high flux, the radius of the investigated loop is about 10 times larger than the average one. We expect the RIS amount to increase with the loop size, because a larger loop should be associated with a larger depleted zone, thereby a larger dislocation spacing h . Besides, RIS increases with h (Eq. (3.40)). Therefore, the measured RIS amount of the investigated loop at high flux could be much higher than the average one.

In order to account for the dispersion of the solute RIS amounts, we apply the Voronoi

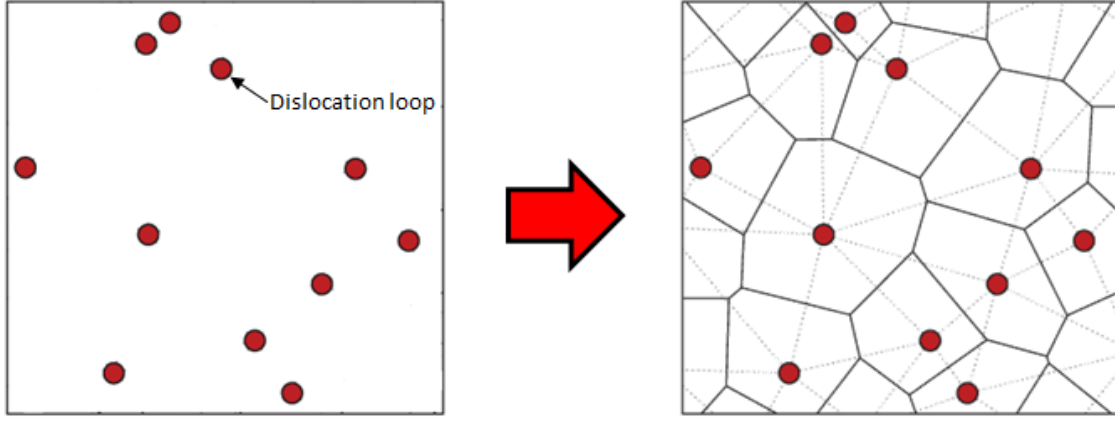


Figure 3.25: Schematic of a two-dimensional Voronoi decomposition.

decomposition method [257] to divide the space into different volumes (see Fig. 3.25). We assume that the dislocation loops are randomly distributed in space. We associate to each dislocation loop an isotropic Voronoi volume. In this case, the probability distribution of the Voronoi volume follows a Poisson-Voronoi distribution [257, 258]:

$$p(v) = \frac{v^{\gamma-1}}{\beta\gamma\Gamma(\gamma)} \exp\left(-\frac{v}{\beta}\right), \quad (3.52)$$

with

$$v = \frac{V_v}{\bar{V}_v}, \quad (3.53)$$

where \bar{V}_v is the average Voronoi volume, Γ is the gamma function, and β and γ are two parameters. Lazar et al. [257] have presented distributions of many topological features of Poisson-Voronoi structures based on a data set of a combined total of 250 000 000 cells. From this data set, they have determined the β and γ parameters: $\beta = 0.1790$ and $\gamma = 1/\beta = 5.586$. The same values have been obtained from object kinetic Monte Carlo simulations [259]. We deduce the average Voronoi volume from the average loop density, $\bar{\rho}_L$: $\bar{V}_v = 1/\bar{\rho}_L$. The mean value and the standard deviation of this distribution are respectively $\bar{v} = 1$ and $\sigma = \sqrt{\beta} = 0.42$. We rely on the Voronoi volume (i.e., the volume of a Voronoi tessellation), V_v , to estimate the local spacing between two neighbouring loops (h):

$$h = \left(\frac{6V_v}{\pi}\right)^{\frac{1}{3}}. \quad (3.54)$$

We expect that the volumes of about 95% of the dislocation loops are in the interval $[\bar{V}_v(1 - 2\sigma), \bar{V}_v(1 + 2\sigma)]$. From the limits of this interval, we compute the interval of Ni RIS amount that could be extracted from the dislocation loop population. We estimate that the solute RIS amount ranges from 10 to 52 nm · at.%. Although the experimental value (81 nm · at.%) is not in this interval, our model predict that a large dislocation loop associated with an exceptionally large Voronoi volume should lead to a RIS amount above the interval limit (52 nm · at.%). To get a Ni RIS amount $S_{\text{Ni}}^{\text{sim}} = 81 \text{ nm} \cdot \text{at.}\%$, the corresponding Voronoi volume should be about 6 times larger than the average one ($h = 76 \text{ nm}$), i.e., about $+12\sigma$ from the mean value.

3.7 Summary and concluding remarks

In this chapter, the cluster version of the self-consistent mean field theory is applied to calculate the transport coefficients of dilute Ni- and Fe-based alloys under irradiation. In addition to the recently published results [41, 181], we include the contribution of FAR to transport coefficients. From the transport coefficients, we compute the flux coupling coefficients, the solute and vacancy diffusion coefficients, and the RIS factors with respect to temperature, radiation flux, and PD sink strength. We highlight the specificity of each alloy as well as the effect of FAR on these parameters.

We provide an improved PD-RIS model yielding the concentration profile of vacancies in the vicinity of sinks. The profile is divided into two regions: a constant vacancy concentration region far from the sinks where PD production, recombination, and elimination at sinks occur, and a second region near the PD sinks where recombination is neglected because PD concentrations are lower. This approximation leads to first-order differential equations that can be solved analytically. We rely on a mean-field rate theory to calculate the uniform bulk concentration of vacancies in the first regime, which is set as the boundary condition of the steady-state PD profile in the second regime.

From the RIS factor relating the solute concentration gradient to the vacancy concentration gradient, we deduce an analytical expression of the steady-state solute RIS profile. This analytical RIS model includes the complete PD reactions, solute-PD interactions, and FAR mechanisms.

The analytical formalism developed in this paper, allows a systematic and quantitative study of the diffusion properties and RIS profiles of vacancies and solute atoms in the investigated iron alloys. The most relevant results are summarized as follows.

- The consideration of the complete PD reactions enables a consistent investigation of RIS behaviors in all PD kinetic domains (recombination/sink/thermal). We show that the RIS kinetic domains are directly related to the PD kinetic domains, i.e. to the variation of PD concentration in the bulk. RIS profiles of PDs do not vary much with the chemical nature of the solute atom, whereas solute RIS profiles are very alloy-specific. In general, the RIS of PDs and solutes is favored in the sink domain because the rate of PD elimination at sinks is significant. In the recombination domain, even if the PD RIS amount is relatively small, the solute RIS amount can be high in certain alloys, for instance, in Fe-Mn because its RIS factor α_1 is relatively large.
- The comparison between our results and a previous study [30] highlights the importance of accounting for recombination reactions in the RIS model. Models that would neglect these reactions would overestimate the vacancy concentration along the RIS profile, especially at low temperatures and sink strengths (i.e. in the recombination domain).
- Parametric T - ϕ - k^2 studies show that the effect of FAR on the solute RIS is significant. At high sink strength, FAR leads to a sharp decrease of solute RIS. Moreover, our results show that, among the investigated alloys, the effect of FAR is the most important in Ni-Ti, Ni-Cr, Fe-Ni and Fe-Cr systems.

- $T-\phi-k^2$ maps of the RIS amount of PDs and solute atoms can be used as a tool to provide quantitative temperature shift criteria to compensate for high irradiation flux. We emphasize that these criteria are alloy specific and kinetic domain specific. Moreover, in the case where we may ignore the variation of sink strength with temperature and dose rate, for instance in alloys with high sink density, we can deduce explicit criteria from the analytical expressions of S_V and S_B . Otherwise, in most cases, analytical criteria require an explicit relationship between the sink strength, temperature, and dose rate.
- A good agreement between the analytical and experimental results on the solute concentration profile and the RIS amount is achieved in Ni-0.4%Ti and Fe-3.3%Ni alloys.

Chapter 4

Effect of strains on the point-defect concentration and solute RIS in pure Fe and Fe-based alloys

Contents

4.1	Introduction	130
4.2	Diffusion and elasticity	130
4.2.1	Linear elasticity	131
4.2.2	Thermodynamics of diffusion including elasticity	132
4.2.3	Elastodiffusion	134
4.3	Elastodiffusion in Fe	135
4.3.1	Elastic properties of iron	135
4.3.2	Elastic properties of point defects	135
4.3.3	DFT-based elastodiffusion in Fe	137
4.3.4	Interactions of point defects with an elastic strain in Fe	140
4.4	Elastodiffusion in Fe-based alloys	141
4.4.1	Elastic dipoles of solute atoms and point defects	141
4.4.2	Elastodiffusion properties in Fe-based alloys	142
4.5	Sink strength and bias factors of an edge-dislocation	145
4.5.1	Simulation setup: coordinate system and boundary conditions	145
4.5.2	Sink properties: stress and strain field of an edge dislocation	146
4.5.3	Pure Fe	147
4.5.3.1	Assessment of the numerical approach	147
4.5.3.2	Effect of the elastic anisotropy of matrix and the PDs	148
4.5.3.3	Effect of the elastodiffusion	149
4.5.3.4	Effect of temperature	152

4.5.4	Fe-based alloys	152
4.5.4.1	Effect of solute atoms	152
4.5.4.2	Effect of temperature	154
4.5.4.3	Effect of solute concentration	155
4.6	Radiation-induced segregation at an edge dislocation in Fe-based alloys	155
4.6.1	Equilibrium distribution of solute atoms	155
4.6.2	Steady-state distribution of solute atoms under irradiation	156
4.7	Summary	160

4.1 Introduction

As shown in Section 3, a quantitative modeling of RIS requires the modelling of the PD kinetics including its interaction with the microstructure, and the kinetic couplings between fluxes of PDs and atomic fluxes. Perturbations of the crystal structure generated by a surface or a large-angle grain-boundary are usually short-ranged. They do not go further than a few atomic planes. Whereas lattice defects such as voids and dislocations may generate long-range stress-strain fields in the material [260]. A strain field modifies the formation and migration energies of PDs [260], and the solute-PD interactions. These modifications lead to sink bias, i.e., preferential absorption of SIAs or vacancies. Note that the dislocation bias for SIAs is the primary mechanism for swelling [117, 261]. Dislocations produce extra lattice sites by a climbing mechanism, leading to the macroscopic swelling of the irradiated material [29, 260]. Another by-product of the preferential absorption of SIA by dislocations is the formation of voids so that the overall elimination rate of PDs obey a matter balance [117]. These phenomena should should interplay with RIS. In order to investigate RIS at extended defects generating large strain fields, it is necessary to correctly describe the stress-strain field, and their effect on PD and solute diffusion.

In this chapter, we briefly present the concepts of linear elasticity, then we present the elastodiffusion properties of vacancy and self-interstitial in Fe and Fe-based alloys. In the last part, we investigate the elastic interactions between PDs and an edge dislocation, and study their effect on the dislocation sink strength and solute RIS in Fe.

4.2 Diffusion and elasticity

Within the framework of linear elasticity, we model the effect of a strain-stress field on the PD diffusion through an elastic dipole formulation. We start this section with a short presentation of the theories of linear elasticity and elastodiffusion.

4.2.1 Linear elasticity

The stress field, $\underline{\sigma}(\mathbf{r})$, and the strain field, $\underline{\epsilon}(\mathbf{r})$, are second-rank tensors depending on position \mathbf{r} in the material [262]. In general, they are inhomogeneous tensors [262]. Both of them are symmetric [262], i.e., $\underline{\sigma}_{ij} = \underline{\sigma}_{ji}$ and $\underline{\epsilon}_{ij} = \underline{\epsilon}_{ji}$ for $i \neq j$. Therefore, there are six independent elements in these two tensors.

The crystal shape changes under applied stress. Provided the stress is below the elastic limit, the strain in response to this stress is recoverable. At equilibrium, the amount of strain is proportional to the applied stress, as given by the so-called Hooke's law. The general form of this law is written as

$$\underline{\epsilon}_{ij} = \underline{S}_{ijkl} \underline{\sigma}_{kl}, \quad (4.1)$$

or alternatively as

$$\underline{\sigma}_{ij} = \underline{C}_{ijkl} \underline{\epsilon}_{kl}, \quad (4.2)$$

where the summation over repeated indices is implicit (Einstein convention). \underline{S}_{ijkl} and \underline{C}_{ijkl} are respectively the constants of compliance and stiffness. \underline{S} and \underline{C} are fourth-rank tensors with 81 components. They are related by:

$$\underline{S} = \underline{C}^{-1}. \quad (4.3)$$

Since $\underline{\sigma}$ and $\underline{\epsilon}$ are symmetric, only 36 of the 81 components of \underline{S}_{ijkl} and \underline{C}_{ijkl} are independent. The symmetry properties of \underline{S}_{ijkl} and \underline{C}_{ijkl} associated with the first two and the last two suffixes make it possible to use the Voigt notation [262, 263]. The first two and last two suffixes are abbreviated into a single one running from 1 to 6, according to the scheme:

Tensor notation	11	22	33	23, 32	13, 31	12, 21
Voigt notation	1	2	3	4	5	6

The symmetry of the crystal reduces further the number of independent coefficients of \underline{S}_{ij} and \underline{C}_{ij} . In a cubic crystal such as the fcc and bcc structures, we have

$$\begin{aligned} \underline{S}_{11} = \underline{S}_{22} = \underline{S}_{33}, \quad \underline{S}_{12} = \underline{S}_{13} = \underline{S}_{23}, \quad \underline{S}_{44} = \underline{S}_{55} = \underline{S}_{66}, \\ \underline{C}_{11} = \underline{C}_{22} = \underline{C}_{33}, \quad \underline{C}_{12} = \underline{C}_{13} = \underline{C}_{23}, \quad \underline{C}_{44} = \underline{C}_{55} = \underline{C}_{66}, \end{aligned}$$

and all the other components are zero. Therefore, only three of these coefficients remain independent, e.g., \underline{C}_{11} , \underline{C}_{12} , and \underline{C}_{44} for the compliance matrix, and \underline{S}_{11} , \underline{S}_{12} , and \underline{S}_{44} for the stiffness matrix. Moreover, in a perfectly isotropic cubic crystal, these three coefficients are related by [262, 264, 265]:

$$\underline{S}_{44} = 2(\underline{S}_{11} - \underline{S}_{12}), \quad (4.4)$$

$$\underline{C}_{44} = (\underline{C}_{11} - \underline{C}_{12})/2. \quad (4.5)$$

Zener [266] proposes to measure the anisotropy by the ratio:

$$A_Z = \frac{2\underline{C}_{44}}{\underline{C}_{11} - \underline{C}_{12}}, \quad (4.6)$$

which is the so-called Zener ratio or Zener anisotropy index. Note that many cubic metals such as Fe (but W and Al) are markedly anisotropic in terms of their elastic behaviour [262, 264].

The elastic constants \underline{C}_{ij} can be measured by experiments [267–270] or computed by *ab initio* methods [271–273]. Though the experiments measure the adiabatic elastic constants, which are the second-order partial derivatives of the free energy with respect to the strain at constant entropy [264, 274], *ab initio* calculations give the isothermal elastic constants, which are second-order partial derivatives of the free energy as well but at constant temperature [264, 265, 274]. For most mechanical properties, the difference between the two classes of elastic constants are negligible, within few percents or less for most of the cases [264].

4.2.2 Thermodynamics of diffusion including elasticity

In this section, we express the PD and alloy thermodynamic driving forces under an applied strain $\underline{\epsilon}$. The isothermal driving forces of diffusion under an applied stress-strain field are the gradients of PD and alloy chemical potentials (see Eq. (4.7)). These chemical potential locally depend on the stress-strain field.

$$\mu_d = k_B T \ln \left(\frac{C_d}{C_d^{\text{eq}}} \right), \quad (4.7)$$

where C_d is the atomic fraction of d in the system, and C_d^{eq} is the equilibrium concentration of d . The latter varies with external strains and local atomic fraction of solute atoms. From a LTE expansion formalism (Eq. (1.26)), for $C_B \gg C_d$, the PD equilibrium concentration writes

$$C_d^{\text{eq}} = C_d^{\text{eq},0} \exp \left(-\frac{E_d^{\text{el}}}{k_B T} \right) \left[1 + \frac{C_B (Z_{Bd}^{\text{el}} - Z_{Bd}^0)}{Z_d} \right], \quad (4.8)$$

where $C_d^{\text{eq},0}$ is the PD equilibrium concentration in unstrained pure A, Z_d is the monomer partition function, Z_{Bd}^{el} is the solute-PD pair partition functions including the elastic interactions, and Z_{Bd}^0 is the number of solute-PD pair configurations. E_d^{el} is the elastic contribution to the formation energy of PD under applied strain $\underline{\epsilon}^{\text{ext}}$. We write E_d^{el} as a sum of two energy terms (as in previous studies presented in Section 1.1.2):

$$E_d^{\text{el}} = - \left[\underline{P}_{ij}^d \underline{\epsilon}_{ij}^{\text{ext}} + s_d K \text{Tr}(\underline{\epsilon}^{\text{ext}}) \Omega \right], \quad (4.9)$$

where \underline{P}^d is the elastic dipole tensor of PD (d), $\underline{\epsilon}^{\text{ext}}$ is the external strain field, K is the bulk modulus, and s_d is the number of created lattice site,

$$s_d = \begin{cases} +1, & \text{for } d = \text{V}, \\ -1, & \text{for } d = \text{I}. \end{cases} \quad (4.10)$$

The first term in the right-hand side of Eq. (4.9), $-\underline{P}_{ij}^d \underline{\epsilon}_{ij}^{\text{ext}}$, describes the energy change due to the relaxation of the system in presence of PD [141]. In presence of PD sources and sinks, PDs are non-conservative species. Their creation or removal makes vary the number of lattice sites. For instance, an atom displaced from its original bulk lattice site to the surface or the core of a dislocation, creates both a vacancy at the original lattice site and an extra lattice

site at the structural defect. The second term, $s_d K \text{Tr}(\underline{\epsilon}^{\text{ext}})\Omega$, corresponds to the work of creating or removing a lattice site under an applied stress [29, 275]. Note that, in previous studies [126, 140, 185, 276], this work energy term was neglected, as if PDs were considered as conservative species, i.e. no lattice site was created or removed in the system. In our work, we are interested in PDs that diffuse and are eliminated at sinks. Therefore, we have to take into account the non-conservative character of PDs.

Note that, we may use the Hooke's laws to express the external stress in function of the external strain, and switch from a formation energy to a formation enthalpy.

We assume that, locally the strain/stress field is uniform. Hence, we may write E_α^{el} as a function of the local stress-strain field, and replace the external strain $\underline{\epsilon}^{\text{ext}}$ by a local strain, $\underline{\epsilon}$. Therefore, a gradient of the elastic strain yields a gradient of E_d^{el} , that modifies the PD driving force. From Eq. (4.7) and Eq. (4.8), we write the CPG of PDs as:

$$\frac{\nabla \mu_d}{k_B T} = \frac{\nabla C_d}{C_d} - \frac{(Z_{Bd} - Z_{Bd}^0) \nabla C_B}{Z_d - C_B(Z_{Bd} - Z_{Bd}^0)} - \frac{C_B \nabla Z_{Bd}}{Z_d - C_B(Z_{Bd} - Z_{Bd}^0)} + \frac{\nabla E_d^{\text{el}}}{k_B T}. \quad (4.11)$$

For an alloy A(B), we may write the alloy chemical potential, $\mu_{BA} = \mu_B - \mu_A$, in function of the concentration of monomer B (isolated solute atoms surrounded by A atoms), C_B^{mono} ,

$$\mu_{BA} = k_B T \ln C_B^{\text{mono}} + H_{s,B}, \quad (4.12)$$

where $H_{s,B}$ is the solution enthalpy of atom B in A:

$$H_{s,B} = H(NA + 1B) - H((N + 1)A), \quad (4.13)$$

where $H(NA + 1B)$ is the enthalpy of a system including N atoms A and one atom B. Note that, C_B^{mono} may depend on the solute and vacancy atomic fractions. $H_{s,B}$ depends on stress only. It is written as

$$H_{s,B} = H_{s,B}^0 + E_B^{\text{el}}, \quad (4.14)$$

where E_B^{el} is the elastic contribution to the solution enthalpy of solute B

$$E_B^{\text{el}} = -\underline{P}_{ij}^\alpha \epsilon_{ij}^{\text{ext}}, \quad (4.15)$$

Note that C_B^{mono} depends on the atomic fractions of PDs and solute atoms; and E_f^B depends on strain. We write the CPG of solute atoms as:

$$\frac{\nabla \mu_{BA}}{k_B T} = \frac{1}{C_B^{\text{mono}}} \frac{\partial C_B^{\text{mono}}}{\partial C_B} \nabla C_B + \frac{1}{C_B^{\text{mono}}} \frac{\partial C_B^{\text{mono}}}{\partial C_V} \nabla C_V + \frac{\nabla E_B^{\text{el}}}{k_B T}. \quad (4.16)$$

For $C_B \gg C_d$, $C_B^{\text{mono}} = C_B$, and Eq. (4.16) can be rewritten as

$$\frac{\nabla \mu_{BA}}{k_B T} = \frac{\nabla C_B}{C_B} + \frac{\nabla E_B^{\text{el}}}{k_B T}. \quad (4.17)$$

To conclude, a stress-strain field generates the extra term $\nabla E_\alpha^{\text{el}}$ in the CPGs of PDs and solute atoms. For PDs, this driving force includes an extra term related to the removing/creation of an atomic volume upon the formation of a PD. This term must be accounted for in the calculation of PD fluxes in strained system.

4.2.3 Elastodiffusion

Elastic interactions between PDs and extended defects modify the migration barriers of PDs. For a PD, initially located at \mathbf{r} , jumping in a direction \mathbf{h} , we write the migration barrier as

$$\tilde{E}^{\text{mig}}(\mathbf{r}, \mathbf{h}) = E^{\text{mig}}(\mathbf{r}, \mathbf{h}) + E_{\text{el}}^{\text{sad}}(\mathbf{r}, \mathbf{h}) - E_{\text{el}}^{\text{sta}}(\mathbf{r}). \quad (4.18)$$

$E^{\text{mig}}(\mathbf{r})$ corresponds to the PD migration barrier in the system free of strain. $E_{\text{el}}^{\text{sad}}(\mathbf{r}, \mathbf{h})$ and $E_{\text{el}}^{\text{sta}}(\mathbf{r})$ are the elastic interaction energies at the saddle-point and stable configurations, respectively. They are deduced from the PD elastic dipoles at stable and saddle points, and their difference are given by

$$E_{\text{el}}^{\text{sad}}(\mathbf{r}) - E_{\text{el}}^{\text{sta}}(\mathbf{r}, \mathbf{h}) = - [\underline{P}_{ij}^{\text{sad}}(\mathbf{r}, \mathbf{h}) - \underline{P}_{ij}^{\text{sta}}(\mathbf{r})] \underline{\epsilon}_{ij}(\mathbf{r}), \quad (4.19)$$

where $\underline{P}_{ij}^{\text{sta}}$ and $\underline{P}_{ij}^{\text{sad}}$ are the elastic dipoles at the stable and saddle-point configurations, respectively.

The variation of the migration barriers with strain determines the change of the PD jump frequencies, thereby the variation of the diffusion coefficients and the phenomenological L -coefficients. The L -coefficient are symmetric second-rank tensor. For the sake of simplicity, we omit the suffixes attached to species. We write the L -coefficients as \underline{L}_{ij} , where i and j suffixes indicate the directions of respectively diffusion and CPG. The partial derivative of \underline{L}_{ij} with respect to the strain tensor $\underline{\epsilon}_{kl}$ forms a symmetric fourth-rank tensor \underline{L}' [277], which is given by

$$\underline{L}'_{ijkl} = \left(\frac{\partial \underline{L}_{ij}}{\partial \underline{\epsilon}_{kl}} \right)_{\underline{\epsilon}=0}. \quad (4.20)$$

This tensor is the so-called elastodiffusion tensor. In a cubic crystal, only three components of this tensor are independent [277]. By applying Voigt notation, we have

$$\underline{L}'_{11} = \underline{L}'_{22} = \underline{L}'_{33}, \quad \underline{L}'_{12} = \underline{L}'_{13} = \underline{L}'_{23}, \quad \underline{L}'_{44} = \underline{L}'_{55} = \underline{L}'_{66}, \quad (4.21)$$

and the other components are zero. Analytical expressions of the elastodiffusion tensor of direct interstitial-diffusion mechanisms in fcc, bcc and hexagonal closed-packed lattices can be obtained [277]. Note that, we proceed to the study on the variation of \underline{L}_{ij} with the volumetric, tetragonal, and shear strains. A strain tensor $\underline{\epsilon}$, having six independent components e_1 through e_6 , can be written as

$$\underline{\epsilon} = e_v \underline{I} + \begin{bmatrix} e_1 - e_v & 0 & 0 \\ 0 & e_2 - e_v & 0 \\ 0 & 0 & e_3 - e_v \end{bmatrix} + \begin{bmatrix} 0 & \frac{1}{2}e_6 & \frac{1}{2}e_5 \\ \frac{1}{2}e_6 & 0 & \frac{1}{2}e_4 \\ \frac{1}{2}e_5 & \frac{1}{2}e_4 & 0 \end{bmatrix}, \quad (4.22)$$

where $e_v = \frac{1}{3}(e_1 + e_2 + e_3)$ and \underline{I} is the identity tensor. The volumetric strain $\underline{\epsilon}_v = e_v \underline{I}$; the tetragonal strain $\underline{\epsilon}_t$ and the shear strain $\underline{\epsilon}_s$ are the final two tensors in Eq. (4.22).

In the present study, we calculate the transport coefficient tensors for different strains by means of the KineCluE code [167], that performs automatic calculations of \underline{L}_{ij} for

$$\underline{\epsilon}_v = \frac{e}{3} \begin{bmatrix} 1 & 0 & 0 \\ 0 & 1 & 0 \\ 0 & 0 & 1 \end{bmatrix}, \quad \underline{\epsilon}_t = \frac{e}{3} \begin{bmatrix} 2 & 0 & 0 \\ 0 & -1 & 0 \\ 0 & 0 & -1 \end{bmatrix}, \quad \underline{\epsilon}_s = \frac{e}{2} \begin{bmatrix} 0 & 0 & 0 \\ 0 & 0 & 1 \\ 0 & 1 & 0 \end{bmatrix},$$

at different values of e .

4.3 Elastodiffusion in Fe

In this section, we focus on the elastic properties of PD diffusion in pure bcc iron. We present the physical parameters that determine the thermodynamic and diffusion properties of PDs in a strain field. The latter include the elastic constants, the elastic dipoles, and the elastodiffusion tensors.

4.3.1 Elastic properties of iron

There exist many studies on the elastic constants, \underline{C}_{ij} , of iron, including experiments [268–270] and *ab initio* calculations [278, 279]. The authors in Ref. [269] report measurements of \underline{C}_{ij} using the technique of resonant ultra-sound spectroscopy. These measurements cover the range of 3–500 K. We define $\underline{C}' \equiv (\underline{C}_{11} - \underline{C}_{12})/2$. In a perfectly isotropic metal, $\underline{C}' = \underline{C}_{44}$. In iron, the difference between \underline{C}' and \underline{C}_{44} is great, leading to a Zener ratio $A_Z = \underline{C}_{44}/\underline{C}' > 2.4$ at $T > 300$ K. Whereas, A_Z of aluminum is about 1.2 at 300 K [140]. Fe is thus strongly anisotropic.

Table 4.1: Set values for elastic constants.

\underline{C}_{11} (GPa)	\underline{C}' (GPa)	\underline{C}_{44} (GPa)	A_Z
225	45	115	2.5

The set values of elastic constants of iron for the following simulations are presented in Tab. 4.1. Note that the strain field generated by PD sinks such as the dislocation lines depends on the elastic properties of the materials. Therefore, we expect an effect of the iron elastic anisotropy on the generated strain field.

4.3.2 Elastic properties of point defects

We list in Tab. 4.2 the elastic dipoles of Fe at the stable and saddle-point configurations. In the same table, we report as well the elastic dipoles of Al [140].

The elastic dipoles of SIAs in Fe are strongly anisotropic at the stable and saddle-point configurations. While, the vacancy elastic dipoles are perfectly isotropic at the stable configuration, whereas, they are anisotropic at the saddle-point configuration.

When compared with the PD elastic dipoles of Al, the anisotropy of dumbbell in Fe is much greater at the stable and saddle-point configurations. As for the vacancy at the saddle-point configuration, the anisotropy is as large in Fe and Al. However, the reason for this anisotropy may not be the same. In Fe, the off-diagonal components of the elastic dipole are large with respect to the diagonal ones. In Al, the off-diagonal terms of the saddle-point elastic dipole are relatively small, but one of the diagonal terms is very different from the other two.

Table 4.2: Elastic dipoles of pure iron and aluminium.

Elastic dipoles	Fe	Al [140]
$\underline{P}_I^{\text{sta}}$ (eV)	$\begin{bmatrix} 23.752 & 4.728 & 0 \\ 4.728 & 23.752 & 0 \\ 0 & 0 & 27.906 \end{bmatrix}$	$\begin{bmatrix} 19.498 & 0 & 0 \\ 0 & 18.518 & 0 \\ 0 & 0 & 18.518 \end{bmatrix}$
$\underline{P}_I^{\text{sad}}$ (eV) ^a	$\begin{bmatrix} 23.838 & 2.845 & -0.696 \\ 2.845 & 22.529 & 2.845 \\ -0.696 & 2.845 & 23.838 \end{bmatrix}$	$\begin{bmatrix} 19.498 & 1.133 & 0 \\ 1.133 & 19.498 & 0 \\ 0 & 0 & 19.034 \end{bmatrix}$
$\underline{P}_V^{\text{sta}}$ (eV)	$\begin{bmatrix} -2.840 & 0 & 0 \\ 0 & -2.840 & 0 \\ 0 & 0 & -2.840 \end{bmatrix}$	$\begin{bmatrix} -3.238 & 0 & 0 \\ 0 & -3.238 & 0 \\ 0 & 0 & -3.238 \end{bmatrix}$
$\underline{P}_V^{\text{sad}}$ (eV) ^b	$\begin{bmatrix} -2.217 & -1.641 & -1.641 \\ -1.641 & -2.217 & -1.641 \\ -1.641 & -1.641 & -2.217 \end{bmatrix}$	$\begin{bmatrix} -2.866 & -0.080 & 0 \\ -0.080 & -2.866 & 0 \\ 0 & 0 & 1.000 \end{bmatrix}$

^a The saddle-point configuration of the [110]-dumbbell in Fe is along a [110]-to-[101] migration path, while the saddle-point configuration of the [100]-dumbbell in Al is along a [100]-to-[010] migration path.

^b The saddle-point configuration of the vacancy in Fe is along the [111] direction, while the saddle-point configuration of the vacancy in Al is along the [110] direction.

From the elastic dipoles, we calculate the relaxation volume V_d^{rel} of PD (d) [141]. For a cubic crystal, the relaxation volume reads

$$V_d^{\text{rel}} = \frac{\text{Tr}(\underline{P}_d^{\text{sta}})}{3K}, \quad (4.23)$$

where the bulk modulus K is equal to $(\underline{C}_{11} + 2\underline{C}_{12})/3$. Note that the relaxation volume corresponds to the volume change resulting from the deformation of the lattice after an exchange of a substitutional atom with a PD. This quantity does not inform on the change of the lattice shape because it does not depend on the off-diagonal terms of the elastic dipole tensor. After Eq. (4.23), the relaxation volumes of SIAs and vacancies in pure Fe are respectively $+2.25\Omega$ and -0.20Ω , with Ω the atomic volume.

To conclude, in addition to the strong elastic anisotropy, the iron shows a strong anisotropy of PD elastic dipoles. Vacancies are strongly anisotropic at the saddle-point configuration, and dumbbells are strongly anisotropic at both the stable and saddle-point configurations. The PD anisotropy at the saddle point has a significant impact on PD diffusion in Al [140]. This effect should be even more important in Fe due to a greater PD anisotropy at the saddle point. Moreover, unlike Al, the anisotropy of the stable SIA configuration is also significant in Fe.

4.3.3 DFT-based elastodiffusion in Fe

In order to separate the anisotropy effect at the stable and saddle-point configurations, we introduce different models, from the full elastic dipoles to simplified versions of these tensors (see Tab. 4.3).

Table 4.3: Elastic dipoles of the various models. Concerning vacancy, Models 2 and 3 are identical because the elastic dipoles are isotropic at the stable configuration.

	Dumbbell elastic dipole (eV)	Vacancy elastic dipole (eV)
Model 0	$\underline{P}_I^{\text{sta}} = \underline{0}$ $\underline{P}_I^{\text{sad}} = \underline{0}$	$\underline{P}_V^{\text{sta}} = \underline{0}$ $\underline{P}_V^{\text{sad}} = \underline{0}$
Model 1	$\underline{P}_I^{\text{sta}} = \begin{bmatrix} 23.752 & 4.728 & 0 \\ 4.728 & 23.752 & 0 \\ 0 & 0 & 27.906 \end{bmatrix}$ $\underline{P}_I^{\text{sad}} = \begin{bmatrix} 23.838 & 2.845 & -0.696 \\ 2.845 & 22.529 & 2.845 \\ -0.696 & 2.845 & 23.838 \end{bmatrix}$	$\underline{P}_V^{\text{sta}} = \begin{bmatrix} -2.840 & 0 & 0 \\ 0 & -2.840 & 0 \\ 0 & 0 & -2.840 \end{bmatrix}$ $\underline{P}_V^{\text{sad}} = \begin{bmatrix} -2.217 & -1.641 & -1.641 \\ -1.641 & -2.217 & -1.641 \\ -1.641 & -1.641 & -2.217 \end{bmatrix}$
Model 2	$\underline{P}_I^{\text{sta}} = \begin{bmatrix} 23.752 & 4.728 & 0 \\ 4.728 & 23.752 & 0 \\ 0 & 0 & 27.906 \end{bmatrix}$ $\underline{P}_I^{\text{sad}} = 23.402 \underline{I}$	$\underline{P}_V^{\text{sta}} = \begin{bmatrix} -2.840 & 0 & 0 \\ 0 & -2.840 & 0 \\ 0 & 0 & -2.840 \end{bmatrix}$ $\underline{P}_V^{\text{sad}} = -2.217 \underline{I}$
Model 3	$\underline{P}_I^{\text{sad}} = 25.137 \underline{I}$ $\underline{P}_I^{\text{sta}} = 23.402 \underline{I}$	$\underline{P}_V^{\text{sad}} = -2.840 \underline{I}$ $\underline{P}_V^{\text{sta}} = -2.217 \underline{I}$

In Model 0, we ignore the elastic interactions. The non-zero terms of the elastodiffusion tensor are only due to the possible change of the PD jump distance resulting from the lattice deformation. Thus, Model 0 highlights this geometric effect.

Model 1 includes the full elastic dipole tensors as given in Tab. 4.2. Models 2 and 3 correspond to approximations of Model 1. They are defined such as to investigate the impact of PD anisotropy on the elastodiffusion behaviors. In Model 2, we introduce an isotropic elastic dipole tensor at the saddle-point configuration, without changing the relaxation volume (i.e., the trace of the dipole is conserved):

$$\underline{P}_2^{\text{sad}} = \frac{1}{3} \text{Tr}(\underline{P}_{\text{real}}^{\text{sad}}) \underline{I}.$$

This approximation allows us to highlight the effect of the saddle-point anisotropy on the elastodiffusion by comparing the results with the ones obtained in Model 1. In Model 3, an additional approximation is made: the elastic dipole tensors in stable configurations are

assumed to be isotropic as well. Therefore, we have:

$$\underline{P}_3^{\text{sta}} = \frac{1}{3} \text{Tr}(\underline{P}_{\text{real}}^{\text{sta}}) \underline{I}, \quad \underline{P}_3^{\text{sad}} = \frac{1}{3} \text{Tr}(\underline{P}_{\text{real}}^{\text{sad}}) \underline{I}.$$

By comparing Models 2 and 3, we highlight the effect of an anisotropy at the stable configuration on elastodiffusion.

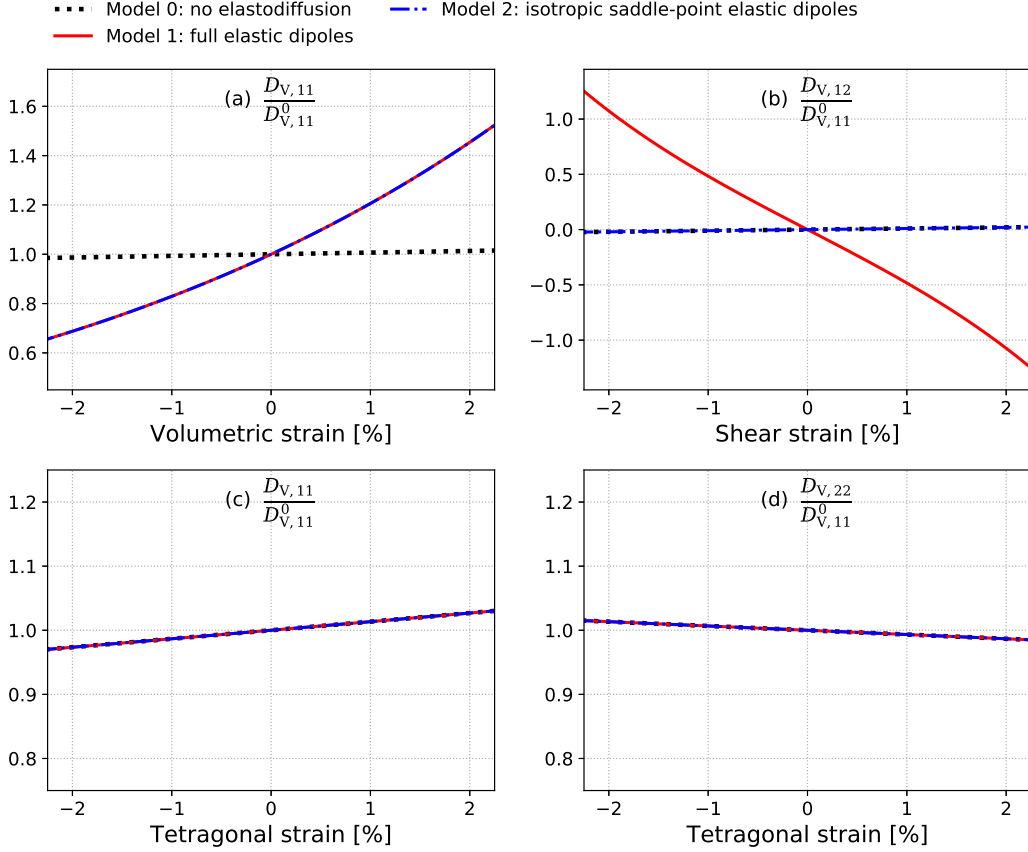


Figure 4.1: Vacancy diffusion coefficients as a function of the external strains obtained from different models. These coefficients are factorized by $D_{V,11}^0$, which is the vacancy diffusion coefficient $D_{V,11}$ in the system without strains. The results are obtained at 400 K, in which $D_{V,11}^0 = 1.70 \times 10^{-15} \text{ m}^{-2}/\text{s}$.

We show in Fig. 4.2 and Fig. 4.1, the variations of the PD diffusion coefficients ($\underline{D}_{d,ij}$ for $d = \text{I}, \text{V}$) with the strains defined in Section 4.2.3, deduced from the various elastic-dipole models at $T = 400 \text{ K}$.

In Model 0, the variations of $\underline{D}_{d,ij}$ with the strains are small. $\underline{D}_{d,11}$ slightly increases with the volumetric ($\underline{\epsilon}_v$) and tetragonal ($\underline{\epsilon}_t$) strains, and $\underline{D}_{d,12}$ slightly increases with the shear strain ($\underline{\epsilon}_s$). This is because a positive deformation (e.g., along the (Ox)-direction) increases the distance of every PD jump along the same direction, and thus, enhances PD diffusion along this direction. However, $\underline{D}_{d,22}$ decreases with $\underline{\epsilon}_t$ because the deformation along the (Oy)-direction is negative.

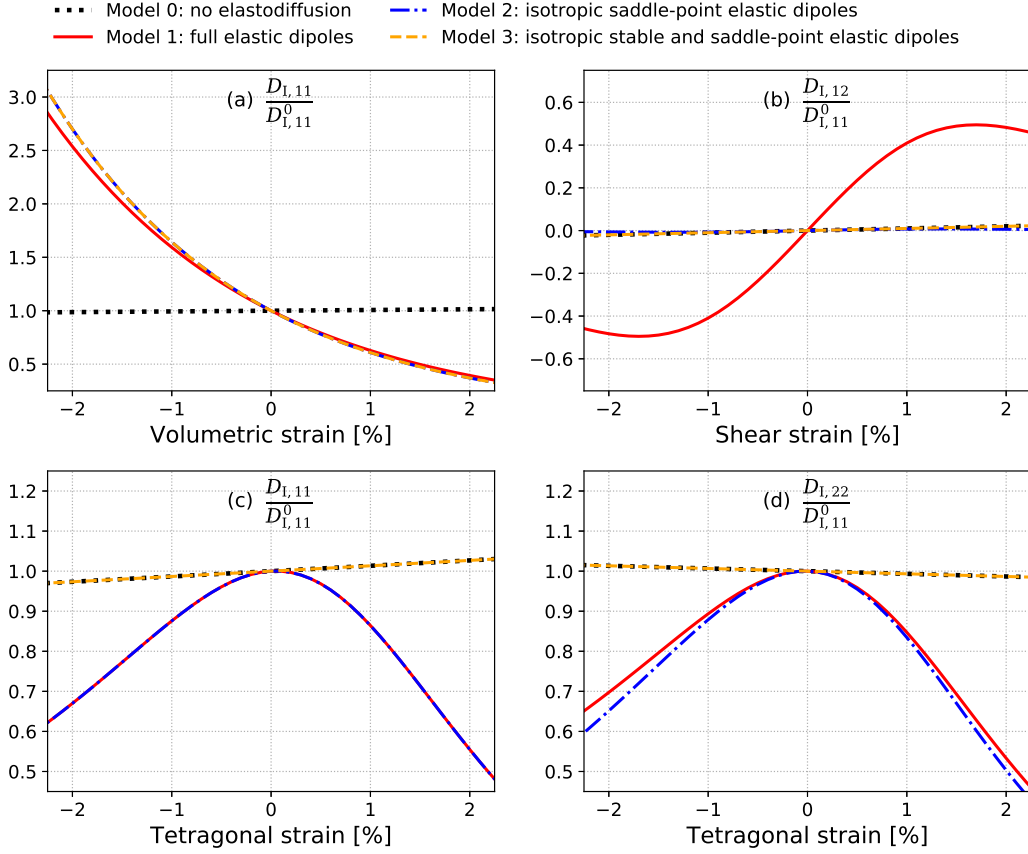


Figure 4.2: SIA diffusion coefficients as a function of the external strains obtained from different models. These coefficients are factorized by $D_{I,11}^0$, which is the SIA diffusion coefficient $D_{I,11}$ in the system without strains. The results are obtained at 400 K, in which $D_{I,11}^0 = 1.99 \times 10^{-11} \text{ m}^2/\text{s}$.

In Model 1, concerning diffusion mediated by vacancies, $\underline{D}_{V,11}$ increases with $\underline{\epsilon}_v$, while $\underline{D}_{V,12}$ decreases with $\underline{\epsilon}_s$. To explain this difference, we investigate the separate contributions of the elastic dipoles at stable and saddle points. $\underline{D}_{V,11}$ is related to the diagonal components of the dipoles. The modification of the vacancy migration barrier upon a positive volumetric strain, $\underline{\epsilon}_v$, is given by $-(\underline{P}_{ii}^{\text{sad}} - \underline{P}_{ii}^{\text{sta}})\underline{\epsilon}_{v,ii}$, which is negative. Therefore, the migration barrier decreases with $\underline{\epsilon}_v$; meaning that the diffusion is enhanced. Thus, $d\underline{D}_{V,11}/d\underline{\epsilon}_v$ is positive. On the other hand, $\underline{D}_{V,12}$ is related to the off-diagonal components of the elastic dipoles. Note that for $i \neq j$, $\underline{P}_{ij}^{\text{sad}} - \underline{P}_{ij}^{\text{sta}} < 0$. Therefore, the vacancy diffusion decreases with shear strain. The variations of $\underline{D}_{V,11}$ and $\underline{D}_{V,22}$ with $\underline{\epsilon}_t$ are negligible. This is because the diagonal terms of the elastic dipoles are equal; thereby the energy variation $\sum \underline{P}_{ii}\underline{\epsilon}_{s,ii} = \underline{P}_{ii} \text{Tr}(\underline{\epsilon}_s) = 0$. Dumbbell diffusion is much more sensitive to strain: $\underline{D}_{I,11}$ decreases with $\underline{\epsilon}_v$, while $\underline{D}_{I,12}$ increases with $\underline{\epsilon}_s$. This is because one of the diagonal components of the stable-point elastic dipole tensor is very different from the other two.

By comparing the results obtained in Models 1 and 2 shown in Figs. 4.1 and 4.2, we deduce that the variation of $\underline{D}_{d,12}$ with the shear strain is due to the anisotropy of the saddle-point elastic dipoles.

In Model 3, the anisotropy of elastic dipole tensors in both the stable and saddle-point configurations is removed. For vacancies, it corresponds to the same situation as Model 2 because the full elastic dipole tensor is isotropic at the stable point. Whereas, the comparison between Models 2 and 3 highlights the essential role of the saddle-point elastic anisotropy on the variation of SIA diffusion coefficient with tetragonal strain.

To conclude, both the elastic anisotropy in the stable and saddle-point configuration of PDs have non-negligible effects on the PD elastodiffusion.

4.3.4 Interactions of point defects with an elastic strain in Fe

Relying on Eq. (4.9), we calculate the energy resulting from the elastic interactions between PD (d) and the external strain field, E_d^{el} , in Fe. The latter depends on the elastic dipole in the stable configuration, \underline{P}_d . Note that the $\langle 110 \rangle$ -dumbbell in a bcc-Fe has six equivalent configurations; each one associated with a different $\langle 110 \rangle$ -direction. From the elastic dipole of a given $\langle 110 \rangle$ -direction, one can deduce the other tensors by applying operations of symmetry of the crystal to the given one. Considering that all equivalent configurations have the same energy in a stress-free state, and denoting by \underline{P}_I^μ the elastic-dipole tensor of the configuration μ , the average dipole of SIA is given by [141]:

$$\underline{P}_{I,ij}^{\text{ave}} = \frac{\sum_{\mu} \exp(\underline{P}_{I,kl}^{\mu} \underline{\epsilon}_{kl}^{\text{ext}} / k_{\text{B}} T) \underline{P}_{I,ij}^{\mu}}{\sum_{\mu} \exp(\underline{P}_{I,kl}^{\mu} \underline{\epsilon}_{kl}^{\text{ext}} / k_{\text{B}} T)}. \quad (4.24)$$

The vacancy has only one configuration. Thus, the corresponding elastic dipole is $\underline{P}_{\text{V}} = \underline{P}_{\text{V}}^{\text{sta}}$. Interestingly, the average dipole resulting from isotropic dipoles does not depend on strain.

In order to investigate the anisotropy effect on the elastic PD-strain field interaction energy, we calculate the interaction energy resulting from anisotropic (Model 1) and isotropic elastic dipoles (Model 2) defined in Tab. 4.3. The expressions of the elastic interaction energies are given in Tab. 4.4.

Table 4.4: Elastic dipoles and the corresponding interaction energies deduced from Models 1 and 3.

	Model 1: full anisotropic dipoles	Model 3: isotropic dipoles
\underline{P}_I	$\underline{P}_{I,ij}^{\text{ave}} = \frac{\sum_{\mu=1}^6 \exp(\underline{P}_{I,kl}^{\mu, \text{sta}} \underline{\epsilon}_{kl}^{\text{ext}} / k_{\text{B}} T) \underline{P}_{I,ij}^{\mu, \text{sta}}}{\sum_{\mu=1}^6 \exp(\underline{P}_{I,kl}^{\mu, \text{sta}} \underline{\epsilon}_{kl}^{\text{ext}} / k_{\text{B}} T)}$	$\frac{1}{3} \text{Tr}(\underline{P}_{\text{I}}^{\text{sta}}) \underline{I}$
E_I^{el}	$-\underline{P}_{I,ij}^{\text{ave}} \underline{\epsilon}_{ij}^{\text{ext}} + K \text{Tr}(\underline{\epsilon}^{\text{ext}}) \Omega$	$-\frac{1}{3} \text{Tr}(\underline{P}_{\text{I}}^{\text{sta}}) \text{Tr}(\underline{\epsilon}^{\text{ext}}) + K \text{Tr}(\underline{\epsilon}^{\text{ext}}) \Omega$
\underline{P}_{V}	$\underline{P}_{\text{V}}^{\text{sta}}$	$\underline{P}_{\text{V}}^{\text{sta}}$
E_{V}^{el}	$-\frac{1}{3} \text{Tr}(\underline{P}_{\text{V}}^{\text{sta}}) \text{Tr}(\underline{\epsilon}^{\text{ext}}) - K \text{Tr}(\underline{\epsilon}^{\text{ext}}) \Omega$	$-\frac{1}{3} \text{Tr}(\underline{P}_{\text{V}}^{\text{sta}}) \text{Tr}(\underline{\epsilon}^{\text{ext}}) - K \text{Tr}(\underline{\epsilon}^{\text{ext}}) \Omega$

In Model 3, we neglect the shear components of the SIA elastic dipole. The resulting average elastic dipole does not depend on strain. The interaction energy is a function of the trace of the latter, and it does not depend on the shear components of the strain tensor. Although we cannot evaluate the difference of E_1^{el} between Models 1 and 3 without knowing the values of the strain, we observe that if the three diagonal components of the dipole tensor have very different values, or the off-diagonal components have relatively large values, the energy difference between Models 1 and 3 should be significant. Concerning the vacancy, there is no difference between Models 1 and 3, because at the stable configuration, the corresponding elastic dipole has no shear component.

4.4 Elastodiffusion in Fe-based alloys

4.4.1 Elastic dipoles of solute atoms and point defects

In the dilute Fe-based alloys, in addition to the elastic dipole of the vacancy and SIA monomers, we include the elastic dipoles of a solute-PD pair. We consider the Fe-Cr, Fe-Ni, and Fe-Mn alloys.

From the *ab initio* calculations of Messina et al. [280], we have the elastic dipole tensors of the solute-PD pair configurations up to a solute-PD distance equal to a cutting radius (that is far below the kinetic radius). For the solute-SIA pair, this radius is set to the 5-th nearest neighbour (5-NN) distance, and for the solute-vacancy pair, it is set to 10-NN one. The elastic dipoles of PD (d) at the k -NN-distance stable configuration are denoted by \underline{P}_{Bd}^k . At very large distance, PD and solute do not interact with each other, and the elastic dipole of the solute-PD pair is the sum of the mono-solute ($\underline{P}_B^{\text{mono}}$) and the mono-PD ($\underline{P}_d^{\text{mono}}$) dipoles. Since the elastic interaction of a PD and a solute atom decreases in $1/R^3$ (with R the solute-PD distance) [141], for the sake of simplicity, we assume that the elastic dipoles of the PD-solute pairs seating on k -NN sites ($k > 10$ for vacancy and $k > 5$ for SIAs) are given by

$$\underline{P}_{Bd}^k = \underline{P}_B^{\text{mono}} + \underline{P}_d^{\text{mono}} + (\underline{P}_{Bd}^c - \underline{P}_B^{\text{mono}} - \underline{P}_d^{\text{mono}}) \left(\frac{R_c}{R_k} \right)^3, \quad (4.25)$$

where R_i is the i -NN distance. We set $c = 10$ for vacancies and $c = 5$ for SIAs.

Concerning the saddle-point energies associated with PD jumps between configurations beyond the cutting radius, the corresponding saddle point energy is obtained from a kinetically-resolved activation (KRA) barrier approximation [281]. We deduce the saddle-point energy from the stable-point energies of the initial and final configurations. Note that for an atomic jump from the k -NN to the l -NN stable configuration in a strain field, $\underline{\epsilon}(\mathbf{r})$, the modification of the migration barrier, $\Delta E_{Bd}^{k \rightarrow l}$, is given by $-\left[(\underline{P}_{Bd}^{k \rightarrow l})_{ij} - (\underline{P}_{Bd}^k)_{ij} \right] \epsilon_{ij}(\mathbf{r})$.

The elastic dipoles tensors of the solute atoms in different alloys are listed in Tab. 4.5. The elastic dipole tensors of the solute-PD pairs in Fe-based alloys are listed in Appendix A.

From the elastic dipole database, we calculate the ensemble average of elastic dipoles

of the PD-solute pairs, and deduce the relaxation volumes of the dumbbell in Fe-B ($B \equiv \text{Cr, Ni, and Mn}$) alloys. Note that the relaxation volume of the single mixed configuration of the dumbbell is smaller than the sum of the dipoles of a mono-dumbbell and a mono-solute atom, which are far from each other. Therefore, under volumetric compression ($\epsilon_v < 0$), the dumbbell is more likely to be close to the solute, whereas under volumetric tension ($\epsilon_v > 0$), it is probably far from the solute.

It is worth noting that, in Fe-Cr and Fe-Ni alloys, for a dumbbell jump connecting the configurations k and l , the trace of the SIA elastic dipoles at saddle point ($\text{Tr}(\underline{P}_{\text{BI}}^{k \rightarrow l})$) are almost systematically larger than that of the initial stable point ($\text{Tr}(\underline{P}_{\text{BI}}^k)$). For instance, the Fe-Cr dumbbell jump shows a difference of about +1.5 eV. The migration barrier of the Fe-Cr dumbbell decreases with volumetric strain. In contrast, the migration barrier of the mono-dumbbell increases with volumetric strain. In Fe-Mn alloy, the trace of the SIA elastic dipole at saddle point is relatively close to the one at stable point. Hence, the variation of L_{II} with strain must be less visible than those in the other two Fe-based alloys.

Table 4.5: Elastic dipoles of solute atoms in Fe-based alloys (eV).

Fe-Cr	Fe-Ni	Fe-Mn
$3.25 \underline{I}$	$3.73 \underline{I}$	$3.26 \underline{I}$

4.4.2 Elastodiffusion properties in Fe-based alloys

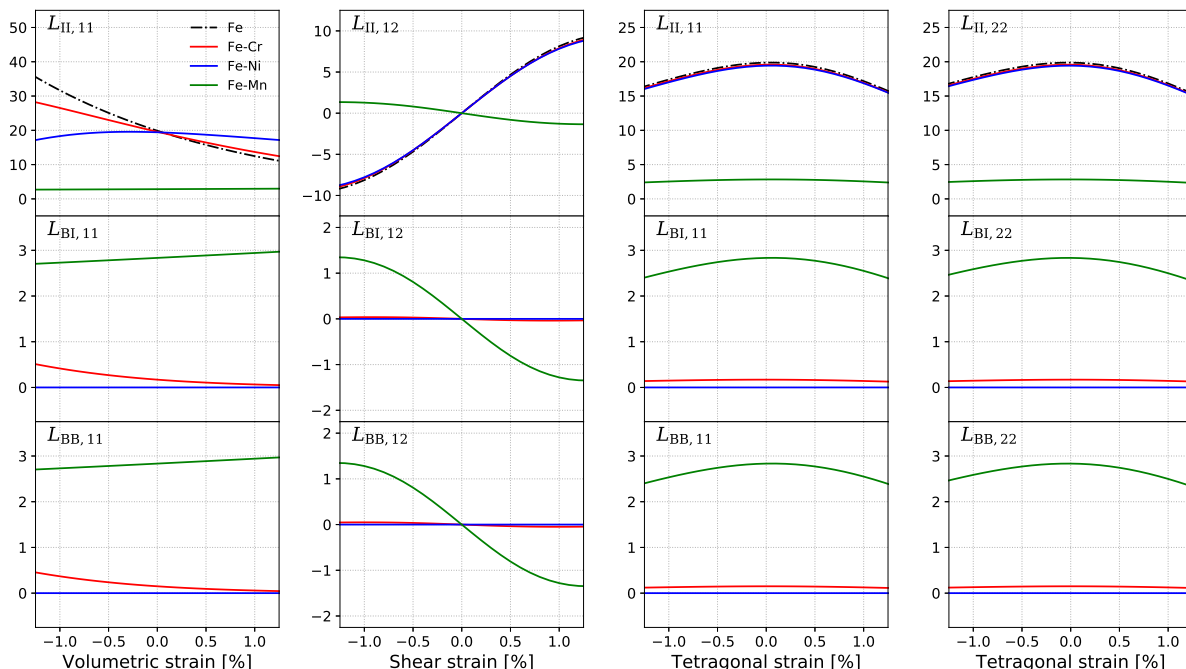


Figure 4.3: SIA-mediated transport coefficients as a function of the external strains. These coefficients are given in $10^{-18} \text{ m}^2/\text{s}$. The results are obtained at 400 K. The SIA concentration is set to 10^{-6} and the solute nominal concentration is set to 10^{-3} .

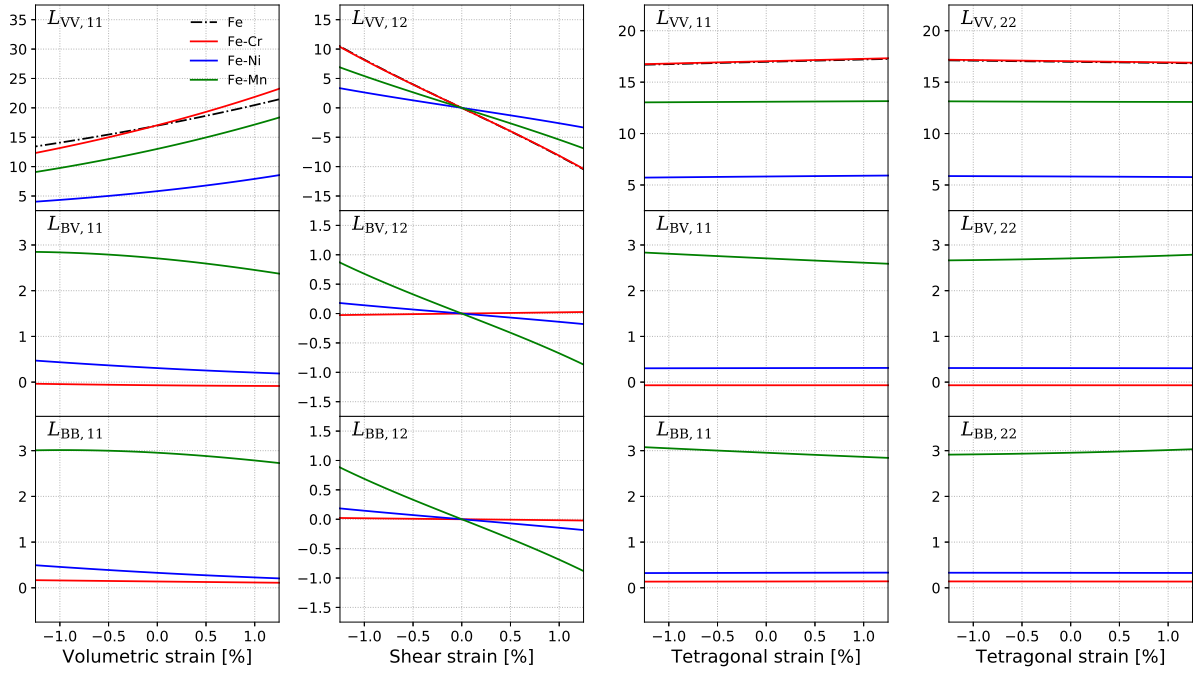


Figure 4.4: Vacancy-mediated transport coefficients as a function of the external strains. These coefficients are given in $10^{-22} \text{ m}^2/\text{s}$. The results are obtained at 400 K. The vacancy concentration is set to 10^{-6} and the solute nominal concentration is set to 0.1 at.%.⁹

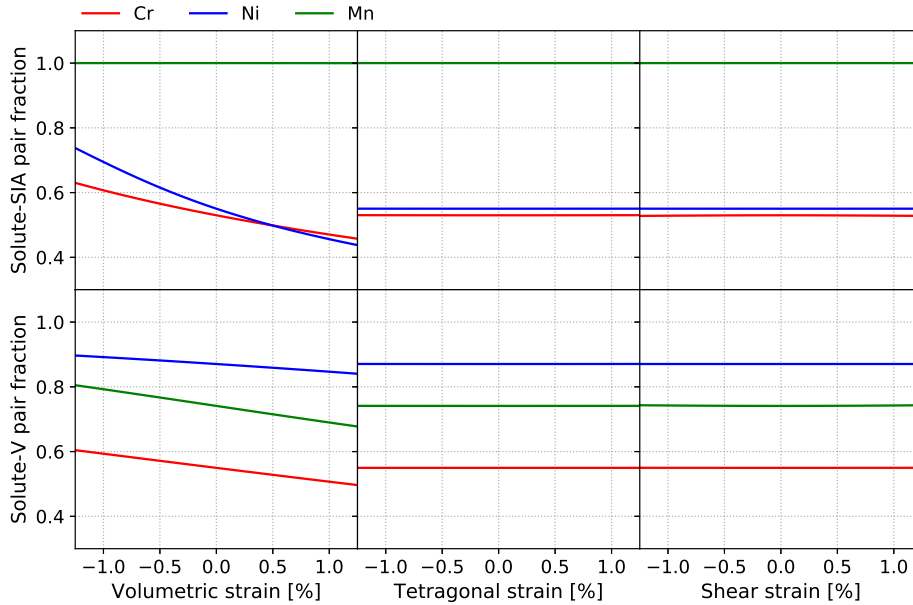


Figure 4.5: Solute-PD pair fractions as a function of the external strains. The results are obtained at 400 K. The vacancy concentration is set to 10^{-6} and the solute nominal concentration is set to 0.1 at.%.⁹

We apply the KineCluE code to the calculation of the transport coefficients $L_{\alpha\beta,ij}$ under the three elementary strains ϵ_v , ϵ_t , and ϵ_s (defined in Section 4.2.3) for Fe-Cr, Fe-Ni, and Fe-Mn

alloys. Note that α and β indicate the chemical species B, V, or I; i and j are for the spatial coordinates. The results related to SIAs are shown in Fig. 4.3 and the ones of vacancies are shown in Fig. 4.4. For a more complete understanding of these results, we plot in Fig. 4.5 the variation of the solute-pair concentration with strains, at 0.1 at.% nominal concentration of solute.

First we consider the SIA-mediated transport coefficients.

- In Fe-Cr, the variation of $L_{II,11}$ with $\underline{\epsilon}_v$ is relatively close to the one in Fe: it decreases with strain. However, for $\underline{\epsilon}_v < 0$, there is a slight difference of between Fe-Cr and Fe. As expected from the elastic dipoles, the dumbbell is more likely to be close to the solute atom, i.e., the Cr-SIA pair fraction is higher (cf. Fig. 4.5). Hence, the dumbbell diffusion in Fe-Cr deviates from the mono-dumbbell in Fe. The variation of $L_{II,12}$ with shear strain, and the variation of $L_{II,11}$ and $L_{II,22}$ with tetragonal strain are similar to those in Fe. Note that $L_{BI,ij}$ and $L_{BB,ij}^I$ are directly related to the solute-SIA pair concentration. The latter decreases with $\underline{\epsilon}_v$, while it is not sensitive to $\underline{\epsilon}_s$ and $\underline{\epsilon}_t$.
- In Fe-Ni, the variation of $L_{II,11}$ with the volumetric strain is different for $\underline{\epsilon}_v < 0$ and $\underline{\epsilon}_v > 0$. Under compression ($\underline{\epsilon}_v < 0$), the solute-pair fraction is relatively high. Since the migration barrier of SIA is lower close to Ni, $L_{II,11}$ increases with $\underline{\epsilon}_v$. Under tension ($\underline{\epsilon}_v > 0$), $L_{II,11}$ decreases with $\underline{\epsilon}_v$ as the mono-dumbbell. The variations of $L_{II,ij}$ with shear and tetragonal strains are similar to those in Fe. Since the mixed-dumbbell configuration in Fe-Ni alloy is not stable, $L_{BI,ij}$ and $L_{BB,ij}^I$ are relatively small, and their variations with strains are not significant.
- In Fe-Mn, as expected from their elastic dipoles, the change of $L_{II,ij}$ with strain is relatively small. The variations of $L_{BI,ij}$ and $L_{BB,ij}^I$ with volumetric and tetragonal strains are small as well. However, $L_{BI,12}$ and $L_{BB,12}^I$ notably change with the shear strain.

Here we consider the vacancy-mediated transport coefficients.

- In Fe-Cr, the variations of $L_{VV,ij}$ with strains are almost the same as those in Fe. Since the Cr-vacancy binding is very weak (cf. Tab. 3.2), $L_{BV,ij}$ and $L_{BB,ij}^V$ are relatively small, and their variations with strains are insignificant.
- In Fe-Ni, the absolute values of $L_{VV,ij}$ are smaller than those in Fe because the Ni-vacancy binding is large; thereby the vacancy diffusion is slowed down. However, the variation of $L_{VV,ij}$ with strains are similar to those in Fe. $L_{BV,11}$ and $L_{BB,11}^V$ decrease with the volumetric strain, and $L_{BV,12}$ and $L_{BB,12}^V$ decrease with the shear strain, while $L_{BV,ij}$ and $L_{BB,ij}^V$ are not sensitive to the tetragonal strain.
- In Fe-Mn, the variation of $L_{\alpha\beta,ij}$ with external strains are similar to those in Fe-Ni alloy, though the values of $L_{\alpha\beta,ij}$ are different in these two alloys because the solute-vacancy binding energies are different.

4.5 Sink strength and bias factors of an edge-dislocation

In this section, we numerically solve the diffusion equations of PDs (Eq. (1.29)) and solute atoms in the strain field generated by an edge-dislocation. Fluxes of PDs and solute atoms are given by Eq. (1.66). From the solution of the PD concentration, we deduce the sink strengths and bias factors from Eq. (1.32) for a Laplace-type boundary condition. Note that analytical solutions of these equations are available in the most simplified model, which we use to validate our numerical approach.

4.5.1 Simulation setup: coordinate system and boundary conditions

Since an edge dislocation has translational symmetry along the dislocation line (cf. Fig. 1.5(c)), for simplicity, we ignore the diffusion of PDs and solute atoms along the dislocation line. The 3D diffusion system is projected on the 2D plane perpendicular to the dislocation line. Therefore, we use a polar coordinate system centered on the dislocation (cf. Fig. 4.6). The simulated domain is an annular region with inner radius r_c , corresponding to the capture radius of the dislocation, and the outer radius R . r_c is set to $12\|\mathbf{b}\|$, ensuring that all strains generated by the dislocation (presented in Section 4.5.2) are within $\pm 1\%$, in order to be within the usual range of linear elasticity theory [141]. R is related to the dislocation density ρ by $\rho = 1/\pi R^2$. The diffusion equations are solved within this domain. In the following, the index ‘1’ stands for the \mathbf{e}_r direction, ‘2’ for the \mathbf{e}_θ direction, and ‘3’ for the \mathbf{e}_z direction.

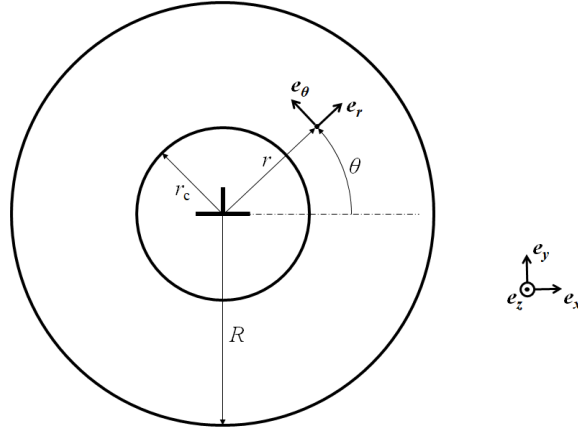


Figure 4.6: Dislocation geometry. $(\mathbf{e}_r, \mathbf{e}_\theta, \mathbf{e}_z)$ is the orthonormal basis of the cylindrical coordinate. $(\mathbf{e}_r, \mathbf{e}_\theta, \mathbf{e}_z)$ is the orthonormal basis of the Cartesian coordinate.

We assume that PDs diffuse fast enough near the dislocation such that PD concentrations at $r = r_c$ are the equilibrium ones. Therefore, the vacancy concentration at the inner radius writes

$$C_d(r_c, \theta) = C_d^{\text{eq}}(r_c, \theta). \quad (4.26)$$

In alloys, C_d^{eq} not only depends on strains, but also on the local solute concentration (see Eq. (4.8)). Hence, it must be computed adaptively in the simulation. Under equilibrium con-

ditions, we apply the equilibrium vacancy concentration at the outer boundary:

$$C_d(R, \theta) = C_d^{\text{eq}}(R, \theta). \quad (4.27)$$

Under irradiation, a bulk supersaturation of PDs is produced. We set the PD concentration at the outer radius to

$$C_d(R, \theta) = C_d^{\text{b}}, \quad (4.28)$$

where C_d^{b} is the bulk concentration of PDs, which can be several orders of magnitude larger than the equilibrium one, depending on the irradiation conditions. In our simulation, we estimate the supersaturated bulk concentration after a mean-field rate theory (Eq. (1.23)).

In Fe-based alloys, we do not expect solute atoms to be absorbed or created by the dislocation. Therefore, the normal flux of solute atoms at the inner boundary is set to zero:

$$\mathbf{e}_r \cdot \mathbf{J}_B(r_c, \theta) = 0. \quad (4.29)$$

We set the bulk solute concentration to C_B^{b} which is changed adaptively in the simulation such that the nominal solute atom concentration \bar{C}_B equals to a predefined value. If not specified, the latter is set to 0.1 at.% such that the local solute concentration in the entire simulated domain does not exceed the dilute limit of ~ 1 at.-%:

$$C_B(R, \theta) = C_B^{\text{b}}. \quad (4.30)$$

Note that our simulation is in the reference of the dislocation, which is always assumed to be in the center of the simulation domain. The dislocation motion is ignored because we assume that the establishment speed of the solute segregation profile is much faster than the dislocation climb velocity.

4.5.2 Sink properties: stress and strain field of an edge dislocation

We express the stress-strain field generated by an edge dislocation as a function of the elastic constants and position relative to the dislocation line. We show how the elastic anisotropy affect the external strain field.

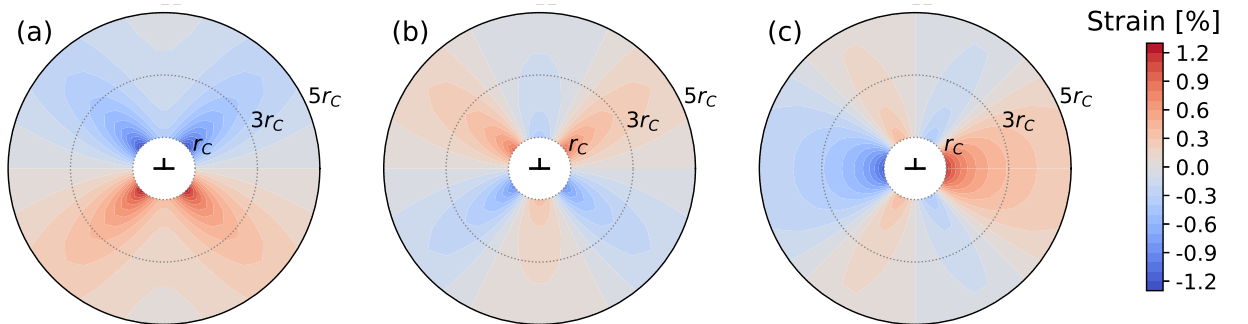


Figure 4.7: The strain field for (a) $\underline{\epsilon}_{11}$, (b) $\underline{\epsilon}_{22}$, and (c) $\underline{\epsilon}_{12}$.

The analytical expression of the anisotropic stress field generated by an edge-dislocation in a cubic crystal is given by [282]:

$$\underline{\sigma}_{11} = -\|\mathbf{b}\| \frac{I}{2\pi} \frac{y[(3+H)x^2+y^2]}{(x^2+y^2)^2+Hx^2y^2}, \quad (4.31)$$

$$\underline{\sigma}_{22} = \|\mathbf{b}\| \frac{I}{2\pi} \frac{y(x^2-y^2)}{(x^2+y^2)^2+Hx^2y^2}, \quad (4.32)$$

$$\underline{\sigma}_{12} = \|\mathbf{b}\| \frac{I}{2\pi} \frac{x(x^2-y^2)}{(x^2+y^2)^2+Hx^2y^2}, \quad (4.33)$$

$$\underline{\sigma}_{33} = \nu(\underline{\sigma}_{11} + \underline{\sigma}_{22}), \quad (4.34)$$

$$\underline{\sigma}_{13} = \underline{\sigma}_{23} = 0, \quad (4.35)$$

where

$$I = (\underline{C}_{11} + \underline{C}_{12}) \left[\frac{\underline{C}_{44}(\underline{C}_{11} - \underline{C}_{12})}{\underline{C}_{11}(2\underline{C}_{44} + \underline{C}_{11} + \underline{C}_{12})} \right]^{1/2}, \quad (4.36)$$

and

$$H = \frac{(\underline{C}_{11} + \underline{C}_{12})(\underline{C}_{11} - \underline{C}_{12} - 2\underline{C}_{44})}{\underline{C}_{11}\underline{C}_{44}}. \quad (4.37)$$

Note that, when $\underline{C}_{44} = (\underline{C}_{11} - \underline{C}_{12})/2$ is satisfied, we recover the isotropic expression of the stress field [129]. From the stress field expression and the general Hooke's law (Eq. (4.1)), we deduce the strain field, $\underline{\epsilon}$. We plot in Fig. 4.7, the strain field generated near an edge dislocation. The lattice is in compression ($\underline{\epsilon}_{11} < 0$) in the radial direction (\mathbf{e}_r) in the area where the coordinate $\theta \in [0^\circ, 180^\circ]$. Therefore, this area is called the compressive region of the dislocation. Conversely, the area where $\theta \in [180^\circ, 360^\circ]$ corresponds to the tensile region. In the area where the radial compression is great ($\theta = 45^\circ, 135^\circ$), the tension in the \mathbf{e}_θ direction is great. Conversely, in the area of great radial dilatation ($\theta = 225^\circ, 315^\circ$), the compression in the \mathbf{e}_θ direction is great. Regarding the shear strain, $\underline{\epsilon}_{12}$, it is great at $\theta = 0^\circ$ and 180° .

4.5.3 Pure Fe

We start this section with an assessment of the numerical approach, by relying on isotropic models of strain and PD elastic dipoles, for which there are analytical solutions of the sink strength and bias factor. Then, we proceed to a numerical simulation of more realistic models. We investigate the effect of the elastic anisotropy of strain and PDs on the sink strength and the bias factor of an edge dislocation in Fe.

4.5.3.1 Assessment of the numerical approach

Analytical solutions of the sink strength and the bias factor are available when the following approximations are made: (i) the material (Fe) is perfectly isotropic ($\underline{C}_{44} = (\underline{C}_{11} - \underline{C}_{12})/2$); (ii) PDs are perfectly spherical and isotropic (spherical inclusion (SI) approximation); (iii) PDs relaxation energy (elastic dipole contribution) is considered only; (iv) elastodiffusion is neglected. In such situation (Model A0), the solution is given by Eq. (1.41). In order to assess

our numerical approach, we solve the diffusion equation using the same approximations and boundary conditions. The results are plotted in Fig. 4.8. The numerical solution of Model A0 is in excellent agreement with the analytical solution (Eq. (1.41)). This comparison reinforces our numerical approach.

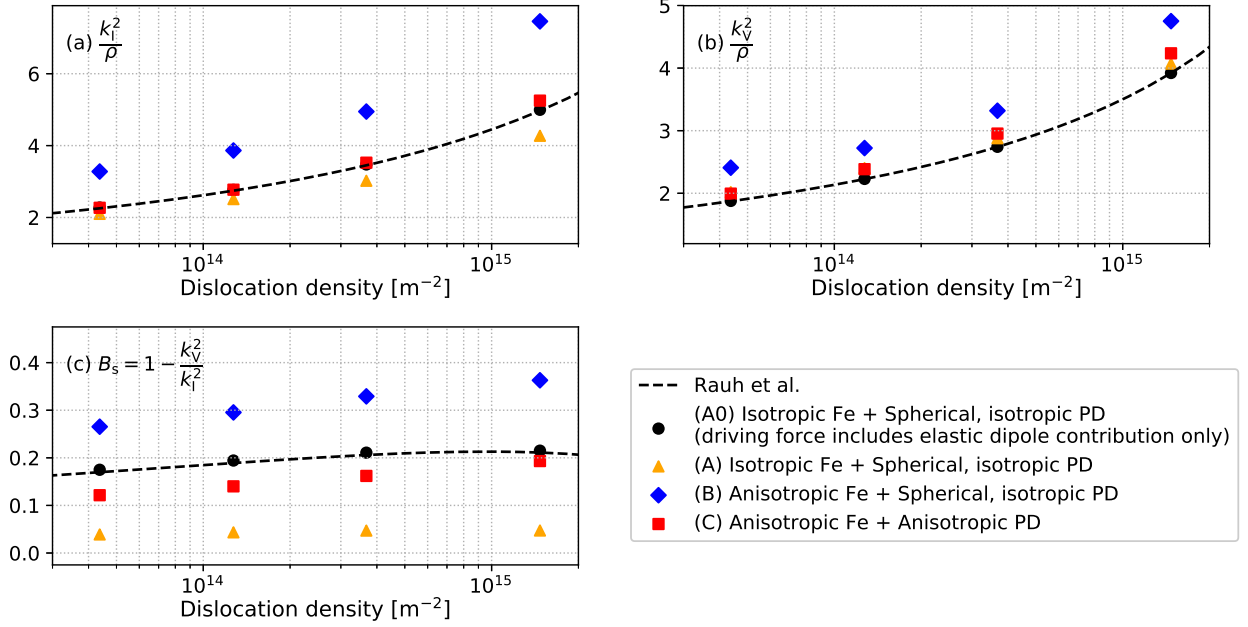


Figure 4.8: Sink strength for (a) SIAs (k_I^2) and (b) vacancies (k_V^2), and (c) sink bias (B_s) of an edge-dislocation as a function of densities (ρ) at $T = 400$ K. The numerical results are obtained with different approximations on elasticity properties of Fe and PDs.

4.5.3.2 Effect of the elastic anisotropy of matrix and the PDs

We solve the same diffusion equation by including one by one the elastic anisotropy contributions (see Tab. 4.6). The corresponding results are also plotted in Fig. 4.8. In Model A, we consider the full PD diffusion driving force, as given in Eq. (4.9). In Model B, Fe matrix is not assumed to be isotropic. Finally, in Model C, we add the PD anisotropy (full elastic dipoles). Among these models, we expect Model C to be the most realistic one. Note that the effect of the elastodiffusion is ignored in these models. It will be later accounted for in Section 4.5.3.3.

Then, we compare Models A0 and A. k_I^2 obtained from Model A is smaller than that from Model A0; whereas k_V^2 obtained from Model A is slightly larger than that from Model A0. Therefore, we obtain a significant decrease of the bias factor when the full elastic PD driving force is accounted for.

We highlight the effects of the elastic anisotropy of Fe on the sink strengths and the bias factor by comparing the results obtained from Models A and B. In the latter model, the elastic anisotropy of the matrix leads to a significant increase of the SIA sink efficiency, resulting in an increase of the dislocation bias factor.

Table 4.6: Calculation models definition.

	Model A0	Model A	Model B	Model C
Elastic property of PDs	Spherical	Spherical	Spherical	Complete description by elastic dipoles
	Isotropic	Isotropic	Isotropic	Anisotropic
Elastic property of Fe	Isotropic	Isotropic	Anisotropic	Anisotropic
Elastic interaction	Eq. (1.39)	Eq. (4.9)	Eq. (4.9)	Eq. (4.9)
Analytical solution	Eq. (1.41)	/	/	/

Furthermore, in order to highlight the role of PD anisotropy, we compare the results from Models B and C. A full description of PD anisotropy leads to a decrease of k_V^2 and k_I^2 , leading to a decrease of the bias factor.

4.5.3.3 Effect of the elastodiffusion

We add to the diffusion solution the variation of PD migration energies with strain, i.e., the elastodiffusion. In order to highlight the PD anisotropy effect on the diffusion properties, sink strength, and the bias factor, we perform simulation of PD diffusion by means of the full elastic dipole tensors or the simplified ones (listed in Tab. 4.3). The results are plotted in Fig. 4.9.

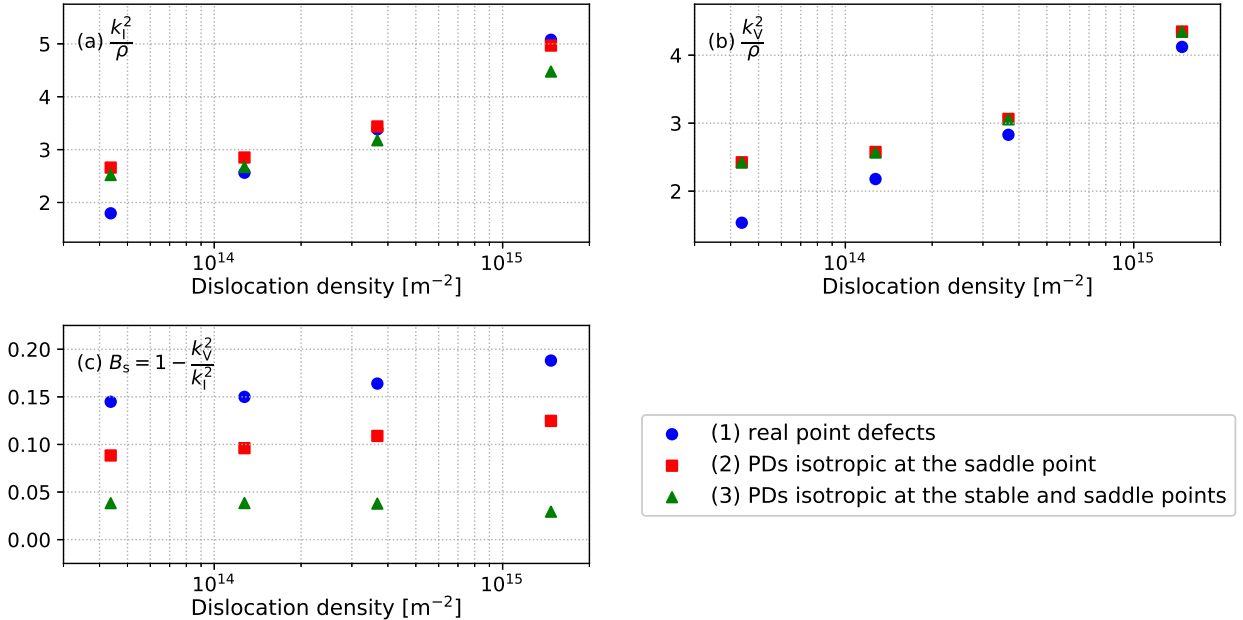


Figure 4.9: Sink strength for (a) SIAs (k_I^2) and (b) vacancies (k_V^2), and (c) sink bias factor (B_s) of an edge-dislocation as a function of the dislocation density (ρ) at $T = 400$ K. The results are obtained from Models 1, 2, and 3 of PD elastic dipoles listed in Tab. 4.3.

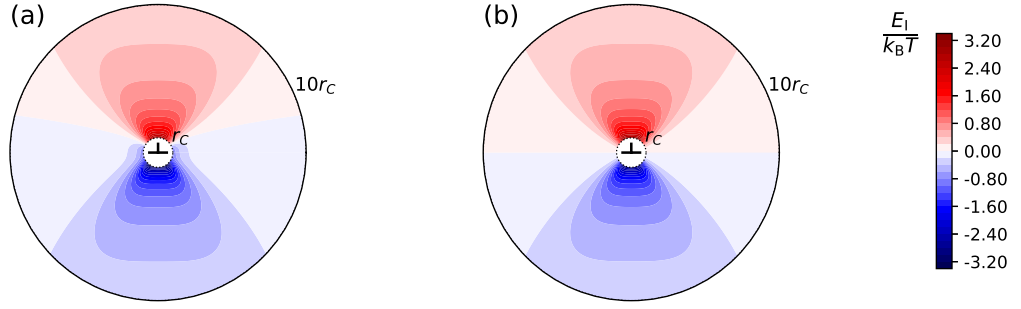


Figure 4.10: Elastic interaction energy obtained from (a) Model 2 and (b) Model 3 at $T = 400$ K. The dislocation density is set to $3.7 \times 10^{14} \text{ m}^{-2}$ ($R = 10 r_c$).

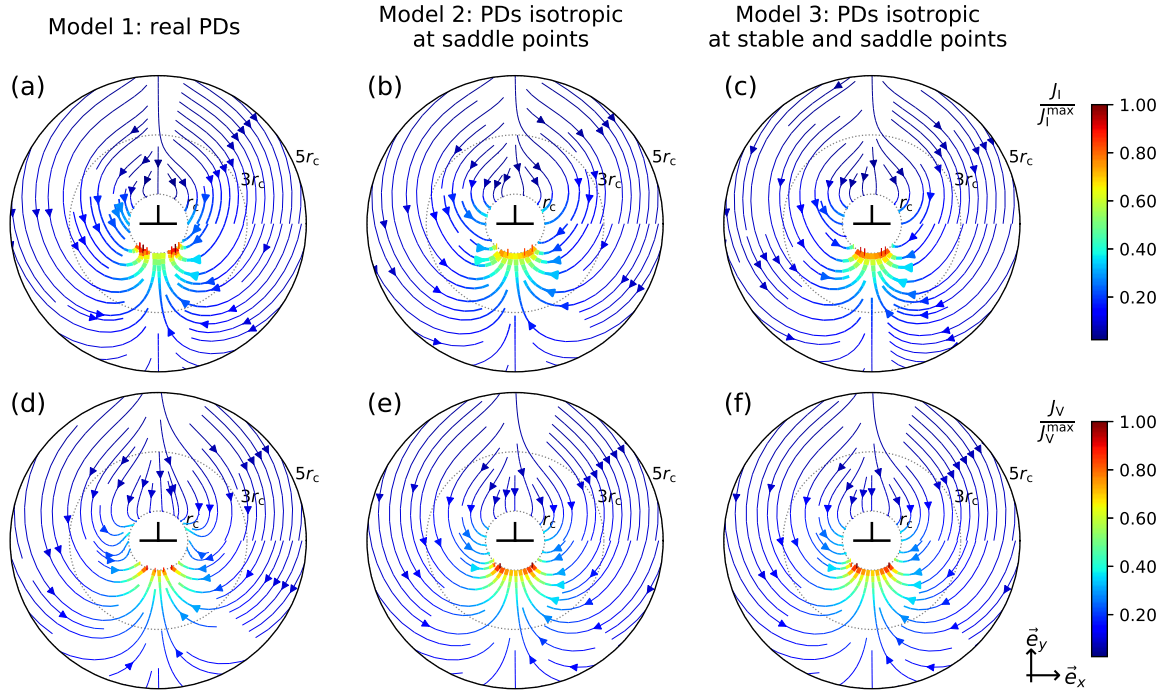


Figure 4.11: Stream lines of SIA flux obtained from (a) Model 1, (b) Model 2, and (c) Model 3, and of vacancy fluxes in (d) Model 1, (e) Model 2, and (f) Model 3 at $T = 400$ K. The dislocation density is set to $3.7 \times 10^{14} \text{ m}^{-2}$ ($R = 10 r_c$). The width of the lines are proportional to the norm of the flux. The color bar represents the norm of the flux factorized by the maximum flux among the results obtained from the three models, with $J_I^{\max} = 0.16 \text{ nm}^{-2} \text{ s}^{-1}$ and $J_V^{\max} = 0.12 \text{ nm}^{-2} \text{ s}^{-1}$.

First, we consider Models 1 and 2. By assuming that PDs are isotropic at the saddle point, k_V^2 is significantly increased, whereas, the change of k_I^2 is small, leading to a decrease of the bias factor. Such an effect of saddle-point anisotropy of PDs has already been highlighted in previous studies [132, 140, 283–285]. As expected from the elastodiffusion properties presented in Section 4.3.3, the effect of a shear strain on sink efficiencies and bias factor in the isotropic Model 2 is very small, whereas it is great in the fully anisotropic Model 1. This resulting in the difference of the sink efficiencies and the bias factor in these two situations.

By comparing Models 2 and 3, we observe that k_I^2 is notably decreased if SIA elastic dipoles are assumed to be isotropic at the stable point. Note that, k_V^2 of these two models is almost the

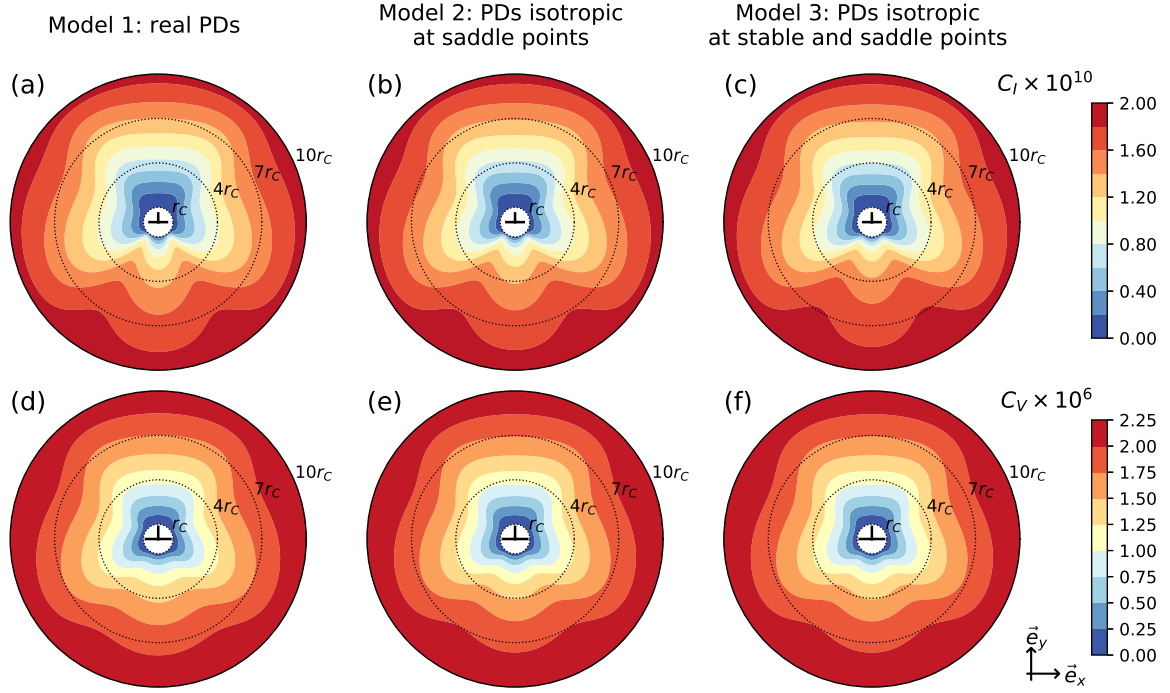


Figure 4.12: Atomic fraction maps of SIA in (a) Model 1, (b) Model 2, and (c) Model 3, and of vacancies in (d) Model 1, (e) Model 2, and (f) Model 3 at $T = 400$ K. The dislocation density is set to $3.7 \times 10^{14} \text{ m}^{-2}$ ($R = 10 r_c$).

same because vacancies are isotropic at the stable point. As a result, the bias factor obtained from Model 3 is smaller than that from Model 2. The impact of the stable-point anisotropy of SIA on the sink efficiency is two-fold. It affects the elastodiffusion behaviors, and the elastic interaction energy between SIA and the edge dislocation. The variation tendencies of the diffusion coefficient with tetragonal strains obtained from these models are very different (see Section 4.3.3). Moreover, the large effect of a tetragonal strain was already present in the elastic interaction of SIA with strain (see Fig. 4.10). The domain of Model 2 where the interaction energy is negative, is larger than that of Model 3. This is because when there is no off-diagonal coefficients of the elastic dipole, there is a coupling with the shear strain, leading to a reduction of the elastic interaction.

In order to achieve a full understanding of the PD-anisotropy effects, we investigate the fluxes of PDs and their concentration profile near an edge dislocation.

We plot in Fig. 4.11 the stream lines of the fluxes of SIA and vacancies. Most of SIA and vacancies flow to the tensile region of the dislocation. The comparison between Models 1 and 2 shows that the saddle-point anisotropy affects the PD trajectories. In Model 2, more vacancies enter the dislocation along the Burgers vector direction ($\pm e_x$). Regarding SIA, differences between both models are smaller because the relative contribution of the deviatoric component of the stable-point elastic dipole tensors (i.e., the ratio between the off-diagonal components and the diagonal ones) is smaller than that of vacancies. The comparison between Models 2 and 3 shows that the SIA trajectories are slightly affected by the stable-point anisotropy because the relative contribution of the deviatoric component of the stable-point elastic dipole tensor

is much smaller than that of the saddle-point tensor. The maps of PD atomic fractions are plotted in Fig. 4.12. From these maps, we obtain the shapes and the sizes of the PD-depleted zones near the edge dislocation. SIAs and vacancies are mostly depleted in the compressive region. The shapes of the SIA-depleted zone are similar in the three models. However, the size of this zone increases with the SIA anisotropy. Regrading vacancy, the vacancy anisotropy at the saddle point affects the shape of the vacancy-depleted zone.

4.5.3.4 Effect of temperature

Table 4.7: Sink strength and bias factor of dislocations in Fe. The results are obtained at 400, 500, 600, and 700 K. The dislocation density is set to $\rho = 3.7 \times 10^{14} \text{ m}^{-2}$.

$T[K]$	400	500	600	700
k_{I}^2/ρ	3.54	3.27	3.12	3.02
k_{V}^2/ρ	2.92	2.85	2.82	2.79
$B_s = 1 - k_{\text{V}}^2/k_{\text{I}}^2$	0.18	0.13	0.10	0.07

In Tab. 4.7, we present sink strengths and bias factors obtained at different temperatures. Both quantities decrease with temperature. An increase of temperature decreases the impact of both chemical and elastic interactions, because all of them are divided by $k_{\text{B}}T$.

4.5.4 Fe-based alloys

4.5.4.1 Effect of solute atoms

Table 4.8: Sink strength and bias factor in Fe and Fe-based alloys. The results are obtained with and without strains at 400 K. The dislocation density is set to $\rho = 3.7 \times 10^{14} \text{ m}^{-2}$.

		Fe	Fe-Cr	Fe-Ni	Fe-Mn
Without strain	k_{I}^2/ρ	2.76	2.74	2.75	3.95
	k_{V}^2/ρ	2.76	2.77	2.97	3.27
	B_s	0	-0.01	-0.08	0.17
With strain	k_{I}^2/ρ	3.54	3.60	3.80	4.54
	k_{V}^2/ρ	2.92	2.94	3.49	3.60
	B_s	0.18	0.18	0.08	0.21

In Fe-based binary alloys, the transport coefficients depend on the local concentration of the solute atoms. Therefore, we solve the solute diffusion equation together with the PD diffusion equations. In this section, we present the calculated PD concentration field in Fe-based alloys only. By comparing with the behavior of PDs in Fe, we investigate the effects of solute atoms on the PD flux, sink strength, and bias factor.

The resulting sink strengths and bias factors of Fe-Cr, Fe-Ni, and Fe-Mn alloys are listed in Tab. 4.8. We compare the results with those obtained in Fe. When no strain is applied, the

presence of Cr atoms does not affect the sink strengths and bias factor. Whereas, in Fe-Ni, the sink strength for vacancies is increased by $\sim 20\%$, leading to a slightly negative bias factor. In Fe-Mn, the sink strengths for both SIAs and vacancies are significantly increased, resulting in a positive sink bias.

When strain is applied, Cr atoms slightly increases the sink strengths for SIAs and vacancies. Whereas, the bias factor is almost equal to the Fe one. In Fe-Ni, the sink strength for vacancies is $\sim 20\%$ higher than that of Fe, and the sink strength for SIAs is $\sim 10\%$ higher than that of Fe. Thus, the bias factor is about one third of the one of Fe. Comparing Fe and Fe-Mn alloy, the presence of Mn atoms notably increases the sink strengths for SIAs ($\sim 40\%$) and vacancies ($\sim 20\%$). Hence, the bias factor is more than twice of the one of Fe. For a more complete understanding of this solute effect in strained systems, we consider the trajectories and distribution of the PDs.

First we plot in Fig. 4.13 the stream lines of PDs near an edge dislocation. We observe that the trajectories of PDs in Fe and the investigated Fe-based alloys are very similar. However, in Fe-Mn, more SIAs enter the dislocation through the $\pm \mathbf{e}_x$ direction than that in Fe and the other Fe-based alloys. This is because, in Fe-Mn, the variation tendencies of the transport coefficients with shear strains are very different from those in other systems (as presented in Section 4.4.2).

We plot in Fig. 4.14 the atomic fraction maps of PDs in Fe and the investigated Fe-based alloys. The size and shape of the vacancy-depleted zones in Fe and Fe-based alloys are similar. Regarding SIAs, we see that the size of SIA-depleted zones in Fe-Cr and Fe-Ni alloys are almost the same as that in Fe. Whereas, the SIA-depleted zone in Fe-Mn alloy is notably smaller than that in Fe because the SIA-Mn binding interaction is great.

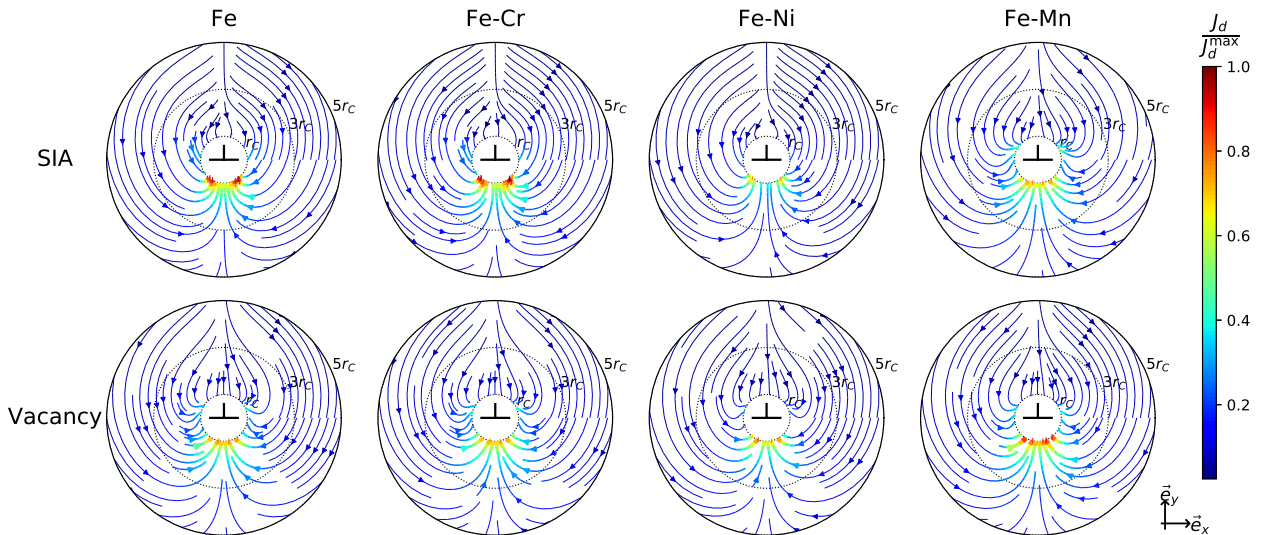


Figure 4.13: Stream lines of the PDs in Fe and the various Fe-based alloys at $T = 400$ K. The dislocation density is set to $3.7 \times 10^{14} \text{ m}^{-2}$ ($R = 10 r_c$). The width of the lines are proportional to the norm of the flux. The color bar represents the norm of the flux normalized by the maximum flux in the four systems, with $J_{\text{I}}^{\text{max}} = 0.21 \text{ nm}^{-2} \cdot \text{s}^{-1}$ and $J_{\text{V}}^{\text{max}} = 0.14 \text{ nm}^{-2} \cdot \text{s}^{-1}$.

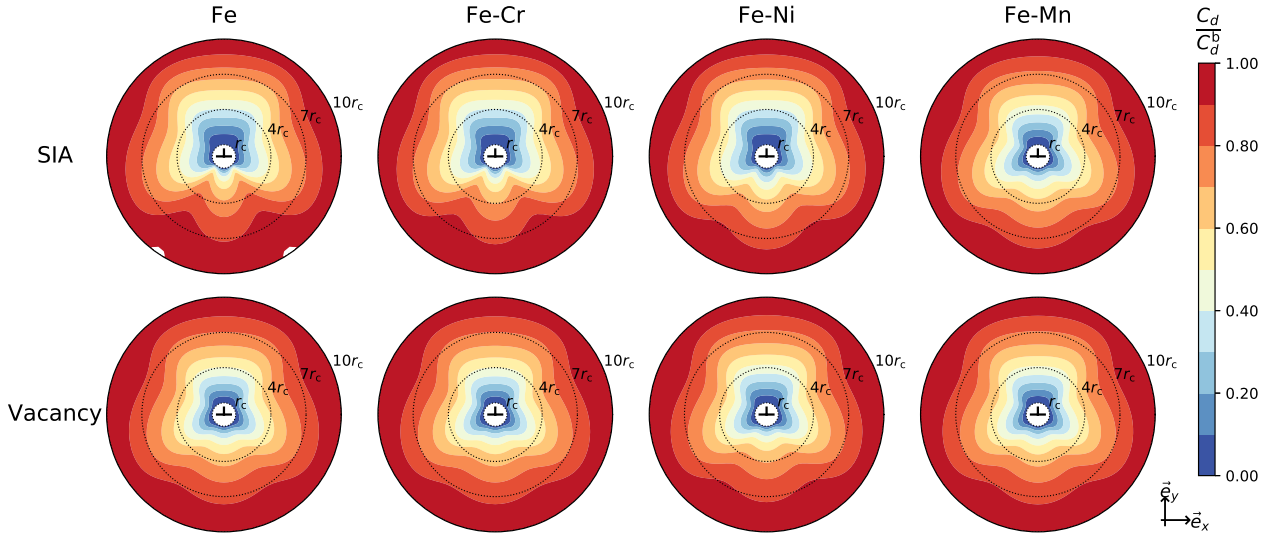


Figure 4.14: Atomic fraction maps of PDs in Fe and the various Fe-based alloys at $T = 400$ K. The dislocation density is set to $3.7 \times 10^{14} \text{ m}^{-2}$ ($R = 10 r_c$). The color bar represents the atomic fraction normalized by the bulk PD concentration.

4.5.4.2 Effect of temperature

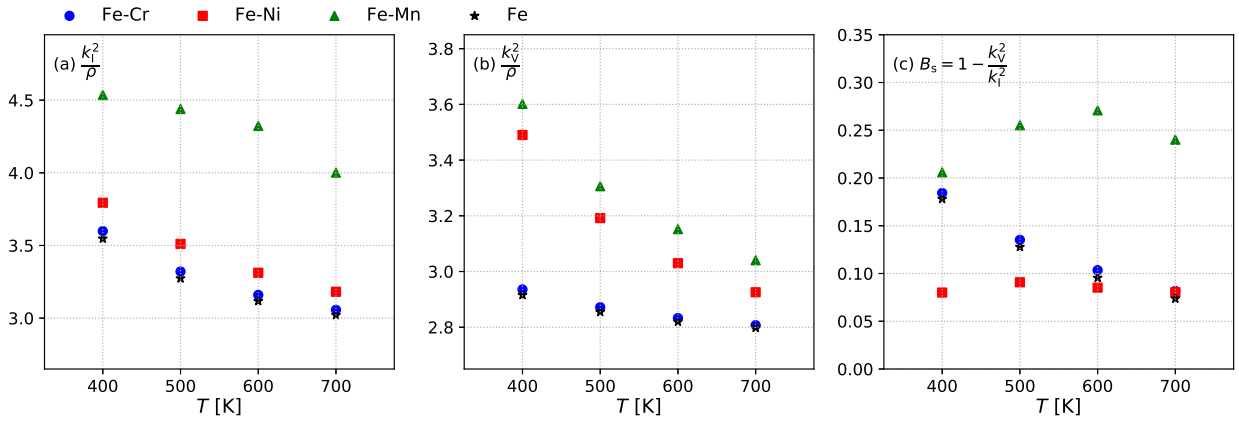


Figure 4.15: Sink strength for (a) SIAs (k_I^2) and (b) vacancies (k_V^2), and (c) sink bias (B_s) of an edge-dislocation in Fe and Fe-based alloys as a function of temperature (T). The dislocation density is set to $3.7 \times 10^{14} \text{ m}^{-2}$ ($R = 10 r_c$). The nominal solute concentration $\bar{C}_B = 0.1 \text{ at.}\%$.

We plot in Fig. 4.15 the sink strengths and bias factors of dislocations in Fe and Fe-based alloys obtained at various temperatures. The variation tendencies of the PD sink strengths in Fe-based alloys are similar to those in Fe: the sink strengths for vacancies and SIAs decrease with temperature. Whereas, the variation of the bias factors with temperature is very different. In Fe-Cr, the bias factor decreases with temperature, and it is very close to the one in Fe at every temperature. In Fe-Ni, the bias factor increases with temperature, and it is nearly the same as the one in Fe at 700 K. Finally, in Fe-Mn alloy, the bias factor is notably higher than the one in Fe at every temperature.

4.5.4.3 Effect of solute concentration

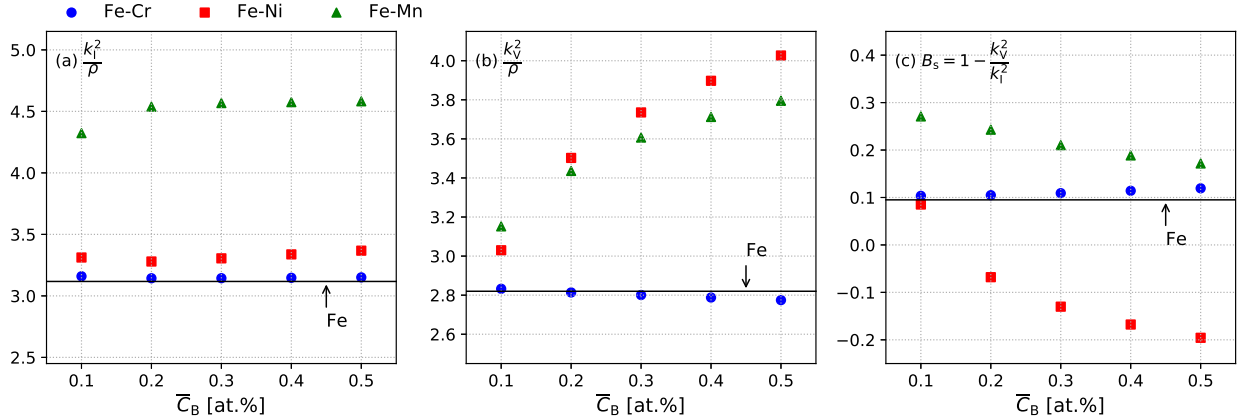


Figure 4.16: Sink strength for (a) SIAs (k_I^2) and (b) vacancies (k_V^2), and (c) sink bias (B_s) of an edge-dislocation in Fe-based alloys as a function of nominal solute concentration (\bar{C}_B). The results are obtained at 600 K. The dislocation density set to $3.7 \times 10^{14} \text{ m}^{-2}$ ($R = 10 r_c$).

We plot in Fig. 4.16 the sink strengths and bias factors of dislocations in the various Fe-based alloys obtained at different nominal solute concentrations. In Fe-Cr, the PD sink strengths slightly decrease with the nominal solute concentration, \bar{C}_B . Whereas, in Fe-Ni and Fe-Mn alloys, the PD sink strengths increases with \bar{C}_B . As for the bias factor, it decreases with \bar{C}_B in the three investigated alloys. It is worth noting that, in Fe-Ni alloy, the bias factor becomes negative when $\bar{C}_B > 0.2$ at.%. Therefore, solute atoms may change the sign of a bias factor.

4.6 Radiation-induced segregation at an edge dislocation in Fe-based alloys

In this section, we investigate the equilibrium segregation and the RIS of solute atoms near an edge dislocation.

4.6.1 Equilibrium distribution of solute atoms

In this section, we compute the equilibrium solute segregation resulting from the solute-dislocation elastic interactions. In principle, an equilibrium segregation is also governed by a modification of the energy landscape close to the sink, that is neglected here. In the dilute limit, we do not account for the interactions between solute atoms. Thus, there is no effect of the alloy ordering tendency on the equilibrium segregation profile. Therefore, the present equilibrium segregation model only accounts for the atom size effects and their interaction with the dislocation strain field. The obtained solute distribution are plotted in Fig. 4.17. As expected from the solute formation volumes, the solute atoms have a positive size effect.

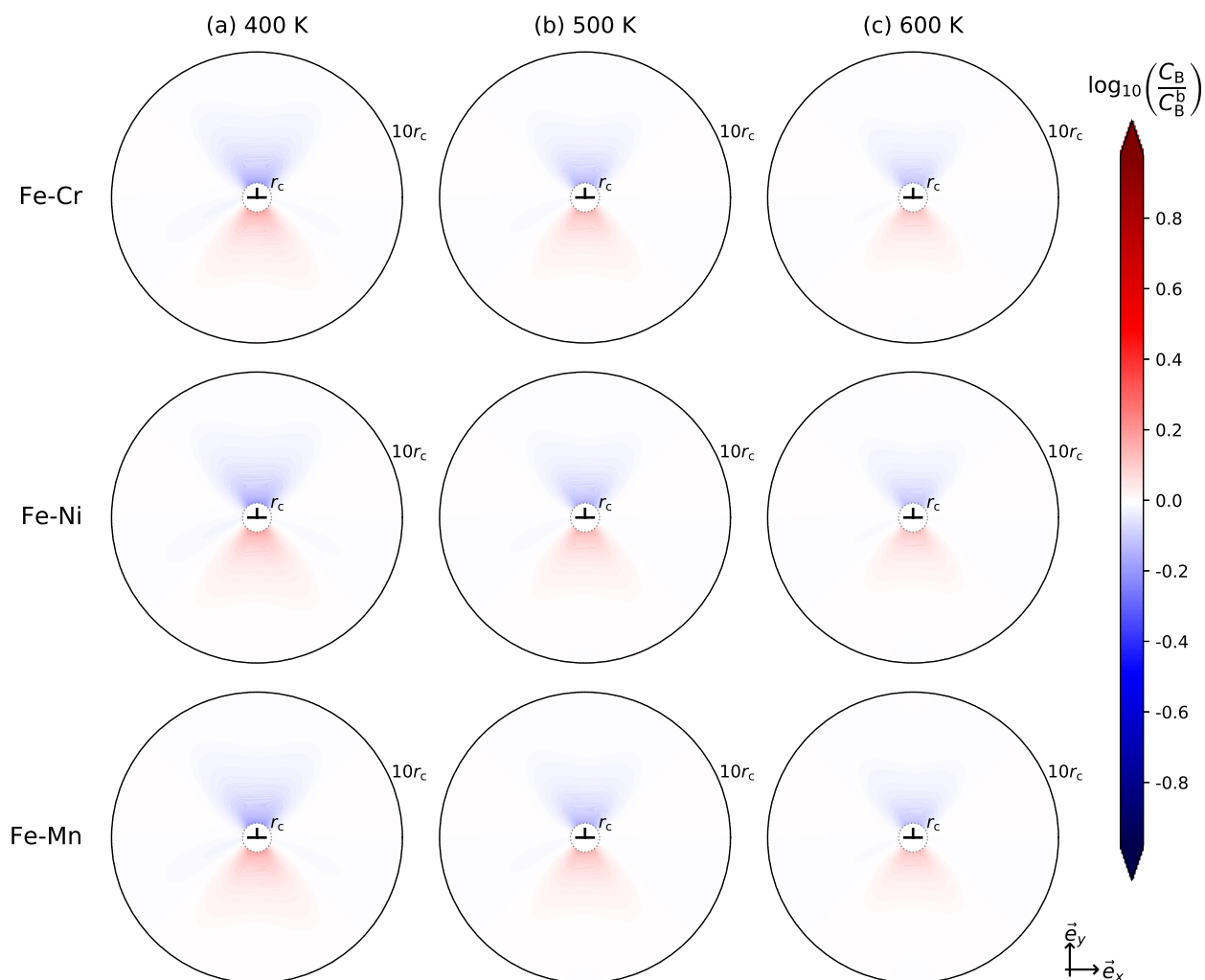


Figure 4.17: Initial distribution of solute atoms in the various Fe-based alloys at different temperatures. The irradiation flux ϕ is set to 10^{-5} dpa/s. The dislocation density is set to $3.7 \times 10^{14} \text{ m}^{-2}$ ($R = 10 r_c$). The nominal solute concentration $\bar{C}_B = 0.1 \text{ at.}\%$.

Hence, the three of them are enriched in the tensile region and depleted in the compressive region. The highest segregated atomic fraction of solute atoms is about twice of the bulk concentration, and the lowest one is about half of the bulk concentration. As expected, the solute segregation tendencies decrease with temperature.

4.6.2 Steady-state distribution of solute atoms under irradiation

Here we consider the radiation-induced steady-state distribution of the solute atoms near the dislocation. We plot in Fig. 4.18 the maps of solute B atomic fraction ($B \equiv \text{Cr, Ni, Mn}$) near the dislocation. The results are obtained for different diffusion models: (a) no strain is applied; (b) the elastodiffusion is ignored and only the PD-strain field interactions are considered; and (c) elastodiffusion and PD-strain field interactions are considered.

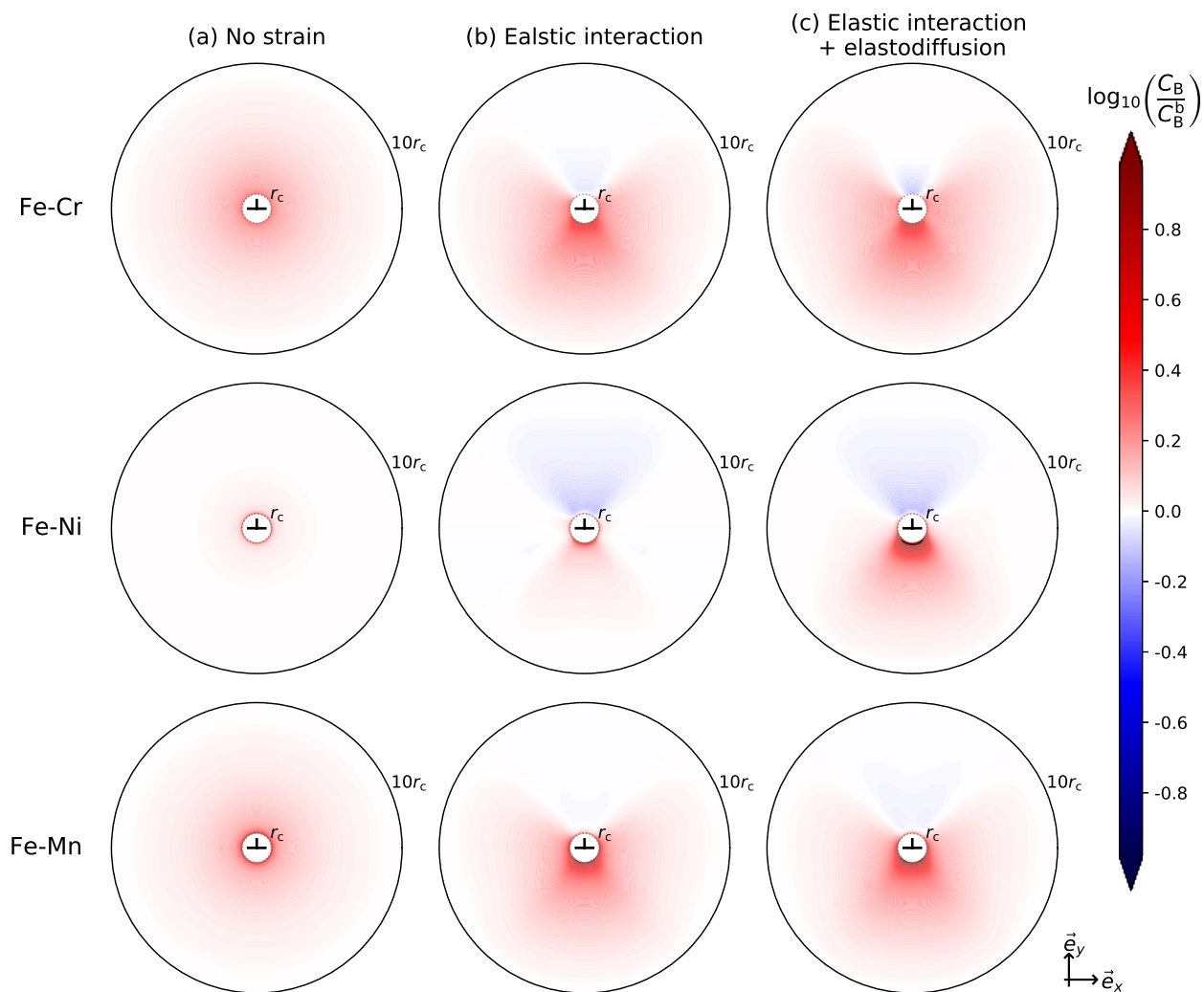


Figure 4.18: Atomic fraction maps of solute atoms $B \equiv \text{Cr, Ni, Mn}$ obtained in the various alloys and from different models. The results are obtained at $T = 400 \text{ K}$ and $\phi = 10^{-5} \text{ dpa/s}$. The dislocation density is set to $3.7 \times 10^{14} \text{ m}^{-2}$ ($R = 10 r_c$). The nominal solute concentration $\bar{C}_B = 0.1 \text{ at.}\%$.

When no strain is applied, the three solute atoms are enriched at the dislocation under the investigated irradiation conditions. This is consistent with the analytical results of Section 3.5.2, for which the strain effect were neglected.

The presence of the PD-strain field interaction changes the steady-state distribution of the solute atoms. The solute concentration in the tensile region of the dislocation is higher than that in the compressive region.

The elastic strain globally increase solute RIS in Fe-Cr and Fe-Mn alloys. In Fe-Ni, the solute RIS is significantly increased by the contribution of elastodiffusion, which may be much larger than the elastic contribution to the PD thermodynamic driving force. For a better understanding of the elastodiffusion effects on the RIS, we compare the solute trajectories obtained from these three models (cf. Fig. 4.19). The PD-strain field interactions dramatically change the solute trajectories. Moreover, when the elastodiffusion is considered, more solute

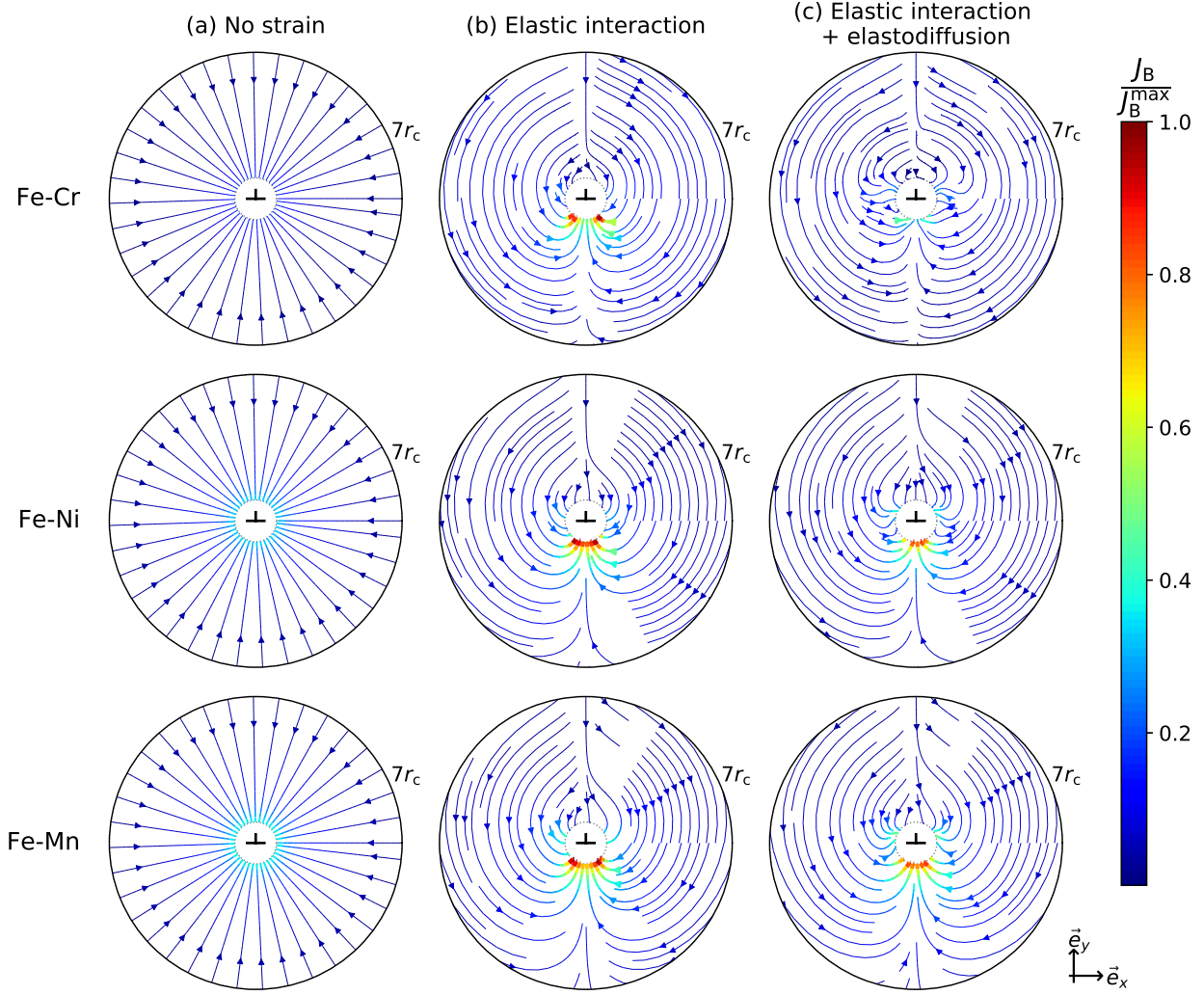


Figure 4.19: Stream lines of solute atoms $B \equiv \text{Cr, Ni, Mn}$ obtained from different models: (a) no elastodiffusion and (b) complete elastodiffusion. The results are obtained at $T = 400 \text{ K}$ and $\phi = 10^{-5} \text{ dpa/s}$. The dislocation density is set to $3.7 \times 10^{14} \text{ m}^{-2}$ ($R = 10 r_c$). The nominal solute concentration $\bar{C}_B = 0.1 \text{ at.}\%$. The line width is proportional to the norm of the flux. The color bar represents the norm of the flux factorized by the maximum flux, with $J_{\text{Cr}}^{\text{max}} = 1.1 \times 10^{-3} \text{ nm}^{-2}\text{s}^{-1}$, $J_{\text{Ni}}^{\text{max}} = 3.8 \times 10^{-3} \text{ nm}^{-2}\text{s}^{-1}$, and $J_{\text{Mn}}^{\text{max}} = 9.9 \times 10^{-2} \text{ nm}^{-2}\text{s}^{-1}$.

atoms enter the dislocation through the directions associated with $\theta = 45^\circ$ and 135° , whereas less solute atoms enter the dislocation through the directions associated with $\theta = 225^\circ$ and 315° .

The solute RIS amount can be deduced from the steady-state solute distribution. By analogy with the Gibbs formalism of interface excess quantities (Eq. (3.19)), we define the solute concentration excess at dislocations by the following integral:

$$S_B = \int_{r_c}^R \int_0^{2\pi} [C_B(r, \theta) - C_B^b] r \, d\theta \, dr. \quad (4.38)$$

In Tab. 4.9, we present the solute RIS amounts normalized by the area of the investigated domain, $S_B/\pi(R^2 - r_c^2)$, of the various Fe-based alloys. The presence of the PD-strain field

Table 4.9: Solute radiation-induced segregation amounts of the Fe-Cr, Fe-Ni, and Fe-Mn alloys. These quantities are normalized by the area of the investigated domain, and given in at.%. The results are obtained at 400 K. The dislocation density $\rho = 3.7 \times 10^{14} \text{ m}^{-2}$ ($R = 10 r_c$). The nominal solute concentration $\bar{C}_B = 0.1$ at.%.

	(a) No strain	(b) Elastic interaction	(c) Elastic interaction + elastodiffusion
Fe-Cr	0.011	0.013	0.014
Fe-Ni	0.003	0.002	0.010
Fe-Mn	0.011	0.013	0.014

interaction slightly increases the solute RIS amounts in Fe-Cr and Fe-Mn alloys. The elastodiffusion significantly increases the Ni RIS amount. Whereas, it slightly decreases the Mn RIS amount, and almost does not affect the Cr RIS amount. The change of RIS amount is much less important at higher temperature. For instance, at 600 K, the normalized solute segregation quantity ($S_B/\pi(R^2 - r_c^2)$) is 0.073 at.% without strains, while it is 0.089 at.% when the elastodiffusion and elastic interactions are accounted for. This difference should be even smaller at higher temperatures.

Table 4.10: Solute radiation-induced segregation amounts of the Fe-Cr, Fe-Ni, and Fe-Mn alloys. These quantities are normalized by the area of the investigated domain, and given in at.%. The results are obtained at 400, 500, and 600 K. The dislocation density $\rho = 3.7 \times 10^{14} \text{ m}^{-2}$ ($R = 10 r_c$). The nominal solute concentration $\bar{C}_B = 0.1$ at.%.

T [K]	400	500	600
Fe-Cr	0.014	0.011	0.009
Fe-Ni	0.010	0.006	0.005
Fe-Mn	0.014	0.014	0.014

We plot in Fig. 4.20 the steady-state solute distribution near an edge dislocation in the various Fe-based alloys at different temperatures. The corresponding solute RIS amounts are presented in Tab. 4.10. The bulk solute concentration get closer to the nominal concentration with temperature. In Fe-Cr, the depletion of Cr atoms at the compressive side increases with temperatures. Whereas, the enrichment of Cr atoms at the tensile side decreases with temperature.

In Fig. 4.21, we present the steady-state solute distribution at different nominal solute concentrations. In Fe-Cr, the depletion of Cr atoms at the compressive side is more important at higher \bar{C}_{Cr} . Whereas, the enrichment of Cr atoms at the tensile side decreases with \bar{C}_{Cr} . In Fe-Ni, the size of the solute-enrichment domain increases with \bar{C}_{Ni} . In Fe-Mn, the solute distribution is not sensitive to the change of \bar{C}_{Mn} . The solute RIS amounts as a function of the nominal solute concentration are plotted in Fig. 4.22. S_{Cr} decreases with \bar{C}_{Cr} , whereas S_{Ni} and S_{Mn} increase almost linearly with \bar{C}_B .

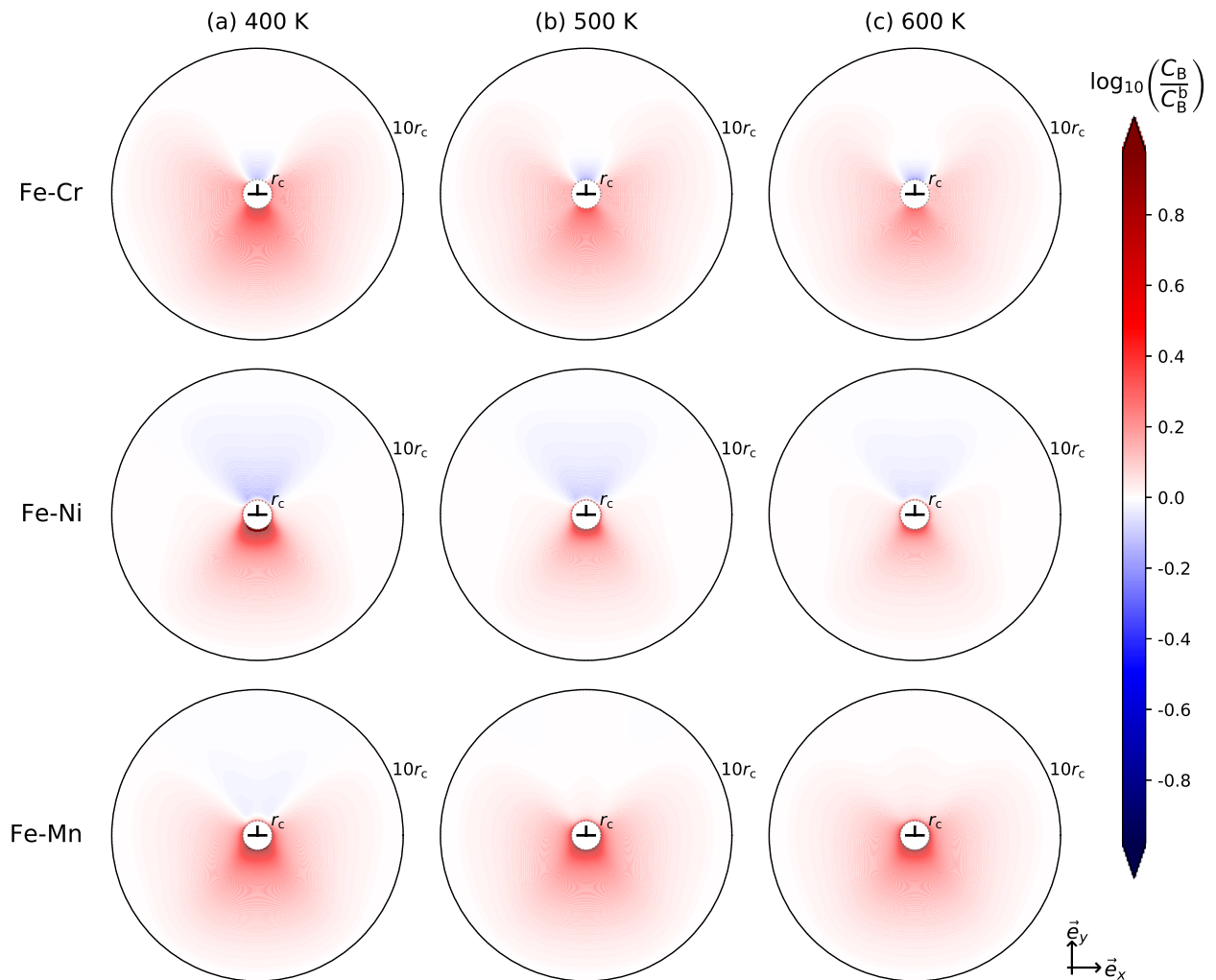


Figure 4.20: Atomic fraction maps of solute atoms $B \equiv \text{Cr, Ni, Mn}$ obtained in the various alloys and at different temperatures. The results are obtained at $\phi = 10^{-5}$ dpa/s. The dislocation density is set to $3.7 \times 10^{14} \text{ m}^{-2}$ ($R = 10 r_c$). The nominal solute concentration $\bar{C}_B = 0.1 \text{ at.}\%$.

4.7 Summary

Based on the elastic dipoles of PDs, solute atoms, and PD-solute pairs, we calculate (i) the thermodynamic driving forces of diffusion and (ii) the transport coefficients under an applied stress-strain field, using the SCMF-based code—KineCluE, in Fe and Fe-B ($B \equiv \text{Cr, Mn, Ni}$) alloys. From these calculations, we highlight the effects of the matrix elastic anisotropy, and the stable and saddle-point PD anisotropy on the PD-strain field elastic interactions, the elastodiffusion, the sink strength, the bias factor, and the solute RIS of an edge dislocation at steady state.

PD behaviors and solute RIS are very different in Fe and the three investigated alloys.

- In Fe, we have introduced a full formulation of the PD diffusion driving forces, including the energy change due to the PD relaxation and the work of creating or removing a

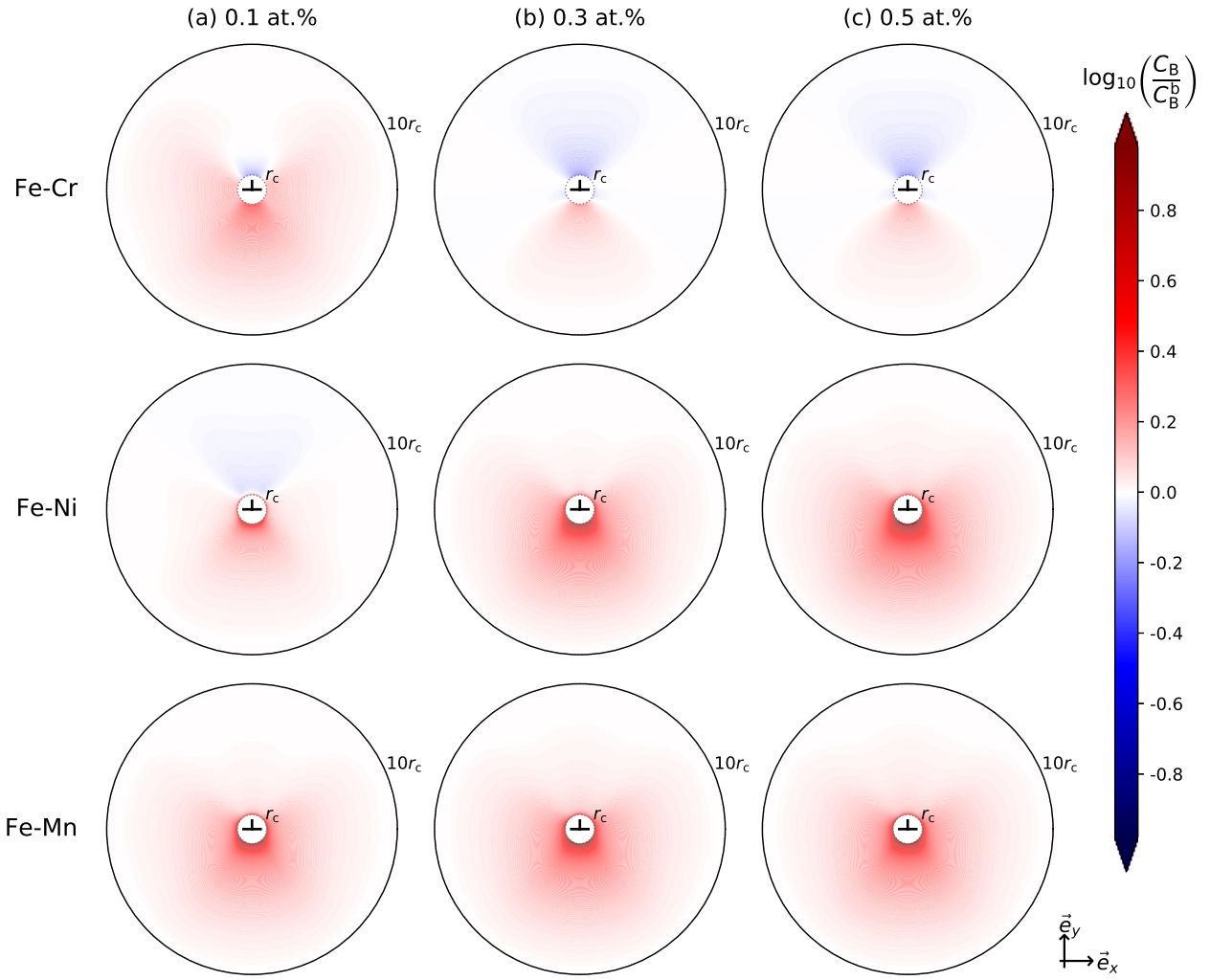


Figure 4.21: Atomic fraction maps of solute atoms $B \equiv \text{Cr, Ni, Mn}$ obtained in the various alloys and at different nominal solute concentrations. The results are obtained at $T = 600 \text{ K}$ and $\phi = 10^{-5} \text{ dpa/s}$. The dislocation density is set to $3.7 \times 10^{14} \text{ m}^{-2}$ ($R = 10 r_c$).

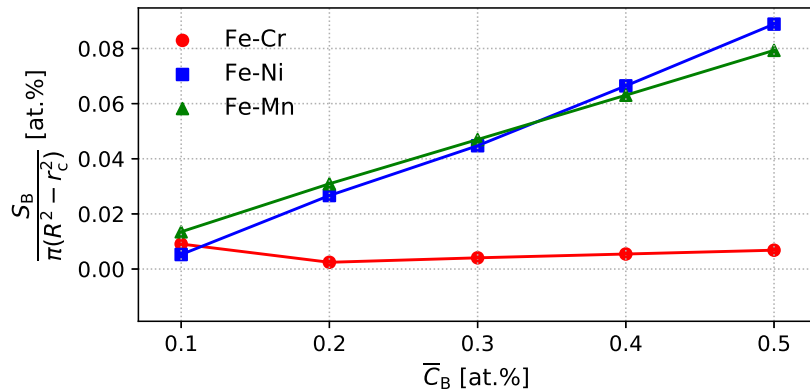


Figure 4.22: Solute radiation-induced segregation amounts of the various Fe-based alloys at 600 K as a function of \bar{C}_B . The dislocation density $\rho = 3.7 \times 10^{14} \text{ m}^{-2}$ ($R = 10 r_c$).

lattice site. In most previous studies, the latter contribution is ignored. This contribution reduces the sink bias factor, up to 400% at 400 K for an edge dislocation.

- In Fe-Cr, PD concentration profiles and trajectories near the edge dislocation are similar to those in Fe. Regarding RIS, a change of sign occurs in the compressive region, as highlighted in a recent study [286]. Moreover, the RIS amount is slightly increased in the presence of strain due to an increase of the diffusion driving force and elastodiffusion effects.
- In Fe-Ni, the fluxes of SIAs towards the edge dislocation are smaller than those in Fe. Moreover, the dislocation bias is negative when we ignore the strain contribution. When strain is included, the dislocation bias is positive as long as \bar{C}_{Ni} is below a threshold value (0.2 at.% at 600 K). Regarding RIS, a dislocation-induced strain significantly increases the amount of solute segregation (up to 300% at 400 K), mainly due to the elastodiffusion. The increase of RIS drops almost to zero at temperatures above 600 K. Note that, an analysis including strain effects of the experimental RIS in ion-irradiated Fe-Ni alloys at $T = 673$ K should not fundamentally change the results that we have presented in the previous chapter by relying on a strain-free model of RIS.
- In Fe-Mn, the fluxes of vacancies and SIAs are larger than those in Fe. When the strain effects are neglected, the Mn atoms lead to a positive dislocation bias. The bias factor is even greater when strain is applied. It is more than 200% of the one of Fe. Therefore, the addition of Mn atoms in microstructures with high dislocation density may promote swelling under irradiation. Regarding the RIS amount under applied strain, it is slightly larger than the one without strain. RIS increases mainly due to the strain effect on the diffusion driving forces, whereas, it is nearly not sensitive to the effects of elastodiffusion.

According to the *ab initio* database of the solute-PD interactions, Cu and Si show strong binding tendency with vacancies, while no interaction with SIAs. These properties are similar to those of Ni. Therefore, we expect the solute effects on the concentration profiles of PDs and solute atoms near an edge dislocation in Fe-Cu and Fe-Si alloys, to be close to those in Fe-Ni. P atoms, which interact positively with both SIAs and vacancies, should behave like Mn atoms.

Conclusions and prospects

This work is dedicated to a comprehensive modeling of the Radiation-Induced Segregation (RIS) phenomenon, including the effects of irradiation and stress on the diffusion properties. The purpose of this work is first to propose an analytical model to calculate the diffusion properties including both thermal and athermal mechanisms under irradiation. The second purpose is to develop a RIS model accounting for the full set of point-defect (PD) reactions and solute-PD interactions in a dilute binary alloy. Finally, we investigate the elastic and solute effects on diffusion and RIS properties of PDs and solute atoms in a few dilute Ni- and Fe-based alloys.

Summary

We start from the atomic-scale modeling of PD and atomic diffusion under irradiation. The on-lattice frequencies of PD and atomic jumps are modeled as thermally-activated jump frequencies. Athermal atomic motions triggered by a displacement cascade are modeled as forced atomic relocations (FARs). Both mechanisms are included in the self-consistent mean-field (SCMF) theory. An implementation of the extended SCMF theory into the KineCluE code yields FAR-dependent transport coefficients in agreement with Monte Carlo simulations. A systematic parametric study is performed to emphasize the effect of FAR distances and the solute-defect interaction on the diffusion properties of dilute binary model alloys. Then, from our analytical modeling of the far from equilibrium properties of a fictive two-frequency model by means of the fluctuation theory [222], we show the extension of the SCMF diffusion theory to athermal diffusion mechanisms, is actually the first step toward a kinetic modeling of far from equilibrium alloys.

In addition to the phenomenological transport coefficients, the magnitude of RIS is directly related to the kinetics of PDs. We derive an analytical model of PD and solute steady-state RIS profiles accounting for the PD production rate, the SIA-vacancy mutual recombination reactions, and the overall sink strength of the microstructure controlling the elimination of PDs at structural defects. The RIS model accounts for the FAR effects, through the modification of both the thermodynamic driving forces and the transport coefficients. We use the KineCluE code to compute the latter from the solute-PD binding energies, and PD jump frequencies. We present a DFT-based investigation of diffusion and RIS properties in a few dilute Ni- and Fe-based binary alloys, in the form of quantitative temperature/radiation flux/sink strength

maps. In each of the particular kinetic regimes for which one of the reactions of the PDs is dominated over the others, we propose an analytical expression of the stationary PD and solute concentration profiles in the vicinity of a planar extended defect. To account for the effect of a stress/strain field generated by an edge dislocation on the PD elimination rate and RIS, we properly define the PD diffusion driving force under applied strain, use the KineCluE code to calculate the strain-dependent transport coefficients from a DFT database of the PD and solute elastic dipoles, and solve the elastodiffusion equations by finite difference. We perform a parametric study by switching off the various anisotropic elastic properties of the matrix and PDs, in order to highlight the contribution of the elastic anisotropy on the elastodiffusion properties, the dislocation bias, and RIS.

Concluding remarks

We summarize below the most relevant results obtained in this work.

- Using the extended SCMF theory, we demonstrate that FAR does not produce a simple additive term to the transport coefficients. When the magnitude of the relocation frequency is in the range of the thermal frequencies, FAR interacts with the thermal diffusion mechanism, yielding non-symmetric off-diagonal transport coefficients and a solute tracer diffusion coefficient deviating from a direct sum of the contributions of thermal jumps and FAR. This deviation increases with the solute kinetic correlations.
- From our analytical RIS models, we show that RIS profiles vary with the chemical nature of the solute atom, especially for solute RIS profiles which are very alloy-specific. In general, the RIS of PDs and solutes is favored in the sink domain because PD elimination at sink is the dominant PD reactions. The comparison between our results and a previous study [30] highlights the sensitivity of RIS to recombination reactions at low temperature and sink strength. The effect of FAR on solute RIS is significant at high sink strength: FAR leads to a sharp decrease of solute RIS, especially in Ni-Cr, Ni-Ti, Fe-Ni and Fe-Cr alloys. Moreover, the Ni-based alloys are more sensitive to FAR effects than the Fe-based ones because of higher PD migration barriers in Ni. The calculated solute RIS profiles in Ni-0.4Ti and Fe-3.3Ni (in at.%) alloys are in good agreement with the experimental ones, both for the sign and the amount of RIS.
- A direct application of our RIS model is to provide quantitative temperature-shift criteria for the comparison between neutron and ion irradiation. We emphasize that these criteria are alloy and kinetic-domain specific. In the case where we may ignore the variation of sink strength with temperature and dose rate, for instance in alloys with a high sink density, we rely on the temperature–radiation flux–sink strength maps to deduce the temperature shifts. Otherwise, in most cases, an estimation of the temperature shift requires an explicit relationship between the sink strength, temperature, and dose rate.
- The significant anisotropy of the elastic constants in Fe affects the strain field generated by structural defects. Stable and saddle-point PD anisotropy affects the elastodiffusion behaviors and the diffusion driving force. These two kinds of anisotropy tend to increase

the sink strength and change the bias factor of an edge dislocation. Moreover, the dislocation strain field dramatically changes the diffusion trajectories of PDs and solute atoms and their steady-state distribution. The interplay between solute and strain effects on diffusion leads to strong modifications of the sink strength and bias. In Fe-Cr, the sign of RIS is changed in the compressive region. In Fe-Ni, the sign of the dislocation bias is governed by a competition between solute and strain effects. The former yields a negative dislocation bias, while the latter yields a positive one. In Fe-Mn, the dislocation bias is significantly promoted by an addition of Mn (up to 200%).

Prospects

This work provides various prospects.

- The defect production and local recombination within the displacement cascade which do not involve long range diffusion must be treated at the same level as diffusive fluxes. These reactions have three contributions, they partially control (i) the solute-point defect cluster distribution, (ii) the flux coupling, and (iii) the total concentration of point defects. Due to technical issues, the KineCluE code does not tackle non-conservative reactions such as the production and elimination of PDs. Hence, we have chosen to introduce different models of FARs of vacancies in order to treat contributions (i) and (ii) at the same level as diffusive fluxes. Whereas, we introduce a mean field rate theory model to account for contribution (iii) at the upper scale. We justify this approach by relying on a dilute approximation. At the end of the displacement cascade, PDs are well-separated. The local recombination occurred in the displacement cascade is folded into our FAR models. Then, the long-range recombination, which requires long-range diffusion, is treated with the mean-field rate model. For a more exact modeling of the local recombination, we should introduce this mechanism into the KineCluE code. For instance, we could consider the configuration of a SIA-vacancy pair below the recombination radius as a dissociated configuration.
- The analytical two-frequency model of a far from equilibrium system could be applied to more complex diffusion models. From our KineCluE module dedicated to the modeling of diffusion mechanisms that do not obey the microscopic detailed balance, we could extend the code to the computation of higher-rank transport tensors representing the variation (higher order derivative) of the transport coefficients with respect to the thermodynamic driving forces. This way, we could build an efficient code for the investigation of far-from-equilibrium kinetics in alloys.
- Our RIS model has been applied to dilute Fe-based and Ni-based binary alloys. We can easily apply it to study RIS in any other alloys, provided that one is able to compute the Onsager transport matrix. Using the same KineCluE code, we could investigate the impact of multiple solute or PD clusters on RIS.
- Radiation-induced solute enrichment at sinks can exceed the alloy solubility limit and trigger the precipitation of a secondary phase. We could apply different boundary conditions

on the solute RIS profile to simulate such a radiation-induced precipitation phenomenon, as for example a backward solute diffusion at sink set to zero, and a matter balance accounting for the precipitate growth. Though a stochastic method such as Atomic Kinetic Monte Carlo should be used to study the nucleation stage of a precipitation phenomenon. This method naturally accounts for the concentration fluctuations initiating a precipitation phenomenon.

- The equilibrium segregation of solutes resulting from the interactions of solutes with the sink other than the elastic interactions, is neglected in our RIS model. We justify this approximation by assuming that the average width of the RIS profiles is much larger than that of the equilibrium segregation; thereby the total amount of solute RIS segregation should not be much affected by the equilibrium segregation. Nevertheless, the solute concentration at the grain boundary plane or at the dislocation core may be the essential quantity that determines the mechanical or corrosion-resistance properties of a material. For a more advanced RIS model, we could perform an *ab initio* investigation of the solute segregation energies and then, introduce an equilibrium solute concentration at sink as a boundary condition of our continuous approach.
- In Chapter 4, we focus on the role of elasticity on solute and PD RIS around an edge dislocation in a few Fe-based alloys. The phase-field method could be used to effectively solve the present RIS-diffusion equation, in order to model systems with larger length scales up to millimeters, and simulate more complex geometries, such as RIS of a sink population including grain boundaries, interfaces, and dislocation loops. The strong alloying effects on sink strength and bias that we have highlighted should be taken into account in irradiation models involving sink strengths.
- A biased absorption of PDs implies a climbing mechanism of the dislocation that is not explicitly taken into account in our approach. Though solute RIS may affect the dislocation climb mechanism and vice versa. According to a recent study [286], the climbing mechanism may affect the solute RIS profiles of a dipole of dislocations. On the other hand, the dislocation core structure may be changed by solute RIS, thereby affecting its climbing mechanisms and its efficiency regarding PD absorption. An accelerated Molecular Dynamics method such as kinetic Activation-Relaxation Technique [287] could be a useful method to model the interplay between the structural evolution of the sink and RIS. Though empirical potentials able to reproduce the detailed kinetic properties of a dilute alloy do not exist yet.

Appendix A

Elastic dipole tensors of solute-point defect pairs

In this appendix, we present the elastic dipole tensors of the solute-PD pair configurations at stable and saddle points in dilute Fe-based alloys. These tensors depend on the direction of the solute-PD pairs and PD jumps. We give the nomenclature of the solute-dumbbell pair in Fig. A.1, the dumbbell jumps in Fig. A.2, the stable solute-vacancy pair configurations in Fig. A.3, and the vacancy jumps in Fig. A.4. These directions correspond to the ones of the elastic dipole tensors shown in the following tables. The dipoles associated with the other configuration and jump directions are deduced by applying symmetry operations to the given ones.

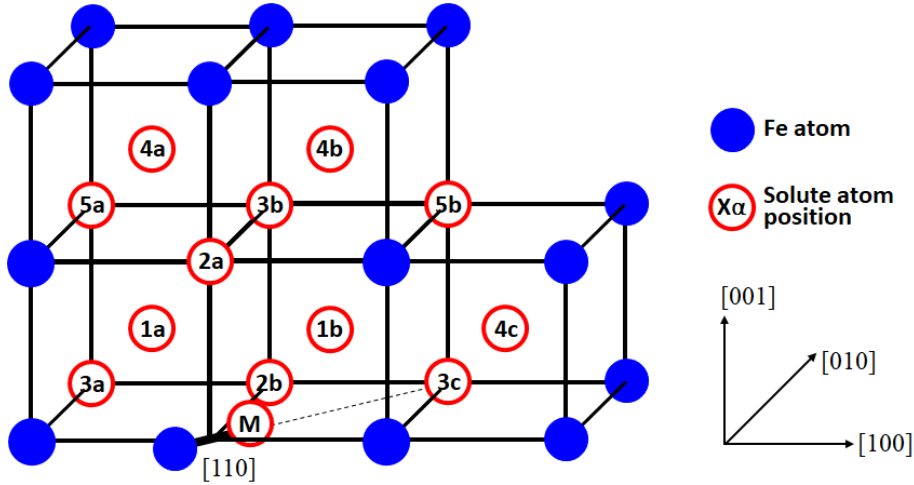


Figure A.1: Solute-SIA pair configurations corresponding to the results of stable-point elastic dipole tensors listed in Tabs. A.1, A.5, and A.9

The elastic dipoles of solute-SIA pairs in the various Fe-based alloys are listed respectively in Tab. A.1, Tab. A.5, Tab. A.9 for the stable-point configurations, and respectively in Tab. A.2, Tab. A.6, Tab. A.10 for the saddle-point configurations. The elastic dipoles of solute-vacancy pairs in the various Fe-based alloys are listed respectively in Tab. A.3, Tab. A.7, Tab. A.11

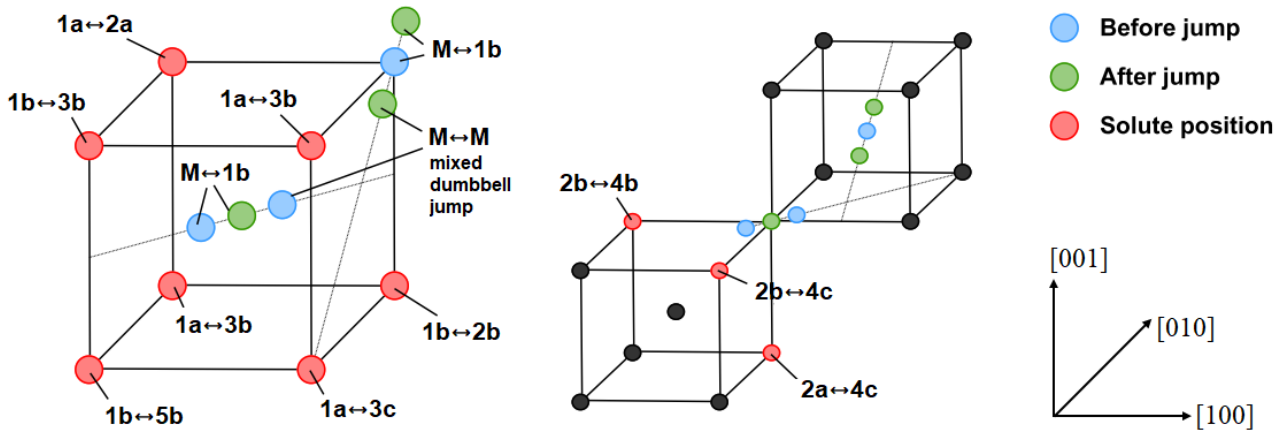


Figure A.2: Solute-SIA pair jumps corresponding to the results of saddle-point elastic dipole tensors listed in Tab. A.2, A.6, and A.10

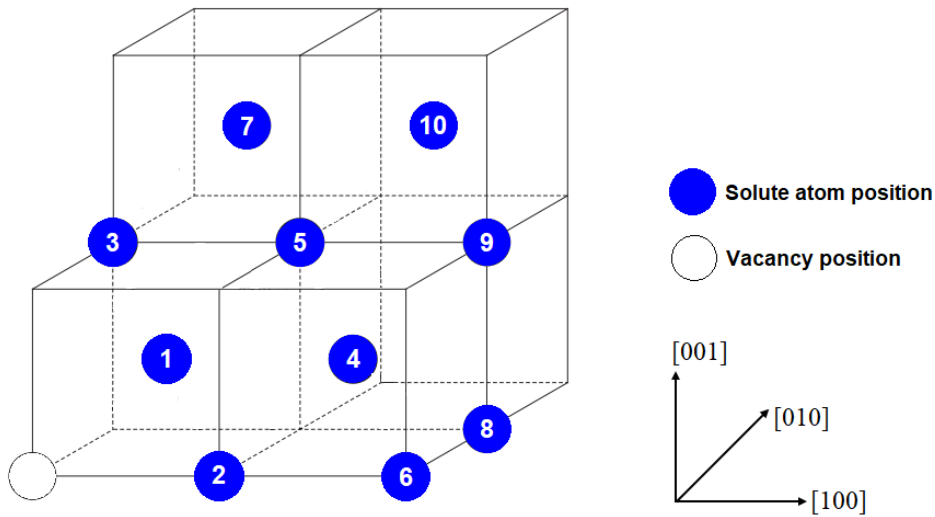


Figure A.3: Solute-vacancy pair configurations corresponding to the results of stable-point elastic dipole tensors listed in Tab. A.3, A.7, and A.11

for the stable-point configurations, and respectively in Tab. A.4, Tab. A.8, Tab. A.12 for the saddle-point configurations.

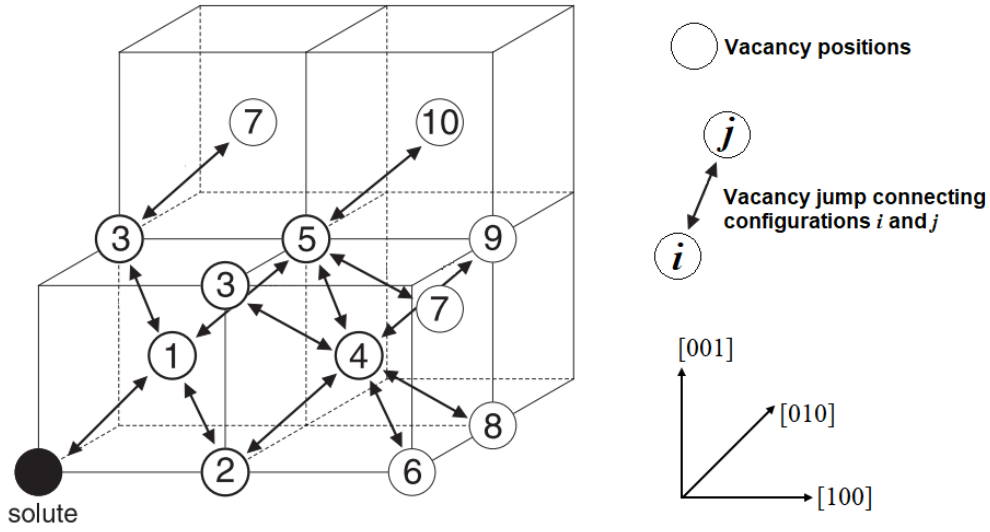


Figure A.4: Solute-vacancy pair jumps corresponding to the results of saddle-point elastic dipole tensors listed in Tab. A.4, A.8, and A.12

Table A.1: Stable-point elastic dipole tensors of solute-SIA pair configuration i in Fe-Cr (eV). Only the six independent coefficients of the dipole tensors are presented.

i	\underline{P}_{11}	\underline{P}_{22}	\underline{P}_{33}	\underline{P}_{23}	\underline{P}_{13}	\underline{P}_{12}	$\text{Tr}(\underline{P})/3$
M	23.99	23.99	25.55	0.00	0.00	4.81	24.51
1a	23.76	23.76	28.59	0.09	-0.09	4.99	25.37
1b	22.91	22.91	27.06	-0.62	-0.62	4.23	24.29
2a	23.99	23.99	28.50	0.00	0.00	4.85	25.49
2b	23.64	23.63	27.78	-0.01	-0.01	4.76	25.02
3a	24.40	24.40	28.49	0.00	0.00	4.73	25.76
3b	24.22	24.06	28.28	0.19	0.02	4.69	25.52
3c	24.54	24.54	27.98	0.00	0.00	5.42	25.69
4a	24.39	24.39	28.57	0.04	-0.04	4.70	25.78
4b	24.55	24.55	28.33	0.04	0.04	4.82	25.81
4c	24.24	24.30	28.42	-0.08	0.05	4.70	25.65
5a	24.38	24.38	28.75	0.16	-0.16	4.53	25.84
5b	23.96	23.96	28.03	-0.15	-0.15	4.17	25.32

Table A.2: Saddle-point elastic dipole tensors of SIA jumps connecting the configurations i and j in Fe-Cr (eV). Only the six independent coefficients of the dipole tensors are presented. For the mixed dumbbell jump, $i = j = \text{M}$.

i	j	\underline{P}_{11}	\underline{P}_{22}	\underline{P}_{33}	\underline{P}_{23}	\underline{P}_{13}	\underline{P}_{12}	$\text{Tr}(\underline{P})/3$
M	M	24.65	25.73	24.65	3.76	1.01	3.76	25.01
M	1b	25.15	24.46	25.00	3.19	-0.02	2.90	24.87
1a	2a	25.51	24.75	25.94	3.10	-0.82	2.82	25.40
1a	2b	25.44	24.59	25.77	2.90	-0.61	2.93	25.26
1a	3b	25.47	24.73	25.74	2.81	-0.48	2.97	25.31
1a	3c	25.59	24.85	26.11	3.48	-0.85	3.00	25.51
1b	2b	25.37	24.08	25.20	3.44	-0.24	2.65	24.88
1b	3b	24.97	24.12	25.18	3.19	-0.78	2.64	24.76
1b	5b	24.55	23.72	25.03	2.50	-1.11	2.46	24.43
2a	4c	26.03	24.79	26.20	2.72	-0.67	3.21	25.67
2b	4b	25.48	24.65	26.03	2.80	-0.80	3.02	25.38
2b	4c	25.69	24.50	26.06	2.74	-0.84	3.09	25.42

Table A.3: Stable-point elastic dipole tensors of the i -NN solute-vacancy pair configuration in Fe-Cr (eV). Only the six independent coefficients of the dipole tensors are presented.

i	\underline{P}_{11}	\underline{P}_{22}	\underline{P}_{33}	\underline{P}_{23}	\underline{P}_{13}	\underline{P}_{12}	$\text{Tr}(\underline{P})/3$
1	-0.46	-0.46	-0.46	-0.37	-0.37	-0.37	-0.46
2	0.10	-0.27	-0.27	0.00	0.00	0.00	-0.15
3	-0.11	-0.34	-0.34	-0.03	0.00	0.00	-0.26
4	-0.10	-0.23	-0.23	-0.12	-0.06	-0.06	-0.19
5	-0.23	-0.23	-0.23	-0.18	-0.18	-0.18	-0.23
6	-0.01	0.06	0.06	0.00	0.00	0.00	0.04
7	-0.03	-0.05	-0.05	-0.12	0.00	0.00	-0.04
8	0.01	-0.02	0.04	0.00	0.00	-0.04	0.01
9	-0.13	-0.13	-0.13	-0.09	-0.04	-0.04	-0.13
10	-0.26	-0.26	-0.26	-0.11	-0.11	-0.11	-0.26

Table A.4: Saddle-point elastic dipole tensors of vacancy jumps connecting the i - and j -NN configurations in Fe-Cr (eV). Only the six independent coefficients of the dipole tensors are presented. For the solute-vacancy exchange, $i = j = 1$.

i	j	\underline{P}_{11}	\underline{P}_{22}	\underline{P}_{33}	\underline{P}_{23}	\underline{P}_{13}	\underline{P}_{12}	$\text{Tr}(\underline{P})/3$
1	1	-1.31	-1.31	-1.31	-1.51	-1.51	-1.51	-1.31
1	2	-0.04	-0.23	-0.23	-1.84	1.35	1.35	-0.17
1	3	-0.14	-0.42	-0.42	-1.79	1.23	1.23	-0.33
1	5	-0.35	-0.35	-0.35	-1.99	-1.99	-1.99	-0.35
2	4	0.44	-0.01	-0.01	-1.71	-1.56	-1.56	0.14
3	4	0.27	0.41	0.26	1.55	1.61	-1.52	0.32
3	7	0.60	0.34	0.34	-1.75	-1.59	-1.59	0.43
4	5	0.72	0.67	0.67	-1.85	1.51	1.51	0.69
4	6	0.38	0.32	0.32	-1.60	1.63	1.63	0.34
4	8	0.49	0.33	0.35	1.51	1.59	-1.70	0.39
4	9	0.55	0.41	0.41	-1.73	-1.71	-1.71	0.46
5	7	0.18	0.18	0.24	1.49	1.49	-1.75	0.20
5	10	0.01	0.01	0.01	-1.82	-1.82	-1.82	0.01

Table A.5: Stable-point elastic dipole tensors of solute-SIA pair configuration i in Fe-Ni (eV). Only the six independent coefficients of the dipole tensors are presented.

i	\underline{P}_{11}	\underline{P}_{22}	\underline{P}_{33}	\underline{P}_{23}	\underline{P}_{13}	\underline{P}_{12}	$\text{Tr}(\underline{P})/3$
M	25.41	25.41	28.85	0.00	0.00	4.97	26.56
1a	24.71	24.71	29.30	-0.13	0.13	5.24	26.24
1b	25.10	25.10	29.72	0.04	0.04	4.80	26.64
2a	25.58	25.58	29.69	0.00	0.00	4.95	26.95
2b	25.12	24.78	29.10	0.00	0.00	4.63	26.34
3a	26.08	26.08	30.16	0.00	0.00	4.77	27.44
3b	26.11	25.67	29.92	0.11	-0.05	4.59	27.24
3c	25.67	25.67	29.94	-0.01	-0.01	5.03	27.09
4a	26.32	26.32	30.25	-0.01	0.01	4.82	27.63
4b	25.80	25.80	29.41	-0.01	-0.01	4.69	27.01
4c	25.59	25.88	30.07	-0.08	0.00	4.64	27.18
5a	26.13	26.13	30.46	0.11	-0.11	4.57	27.57
5b	26.19	26.19	30.04	-0.01	-0.01	4.80	27.48

Table A.6: Saddle-point elastic dipole tensors of SIA jumps connecting the configurations i and j in Fe-Ni (eV). Only the six independent coefficients of the dipole tensors are presented. For the mixed dumbbell jump, $i = j = \text{M}$.

i	j	\underline{P}_{11}	\underline{P}_{22}	\underline{P}_{33}	\underline{P}_{23}	\underline{P}_{13}	\underline{P}_{12}	$\text{Tr}(\underline{P})/3$
M	M	28.68	27.32	28.71	3.69	0.98	3.72	28.24
M	1b	27.44	27.05	28.21	2.48	-0.65	3.78	24.87
1a	2a	27.58	27.41	28.26	3.32	-0.78	2.68	27.75
1a	2b	27.38	26.52	27.41	3.07	-0.95	3.02	27.10
1a	3b	28.22	27.55	28.78	2.56	-0.46	2.58	28.18
1a	3c	27.77	26.27	27.85	3.01	-0.77	2.94	27.30
1b	2b	27.71	27.01	28.25	2.45	-0.95	2.98	27.66
1b	3b	26.83	25.94	29.10	3.08	-0.53	2.35	27.29
1b	5b	26.54	25.70	28.06	3.14	-0.83	2.46	26.77
2a	4c	29.80	28.66	29.73	2.86	-0.55	3.28	29.40
2b	4b	28.07	27.12	28.49	2.74	-0.88	2.98	27.89
2b	4c	28.87	27.33	29.04	2.93	-0.87	2.88	28.41

Table A.7: Stable-point elastic dipole tensors of the i -NN solute-vacancy pair configuration in Fe-Ni (eV). Only the six independent coefficients of the dipole tensors are presented.

i	\underline{P}_{11}	\underline{P}_{22}	\underline{P}_{33}	\underline{P}_{23}	\underline{P}_{13}	\underline{P}_{12}	$\text{Tr}(\underline{P})/3$
1	-0.89	-0.89	-0.89	-0.26	-0.26	-0.26	-0.89
2	0.44	0.06	0.06	0.00	0.00	0.00	0.19
3	0.26	0.11	0.11	-0.15	0.00	0.00	0.16
4	0.41	0.31	0.31	-0.01	-0.09	-0.09	0.35
5	0.10	0.10	0.10	-0.24	-0.24	-0.24	0.10
6	0.24	0.39	0.39	0.00	0.00	0.00	0.34
7	0.35	0.41	0.41	-0.13	-0.03	-0.03	0.39
8	0.32	0.30	0.38	0.00	0.00	-0.04	0.33
9	0.28	0.32	0.32	-0.04	-0.03	-0.03	0.31
10	0.47	0.47	0.47	-0.04	-0.04	-0.04	0.47

Table A.8: Saddle-point elastic dipole tensors of vacancy jumps connecting the i - and j -NN configurations in Fe-Ni (eV). Only the six independent coefficients of the dipole tensors are presented. For the solute-vacancy exchange, $i = j = 1$.

i	j	\underline{P}_{11}	\underline{P}_{22}	\underline{P}_{33}	\underline{P}_{23}	\underline{P}_{13}	\underline{P}_{12}	$\text{Tr}(\underline{P})/3$
1	1	-1.17	-1.17	-1.17	-1.64	-1.64	-1.64	-1.17
1	2	0.30	0.17	0.17	-1.80	1.41	1.41	0.21
1	3	0.05	-0.25	-0.25	-2.15	1.41	1.41	-0.15
1	5	-0.50	-0.50	-0.50	-1.88	-1.88	-1.88	-0.50
2	4	1.50	0.55	0.55	-1.73	-1.50	-1.50	0.86
3	4	0.90	1.00	0.86	1.71	1.60	-1.54	0.92
3	7	0.96	0.84	0.84	-1.89	-1.62	-1.62	0.88
4	5	0.96	0.93	0.93	-1.85	1.54	1.54	0.94
4	6	0.62	0.74	0.74	-1.53	1.59	1.59	0.70
4	8	0.99	0.89	0.90	1.57	1.54	-1.75	0.93
4	9	0.97	0.90	0.90	-1.64	-1.74	-1.74	0.92
5	7	0.72	0.72	0.81	1.48	1.48	-1.77	0.75
5	10	0.45	0.45	0.45	-1.85	-1.85	-1.85	0.45

Table A.9: Stable-point elastic dipole tensors of solute-SIA pair configuration i in Fe-Mn (eV). Only the six independent coefficients of the dipole tensors are presented.

i	\underline{P}_{11}	\underline{P}_{22}	\underline{P}_{33}	\underline{P}_{23}	\underline{P}_{13}	\underline{P}_{12}	$\text{Tr}(\underline{P})/3$
M	23.87	23.87	27.20	0.00	0.00	4.65	24.98
1a	24.96	24.96	30.22	-0.24	0.24	5.50	26.72
1b	23.75	23.75	27.71	-0.50	-0.50	4.43	25.07
2a	25.42	25.42	29.49	0.00	0.00	4.90	26.78
2b	24.59	24.58	29.01	0.00	0.00	4.86	26.06
3a	25.66	25.66	29.80	0.00	0.00	4.77	27.04
3b	25.64	25.11	29.39	0.15	0.03	4.64	26.71
3c	25.44	25.44	29.88	-0.01	-0.01	5.19	26.92
4a	25.81	25.81	30.08	0.01	-0.01	4.70	27.23
4b	25.76	25.76	28.86	0.01	0.01	4.75	26.79
4c	25.30	25.69	29.90	-0.08	0.12	4.77	26.96
5a	25.78	25.78	30.28	0.13	-0.13	4.57	27.28
5b	25.18	25.18	29.02	-0.16	-0.16	4.27	26.46

Table A.10: Saddle-point elastic dipole tensors of SIA jumps connecting the configurations i and j in Fe-Mn (eV). Only the six independent coefficients of the dipole tensors are presented. For the mixed dumbbell jump, $i = j = \text{M}$.

i	j	\underline{P}_{11}	\underline{P}_{22}	\underline{P}_{33}	\underline{P}_{23}	\underline{P}_{13}	\underline{P}_{12}	$\text{Tr}(\underline{P})/3$
M	M	25.38	24.49	25.38	3.05	-0.45	3.05	25.02
M	1b	25.43	24.08	25.41	3.09	-0.83	2.53	24.97
1a	2a	25.22	24.89	25.92	3.10	-0.67	2.98	25.34
1a	2b	25.87	25.02	26.39	3.49	-0.95	2.92	25.76
1a	3b	26.59	26.45	27.24	3.07	-0.86	2.78	26.76
1a	3c	26.19	25.00	26.92	3.24	-0.80	3.06	26.04
1b	2b	25.34	24.00	24.80	3.16	-0.40	2.39	24.71
1b	3b	24.18	23.47	25.59	3.50	-0.79	2.04	24.41
1b	5b	25.99	25.37	27.19	2.88	-1.32	1.85	26.18
2a	4c	23.48	22.17	23.77	2.84	-0.63	2.71	23.14
2b	4b	26.40	26.16	27.48	2.85	-0.95	3.02	26.68
2b	4c	26.94	25.52	27.43	3.01	-1.11	3.04	26.63

Table A.11: Stable-point elastic dipole tensors of the i -NN solute-vacancy pair configuration in Fe-Mn (eV). Only the six independent coefficients of the dipole tensors are presented.

i	\underline{P}_{11}	\underline{P}_{22}	\underline{P}_{33}	\underline{P}_{23}	\underline{P}_{13}	\underline{P}_{12}	$\text{Tr}(\underline{P})/3$
1	-1.16	-1.16	-1.16	-0.57	-0.57	-0.57	-1.16
2	0.44	-0.38	-0.38	0.00	0.00	0.00	-0.11
3	0.03	-0.13	-0.13	-0.04	0.00	0.00	-0.07
4	-0.09	-0.34	-0.34	-0.04	-0.09	-0.09	-0.25
5	-0.12	-0.12	-0.12	-0.24	-0.24	-0.24	-0.12
6	-0.03	0.05	0.05	0.00	0.00	0.00	0.03
7	0.28	0.26	0.26	-0.17	-0.04	-0.04	0.27
8	0.09	0.02	0.10	0.00	0.00	-0.04	0.07
9	0.00	0.01	0.01	-0.10	-0.02	-0.02	0.01
10	-0.01	-0.01	-0.01	-0.11	-0.11	-0.11	-0.01

Table A.12: Saddle-point elastic dipole tensors of vacancy jumps connecting the i - and j -NN configurations in Fe-Mn (eV). Only the six independent coefficients of the dipole tensors are presented. For the solute-vacancy exchange, $i = j = 1$.

i	j	\underline{P}_{11}	\underline{P}_{22}	\underline{P}_{33}	\underline{P}_{23}	\underline{P}_{13}	\underline{P}_{12}	$\text{Tr}(\underline{P})/3$
1	1	-1.54	-1.54	-1.54	-1.78	-1.78	-1.78	-1.54
1	2	0.01	-0.66	-0.66	-1.92	1.17	1.17	-0.44
1	3	-0.30	-0.61	-0.61	-2.16	0.97	0.97	-0.50
1	5	-0.42	-0.42	-0.42	-2.23	-2.23	-2.23	-0.42
2	4	1.10	-0.20	-0.20	-1.74	-1.51	-1.51	0.23
3	4	0.43	0.59	0.40	1.59	1.64	-1.45	0.47
3	7	0.68	0.54	0.54	-1.82	-1.61	-1.61	0.58
4	5	0.46	0.35	0.35	-1.81	1.50	1.50	0.39
4	6	0.36	0.42	0.42	-1.53	1.59	1.59	0.40
4	8	0.79	0.52	0.53	1.59	1.55	-1.76	0.62
4	9	0.75	0.51	0.51	-1.70	-1.74	-1.74	0.59
5	7	0.66	0.66	0.75	1.50	1.50	-1.76	0.69
5	10	0.47	0.47	0.47	-1.90	-1.90	-1.90	0.47

Appendix B

Résumé substantiel

Les défauts ponctuels (DPs) sont massivement générés dans les matériaux sous irradiation [1–3] ou lors de déformations plastiques sévères telles que la déformation sous cisaillement [4, 5], la déformation en torsion [6, 7] et le procédé de broyage [8–10]. L’irradiation produit des paires de Frenkel de lacune et d’auto-interstitiel. Les lacunes et auto-interstitiels sont tous deux des défauts ponctuels du réseau cristallin. La lacune correspond à un site inoccupé du cristal, alors que l’auto-interstitiel correspond à un atome en trop qui n’est pas localisé sur un site du réseau cristallin. Les DPs diffusent en échangeant avec les atomes. Ils interagissent entre eux, ou avec les atomes de soluté, ainsi qu’avec la microstructure du matériau [11]. Les défauts ponctuels sont absorbés par les défauts structuraux étendus, comme par exemple, les joints de grains et les lignes de dislocation, qui agissent comme des puits de DPs. L’élimination des DPs au niveau des défauts étendus induit des flux permanents de DPs du volume vers les puits. En s’échangeant avec les atomes voisins, les DPs produisent des flux nets d’atomes : c’est ce que l’on appelle le phénomène de couplage de flux. Contrairement aux DPs, les flux d’atomes de soluté peuvent se produire dans les deux sens, vers le puits ou dans le sens opposé, selon le signe des corrélations cinétiques soluté-lacune. Le couplage de flux est le principal processus cinétique contrôlant la redistribution des atomes du soluté dans les alliages soumis à un excès de DP [12–20].

Dans les matériaux sous irradiation, la redistribution des atomes de soluté au voisinage des puits de DP est un processus hors d’équilibre appelé ségrégation induite par irradiation (SII). Non seulement les espèces chimiques mais aussi les DPs forment un profil de concentration au niveau des puits. Nous avons choisi de les désigner respectivement par SII des DPs et SII des solutés. La SII des DPs est systématiquement négative : leur profil de concentration décroît, de leur concentration de volume à leur concentration d’équilibre au niveau des puits. La SII des solutés résulte de la SII des DPs. Celle-ci se produit à chaque puits de DPs, ceci même

à une très faible dose d'irradiation [21]. Par conséquent, la SII est souvent un phénomène précurseur de la précipitation hétérogène de phases secondaires aux puits de DP [19]. La SII peut entraîner de fortes modifications des propriétés mécaniques, de la résistance à la corrosion et des propriétés dimensionnelles des matériaux [11].

Il existe des études expérimentales qui étudient la variation de la SII avec la nature de la microstructure formée sous irradiation et aux conditions d'irradiation. Ces études montrent que la SII est sensible à la nature des particules d'irradiation [22, 23], à la dose d'irradiation et au taux d'endommagement [24, 25], et à la température [16, 26]. Cependant, il est toujours très difficile d'obtenir une estimation précise de la quantité de ségrégation des DP et des atomes de solutés dans les différentes conditions. Il convient donc de compléter ces données par des études théoriques. Jusqu'à présent, il n'existe pas de méthode de modélisation de la SII prenant en compte l'ensemble des réactions entre les DP, les atomes de solutés et les défauts étendus.

Tant que la SII n'est pas couplée à un phénomène de précipitation, les profils de la SII peuvent être obtenus en résolvant les équations de diffusion du DP et du soluté à proximité des puits de DP. Les principaux paramètres d'entrée des équations de diffusion sont les coefficients de transport (i.e., les coefficients phénoménologiques ou les coefficients d'Onsager) des systèmes. Ces coefficients résultant du transport atomique sont affectés par l'irradiation et le champ de contrainte induit par les défauts structuraux.

L'irradiation introduit de nouveaux mécanismes de transport atomique—les déplacements atomiques forcés (DAFs), qui impliquent le mouvement collectif des atomes dans des cascades de déplacement sous irradiation. Contrairement aux mécanismes activés thermiquement qui conduisent le système vers l'équilibre, les DAFs sont principalement athermiques. Ils n'obéissent pas au bilan détaillé microscopique. Ils entrent en compétition avec les mécanismes de diffusion thermique en favorisant des configurations atomiques désordonnées [27]. La microstructure d'un matériau irradié résulte de la compétition entre les réactions des DP avec la microstructure, les DP et les atomes de soluté et la migration thermique et athermique des atomes. Les mécanismes athermiques empêchent l'utilisation des méthodes de diffusion standards. Le champ de contrainte-déformation généré par les défauts étendus modifie les propriétés de diffusion du DP et du soluté [28]. Un champ de contrainte-déformation hétérogène modifie également les forces motrices de la diffusion, c'est-à-dire les gradients de potentiel chimique [29].

Les objectifs de ce travail sont (i) détendre la théorie de champ-moyen auto-cohérent (SCMF, pour Self-Consistent Mean-Field en anglais) aux mécanismes de diffusion athermiques pour calculer les coefficients de transport à partir d'une base de données *ab initio* des fréquences de saut des DP ; (ii) de développer un modèle SII prenant en compte l'ensemble des réactions

des DP's et des interactions soluté-DP's dans les alliages dilués ; (iii) détudier les effets d'une déformation dans le domaine élastique sur la diffusion et les propriétés SII des DP's et des atomes du soluté. Chacun de ces objectifs fait l'objet d'un chapitre de thèse.

- Extension de la théorie de diffusion de champ moyen aux sauts athermiques : Nous commençons par la modélisation à l'échelle atomique des propriétés de diffusion des DP's et des atomes sous irradiation. Les probabilités de saut des DP's et des atomes sont modélisées comme des fréquences de saut thermiquement activées. Les sauts athermiques des atomes induits par une cascade de déplacements sont modélisés sous la forme d'une séquence d'événements DAFs avec une fréquence posée proportionnelle au taux d'endommagement. Nous étendons la théorie de diffusion SCMF aux événements DAFs. Une implémentation de ces développements théoriques dans le code KineCluE nous permet d'obtenir des coefficients de transport qui dépendent des fréquences DAFs, en accord avec les simulations de Monte Carlo. Une étude paramétrique systématique est réalisée pour mettre en évidence l'effet de la portée des sauts DAFs et de l'interaction soluté-DP sur les propriétés de diffusion des alliages binaires dilués. Dans une dernière partie de ce chapitre, nous replaçons nos développements théoriques dans le contexte plus général de la modélisation en physique statistique des phénomènes loin de l'équilibre [222]. A partir d'un modèle de fréquences de saut simplifié qui se limite à deux configurations atomiques d'une chaîne linéaire, la paire soluté-lacune associée et la paire soluté-lacune dissociée, nous dérivons des équations analytiques de l'évolution temporelle des probabilités d'occupation des sites de la chaîne. Nous montrons dans quel cas nous retrouvons les équations SCMF avec DAFs.
- Modèle SII dans les alliages dilués : L'amplitude d'une ségrégation induite SII d'atomes de soluté dépend des coefficients de transport mais aussi de la sursaturation de DP's. Nous dérivons un modèle analytique des profils de DP's en régime permanent, qui prend en compte le taux de production de DP's, les réactions de recombinaison mutuelle entre lacunes et auto-interstitiels, et la force de puits globale de la microstructure contrôlant le taux d'élimination des DP's sur les défauts étendus. Nous en déduisons le profil de ségrégation des atomes de soluté. Le modèle de SII tient compte des effets de DAFs, à travers la modification des forces motrices thermodynamiques et des coefficients de transport avec les fréquences DAFs. Nous utilisons le code KineCluE pour calculer les coefficients de transport à partir des énergies de liaison soluté-DP et des fréquences de saut des DP's en fonction de leur voisinage en atomes de soluté calculées ab initio. Nous obtenons ainsi une modélisation quantitative des propriétés de diffusion et de la SII dans les alliages binaires dilués à base de Ni et de Fe, sous la forme de cartes en température/flux d'irradiation/force du puits. Dans chacun des régimes cinétiques particuliers

pour lesquels l'une des réactions des DP's peut être considérée comme la réaction dominante qui contrôle la cinétique des DP's, nous proposons une expression analytique des profils stationnaires de concentration des DP's et des solutés au voisinage d'un défaut étendu planaire.

- Effect d'un champ de contrainte sur la SII : Pour prendre en compte l'effet d'un champ de contrainte/déformation généré par une dislocation coin sur le taux d'élimination de DP et la SII, nous corrigeons la définition de la force motrice de diffusion des DP's récemment proposée dans la littérature. Nous calculons le tenseur délastodiffusion à l'aide du code KineCluE et d'une base de données ab initio des dipôles élastiques des DP's et du soluté. Nous résolvons les équations d'élastodiffusion par différence finie. Nous réalisons une étude paramétrique en désactivant une par une les contributions anisotropes produites par les interactions élastiques entre le défaut structural, les atomes de soluté et les DP's, afin de mettre en évidence les contributions de l'anisotropie élastique sur les propriétés d'élastodiffusion, la SII, et le taux d'élimination des DP's sur la dislocation.

Nous résumons ci-dessous les résultats les plus importants obtenus dans le cadre de ce travail.

- En utilisant la théorie SCMF étendue, nous démontrons que les sauts DAF's ne se réduisent pas à un terme additif sur les propriétés de transport de l'alliage. Lorsque l'amplitude de la fréquence de DAF est du même ordre de grandeur ou plus grande que les fréquences thermiques, le mécanisme de saut DAF interagit avec le mécanisme de diffusion thermique, produisant ainsi une matrice de coefficients de transport non symétrique et un coefficient de diffusion de soluté qui s'écarte d'une somme directe d'un coefficient de diffusion thermique et d'un coefficient de diffusion effectif DAF. Ce caractère non additif augmente avec les corrélations cinétiques du soluté.
- À partir du modèle analytique de SII, nous montrons que les profils de SII varient grandement avec la nature chimique de l'atome de soluté introduit dans la matrice de fer. En général, la SII des DP's et des solutés est favorisée dans le domaine cinétique contrôlé par la réaction d'élimination des DP's aux puits. La comparaison entre nos résultats et une étude précédente [30] met en évidence la sensibilité de la SII aux réactions de recombinaison entre défauts ponctuels à basse température et aux réactions d'élimination des DP's aux puits. L'effet des sauts DAF sur la SII du soluté est d'autant plus important que la force de puits est élevée : les sauts DAF conduisent à une forte diminution de la SII du soluté, en particulier dans les alliages de Ni-Cr, Ni-Ti, Fe-Ni et Fe-Cr. En outre, les alliages à base de nickel sont plus sensibles aux effets du DAF que ceux à base de fer en raison de la barrière de migration des lacunes qui sont plus élevées dans le nickel. Les

profils de SII calculés pour les alliages Ni-0,4Ti et Fe-3,3Ni (en at.%) sont en bon accord avec ceux des alliages expérimentaux, tant pour le signe que pour la quantité de SII.

- Une application directe de notre modèle de SII consiste à fournir des critères quantitatifs de décalage en température pour la comparaison entre une irradiation neutronique et une irradiation aux ions. Nous soulignons que ces critères sont spécifiques à l'alliage et au domaine cinétique. Dans le cas où nous pouvons négliger la variation de la force de puits en fonction de la température et du flux d'irradiation, par exemple dans les alliages fortement écrouis, nous nous appuyons sur les cartes de température, flux d'irradiation et force de puits, pour déduire les décalages en température. Cependant, dans la plupart des cas, une estimation du décalage en température nécessite une modélisation poussée de la relation entre la force de puits, la température et le flux d'irradiation.
- L'anisotropie significative des constantes élastiques dans Fe affecte le champ de contrainte généré par les défauts structuraux. L'anisotropie du dipôle élastique des DP's en configuration stable et en configuration de col affecte les comportements d'élastodiffusion et la force motrice de diffusion. Ces deux types d'anisotropie ont tendance à augmenter l'efficacité d'un puits à absorber les DP's (augmentation de la force de puits) et à modifier le facteur de biais, c.-à-d. la différence d'efficacité d'absorption entre lacune et auto-interstitiel, d'une dislocation coin. De plus, le champ de contrainte de la dislocation modifie considérablement les trajectoires de diffusion des DP's et des atomes du soluté ainsi que leur distribution en régime permanent. L'interaction entre les effets du soluté et de la contrainte sur la diffusion entraîne une modification de la force de puits et du biais. Dans l'alliage Fe-Cr, le signe de la SII des atomes de chrome n'est pas le même dans les zones en compression et en tension autour de la dislocation coin. Dans l'alliage Fe-Ni, le signe du biais de dislocation dépend de la compétition entre les effets des atomes de soluté ségrégués au voisinage de la dislocation et du champ de déformation induit par la dislocation. Le premier aboutit à un biais de dislocation négatif, tandis que le second induit un biais positif. Dans l'alliage Fe-Mn, le biais de la dislocation augmente de manière significative en présence d'atomes Mn au voisinage de la dislocation.

Bibliography

- [1] P. K. Haff and Z. E. Switkowski. Ion-beam-induced atomic mixing. *J. Appl. Phys.*, 48(8):3383–3386, 1977.
- [2] Arthur T. Motta and Clément Lemaignan. A ballistic mixing model for the amorphization of precipitates in Zircaloy under neutron irradiation. *J. Nucl. Mater.*, 195(3):277–285, 1992.
- [3] R.S. AVERBACK and T. DIAZ DE LA RUBIA. Displacement Damage in Irradiated Metals and Semiconductors. *Solid State Phys.*, 27(2):281–402, mar 1998.
- [4] Nhon Q. Vo, Jian Zhou, Yinon Ashkenazy, Daniel Schwen, Robert S. Averback, and Pascal Bellon. Atomic mixing in metals under shear deformation. *Jom*, 65(3):382–389, 2013.
- [5] Yinon Ashkenazy, Nirab Pant, Jian Zhou, Pascal Bellon, and Robert S. Averback. Phase evolution of highly immiscible alloys under shear deformation: Kinetic pathways, steady states, and the lever-rule. *Acta Mater.*, 139:205–214, 2017.
- [6] M. Pouryazdan, D. Schwen, D. Wang, T. Scherer, H. Hahn, R. S. Averback, and P. Bellon. Forced chemical mixing of immiscible Ag-Cu heterointerfaces using high-pressure torsion. *Phys. Rev. B - Condens. Matter Mater. Phys.*, 86(14):1–8, 2012.
- [7] J. A. Beach, M. Wang, P. Bellon, S. Dillon, Yu Ivanisenko, T. Boll, and R. S. Averback. Self-organized, size-selection of precipitates during severe plastic deformation of dilute Cu-Nb alloys at low temperatures. *Acta Mater.*, 140:217–223, 2017.
- [8] P. Pochet, E. Tominez, L. Chaffron, and G. Martin. Order-disorder transformation in Fe-Al under ball milling. *Phys. Rev. B*, 52(6):4006, 1995.
- [9] T. Klassen, U. Herr, and R. S. Averback. Ball milling of systems with positive heat of mixing: Effect of temperature in Ag-Cu. *Acta Mater.*, 45(7):2921–2930, 1997.
- [10] Cury Suryanarayana. Mechanical alloying and milling. *Mech. Alloy. Milling*, 46:1–472, 2004.
- [11] Gary S Was. *Fundamentals of Radiation Materials Science*. Springer, Berlin, Heidelberg, 2007.
- [12] T. R. Anthony and R. E. Hanneman. Non-equilibrium segregation of impurities in quenched dilute alloys. *Scr. Metall.*, 2(11):611–614, 1968.

- [13] T. R. Anthony. Solute segregation in vacancy gradients generated by sintering and temperature changes. *Acta Metall.*, 17(5):603–609, 1969.
- [14] P. R. Okamoto and H. Wiedersich. Segregation of alloying elements to free surfaces during irradiation. *J. Nucl. Mater.*, 53(C):336–345, 1974.
- [15] A. Barbu and A. J. Ardell. Irradiation-induced precipitation in NiSi alloys. *Scr. Metall.*, 9(11):1233–1237, 1975.
- [16] P.R. Okamoto and L.E. Rehn. Radiation-induced segregation in binary and ternary alloys. *J. Nucl. Mater.*, 83:2–23, 1979.
- [17] Takahiko Kato, Heishichiro Takahashi, and Masakiyo Izumiya. Grain boundary segregation under electron irradiation in austenitic stainless steels modified with oversized elements. *J. Nucl. Mater.*, 189(2):167–174, 1992.
- [18] S. M. Bruemmer, E. P. Simonen, P. M. Scott, P. L. Andresen, G. S. Was, and J. L. Nelson. Radiation-induced material changes and susceptibility to intergranular failure of light-water-reactor core internals. *J. Nucl. Mater.*, 274(3):299–314, 1999.
- [19] M. Nastar and F. Soisson. *Radiation-induced segregation*, volume 1. Elsevier Inc., 2012.
- [20] Alan J. Ardell and Pascal Bellon. Radiation-induced solute segregation in metallic alloys. *Curr. Opin. Solid State Mater. Sci.*, 20(3):115–139, 2016.
- [21] Y. Dong, B.H. Sencer, F.A. Garner, and E.A. Marquis. Microchemical and microstructural evolution of aisi 304 stainless steel irradiated in ebr-ii at pwr-relevant dpa rates. *Journal of Nuclear Materials*, 467:692 – 702, 2015.
- [22] G. S. Was, J. T. Busby, T. Allen, E. A. Kenik, A. Jensson, S. M. Bruemmer, J. Gan, A. D. Edwards, P. M. Scott, and P. L. Andreson. Emulation of neutron irradiation effects with protons: Validation of principle. *J. Nucl. Mater.*, 300(2-3):198–216, 2002.
- [23] Z. Jiao, J. Michalicka, and G. S. Was. Self-ion emulation of high dose neutron irradiated microstructure in stainless steels. *J. Nucl. Mater.*, 501:312–318, 2018.
- [24] L.E. REHN, P R Okamoto, and H Wiedersich. DOSE DEPENDENCE OF RADIATION-INDUCED SEGREGATION IN Ni-1 at%Si. *J. Nucl. Mater.*, 80:172–179, 1979.
- [25] T. R. Allen, J. I. Cole, E. A. Kenik, and G. S. Was. Analyzing the effect of displacement rate on radiation-induced segregation in 304 and 316 stainless steels by examining irradiated EBR-II components and samples irradiated with protons. *J. Nucl. Mater.*, 376(2):169–173, 2008.
- [26] L. E. Rehn, P. R. Okamoto, D. I. Potter, and H. Wiedersich. Effect of solute misfit and temperature on irradiation-induced segregation in binary Ni alloys. *J. Nucl. Mater.*, 74(2):242–251, 1978.
- [27] Georges Martin and Pascal Bellon. Driven Alloys. *Solid State Phys.*, 50:189–331, 1996.
- [28] P. H. Dederichs and K. Schroeder. Anisotropic diffusion in stress fields. *Phys. Rev. B*, 17(6):2524–2536, 1978.

- [29] J. Lothe and J. P. Hirth. Dislocation Climb Forces. *J. Appl. Phys.*, 38(2):845–848, feb 1967.
- [30] Enrique Martínez, Oriane Senninger, Alfredo Caro, Frédéric Soisson, Maylise Nastar, and Blas P. Uberuaga. Role of Sink Density in Nonequilibrium Chemical Redistribution in Alloys. *Phys. Rev. Lett.*, 120(10):106101, mar 2018.
- [31] Wei Cai and William D. Nix. *Imperfections in Crystalline Solids*. Cambridge University Press, sep 2016.
- [32] C. P. Flynn, J. Bass, and D. Lazarus. The vacancy formation and motion energies in gold. *Philos. Mag.*, 11(111):521–538, mar 1965.
- [33] W.G. Wolfer. Fundamental Properties of Defects in Metals. In *Compr. Nucl. Mater.*, volume 1, pages 1–45. Elsevier, 2012.
- [34] W.M. Lomer. *Vacancies and other point defects in metals and alloys*. London, nov 1958.
- [35] F.W. Schapink. The vacancy concentration in dilute binary alloys. *Acta Metall.*, 14(9):1130–1131, sep 1966.
- [36] C. Kinoshita and T. Eguchi. Vacancy concentration and arrangement of atoms and vacancies in metals and alloys. *Acta Metall.*, 20(1):45–52, jan 1972.
- [37] M. F. Sykes, D. S. Gaunt, S. R. Mattingly, J. W. Essam, B. R. Heap, and C. J. Elliott. Derivation of low-temperature expansions for Ising model. V. Three-dimensional lattices-field grouping. *J. Phys. A Gen. Phys.*, 6(10):1498–1506, 1973.
- [38] F. Ducastelle. Order and Phase Stability in Alloys. pages 133–142. Springer, Berlin, Heidelberg, 1993.
- [39] Thomas Schuler, Dallas R. Trinkle, Pascal Bellon, and Robert Averback. Design principles for radiation-resistant solid solutions. *Phys. Rev. B*, 95(17), 2017.
- [40] Liangzhao Huang, Thomas Schuler, and Maylise Nastar. Atomic-scale modeling of the thermodynamic and kinetic properties of dilute alloys driven by forced atomic relocations. *Phys. Rev. B*, 100:224103, 2019.
- [41] Luca Messina, Thomas Schuler, Maylise Nastar, Mihai-Cosmin Marinica, and Pär Olsson. Solute Diffusion by Self-Interstitial Defects and Radiation-Induced Segregation in Ferritic Fe- X (X=Cr, Cu, Mn, Ni, P, Si) Dilute Alloys. *SSRN Electron. J.*, 2019.
- [42] Thomas Schuler, Caroline Barouh, Maylise Nastar, and Chu-Chun Fu. Equilibrium Vacancy Concentration Driven by Undetectable Impurities. *Phys. Rev. Lett.*, 115(1):015501, jun 2015.
- [43] J. Willard Gibbs. *The collected works of J. Willard Gibbs*. Yale Univ. Press, New Haven, 1948.
- [44] S Hofmann. Sputter depth profile analysis of interfaces. *Reports Prog. Phys.*, 61(7):827–888, jul 1998.

- [45] Frederic Christien, R. Le Gall, and G. Saindrenan. Phosphorus grain boundary segregation in steel 17-4 PH. *Scr. Mater.*, 48(3):301–306, feb 2003.
- [46] H BRONGERSMA, M DRAXLER, M DERIDDER, and P BAUER. Surface composition analysis by low-energy ion scattering. *Surf. Sci. Rep.*, 62(3):63–109, mar 2007.
- [47] Kaoru Nakajima, Shunto Nakanishi, Zdeněk Chval, Martin Lísal, and Kenji Kimura. Surface segregation in a binary mixture of ionic liquids: Comparison between high-resolution RBS measurements and molecular dynamics simulations. *J. Chem. Phys.*, 145(18):184704, nov 2016.
- [48] H. Tsubakino, A. Nogami, Y. Yamamoto, A. Yamamoto, M. Terasawa, T. Mitamura, A. Kinomura, and Y. Horino. Surface segregation phenomena of solute elements in AlPb and AlFe dilute binary alloys. *Appl. Surf. Sci.*, 238(1-4):464–468, nov 2004.
- [49] C. L. White. Grain boundary segregation and intergranular fracture in molybdenum. *Proc. R. Soc. London. A. Math. Phys. Sci.*, 370(1743):431–458, apr 1980.
- [50] F. Christien and R. Le Gall. Measuring surface and grain boundary segregation using wavelength dispersive X-ray spectroscopy. *Surf. Sci.*, 602(14):2463–2472, jul 2008.
- [51] P. Nowakowski, F. Christien, M. Allart, Y. Borjon-Piron, and R. Le Gall. Measuring grain boundary segregation using Wavelength Dispersive X-ray Spectroscopy: Further developments. *Surf. Sci.*, 605(7-8):848–858, apr 2011.
- [52] Pawel Nowakowski, Frédéric Christien, Marion Allart, and René Le Gall. Recent Developments in the Study of Grain Boundary Segregation by Wavelength Dispersive X-Ray Spectroscopy (WDS). *Defect Diffus. Forum*, 309-310:39–44, mar 2011.
- [53] Knut W. Urban. Studying Atomic Structures by Aberration-Corrected Transmission Electron Microscopy. *Science (80-.)*, 321(5888):506–510, jul 2008.
- [54] David N. Seidman. Three-Dimensional Atom-Probe Tomography: Advances and Applications. *Annu. Rev. Mater. Res.*, 37(1):127–158, aug 2007.
- [55] Didier Blavette, Talaat Al Kassab, Emanuel Cadel, Alexander Mackel, François Vurpillot, Mathieu Gilbert, Oana Cojocaru, and Bernard Deconihout. Laser-assisted atom probe tomography and nanosciences. *Int. J. Mater. Res.*, 99(5):454–460, may 2008.
- [56] Alfiya Akhatova, Frédéric Christien, Vincent Barnier, Bertrand Radiguet, Emmanuel Cadel, Fabien Cuvilly, and Philippe Pareige. Investigation of the dependence of phosphorus segregation on grain boundary structure in Fe-P-C alloy: ross comparison between Atom Probe Tomography and Auger Electron Spectroscopy. *Appl. Surf. Sci.*, 463(May 2018):203–210, jan 2019.
- [57] D. Blavette, E. Cadel, A. Fraczkiewicz, and A. Menand. Three-Dimensional Atomic-Scale Imaging of Impurity Segregation to Line Defects. *Science (80-.)*, 286(5448):2317–2319, dec 1999.

- [58] Eita Tochigi, Yuki Kezuka, Akiho Nakamura, Atsutomu Nakamura, Naoya Shibata, and Yuichi Ikuhara. Direct Observation of Impurity Segregation at Dislocation Cores in an Ionic Crystal. *Nano Lett.*, 17(5):2908–2912, may 2017.
- [59] G. Tréglia, B. Legrand, F. Ducastelle, A. Saúl, C. Gallis, I. Meunier, C. Mottet, and A. Senhaji. Alloy surfaces: segregation, reconstruction and phase transitions. *Comput. Mater. Sci.*, 15(2):196–235, jun 1999.
- [60] Guillermo Bozzolo, John Ferrante, Ronald D. Noebe, Brian Good, Frank S. Honey, and Phillip Abel. Surface segregation in multicomponent systems: Modeling of surface alloys and alloy surfaces. *Comput. Mater. Sci.*, 15(2):169–195, jun 1999.
- [61] V. Drchal, A. Pasturel, R. Monnier, J. Kudrnovský, and P. Weinberger. Theory of surface segregation in metallic alloys: The generalized perturbation method. *Comput. Mater. Sci.*, 15(2):144–168, jun 1999.
- [62] Micha Polak and Leonid Rubinovich. The interplay of surface segregation and atomic order in alloys. *Surf. Sci. Rep.*, 38(4-5):127–194, may 2000.
- [63] Jérôme Creuze. Atomic-Scale Modelling of Intergranular Segregation: The Case of Alloys with Strong Size-Effect. *Defect Diffus. Forum*, 203-205:3–36, feb 2002.
- [64] Florent Fournier Dit Chabert, Franck Tancret, Frédéric Christien, René Le Gall, and Jean-François Castagné. Finite element simulation of interfacial segregation in dilute alloys. *J. Mater. Sci.*, 42(23):9765–9774, dec 2007.
- [65] W. Schweika, K. Binder, and D. P. Landau. Surface-induced ordering in models for frustrated” face-centered-cubic alloys. *Phys. Rev. Lett.*, 65(26):3321–3324, dec 1990.
- [66] R. Lipowsky. Critical Surface Phenomena at First-Order Bulk Transitions. *Phys. Rev. Lett.*, 49(21):1575–1578, nov 1982.
- [67] Y. Teraoka and T Seto. Surface segregation and bulk phase separation in segregating alloys. *Surf. Sci.*, 255(3):209–218, sep 1991.
- [68] Y. Teraoka. $(\sqrt{3} \times \sqrt{3})R30^\circ$ substitutionally ordered structure on fcc (111) surfaces of binary alloys. *Surf. Sci.*, 235(2-3):249–258, sep 1990.
- [69] Jean-Marc Roussel and Pascal Bellon. Self-diffusion and solute diffusion in alloys under irradiation: Influence of ballistic jumps. *Phys. Rev. B*, 65(14):144107, apr 2002.
- [70] T. Diaz de la Rubia, R. S. Averback, R Benedek, and W E King. Role of thermal spikes in energetic displacement cascades. *Phys. Rev. Lett.*, 59(17):1930–1933, oct 1987.
- [71] Andrew E. Stuchbery and Eva Bezakova. Thermal-Spike Lifetime from Picosecond-Duration Preequilibrium Effects in Hyperfine Magnetic Fields Following Ion Implantation. *Phys. Rev. Lett.*, 82(18):3637–3640, may 1999.
- [72] R.E. Stoller. Primary Radiation Damage Formation. In *Compr. Nucl. Mater.*, pages 293–332. Elsevier, 2012.

- [73] John A Brinkman. On the Nature of Radiation Damage in Metals. *J. Appl. Phys.*, 25(8):961–970, aug 1954.
- [74] J. A. Brinkman. Production of Atomic Displacements by High-Energy Particles. *Am. J. Phys.*, 24(4):246–267, apr 1956.
- [75] T. W. Workman, Y. T. Cheng, W. L. Johnson, and MA. Nicolet. Effect of thermodynamics on ion mixing. *Appl. Phys. Lett.*, 50(21):1485–1487, may 1987.
- [76] Peter Jung. Average atomic-displacement energies of cubic metals. *Phys. Rev. B*, 23(2):664–670, jan 1981.
- [77] G. Wallner, M.S. Anand, L.R. Greenwood, M.A. Kirk, W. Mansell, and W. Waschkowski. Defect production rates in metals by reactor neutron irradiation at 4.6 K. *J. Nucl. Mater.*, 152(2-3):146–153, may 1988.
- [78] H. Franz, G. Wallner, and J. Peisl. Correlation of vacancies in α -iron and copper after low temperature neutron irradiation observed by small-angle scattering of synchrotron radiation. *Radiat. Eff. Defects Solids*, 128(3):189–204, apr 1994.
- [79] P. Asoka-Kumar and K. G. Lynn. Applications of Positron Annihilation Spectroscopy. *Le J. Phys. IV*, 05(C1):C1–15–C1–25, jan 1995.
- [80] F. Bergner, A. Ulbricht, M. Hernandez-Mayoral, and P.K. Pranzas. Small-angle neutron scattering study of neutron-irradiated iron and an ironnickel alloy. *J. Nucl. Mater.*, 374(1-2):334–337, feb 2008.
- [81] C.A. English and M. Jenkins. Insight into Cascade Processes Arising from Studies of Cascade Collapse. *Mater. Sci. Forum*, 15-18:1003–1022, jan 1987.
- [82] M.L. Jenkins, M.A. Kirk, and W.J. Phythian. Experimental studies of cascade phenomena in metals. *J. Nucl. Mater.*, 205(C):16–30, oct 1993.
- [83] Michio Kiritani. Similarity and difference between fcc, bcc and hcp metals from the view point of point defect cluster formation. *J. Nucl. Mater.*, 276(1-3):41–49, jan 2000.
- [84] M.J. Norgett, M.T. Robinson, and I.M. Torrens. A proposed method of calculating displacement dose rates. *Nucl. Eng. Des.*, 33(1):50–54, aug 1975.
- [85] R.S. Averback. Atomic displacement processes in irradiated metals. *J. Nucl. Mater.*, 216(C):49–62, oct 1994.
- [86] Kai Nordlund, Steven J. Zinkle, Andrea E. Sand, Fredric Granberg, Robert S. Averback, Roger E. Stoller, Tomoaki Suzudo, Lorenzo Malerba, Florian Banhart, William J. Weber, Francois Willaime, Sergei L. Dudarev, and David Simeone. Primary radiation damage: A review of current understanding and models. *J. Nucl. Mater.*, 512:450–479, 2018.
- [87] Kai Nordlund, Steven J. Zinkle, Andrea E. Sand, Fredric Granberg, Robert S. Averback, Roger Stoller, Tomoaki Suzudo, Lorenzo Malerba, Florian Banhart, William J. Weber, Francois Willaime, Sergei L. Dudarev, and David Simeone. Improving atomic displacement and replacement calculations with physically realistic damage models. *Nat. Commun.*, 9(1):1084, dec 2018.

- [88] Uffe Littmark and Wolfgang O. Hofer. Recoil mixing in solids by energetic ion beams. *Nucl. Instruments Methods*, 168(1-3):329–342, 1980.
- [89] G H Vineyard. Thermal spikes and activated processes. *Radiat. Eff.*, 29(4):245–248, 1976.
- [90] R Benedek, W E King, and T Diaz De Rubia. Role of Thermal Spikes in Energetic Displacement Cascades. *Phys. Rev. Lett.*, 59(17):1930–1933, 1987.
- [91] K. Nordlund and R. S. Averback. Inverse kirkendall mixing in collision cascades. *Phys. Rev. B*, 59(1):20–23, 1999.
- [92] Mark T. Robinson. Basic physics of radiation damage production. *J. Nucl. Mater.*, 216(C):1–28, 1994.
- [93] L. Malerba. Molecular dynamics simulation of displacement cascades in α -Fe: A critical review. *J. Nucl. Mater.*, 351(1-3):28–38, jun 2006.
- [94] A.F. Calder and D.J. Bacon. A molecular dynamics study of displacement cascades in α -iron. *J. Nucl. Mater.*, 207(C):25–45, dec 1993.
- [95] K. Nordlund, J. Keinonen, M. Ghaly, and R. S. Averback. Coherent displacement of atoms during ion irradiation. *Nature*, 398(6722):49–51, mar 1999.
- [96] A.F. Calder, D.J. Bacon, A.V. Barashev, and Yu.N. Osetsky. On the origin of large interstitial clusters in displacement cascades. *Philos. Mag.*, 90(7-8):863–884, mar 2010.
- [97] L. Malerba, D. Terentyev, P. Olsson, R. Chakarova, and J. Wallenius. Molecular dynamics simulation of displacement cascades in FeCr alloys. *J. Nucl. Mater.*, 329-333(1-3 PART B):1156–1160, aug 2004.
- [98] D.A. Terentyev, L. Malerba, R. Chakarova, K. Nordlund, P. Olsson, M. Rieth, and J. Wallenius. Displacement cascades in FeCr: A molecular dynamics study. *J. Nucl. Mater.*, 349(1-2):119–132, feb 2006.
- [99] A. Okada, H. Maeda, K. Hamada, and I. Ishida. Defect structure development in a pure iron and dilute iron alloys irradiated with neutrons and electrons. *J. Nucl. Mater.*, 271-272:133–138, may 1999.
- [100] K. Arakawa, M. Hatanaka, H. Mori, and K. Ono. Effects of chromium on the one-dimensional motion of interstitial-type dislocation loops in iron. *J. Nucl. Mater.*, 329-333(1-3 PART B):1194–1198, aug 2004.
- [101] C.S. Becquart, C. Domain, J.C. van Duysen, and J.M. Raulot. The role of Cu in displacement cascades examined by molecular dynamics. *J. Nucl. Mater.*, 294(3):274–287, apr 2001.
- [102] Andrew F. Calder, David J. Bacon, Alexander V. Barashev, and Yuri N. Osetsky. Computer simulation of cascade damage in α -iron with carbon in solution. *J. Nucl. Mater.*, 382(2-3):91–95, dec 2008.

- [103] Donghua Xu, Alicia Certain, Hyon-Jee Lee Voigt, Todd Allen, and Brian D. Wirth. Ballistic effects on the copper precipitation and re-dissolution kinetics in an ion irradiated and thermally annealed FeCu alloy. *J. Chem. Phys.*, 145(10):104704, sep 2016.
- [104] Frédéric Soisson, Estelle Meslin, and Olivier Tissot. Atomistic modeling of α' precipitation in Fe-Cr alloys under charged particles and neutron irradiations: Effects of ballistic mixing and sink densities. *J. Nucl. Mater.*, 508:583–594, sep 2018.
- [105] K.-Y. Liou and P. Wilkes. The radiation disorder model of phase stability. *J. Nucl. Mater.*, 87(2-3):317–330, dec 1979.
- [106] Sidney Siegel. Effect of Neutron Bombardment on Order in the Alloy Cu₃Au. *Phys. Rev.*, 75(12):1823–1824, jun 1949.
- [107] P. Sigmund and A. Gras-Marti. Theoretical aspects of atomic mixing by ion beams. *Nucl. Instruments Methods*, 182-183(September):25–41, apr 1981.
- [108] W.L. Johnson, Y.T. Cheng, M. Van Rossum, and M-A. Nicolet. When is thermodynamics relevant to ion-induced atomic rearrangements in metals? *Nucl. Instruments Methods Phys. Res. Sect. B Beam Interact. with Mater. Atoms*, 7-8(PART 2):657–665, mar 1985.
- [109] M. Van Rossum, YT. Cheng, MA. Nicolet, and W. L. Johnson. Correlation between cohesive energy and mixing rate in ion mixing of metallic bilayers. *Appl. Phys. Lett.*, 46(6):610–612, mar 1985.
- [110] K. Nordlund, M. Ghaly, and R. S. Averback. Mechanisms of ion beam mixing in metals and semiconductors. *J. Appl. Phys.*, 83(3):1238–1246, feb 1998.
- [111] S.-J. Kim, M-A. Nicolet, R. S. Averback, and D. Peak. Low-temperature ion-beam mixing in metals. *Phys. Rev. B*, 37(1):38–49, jan 1988.
- [112] J.P. Biersack and L.G. Haggmark. A Monte Carlo computer program for the transport of energetic ions in amorphous targets. *Nucl. Instruments Methods*, 174(1-2):257–269, aug 1980.
- [113] C. Borschel and C. Ronning. Ion beam irradiation of nanostructures A 3D Monte Carlo simulation code. *Nucl. Instruments Methods Phys. Res. Sect. B Beam Interact. with Mater. Atoms*, 269(19):2133–2138, oct 2011.
- [114] Jean-Paul Crocombette and Christian Van Wambeke. Quick calculation of damage for ion irradiation: implementation in Iradina and comparisons to SRIM. *EPJ Nucl. Sci. Technol.*, 5:7, may 2019.
- [115] L. E. Rehn. Production of freely-migrating defects. *J. Nucl. Mater.*, 174(2-3):144–150, 1990.
- [116] V. Naundorf, M. P. Macht, and H. Wollenberger. Production rate of freely migrating defects for ion irradiation. *J. Nucl. Mater.*, 186(3):227–236, 1992.
- [117] G. W. Greenwood, A. J.E. Foreman, and D. E. Rimmer. The role of vacancies and dislocations in the nucleation and growth of gas bubbles in irradiated fissile material. *J. Nucl. Mater.*, 1(4):305–324, 1959.

- [118] A. D. Brailsford and R. Bullough. The rate theory of swelling due to void growth in irradiated metals. *J. Nucl. Mater.*, 44(2):121–135, 1972.
- [119] F. A. Nichols. On the estimation of sink-absorption terms in reaction-rate-theory analysis of radiation damage. *J. Nucl. Mater.*, 75(1):32–41, 1978.
- [120] P. T. Heald and M. V. Speight. Point defect behaviour in irradiated materials. *Acta Metall.*, 23(11):1389–1399, 1975.
- [121] Thomas Schuler, Maylise Nastar, and Frédéric Soisson. Vacancy-induced dissolution of precipitates in out-of-equilibrium systems: A test case of FeX (X= C,N,O) alloys. *Phys. Rev. B*, 95(1):014113, 2017.
- [122] Thomas Schuler, Pascal Bellon, Dallas R. Trinkle, and Robert S. Averback. Modeling the long-term evolution of dilute solid solutions in the presence of vacancy fluxes. *Phys. Rev. Mater.*, 2(7):073605, 2018.
- [123] H Wiedersich. On the theory of void formation during irradiation. *Radiat. Eff.*, 12(1-2):111–125, 1972.
- [124] H. Rouchette, L. Thuinet, A. Legris, A. Ambard, and C. Domain. Quantitative phase field model for dislocation sink strength calculations. *Comput. Mater. Sci.*, 88:50–60, 2014.
- [125] A. Seeger and U. Gösele. Steady-state diffusion of point defects to dislocation loops. *Phys. Lett. A*, 61(6):423–425, 1977.
- [126] H. Rauh and D. Simon. On the diffusion process of point defects in the stress field of edge dislocations. *Phys. Status Solidi*, 46(2):499–510, 1978.
- [127] J.D. Eshelby. The Continuum Theory of Lattice Defects. In *Solid State Phys. - Adv. Res. Appl.*, volume 3, pages 79–144. 1956.
- [128] R. Bullough and R. C. Newman. The kinetics of migration of point defects to dislocations. *Reports Prog. Phys.*, 33(1):303, jan 1970.
- [129] D. Hull and D.J. Bacon. *Introduction to Dislocations*. Elsevier, 2011.
- [130] V. A. Borodin, A. I. Ryazanov, and C. Abromeit. Void bias factors due to the anisotropy of the point defect diffusion. *J. Nucl. Mater.*, 207(C):242–254, 1993.
- [131] V. I. Dubinko, A. S. Abyzov, and A. A. Turkin. Numerical evaluation of the dislocation loop bias. *J. Nucl. Mater.*, 336(1):11–21, 2005.
- [132] C. N. Tomé, H. A. Cecatto, and E. J. Savino. Point-defect diffusion in a strained crystal. *Phys. Rev. B*, 25(12):7428–7440, 1982.
- [133] Zhongwen Chang, Pär Olsson, Dmitry Terentyev, and Nils Sandberg. Dislocation bias factors in fcc copper derived from atomistic calculations. *J. Nucl. Mater.*, 441(1-3):357–363, 2013.

- [134] Zhongwen Chang, Nils Sandberg, Dmitry Terentyev, Karl Samuelsson, Giovanni Bonny, and Pär Olsson. Assessment of the dislocation bias in fcc metals and extrapolation to austenitic steels. *J. Nucl. Mater.*, 465:13–19, 2015.
- [135] T. Jourdan. Influence of dislocation and dislocation loop biases on microstructures simulated by rate equation cluster dynamics. *J. Nucl. Mater.*, 467:286–301, 2015.
- [136] H. Rouchette, L. Thuinet, A. Legris, A. Ambard, and C. Domain. Numerical evaluation of dislocation loop sink strengths: A phase-field approach. *Nucl. Instruments Methods Phys. Res. Sect. B Beam Interact. with Mater. Atoms*, 352:31–35, 2015.
- [137] L. Thuinet, H. Rouchette, and A. Legris. 3D phase-field modelling of dislocation loop sink strengths. *J. Nucl. Mater.*, 483:62–81, 2017.
- [138] Lorenzo Malerba, Charlotte S. Becquart, and Christophe Domain. Object kinetic Monte Carlo study of sink strengths. *J. Nucl. Mater.*, 360(2):159–169, 2007.
- [139] A. Vattré, T. Jourdan, H. Ding, M. C. Marinica, and M. J. Demkowicz. Non-random walk diffusion enhances the sink strength of semicoherent interfaces. *Nat. Commun.*, 7, 2016.
- [140] D. Carpentier, T. Jourdan, Y. Le Bouar, and M. C. Marinica. Effect of saddle point anisotropy of point defects on their absorption by dislocations and cavities. *Acta Mater.*, 136:323–334, 2017.
- [141] Emmanuel Clouet, Céline Varvenne, and Thomas Jourdan. Elastic modeling of point-defects and their interaction. *Comput. Mater. Sci.*, 147:49–63, 2018.
- [142] P. Glansdorff, I. Prigogine, and Robert Nyden Hill. Thermodynamic Theory of Structure, Stability and Fluctuations. *Am. J. Phys.*, 41(1):147–148, jan 1973.
- [143] R. P. Agarwala (Ed.). *Diffusion processes in nuclear materials*. Netherlands: North-Holland, 1992.
- [144] A. Müller, V. Naundorf, and M. P. Macht. Point defect sinks in self-ion-irradiated nickel: A self-diffusion investigation. *J. Appl. Phys.*, 64(7):3445–3455, 1988.
- [145] H.P. Bonzel. Diffusion of Ni-63 in alpha-irradiated copper. *Acta Metall.*, 13(10):1084–1086, oct 1965.
- [146] D. Acker, M. Beyeler, G. Brebec, M. Bendazzoli, and J. Gilbert. Effet de l’irradiation aux neutrons sur l’hétérodifffusion à dilution infinie de l’or et du cuivre dans l’aluminium. *J. Nucl. Mater.*, 50(3):281–297, 1974.
- [147] S. M. Myers and S. T. Picraux. Enhanced diffusion of Zn in Al under high-flux heavy-ion irradiation. *J. Appl. Phys.*, 46(11):4774–4776, 1975.
- [148] M Macht, V Naundorf, and H R Wollenber. Irradiation induced self- and solute-diffusion in Ni and Fe-20Cr-20Ni. *J. Nucl. Mater.*, 133-134:420–422, 1985.

- [149] M. P Macht, A. Müller, V. Naundorf, and H. Wollenberger. Determination of temperaturedependent sink concentrations in ionirradiated nickel and copper by diffusion measurements. *Phys. Status Solidi*, 104(1):287–295, 1987.
- [150] A. R. Allnatt and E. L. Allnatt. Computer simulation of phenomenological coefficients for atom transport in a random alloy. *Philos. Mag. A*, 49(5):625–635, nov 1984.
- [151] A. R. Allnatt. Theory of phenomenological coefficients in solid-state diffusion. I. General expressions. *J. Chem. Phys.*, 43(6):1855–1863, 1965.
- [152] A R Allnatt. Einstein and linear response formulae for the transport in solids. *J. Phys. C Solid State Phys.*, 15:5605, 1982.
- [153] V Barbe and M Nastar. Phenomenological coefficients in a dilute BCC alloy for the dumbbell mechanism. *Philos. Mag.*, 87(11):1649–1669, 2007.
- [154] V. Barbe and M. Nastar. Split interstitials in an interacting bcc alloy. II. Transport coefficients. *Phys. Rev. B - Condens. Matter Mater. Phys.*, 76(5):054206, 2007.
- [155] John R. Manning. Correlation factors for diffusion in nondilute alloys. *Phys. Rev. B*, 4(4):1111–1121, 1971.
- [156] J. L. Bocquet. Percolative diffusion of a dumbbell interstitial defect on a fcc lattice: Calculation of a percolation threshold with use of a series method. *Phys. Rev. B*, 50(22):16386–16402, dec 1994.
- [157] H Barker. On diffusion kinetics in ordered binary alloys. *Philos. Mag. A*, 40(4):525–540, 1979.
- [158] N. A. Stolwijk. Correlation Factors for Diffusion in Binary Alloys with ShortRange Order. *Phys. Status Solidi*, 105(1):223–232, 1981.
- [159] Maylise Nastar and Emmanuel Clouet. Mean field theories for the description of diffusion and phase transformations controlled by diffusion. *Phys. Chem. Chem. Phys.*, 6(13):3611–3619, 2004.
- [160] M. Nastar. A mean field theory for diffusion in a dilute multi-component alloy: A new model for the effect of solutes on self-diffusion. *Philos. Mag.*, 85(32):3767–3794, 2005.
- [161] Maylise Nastar and Vincent Barbe. A self-consistent mean field theory for diffusion in alloys. *Faraday Discuss.*, 134:331–342, 2007.
- [162] Maylise Nastar. Diffusion and coupled fluxes in concentrated alloys under irradiation: a self-consistent mean-field approach. *Comptes Rendus Phys.*, 9(3-4):362–369, 2008.
- [163] Ryoichi Kikuchi and Hiroshi Sato. Correlation factor in substitutional diffusion in binary alloys. *J. Chem. Phys.*, 53(7):2702–2713, 1970.
- [164] Ryoichi Kikuchi and Hiroshi Sato. Diffusion coefficient in an ordered binary alloy. *J. Chem. Phys.*, 57(11):4962–4979, 1972.

- [165] Hiroshi Sato and Ryoichi Kikuchi. Kinetics of order-disorder transformations in alloys. *Acta Metall.*, 24(9):797–809, 1976.
- [166] V. Barbe and M. Nastar. Phenomenological coefficients in a concentrated alloy for the dumbbell mechanism. *Philos. Mag.*, 86(23):3503–3535, 2006.
- [167] Thomas Schuler, Luca Messina, and Maylise Nastar. KineCluE: A kinetic cluster expansion code to compute transport coefficients beyond the dilute limit. *Comput. Mater. Sci.*, 172(May 2019):109191, feb 2020.
- [168] D. L. Porter. Ferrite formation in neutron-irradiated type 304L stainless steel. *J. Nucl. Mater.*, 79(2):406–411, 1979.
- [169] T. R. Anthony. Segregation of zinc to vacancy sinks in aluminum. *J. Appl. Phys.*, 41(10):3969–3976, 1970.
- [170] G. C. Kuczynski, G. Matsumura, and B. D. Cullity. Segregation in homogeneous alloys during sintering. *Acta Metall.*, 8(3):209–215, 1960.
- [171] K. T. Aust, R. E. Hanneman, P. Niessen, and J. H. Westbrook. Solute induced hardening near grain boundaries in zone refined metals. *Acta Metall.*, 16(3):291–302, 1968.
- [172] S. D. Okamoto, P. R.; Harkness and J. J. Laidler. Solute induced hardening near grain boundaries in zone refined metals. *Trans. Am. Nucl. Soc.*, 16:70–70, 1973.
- [173] A. D. Marwick. Segregation in irradiated alloys: The inverse Kirkendall effect and the effect of constitution on void swelling. *J. Phys. F Met. Phys.*, 8(9):1849–1861, 1978.
- [174] Gary S. Was, Janelle P. Wharry, Brian Frisbie, Brian D. Wirth, Dane Morgan, Julie D. Tucker, and Todd R. Allen. Assessment of radiation-induced segregation mechanisms in austenitic and ferritic-martensitic alloys. *Journal of Nuclear Materials*, 411(1-3):41–50, apr 2011.
- [175] Janelle P. Wharry and Gary S. Was. A systematic study of radiation-induced segregation in ferritic-martensitic alloys. *Journal of Nuclear Materials*, 442(1-3):7–16, 2013.
- [176] Janelle P. Wharry and Gary S. Was. The mechanism of radiation-induced segregation in ferritic-martensitic alloys. *Acta Materialia*, 65:42–55, 2014.
- [177] A. D. Marwick, R. C. Piller, and P. M. Sivell. Mechanisms of radiation-induced segregation in dilute nickel alloys. *J. Nucl. Mater.*, 83(1):35–41, 1979.
- [178] D. I. Potter, P. R. Okamoto, H. Wiedersich, J. R. Wallace, and A. W. McCormick. Heterogeneous precipitation at internal and external surfaces during irradiation of Ni-12.7 at.% Si. *Acta Metall.*, 27(7):1175–1185, 1979.
- [179] T. Ezawa, E. Wakai, and R. Oshima. Radiation-induced segregation in model alloys. *J. Nucl. Mater.*, 283-287(PART I):244–248, 2000.
- [180] Thomas Garnier, Dallas R Trinkle, Maylise Nastar, and Pascal Bellon. Quantitative modeling of solute drag by vacancies in face-centered-cubic alloys. *Phys. Rev. B*, 89(14):144202, apr 2014.

- [181] Luca Messina, Maylise Nastar, Thomas Garnier, Christophe Domain, and Pär Olsson. Exact ab initio transport coefficients in bcc Fe–X (X = Cr, Cu, Mn, Ni, P, Si) dilute alloys. *Phys. Rev. B*, 90(10):104203, sep 2014.
- [182] Robert A. Johnson and Nghi Q. Lam. Solute segregation in metals under irradiation. *Phys. Rev. B*, 13(10):4364–4375, 1976.
- [183] Rudolf Sizmann. The effect of radiation upon diffusion in metals. *Journal of Nuclear Materials*, 69-70:386 – 412, 1978.
- [184] L. K. Mansur. Theory of transitions in dose dependence of radiation effects in structural alloys. *J. Nucl. Mater.*, 206(2-3):306–323, 1993.
- [185] Thomas Garnier, Venkateswara R. Manga, Dallas R. Trinkle, Maylise Nastar, and Pascal Bellon. Stress-induced anisotropic diffusion in alloys: Complex Si solute flow near a dislocation core in Ni. *Phys. Rev. B*, 88(13):134108, oct 2013.
- [186] Thomas Garnier, Venkateswara R. Manga, Pascal Bellon, and Dallas R. Trinkle. Diffusion of Si impurities in Ni under stress: A first-principles study. *Phys. Rev. B*, 90(2):024306, jul 2014.
- [187] Thomas Garnier, Zebo Li, Maylise Nastar, Pascal Bellon, and Dallas R. Trinkle. Calculation of strain effects on vacancy-mediated diffusion of impurities in fcc structures: General approach and application to ni-si. *Phys. Rev. B*, 90(18):184301, nov 2014.
- [188] H. Wiedersich, P. R. Okamoto, and N. Q. Lam. A theory of radiation-induced segregation in concentrated alloys. *J. Nucl. Mater.*, 83(1):98–108, 1979.
- [189] W. G. Wolfer. Drift forces on vacancies and interstitials in alloys with radiation-induced segregation. *J. Nucl. Mater.*, 114(2-3):292–304, 1983.
- [190] R. A. Johnson. Point-Defect Calculations for an fcc Lattice. *Phys. Rev.*, 145(2):423–433, may 1966.
- [191] C. Domain and C. S. Becquart. Ab initio calculations of defects in Fe and dilute Fe-Cu alloys. *Phys. Rev. B*, 65(2):024103, dec 2001.
- [192] George H. Vineyard. Frequency factors and isotope effects in solid state rate processes. *J. Phys. Chem. Solids*, 3(1-2):121–127, 1957.
- [193] J. D. Tucker, R. Najafabadi, T. R. Allen, and D. Morgan. Ab initio-based diffusion theory and tracer diffusion in Ni-Cr and Ni-Fe alloys. *J. Nucl. Mater.*, 405(3):216–234, 2010.
- [194] A.B. Lidiard. CXXXIII. Impurity diffusion in crystals (mainly ionic crystals with the sodium chloride structure). *London, Edinburgh, Dublin Philos. Mag. J. Sci.*, 46(382):1218–1237, nov 1955.
- [195] A B Lidiard. The influence of solutes on self-diffusion in metals. *Philos. Mag.*, 5(59):1171–1180, nov 1960.
- [196] R. Siems. Mechanical Interactions of Point Defects. *Phys. Status Solidi*, 30(2):645–658, 1968.

- [197] H Lehmann G Leibfried W Paul. *Point Defects in Metals I*, volume 81 of *Springer Tracts in Modern Physics 81*. Springer-Verlag, Berlin/Heidelberg, 1978.
- [198] D.J. Bacon, D.M. Barnett, and R.O. Scattergood. Anisotropic continuum theory of lattice defects. *Prog. Mater. Sci.*, 23(C):51–262, jan 1980.
- [199] Cristian Teodosiu. *Elastic Models of Crystal Defects*. Springer Berlin Heidelberg, Berlin, Heidelberg, 1982.
- [200] H. Kanzaki. Point defects in face-centred cubic lattice I distortion around defects. *J. Phys. Chem. Solids*, 2(1):24–36, mar 1957.
- [201] V.K. Tewary. Green-function method for lattice statics. *Adv. Phys.*, 22(6):757–810, nov 1973.
- [202] C. Domain, C. S. Becquart, and J. Foct. Ab initio study of foreign interstitial atom (C, N) interactions with intrinsic point defects in α -Fe. *Phys. Rev. B*, 69(14):144112, apr 2004.
- [203] Erin Hayward, Chaitanya Deo, Blas P. Uberuaga, and Carlos N. Tomé. The interaction of a screw dislocation with point defects in bcc iron. *Philos. Mag.*, 92(22):2759–2778, aug 2012.
- [204] H. R. Schober and K. W. Ingle. Calculation of relaxation volumes, dipole tensors and Kanzaki forces for point defects. *J. Phys. F Met. Phys.*, 10(4):575–581, apr 1980.
- [205] K H Robrock and W Schilling. Diaelastic modulus change of aluminium after low temperature electron irradiation. *J. Phys. F Met. Phys.*, 6(3):303–314, mar 1976.
- [206] V. Spirić, L. E. Rehn, K.-H. Robrock, and W. Schilling. Anelastic relaxation due to single self-interstitial atoms in electron-irradiated Al. *Phys. Rev. B*, 15(2):672–679, jan 1977.
- [207] Raúl A. Enrique and Pascal Bellon. Compositional patterning in systems driven by competing dynamics of different length scale. *Phys. Rev. Lett.*, 84(13):2885–2888, 2000.
- [208] G Martin. Phase stability under irradiation: Ballistic effects. *Phys. Rev. B*, 30(3):1424–1436, 1984.
- [209] R. S. Averback. Fundamental aspects of ion beam mixing. *Nucl. Inst. Methods Phys. Res. B*, 15(1-6):675–687, 1986.
- [210] C. A. English and M. L. Jenkins. Characterization of displacement cascade damage produced in Cu₃Au by fast-particle irradiation. *J. Nucl. Mater.*, 96(3):341–357, 1981.
- [211] Dipankar Pramanik and David N. Seidman. Atomic resolution study of displacement cascades in ion-irradiated platinum. *J. Appl. Phys.*, 60(1):137–150, 1986.
- [212] Dilpuneet S Aidhy, Chenyang Lu, Ke Jin, Hongbin Bei, Yanwen Zhang, Lumin Wang, and William J Weber. Acta Materialia Point defect evolution in Ni, NiFe and NiCr alloys from atomistic simulations and irradiation experiments q. *Acta Mater.*, 99:69–76, 2015.

- [213] Yaxuan Zhang, Daniel Schwen, and Xian Ming Bai. Molecular dynamics simulations of concentration-dependent defect production in Fe-Cr and Fe-Cu alloys. *J. Appl. Phys.*, 122(22), 2017.
- [214] Hyeon-Seok Do and Byeong-Joo Lee. Origin of radiation resistance in multi-principal element alloys. *Sci. Rep.*, pages 1–9, 2018.
- [215] C. R. Lear, P. Bellon, and R. S. Averback. Novel mechanism for order patterning in alloys driven by irradiation. *Phys. Rev. B*, 96(10):1–11, 2017.
- [216] Raúl A. Enrique and Pascal Bellon. Compositional patterning in immiscible alloys driven by irradiation. *Phys. Rev. B*, 63(13):134111, mar 2001.
- [217] Lars Onsager. RECIPROCAL RELATIONS IN IRREVERSIBLE PROCESSES. I. *Phys. Rev.*, 37:405–426, 1931.
- [218] Lars Onsager. RECIPROCAL RELATIONS IN IRREVERSIBLE PROCESSES. II. *Phys. Rev.*, 38:2265–2279, 1931.
- [219] Denis J. Evans, E. G D Cohen, and G. P. Morriss. Probability of second law violations in shearing steady states. *Phys. Rev. Lett.*, 71(15):2401–2404, 1993.
- [220] Giovanni Gallavotti. Extension of onsager’s reciprocity to large fields and the chaotic hypothesis. *Phys. Rev. Lett.*, 77(21):4334–4337, 1996.
- [221] A. W.C. Lau, D. Lacoste, and K. Mallick. Nonequilibrium fluctuations and mechanochemical couplings of a molecular motor. *Phys. Rev. Lett.*, 99(15):1–4, 2007.
- [222] D. Lacoste, A. W.C. Lau, and K. Mallick. Fluctuation theorem and large deviation function for a solvable model of a molecular motor. *Phys. Rev. E*, 78(1), 2008.
- [223] A R Allnatt and A B Lidiard. *Atomic Transport in Solids*. Cambridge University Press, 1993.
- [224] Luca Messina, Maylise Nastar, Nils Sandberg, and Pär Olsson. Systematic electronic-structure investigation of substitutional impurity diffusion and flux coupling in bcc iron. *Phys. Rev. B*, 93(18):1–18, 2016.
- [225] Thomas Schuler and Maylise Nastar. Transport properties of dilute Fe(X) solid solutions (X = C, N, O). *Phys. Rev. B*, 93(22):224101, jun 2016.
- [226] Abhinav C P Jain, Patrick A Burr, and Dallas R Trinkle. First-principles calculations of solute transport in zirconium: Vacancy-mediated diffusion with metastable states and interstitial diffusion. *Phys. Rev. Mater.*, 3(3):33402, mar 2019.
- [227] R. A. Enrique, K. Nordlund, R. S. Averback, and P. Bellon. Simulations of dynamical stabilization of Ag–Cu nanocomposites by ion-beam processing. *J. Appl. Phys.* 93, 93(5):2917–2923, 2003.
- [228] G. Demange, E. Antoshchenkova, M. Hayoun, L. Lunéville, and D. Simeone. Simulating the ballistic effects of ion irradiation in the binary collision approximation: A first step toward the ion mixing framework. *J. Nucl. Mater.*, 486:26–33, 2017.

- [229] W. J. Phythian, R. E. Stoller, A. J.E. Foreman, A. F. Calder, and D. J. Bacon. A comparison of displacement cascades in copper and iron by molecular dynamics and its application to microstructural evolution. *J. Nucl. Mater.*, 223(3):245–261, 1995.
- [230] J. P. Rivière and J. F. Dinhut. Low-temperature fission-neutron disordering of Fe-Co and Fe-Co-X (X = Mn, V, Ti) ordered alloys. *J. Nucl. Mater.*, 118(2-3):333–341, 1983.
- [231] K. C. Russell. Phase stability under irradiation. *Prog. Mater. Sci.*, 28(3-4):229–434, 1984.
- [232] M. Nastar, V. Yu Dobretsov, and G. Martin. Self-consistent formulation of configurational kinetics close to equilibrium: The phenomenological coefficients for diffusion in crystalline solids. *Philos. Mag. A*, 80(1):155–184, 2000.
- [233] R E Howard and A B Lidiard. Matter transport in solids. *Rep. Prog. Phys.*, 161, 1964.
- [234] Henry Wu, Tam Mayeshiba, and Dane Morgan. High-Throughput ab-initio dilute solute diffusion database. *Sci. Data*, 3:1–11, 2016.
- [235] E. Meslin, A. Barbu, L. Boulanger, B. Radiguet, P. Pareige, K. Arakawa, and C. C. Fu. Cluster-dynamics modelling of defects in α -iron under cascade damage conditions. *J. Nucl. Mater.*, 382(2-3):190–196, 2008.
- [236] H.T. Davis. *Introduction to Nonlinear Differential and Integral Equations*. Dover, New York, 1962.
- [237] Nghi Q Lam, Steven J Rothman, and Rudolf Sizmanns. Steady-state point-defect diffusion profiles in solids during irradiation. *Radiat. Eff.*, 23(1):53–59, 1974.
- [238] H Rauht, M H Wood, and R Bullough. Void sink strength including bulk recombination. *Philos. Mag. A*, 44(6):1255–1276, 1981.
- [239] Stephen M. Foiles. Calculation of grain-boundary segregation in Ni-Cu alloys. *Phys. Rev. B*, 40(17):11502–11506, dec 1989.
- [240] M. Menyhard, Min Yan, and V. Vitek. Atomistic vs phenomenological approaches to grain boundary segregation: Computer modeling of CuAg alloys. *Acta Metall. Mater.*, 42(8):2783–2796, aug 1994.
- [241] Jérôme Creuze, Fabienne Berthier, Robert Tétot, and Bernard Legrand. Intergranular segregation and ordering effect: A mixed monte carlo mean-field approach. *Phys. Rev. B*, 62:2813–2824, Jul 2000.
- [242] Christopher M. Barr, Peter J. Felfer, James I. Cole, and Mitra L. Taheri. Observation of oscillatory radiation induced segregation profiles at grain boundaries in neutron irradiated 316 stainless steel using atom probe tomography. *J. Nucl. Mater.*, 504:181–190, jun 2018.
- [243] George E. Andrews, Richard Askey, and Ranjan Roy. *Special Functions*. Cambridge University Press, jan 1999.
- [244] Elin troijer, Luca Messina, Julien Vidal, Christophe Domain, Charlotte Becquart, and Pär Olsson. Point Defect Interactions and Kinetics in FCC Nickel. In *Euromat 2019*, Stockholm, Sweden, September 2019.

- [245] G. Kresse and J. Hafner. Ab initio molecular dynamics for liquid metals. *Phys. Rev. B*, 47(1):558–561, jan 1993.
- [246] G. Kresse and J. Hafner. Norm-conserving and ultrasoft pseudopotentials for first-row and transition elements. *J. Phys. Condens. Matter*, 6(40):8245–8257, oct 1994.
- [247] G. Kresse and J. Hafner. Ab initio molecular-dynamics simulation of the liquid-metalamorphous-semiconductor transition in germanium. *Phys. Rev. B*, 49(20):14251–14269, may 1994.
- [248] P. E. Blöchl. Projector augmented-wave method. *Phys. Rev. B*, 50(24):17953–17979, dec 1994.
- [249] G. Kresse and D. Joubert. From ultrasoft pseudopotentials to the projector augmented-wave method. *Phys. Rev. B*, 59(3):1758–1775, jan 1999.
- [250] Daniel Farhat. Bookworms and party animals: an artificial labour market with human and social capital accumulation. *J. Educ. Work*, 27(1):1–42, jan 2014.
- [251] A. Janotti, M. Krčmar, C. L. Fu, and R. C. Reed. Solute Diffusion in Metals: Larger Atoms Can Move Faster. *Phys. Rev. Lett.*, 92(8):085901, feb 2004.
- [252] Toshiharu Ohnuma, Naoki Soneda, and Misako Iwasawa. First-principles calculations of vacancy-solute element interactions in body-centered cubic iron. *Acta Mater.*, 57(20):5947–5955, 2009.
- [253] A. J. E. Foreman. The diffusion of point defects to the foil surface during irradiation damage experiments in the high voltage electron microscope. *Radiat. Eff.*, 14(3-4):175–179, jun 1972.
- [254] Frédéric Soisson and Thomas Jourdan. Radiation-accelerated precipitation in Fe-Cr alloys. *Acta Mater.*, 103:870–881, 2016.
- [255] Kan Ma. private communication, September 2019.
- [256] Lisa Belkacemi. private communication, May 2020.
- [257] Emanuel A. Lazar, Jeremy K. Mason, Robert D. MacPherson, and David J. Srolovitz. Statistical topology of three-dimensional Poisson-Voronoi cells and cell boundary networks. *Phys. Rev. E*, 88(6):063309, dec 2013.
- [258] Susmit Kumar, Stewart K. Kurtz, Jayanth R. Banavar, and M. G. Sharma. Properties of a three-dimensional Poisson-Voronoi tessellation: A Monte Carlo study. *J. Stat. Phys.*, 67(3-4):523–551, may 1992.
- [259] Denise Carpentier. *Simulation of absorption kinetics of point defects by dislocations and defect clusters*. Theses, Université Paris-Saclay, October 2018.
- [260] J. P. Hirth, J. Lothe, and T. Mura. Theory of Dislocations (2nd ed.). *J. Appl. Mech.*, 50(2):476–477, jun 1983.

- [261] C. CAWTHORNE and E. J. FULTON. Voids in Irradiated Stainless Steel. *Nature*, 216(5115):575–576, nov 1967.
- [262] J.F. Nye. *Physical Properties of Crystals: Their Representation by Tensors and Matrices*. Oxford science publications. Clarendon Press, 1985.
- [263] Woldemar Voigt. *Lehrbuch der Kristallphysik*. Vieweg+Teubner Verlag, Wiesbaden, 1966.
- [264] R. F. S. Hearmon. *An introduction to applied anisotropic elasticity*. Oxford University Press, Oxford, 1961.
- [265] H. M. Ledbetter and R. P. Reed. Elastic Properties of Metals and Alloys, I. Iron, Nickel, and IronNickel Alloys. *J. Phys. Chem. Ref. Data*, 2(3):531–618, jul 1973.
- [266] Clarence Melvin Zener. *Elasticity and anelasticity of metals*. University of Chicago Press, Chicago, 1948.
- [267] H. J. McSkimin, W. L. Bond, E. Buehler, and G. K. Teal. Measurement of the Elastic Constants of Silicon Single Crystals and Their Thermal Coefficients. *Phys. Rev.*, 83(5):1080–1080, sep 1951.
- [268] J. A. Rayne and B. S. Chandrasekhar. Elastic Constants of Iron from 4.2 to 300řK. *Phys. Rev.*, 122(6):1714–1716, jun 1961.
- [269] J. J. Adams, D. S. Agosta, R. G. Leisure, and H. Ledbetter. Elastic constants of monocrystal iron from 3 to 500 K. *J. Appl. Phys.*, 100(11):113530, 2006.
- [270] Mattias Lundberg, Jonas Saarimäki, Johan J. Moverare, and Ru Lin Peng. Effective X-ray elastic constant of cast iron. *J. Mater. Sci.*, 53(4):2766–2773, feb 2018.
- [271] P. Ravindran, Lars Fast, P. A. Korzhavyi, B. Johansson, J. Wills, and O. Eriksson. Density functional theory for calculation of elastic properties of orthorhombic crystals: Application to TiSi₂. *J. Appl. Phys.*, 84(9):4891–4904, nov 1998.
- [272] Gerald L. Jones. Elastic constants in density-functional theory. *Mol. Phys.*, 61(2):455–466, jun 1987.
- [273] Kamal Choudhary, Gowoon Cheon, Evan Reed, and Francesca Tavazza. Elastic properties of bulk and low-dimensional materials using van der Waals density functional. *Phys. Rev. B*, 98(1):014107, jul 2018.
- [274] T. Paszkiewicz. Adiabatic and isothermal elastic constants for highly anharmonic crystals. *Phys. Condens. Matter*, 18(1):1–15, jul 1974.
- [275] J. Weertman. The PeachKoehler equation for the force on a dislocation modified for hydrostatic pressure. *Philos. Mag. A J. Theor. Exp. Appl. Phys.*, 11(114):1217–1223, jun 1965.
- [276] Zebo Li and Dallas R. Trinkle. Mesoscale modeling of vacancy-mediated Si segregation near an edge dislocation in Ni under irradiation. *Phys. Rev. B*, 95(14):144107, apr 2017.

- [277] Dallas R. Trinkle. Diffusivity and derivatives for interstitial solutes: activation energy, volume, and elastodiffusion tensors. *Philos. Mag.*, 96(26):2714–2735, sep 2016.
- [278] M. Friák, T. Hickel, F. Körmann, A. Udyansky, A. Dick, J. von Pezold, D. Ma, O. Kim, W.A. Counts, M. Šob, T. Gebhardt, D. Music, J. Schneider, D. Raabe, and J. Neugebauer. Determining the Elasticity of Materials Employing Quantum-mechanical Approaches: From the Electronic Ground State to the Limits of Materials Stability. *steel Res. Int.*, 82(2):86–100, feb 2011.
- [279] D. Psiachos, T. Hammerschmidt, and R. Drautz. Ab initio study of the modification of elastic properties of α -iron by hydrostatic strain and by hydrogen interstitials. *Acta Mater.*, 59(11):4255–4263, jun 2011.
- [280] Luca Messina. private communication, March 2020.
- [281] A. Van der Ven and G. Ceder. First Principles Calculation of the Interdiffusion Coefficient in Binary Alloys. *Phys. Rev. Lett.*, 94(4):045901, feb 2005.
- [282] R. Chang. The dilatational strain field associated with edge dislocations and edge dislocation walls based on anisotropic elasticity. *Acta Metall.*, 10(10):951–958, oct 1962.
- [283] C.H. Woo. Intrinsic bias differential between vacancy loops and interstitial loops. *J. Nucl. Mater.*, 107(1):20–30, may 1982.
- [284] I.-W. Chen. Anisotropic diffusion of point defects to edge dislocations. *J. Nucl. Mater.*, 125(1):52–63, jun 1984.
- [285] V.A. Borodin and A.I. Ryazanov. The effect of diffusion anisotropy on dislocation bias and irradiation creep in cubic lattice materials. *J. Nucl. Mater.*, 210(3):258–267, jun 1994.
- [286] Gabriel Franck Bouobda Moladje, Ludovic Thuinet, Charlotte S. Becquart, and Alexandre Legris. A phase field model for dislocation climb under irradiation: Formalism and applications to pure bcc iron and ferritic alloys. *Int. J. Plast.*, 134:102810, nov 2020.
- [287] G.T Barkema and Normand Mousseau. The activationrelaxation technique: an efficient algorithm for sampling energy landscapes. *Comput. Mater. Sci.*, 20(3-4):285–292, mar 2001.

Titre: Modélisation multi-échelle de la ségrégation induite par irradiation dans des alliages dilués base nickel et base fer

Mots clés: Thermodynamique - Diffusion - Physique statistique - Défaut ponctuel - Effets de l'irradiation - Force de puits - Élastodiffusion - Ségrégation induite par irradiation - Alliages dilués

Résumé: Nous présentons une modélisation quantitative de la redistribution des défauts ponctuels (DPs) et de la ségrégation induite par irradiation (SII) sur les défauts étendus, dans des alliages modèles dilués Ni(B \equiv Ti, Cr) et Fe(B \equiv P, Mn, Cr, Si, Ni, Cu). Le changement de composition chimique au voisinage des défauts étendus joue un rôle décisif sur l'évolution de la microstructure et les propriétés mécaniques d'un matériau. L'irradiation génère des défauts ponctuels, qui diffusent en s'échangeant avec les atomes voisins, s'annihilent en se recombinaison entre eux ou en interagissant avec des défauts étendus (qui agissent comme des puits de DPs). Les flux de DPs vers les puits induisent des flux atomiques dans le même sens ou le sens opposé des flux de DPs, produisant ainsi la SII aux puits. Nous étendons la théorie de champ moyen auto-cohérent aux déplacements atomiques forcés (DAF), mécanismes de diffusion athermiques générés par une cascade de déplacements sous irradiation. L'implémentation de nos développements théoriques dans le code KineCluE, nous permet de calculer les flux de DPs et d'atomes, et leurs couplages. À partir du calcul des flux en fonction de la température, de la composition, et du champ de déformation ; et d'un traitement de type cinétique chimique des réactions de production et d'annihilation des DPs, nous obtenons les profils stationnaires de SII. Dans chacun des régimes cinétiques particuliers pour lequel, l'une des réactions des DPs domine par rapport aux autres, nous obtenons les expressions analytiques des profils stationnaires des DPs et solutés sur les puits planaires. Pour rendre compte de l'effet du champ de déformation généré par une dislocation coin

sur la SII et sur les taux d'élimination des DPs sur la dislocation, nous résolvons numériquement les équations d'élastodiffusion. À partir d'une base de données ab initio des énergies de liaison, des dipôles élastiques, et des fréquences d'échange atome-DP dans, nous réalisons une étude systématique des effets de la microstructure et des conditions d'irradiation sur les propriétés de diffusion, les taux d'élimination des DPs aux puits, et la SII. Nous montrons que : (i) les boucles de dislocations sont enrichies en Ni dans Fe(Ni) et appauvries en Ti dans Ni(Ti), et les quantités ségréguées sont en bon accord avec les valeurs expérimentales mesurées dans les alliages modèles Fe(Ni) et Ni(Ti) irradiés aux ions ; (ii) à fort flux, basse température, et grande force de puits de la microstructure, les événements DAF réduisent sensiblement la SII, tout particulièrement dans les alliages base Ni ; (iii) les décalages en température calculés pour simuler les effets d'une irradiation aux neutrons par une irradiation aux ions, peuvent être très différents selon le phénomène induit par irradiation que l'on étudie, le régime cinétique dans lequel le système évolue, et la nature chimique de l'alliage étudié ; (iv) l'interaction entre les DPs et les atomes de soluté modifie le facteur de biais d'absorption entre lacunes et interstitiels d'une dislocation coin. Ainsi l'ajout de Ni produit un biais négatif alors que l'ajout de Mn augmente le facteur de biais (jusqu'à 200% de la valeur dans Fe pur sous contrainte), suivant la température et la composition ; (v) la contrainte augmente significativement la quantité de la ségrégation de soluté dans Fe(Ni) (par exemple, 400% de la valeur sans élasticité à 400 K), et change le signe de la SII dans Fe(Cr).

Title: Multiscale modeling of the radiation-induced segregation in Ni-based and Fe-based dilute alloys

Keywords: Thermodynamics - Diffusion - Statistical mechanics - Point defect - Irradiation effects - Sink strength - Elastodiffusion - Radiation-induced segregation - Dilute alloys

Abstract: We present a quantitative modeling of the point-defect (PD) redistribution and solute radiation-induced segregation (RIS) at extended defects in dilute Ni(B \equiv Ti, Cr) and Fe(B \equiv P, Mn, Cr, Si, Ni, Cu) alloys. The change in chemical composition, in the vicinity of extended defects, plays a decisive role on the evolution of the microstructure and mechanical properties of materials. Irradiation produces PDs, that diffuse by exchanging with neighboring atoms, annihilate by mutual recombination or by interacting with extended defects (that act as PD sinks). The fluxes of PDs towards sinks lead to atomic fluxes in the same or opposite direction of the PD flux; thereby producing RIS at sinks. We extend the self-consistent mean-field theory to forced atomic relocations (FARs), athermal diffusion mechanisms generated by displacement cascades under irradiation. The implementation of the extended theory in the KineCluE code allows us to compute PD and atomic fluxes, and their couplings. From the calculation of fluxes as a function of temperature, composition, and strain field; and a mean-field treatment of the production and annihilation reactions of PDs, we obtain the steady-state RIS profiles. In each of the particular kinetic regimes for which one of the PD reactions dominates over the others, we derive analytical expressions of steady-state profiles of PDs and solute atoms at planar sinks. To account for the effect of strain gener-

ated by an edge dislocation on the RIS and PD elimination rates, we numerically solve the elastodiffusion equations. Based on an ab initio database of binding energies, elastic dipoles, and atom-PD exchange frequencies, we perform a systematic study of the effects of the microstructure and irradiation conditions on diffusion properties, PD elimination rates at sinks, and RIS. We show that: (i) the dislocation loops are enriched in Ni in Fe(Ni) and depleted in Ti in Ni(Ti), and the calculated amounts of RIS are in good agreement with the experimental values measured in model Fe(Ni) and Ni(Ti) alloys irradiated by ions; (ii) at high flux, low temperature, and high sink strength, forced atomic relocations significantly reduce RIS, especially in Ni-based alloys; (iii) the temperature shifts calculated to simulate the effects of neutron irradiation by ion irradiation can be very different depending on the radiation-induced phenomenon, the kinetic regime in which the system evolves, and the chemical nature of the investigated alloy; (iv) the interactions between PDs and solute atoms change the absorption bias between vacancies and interstitials of an edge dislocation, as for instance, the addition of Ni leads to a negative bias while the addition of Mn increases the bias factor (up to 200% of the strained pure Fe value), depending on temperature and composition; (v) the dislocation strain field significantly increases Ni RIS (e.g., about 400% of the strain-free value at 400 K) in Fe(Ni), and changes the sign of RIS in Fe(Cr).